Spontaneous Uptake Dynamics of Gaseous and Liquid n-Alcohols in Nanoporous Vycor Glass

– Dissertation –

zur Erlangung des Grades
des Doktors der Naturwissenschaften
der Naturwissenschaftlich-Technischen Fakultät
der Universität des Saarlandes

von

Sebastian Andreas Kiepsch

Saarbrücken
2017

Tag des Kolloquiums:	12.01.2018
Dekan:	Univ.-Prof. Dr. rer. nat. Guido Kickelbick
Mitglieder des Prüfungsausschusses:	Univ.-Prof. Dr. techn. Romanus Dyczij-Edlinger (Vorsitz) Univ.-Prof. Dr. rer. nat. Rolf Pelster (Gutachter) Univ.-Prof. Dr. rer. nat. Christian Wagner (Gutachter)
Akademischer Mitarbeiter:	Dr. rer. nat. Herbert Wolf

Abstract

This work focusses on the experimental study of transport dynamics for different n-alcohols in the spatial confinement of a three-dimensional, isotropic network of meandering, cylindrical nanopores (radius $r_0 \approx 5\,\mathrm{nm}$) in monolithic Vycor glass.

Due to the high surface-to-volume ratio, interfacial effects are particularly important in nanoporous materials. Two such phenomena are the adsorption of molecules from a surrounding vapour phase as well as a spontaneous capillary rise into the pore space when in contact to a liquid. Using dielectric spectroscopy, the dynamic uptake of molecules has been studied for both individual processes and a combination thereof.

As a result of the strong interactions of n-alcohols with the silica surface of the Vycor matrix, a fixed boundary layer can form on the pore walls exhibiting properties different from the remaining pore filling. The equilibrium states and kinetics of adsorption can be used to determine the extent and mobility of this layer as a function of pore loading. Moreover, since the radius of the nanopores is comparable to molecular dimensions, a significant change in the hydrodynamic boundary condition ensues for liquid transport. This has been investigated for stationary, pressure-driven flows and spontaneous capillary flows as a function of the molecule length.

Kurzdarstellung

Im Fokus dieser Arbeit steht die experimentelle Untersuchung der Transportdynamik verschiedener n-Alkohole in der beschränkten Geometrie eines dreidimensionalen, isotropen Netzwerks von mäandrierenden, zylinderförmigen Nanoporen (Radius $r_0 \approx 5\,\mathrm{nm}$) in monolithischem Vycor-Glas.

Aufgrund des hohen Oberfläche-zu-Volumen-Verhältnisses sind Grenzflächeneffekte in nanoporösen Materialien von besonderer Bedeutung. Zwei solche Phänomene sind die Adsorption von Molekülen aus einer umgebenden Dampfphase sowie ein spontanes Kapillarsteigen in den Porenraum im Kontakt mit einer Flüssigkeit. Mittels dielektrischer Spektroskopie wurde die dynamische Aufnahme von Molekülen für die einzelnen Mechanismen und eine Überlagerung beider Prozesse untersucht.

Durch starke Wechselwirkungen der n-Alkohole mit der Siliziumoxidoberfläche der Vycor-Matrix kann sich an den Porenwänden eine gebundene Grenzschicht ausbilden, die sich in ihren Eigenschaften von der restlichen Porenfüllung unterscheidet. Gleichgewichtszustände und Kinetik der Gasadsorption können zur Bestimmung der Ausdehnung und Mobilität der Wandlage in Abhängigkeit der Porenfüllung genutzt werden. Da der Radius der Nanoporen zudem vergleichbar mit molekularen Größenordnungen ist, ergibt sich für den Transport von Flüssigkeiten eine signifikante Änderung der hydrodynamischen Randbedingung. Diese wurde für stationäre, druckgetriebene Flüsse und dynamische Kapillarflüsse in Abhängigkeit der Moleküllänge ermittelt.

Table of Contents

I

Introduction

1 Preface

Ever since ancient times, the microcosm fascinated philosophers and scientists alike. The idea that a world beyond our perception exists not only in the vastness of the universe but also in a miniature realm within our grasp inspired Demokrit, Dalton, Rutherford, Bohr and many others to theorize what makes up material objects and causes phenomena we encounter in our day-to-day lives.

With improved experimental methods and theoretical understanding, the striving to learn about these things we cannot see and the curiosity to venture into smaller and smaller dimensions has pioneered many scientific disciplines, e.g. atomic, nuclear, particle and quantum physics, along with microbiology and chemistry. Besides a purely academic interest of comprehensive theoretical understanding, the field of nanotechnology that has emerged in the past decades has been particularly successful in finding technical applications beyond the fundamental research. These include microscopic techniques capable of resolving and manipulating single atoms (AFM, STM, SEM), miniaturized microelectronics for advanced microprocessors and the development of functional nanoparticles and nanomaterials.

The goal of this thesis is to explore the transport properties of nanoporous solids, which are synthesized with the purpose of introducing voids (pores) of defined nanoscale dimensions into a solid. On one hand, the pores are molecular sieves, allowing selective, size-dependent passage of particles through the pore entrances [1, 2]. On the other hand, they act as a combined flow channel and geometric confinement holding a chosen medium, e.g. condensed gases, simple liquids and complex molecules such as proteins and polymers [3]. In the production processes of many nanoporous materials, molecular self-organization is exploited to ensure uniform properties over macroscopic distances. This is also the case for the material of choice in this work, nanoporous Vycor glass, which is manufactured as a monolithic solid of macroscopic extent. On the inside, Vycor features an isotropic, interconnected network of meandering, nearly cylindrical pores with a tunable, narrow distribution of pore sizes in the order of $\sim 10\,\mathrm{nm}$ [4]. These characteristics of Vycor are beneficial for the use as a model pore system in experiments on transport dynamics in nanoscale geometries [5].

Detailed knowledge of the fluid dynamics and interactions of matter on molecular scales is a crucial requirement for many technical applications of nanoporous materials, e.g. in chemical catalysis, microbiological research and medical technology [6, 7, 8, 9]. As the widths of nanopores are comparable with typical molecular sizes, liquid and gas flow exhibit phenomenological differences to their respective counterparts in macroscopic settings [10, 11]. In particular, as a result of the high surface-to-volume ratio in nanoporous materials, interfacial effects of the pore walls have substantial impact on total macroscopic transport of matter [12].

In this work, the transport of gases and liquids in nanoporous materials will be studied experimentally: The adsorption and diffusion of molecules from a gaseous phase into the pores as well as a flow of liquid by spontaneous capillary rise or resulting from a constant driving pressure difference. All of these processes are in some way dependent on molecular interactions with the interfaces. Hence, the combination of the porous solid and the liquid or gas filling is of great importance. For the experiments, the n-alcohols ($C_nH_{2n+2}O$) have been chosen as pore fillings. These polar, organic molecules exhibit similar characteristics for a variable alkyl chain length along with strong dipolar interactions because of the functional OH^- group, allowing a comparison of effects for a similar chemistry and different molecular sizes. When introduced to the nanoscale confinement of Vycor, strong interactions with the high-energy silica surface are expected. As a result, the intermolecular forces within the pore filling, the molecular mobility and the possible mechanisms are different from macroscopic bulk transport.

The experiments carried out in this work utilise macroscopic measurements on the samples containing alcohols, mainly dielectric spectroscopy. This allows the detection of polar pore fillings by the additional contribution to the resulting complex permittivity spectra. In contrast to other macroscopic methods such as gravimetric measurements [5], dielectric spectroscopy offers spatial selectivity by the electrode placement. Moreover, the dielectric spectra also potentially provide insight into the molecular mobility, e.g. as a modified dipole relaxation. Although a macroscopic detection seems counter-intuitive in the study of effects in the nanometre and sub-nanometre range, it will be shown conclusively that a consistent microscopic behaviour can be observed with this technique.

2 Methods and Materials

2.1. Properties of the Nanoporous Matrix

2.1.1. Introduction to Porous Solids

Porous solids are a class of heterogeneous condensed matter. They consist of a solid phase (*matrix*) and embedded voids (*pores*). Depending on the microstructure, pore space connectivity and pore geometry, further classifications can be introduced.

A simple means of describing a porous solid is the characteristic width d_p of the pores. Generally, d_p can take values from macroscopic sizes, e.g. in porous rocks such as pumice down to atomic dimensions, as in zeolite molecular sieves. Within the scope of this work, the focus is set on nanoporous matrices. By definition, these materials contain pores that measure less than $100\,\mathrm{nm}$ in at least one dimension. A more detailed naming scheme has been defined by the IUPAC [13]:

Microporous solids: $d_p \leq 2\,\mathrm{nm}$

Mesoporous solids: $2\,\mathrm{nm} < d_p \leq 50\,\mathrm{nm}$

Macroporous solids: $50\,\mathrm{nm} < d_p$

Although the above classification and the respective limits seem arbitrary, there are some characteristic differences in physical properties that separate micro-, meso- and macroporous solids, e.g. for vapour condensation inside the pores, see Sec. 3.4.1.

A common feature to all nanoporous materials is a high internal surface area and consequently a high surface-to-volume ratio in the pore space. Therefore, surface forces and interfacial effects in nanopores are of utmost importance in the understanding of molecular transport. Moreover, with pore radii approaching molecular dimensions, the validity of continuum theory and macroscopic transport equations has to be questioned. A more in-depth discussion of fluid transport in nanopores can be found in Sec. 5 and Sec. 7.

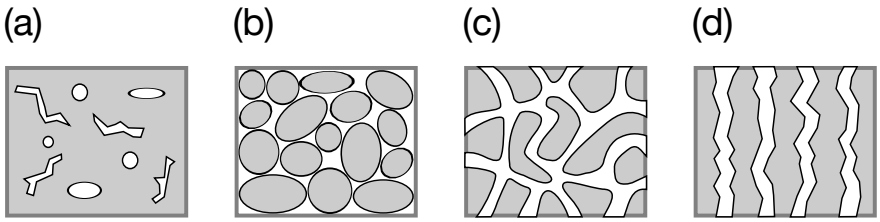

Figure 2.1.: Illustration of cross-sections through different porous media: (a) Solid containing only closed pores, (b) In granular porous media, solid grains in aggregation define an interstitial pore volume, (c) Rigid solid matrix containing a network of pores, (d) Ordered pore array.

Besides the typical length scales, it is important to consider the spatial arrangement of pores within the matrix and their connectivity to the boundary of the finite porous solid. An overview of some possible configurations is depicted in Fig. 2.1.

A simple system is given by a distribution of (arbitrarily shaped) void bubbles within a solid matrix with no connections to the outside, see Fig. 2.1(a). These so-called 'closed pores' are often found as structural defects in many materials such as rocks or cast metal due to their natural formation or fabrication processes. As closed pores do not allow liquid or gas exchange (with respect to diffusion through the solid), these materials are not of interest for this work.

One type of porous media with 'open pores' is given by the inverse structure to a closed pore system, as depicted in Fig. 2.1(b). Here, solid grains are aggregated in close proximity and the interstitial spacing between the particles forms a connected pore space, in which liquid and gas transport can occur. However, this void space features a complex geometry with a broad distribution of characteristic widths. These systems are usually referred to as 'granular porous media', with many examples occuring naturally, e.g. soils, sandstone.

A third type of porous material is a rigid, monolithic solid phase containing a network of interconnected, open pores. The pore shape in these systems can range from random cracks to well defined ducts. The vast majority of porous solids features pores with random orientation, see Fig. 2.1(c). The nanoporous Vycor matrix used in this work belongs to this class of porous media.

A special case of pore networks are 'ordered porous materials', see Fig. 2.1(d). This class of nanomaterials with non-connecting pores in parallel to a specific axis is mainly produced in self-organising processes, e.g. porous silicon, silica compounds with hierarchic pore structure (MCM-41, SBA-15) and anodized aluminium oxide (AAO) [14, 15, 16].

In all of the above structures, an important parameter for the characterization of porous solids is the relative volume fraction of pore space in relation to the sample volume that con-

stitutes the sample porosity Φ:

$$\Phi = \frac{V_{\text{pores}}}{V_{\text{sample}}} \tag{2.1}$$

In the context of fluid flow, the porosity directly relates to both the amount of fluid the matrix can hold as well as the hydraulic permeability, see Sec. 7.2.2. The value of Φ can be determined experimentally, e.g. by the mass increase of a porous sample upon filling or by other techniques probing the molar uptake into the pore space, see Sec. 4. For different porous media, porosities can range from very low values $\Phi \approx 0$ in closed pore systems to $\Phi > 95\,\%$ in aerogels [17].

2.1.2. Fabrication and Structure of Porous Vycor Glass

Vycor® is a trademark of Corning Inc. for porous and reconstructed glasses produced from sodium borosilicate glass SiO_2 / B_2O_3 / Na_2O, as patented in 1934 [18]. Originally, the goal was the production of non-porous, high purity silica glass without the need for high temperatures $T > 2000\,°\text{C}$ that are required in the manufacturing of fused quartz glass. Porous Vycor glass was at first considered only an intermediate product in this process. The production work flow consists of three consecutive process steps:

1. Heat treatment of homogeneous alkali borosilicate glass induces phase separation.

2. Chemical etching dissolves the alkali-/boron rich phase and yields porous Vycor glass (trade name VYCOR 7930).

3. Sintering of VYCOR 7930 produces reconstructed, non-porous glass with high silica content (trade name VYCOR 7913).

From now on, the term Vycor will be used exclusively for the porous variety, VYCOR 7930. The characteristics of the nanopores result from a self-organising behaviour and subsequent selective etching in the first two process steps, which will now be elucidated. Additional information can be found in [4, 19].

Step 1 of this process relies on the spontaneous de-mixing of certain compositions of sodium borosilicate glasses, e.g. 67 at.% SiO_2 / 26 at.% B_2O_3 / 7 at.% Na_2O. In the melt, the components mix readily and on fast cooling ('quenching'), this state is preserved in the resulting glass. If subsequently heated above a critical temperature $T > 500\,°\text{C}$ to $\sim 740\,°\text{C}$ depending on the composition, the miscibility of silica (SiO_2) with the alkali-/boric oxide (Na_2O/B_2O_3) is reduced. Over time, a spontaneous phase separation is observed.

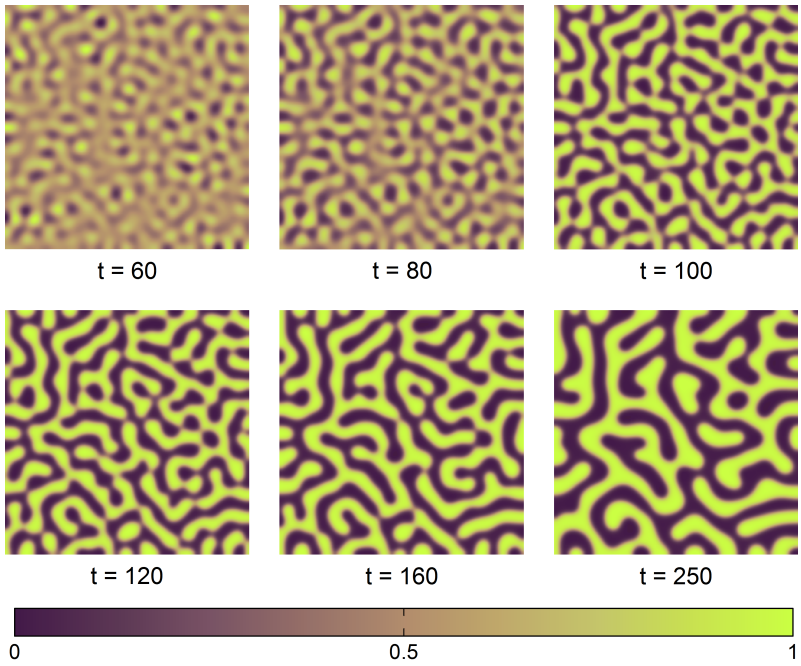

Figure 2.2.: Numerical simulation of spinodal decomposition in a two-dimensional binary liquid (A-B), reproduced using an algorithm from [21]. The color-coded images depict the relative concentration $c = 0$ to 1 of phase A in a 256×256 grid for simulation times t. Very small initial fluctuations result in clearly separated structures that show a narrow distribution of structure widths for all times. As time passes, the separated domains increase in size. An animated version of the above simulation is found in the supplemental material to this document.

The physical mechanism for this dynamic behaviour is spinodal decomposition: Random initial fluctuations in concentration are amplified over time by a diffusion flux[1] so that the free energy of the system is minimized. A theoretical model is given by the Cahn-Hilliard equation that describes the evolution of the concentration scalar field $c(x, y, z, t)$ [20]. A numerical solution for small and random initial fluctuations in 2D has been realized in a MATLAB program in [21]. Simulated results using this algorithm are depicted in Fig. 2.2.

In step 2, the Na_2O/B_2O_3 phase is removed by a selective acid leaching process with HCl, HNO_3 or H_2SO_4. As SiO_2 is insoluble and does not react with the chemicals, a final composition of almost pure silica ($\geq 96\%$) is achieved. The remaining impurities can be attributed to small concentrations of the alkali/boron phase captured in the silica phase as well as on the phase boundaries. From the initial composition, one can deduce that the resulting volume fraction removed by acid leaching and thus the porosity is in the order of $\sim 30\,\%$.

[1] In contrast to nucleation and nucleus growth, the diffusive process results from a gradient in chemical potential in opposite direction to the concentration gradient (= uphill diffusion).

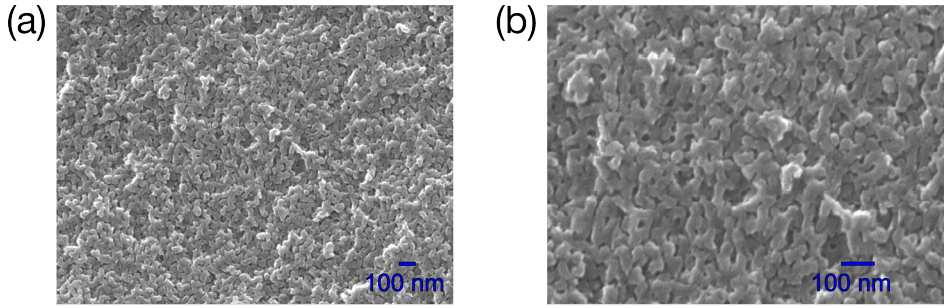

Figure 2.3.: Electron micrographs of porous Vycor glass, recorded by scanning electron microscopy at different magnifications: (a) $\times 50000$ magnification, (b) $\times 100000$ magnification. The microstructure of the silica matrix, as resolved by this imaging technique, exhibits a random orientation and narrow width distribution. These characteristics persist over the entire sample surface. Images courtesy of J. Schmauch, AG Birringer, Saarland University.

The structure of Vycor can be visualised by scanning electron microscopy of its surface, which is depicted in Fig. 2.3. Here, the interconnected microstructure of the silica matrix is clearly visible and a remarkable similarity to the two-dimensional simulation in Fig. 2.2 can be noted, as the resolved silica structures all have comparable widths. The surface characteristics of a cut Vycor sample are uniform over macroscopic distances, hence it is a reasonable assumption that this is also true in the sample volume. Fig. 2.3 also allows a first estimate of pore shape and size by image analysis of pore entrances perpendicular to the image plane. These pore cross-sections exhibit a nearly circular shape, hence it is appropriate to use an equivalent diameter d_p as a size reference. However, this method has poor statistical significance, since only a very limited section of the pore space is assessed. A better experimental technique will be introduced in Sec. 3.4.

2.1.3. Mechanical Properties and Sample Preparation

Due to the rigid, connected structure of its silica matrix, the mechanical properties of Vycor are comparable to non-porous glasses. It is thus possible to utilise many widespread machining techniques such as cutting and turning with diamond tools or mechanical polishing for sample preparation. The monolithic Vycor samples can be tailored to fit the individual geometric requirements for an experimental application, which is one of the key advantages compared to other porous materials.

The downside of Vycor glass are the brittle fracture characteristics. This is problematic in high-pressure applications and introduces experimental limitations that will be further addressed in Sec. 8.2.

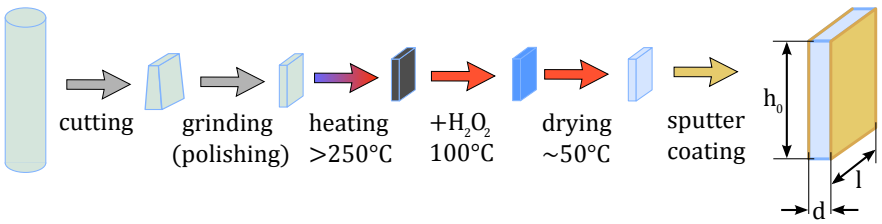

Figure 2.4.: Typical sample preparation procedure and sample geometry. The porous glass rods are machined to size, chemically cleansed and electrodes are applied to the cuboid samples. The final dimensions are given as a length l, height h_0 and depth d.

The total work sequence for sample preparation is illustrated in Fig. 2.4. For most experiments, a cuboid sample geometry of $\sim 10 \times 10 \times 1\,\mathrm{mm}$ ($l \times h_0 \times d$) has been chosen[2]. Samples were cut to size from cylindrical rods with a circular diamond saw. By subsequent abrasive smoothing of the sample faces, macroscopic surface roughness could be reduced to $\Delta d \approx 50\,\mu\mathrm{m}$. For equilibrium adsorption experiments in Sec. 4, where $d < 1\,\mathrm{mm}$ was required, a mechanical polishing apparatus was utilised to further reduce the sample thickness. After machining, the samples were cleaned using a chemical treatment, see Sec. 2.1.4 for details. Before use in an experiment, electrodes were applied on the large opposite sample faces. For most experiments, a sputter coating with gold ensures the electrical contact of the entire surface in a dielectric spectroscopy setup, see Sec. 2.2. The gold layer does not obstruct gas or liquid flow into the pore space, which was verified in preliminary experiments for this work and was even observed when trying to forcefully plug the pore entrances by additional sputter coating with SiO_2 [22]. In some cases, a sealing of the external surface is required, e.g. when vapour intake needs to be excluded. This is achieved by coating the with sample epoxy resin, which also serves as an adhesive for solid plate electrodes (Cu sheet metal).

2.1.4. Chemical properties

The almost pure silica matrix of Vycor is chemically very stable and does not react with most chemicals because of the strong bonding of silicon and oxygen atoms. On the pore walls, the situation is different: On one hand, it is expected that a considerable amount of unknown impurities from the manufacturing process agglomerates on the interfaces. On the other hand, the silica surface features silanol groups (Si−OH) that result from the reaction of unsaturated surface bonds (Si·, Si−O·) with water during manufacturing [23]. These covalent-bonded surface silanol groups are highly polarized and tend to form hydrogen bonds to one another when in close proximity, or to other chemicals, when present [24].

[2] A detailed sample reference including the individual dimensions is given in Appendix A.

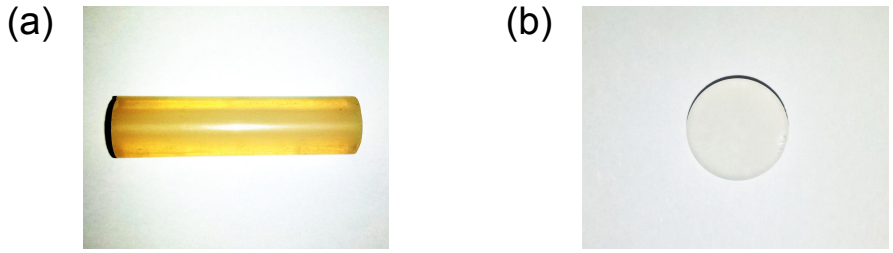

Figure 2.5.: Enhanced contrast photographs of contaminated and clean Vycor. (a) When exposed to air, the uptake of organic molecules from the surroundings causes a discoloration of the porous matrix. (b) When applying a cleaning procedure, organic contaminants can be fully removed, resulting in a transparent sample.

Because of these strong interactions on the internal surface, Vycor is prone to contaminants from the outside. Most notably, a water layer is expected when Vycor is stored in an aqueous or humid environment [25]. Besides, it is also observed that organic molecules from the surroundings contaminate porous solids. If Vycor is exposed to ambient conditions for a prolonged time, these impurities become noticeable as a brownish hue, as depicted in Fig. 2.5(a). The following cleaning procedure, as sketched in Fig. 2.4, was applied to every sample before use in an experiment:

1. Heating of the sample in air to temperatures $> 200\,^{\circ}\mathrm{C}$ causes chemical decomposition of complex organic compounds into simpler molecules, sample blackens.
2. Chemical treatment in hydrogen peroxide (H_2O_2) at $\approx 100\,^{\circ}\mathrm{C}$ until sample becomes transparent. In the process, contaminants are oxidised mostly into water and gaseous carbon dioxide.
3. Storage in dilute hydrogen peroxide until needed.
4. Heating and evaporation of liquid from the pores at elevated temperatures $\sim 50\,^{\circ}\mathrm{C}$.
5. Short-term storage in desiccator with microporous silica gel drying agent.

By following these steps, it is ensured that no organic impurities remain in the pore space. The sample is then transparent, see Fig. 2.5(b). In order to avoid recontamination, exposure to ambient air is minimized to the process of mounting into the sample setup ($\sim 5\,\mathrm{min}$). Still, due to the aqueous environment during cleaning, a strongly adsorbed water monolayer is expected to remain on the pore walls. Only if a strong vacuum ($\approx 10^{-6}\,\mathrm{mbar}$) and high temperatures ($> 190\,^{\circ}\mathrm{C}$) are applied for a prolonged time period, a complete removal of residual water is guaranteed [23]. Accordingly, r_0 will refer to the pore radius in this state without water layers.

2.2. Dielectric Spectroscopy

2.2.1. Introduction to Dielectric Spectroscopy

The main experimental technique in this work is dielectric spectroscopy. This method is used to analyse the frequency dependent response of a macroscopic dielectric sample to an external electrical excitation field. The resulting signal is closely related to the dynamics of both free and bound charged particles, in particular molecules with a static dipole moment. In the following, the theory of dielectrics shall be elucidated, these concepts are taken from [26].

In Maxwell's theory of electromagnetism, the static electric displacement field $\boldsymbol{D}$ in a dielectric material is defined as the sum of the contributions from an external electric field $\boldsymbol{E}$ and a polarization density $\boldsymbol{P}$,

$$\boldsymbol{D} = \varepsilon_0 \boldsymbol{E} + \boldsymbol{P}, \tag{2.2}$$

where $\varepsilon_0 = 8.854 \cdot 10^{-12}\ \frac{\mathrm{A\,s}}{\mathrm{V\,m}}$ denotes the vacuum permittivity.

According to Gauss' law, the electric field $\boldsymbol{E}$ is defined by a spatial density ρ_f of free charge carriers, e.g. a static charge in an electrode at the boundary of the dielectric material, whereas the polarization density P results from bound charges ρ_d inside the dielectric. There are many microscopic mechanisms contributing to the polarization, which will be discussed in Sec. 2.2.3. For now, $\boldsymbol{P}$ can be described as a linear function of $\boldsymbol{E}$,

$$\boldsymbol{P} = \varepsilon_0 \chi \boldsymbol{E}. \tag{2.3}$$

Here, χ denotes the electric susceptibility, i.e. a coefficient of responsiveness to the external field. Inserting this into Eq. (2.2) yields

$$\boldsymbol{D} = \varepsilon_0 \left(1 + \chi\right) \boldsymbol{E} = \varepsilon_0 \varepsilon \boldsymbol{E}, \tag{2.4}$$

with a dimensionless coefficient ε, known as the relative permittivity or dielectric constant. In order to access this quantity that holds information on the microscopic behaviour of the dielectric material, the capacitance of the sample as a macroscopic property can be measured.

The capacitance of an object quantifies its ability to hold two separated electric charges $+Q$ and $-Q$ at a voltage U which is in turn related to the geometric distribution of the respective vector fields $\boldsymbol{D}$ and $\boldsymbol{E}$:

$$C = \frac{Q}{U} = \frac{\oint \boldsymbol{D}\,\mathrm{d}\boldsymbol{A}}{\int \boldsymbol{E}\,\mathrm{d}\boldsymbol{l}}. \tag{2.5}$$

The surface integral on the right hand side of Eq. (2.5) is applied over the volume enclosing one of the charge distributions, the integral in the denominator for a line segment connecting

both opposite charges.

A simple geometric example is a parallel plate capacitor consisting of two parallel, flat electrodes of area A and distance d, filled with a homogeneous dielectric material of relative permittivity ε. For large plate areas $A \to \infty$, the electric field is limited to the space between the plates, perpendicular to the electrodes and homogeneous, so that $U = Ed$. As the exterior of the capacitor is free from electric fields, the surface integral also simplifies to $D \int \mathrm{d}A = \varepsilon E A$. In total, the capacitance of the ideal parallel plate capacitor is given by

$$C = \varepsilon_0 \varepsilon \frac{A}{d}. \tag{2.6}$$

In finite geometries, the boundary effects of the electric field at the edge of the capacitor plates cause an inhomogeneous stray field that extends into the space outside of the capacitor plates. Depending on the dimensions of the capacitor (and the permittivity of the surrounding medium), this can be a significant contribution to the total capacitance and has to be considered in most cases when performing spectroscopy.

2.2.2. The Complex Dielectric Function

When applying an alternating electric field to a dielectric material, $E(t) = E_0 \cos(\omega t)$, with an amplitude E_0 and a frequency $\omega = 2\pi\nu$, the material polarization $P(t)$ reacts to this external stimulus. As a consequence, $D(t) = E(t) + P(t)$ also becomes a function of time,

$$D(t) = D_0 \cos(\omega t - \phi). \tag{2.7}$$

Here, a phase shift ϕ has been introduced that accounts for a deferred response of the polarization. Eq. (2.7) can be rewritten as

$$D(t) = D_0 \cos(\phi) \cos(\omega t) + D_0 \sin(\phi) \sin(\omega t). \tag{2.8}$$

Of the two summands on the right hand side of Eq. (2.8), one is in phase with the external field and one exhibits a phase shift of $\pi/2$. Using Eq. (2.4), two permittivity parameters ε' and ε'' can be identified accordingly,

$$D(t) = \varepsilon'(\omega)\varepsilon_0 E_0 \cos(\omega t) + \varepsilon''(\omega)\varepsilon_0 E_0 \sin(\omega t). \tag{2.9}$$

The coefficient of the in-phase contribution, $\varepsilon'(\omega)$, is equal to the relative permittivity in the static case $\omega \to 0$. Similarly, when $\omega > 0$, ε' is a measure of the frequency dependent

polarization in the material. Conversely, $\varepsilon''(\omega)$ describes the energy dissipation due to the phase shift and is thus referred to as a 'dielectric loss' coefficient.

An equal form of the above relation can also be found when interpreting the fields as complex quantities E^* and D^*. Then, using the complex representation $E^* = E_0 \exp(-i\omega t)$ in Eq. (2.9), a complex permittivity can be defined as

$$\varepsilon^*(\omega) = \varepsilon'(\omega) - i\varepsilon''(\omega). \tag{2.10}$$

ε^* is also known as the complex dielectric function. Similarly, a complex capacitance can be defined as

$$C^*(\omega) = \varepsilon^*(\omega)C_0 = C'(\omega) - iC''(\omega), \tag{2.11}$$

with a geometric capacitance $C_0 = \varepsilon_0 A/d$ for a plate capacitor.

In non-ideal dielectrics, especially liquids, there is also a finite ionic or electronic conductivity σ of the material. Due to the movement of charge-carriers, more energy is dissipated and the apparent dielectric function $\varepsilon^*_{\text{meas}}$ in an experiment exhibits an additional contribution in the imaginary part. In order to account for this, the definition of the complex dielectric function in Eq. (2.10) can be altered to

$$\varepsilon^*_{\text{meas}} = \varepsilon' - i\left(\varepsilon'' + \frac{\sigma}{\omega\varepsilon_0}\right). \tag{2.12}$$

Eq. (2.12) also results from a parallel circuit of a discrete (complex) capacitance and conductance. Since the losses attributed to conductivity are attenuated as a function of ω^{-1}, conductivity effects are most noticeable in the low frequency domain.

2.2.3. Polarization Mechanisms in Dielectrics

As briefly mentioned in Sec. 2.2.1, the total polarization of a material results from multiple different sources. Fig. 2.6 gives an overview of the most common microscopic mechanisms:

Electronic polarization: In an external electric field, the atomic nuclei and their orbiting electrons experience a separation of the centres of the positive and negative charges, which results in an atomic dipole moment.

Ionic polarization: In ionic crystals, the partial lattices of anions and cations can also be shifted from their equilibrium position under the influence of an electric field, producing an ionic dipole moment.

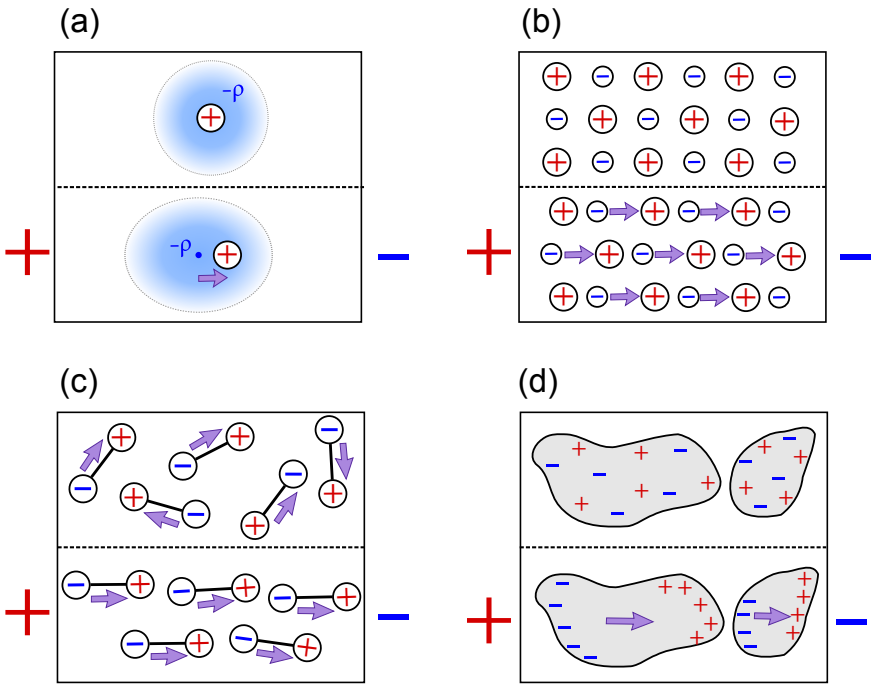

Figure 2.6.: Polarization mechanisms in dielectrics: (a) electronic polarization, (b) ionic polarization, (c) orientation polarization, (d) interfacial polarization. A description of the physical background of these processes is given below.

Orientation polarization: For materials that contain permanent dipoles, these are normally disordered according to statistical mechanics. If the dipoles are free to rearrange, there is a preferred orientation when applying an external field, resulting in an additional polarization.

Interfacial polarization: In heterogeneous, microstructured materials with a finite conductivity, mobile charge-carriers can accumulate at the phase boundaries. This charge separation causes an additional dipole moment, which is known as the Maxwell-Wagner effect. In Vycor, this applies to ions in liquid-filled pores. A special case of interfacial polarization at the macroscopic electrodes (thus named 'electrode polarization') is present in the low frequency domain even for homogeneous dielectrics.

Each of the above mechanisms is governed by different dynamic behaviour. In general, the lower the frequency, the more effects add up to total polarization, ε'. The upper frequency limit for the respective mechanism is critically determined by the length scale, e.g. sub-Å shifts of atomic electron shells take significantly less time than a displacement of ionic space

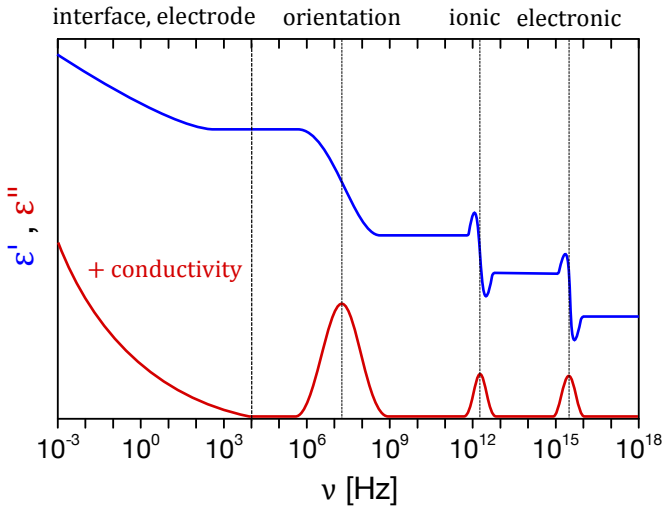

Figure 2.7.: Frequency dependence of the complex permittivity and typical frequency limits for respective mechanisms. In the low frequency domain, interfacial polarization and conductivity dominate the real and imaginary part of the permittivity. As limiting frequencies for the above mechanisms are reached, a drop in the real part in conjunction with a peak in the imaginary part is observed.

charges over macroscopic distances. As a result, the transition frequencies of the different polarization effects vary by orders of magnitude, as shown in Fig. 2.7. If one of these critical frequencies is reached, a significant drop in ε' is expected. Meanwhile, the dielectric losses ε'' reach a maximum.

2.2.4. Dipole relaxation

For the experiments performed in this work, the frequency range was typically chosen to $\nu = 1\,\mathrm{kHz}$ to $2\,\mathrm{MHz}$. Within this frequency window, the interfacial polarization and the orientation polarization can potentially reach a limiting frequency. In case of the latter mechanism, an analytical description of the frequency behaviour is possible using a simple model.

From a microscopic viewpoint, dipoles can dynamically reorient in an external field $E(\omega)$. The speed of this process is limited by the characteristics of the dipoles. A relaxation, i.e. a retarded reaction of the polarization to the stimulating electric field, is expected, as sketched in Fig. 2.8 for a square-wave signal. For very high frequencies, the dipoles cannot follow the external excitation, their orientation is random. The polarization is solely caused by fast-acting mechanisms, e.g. electronic polarization, and according to Eq. (2.3) equal to

$$P_\infty = \underbrace{(\varepsilon_\infty - 1)}_{\chi_\infty} \varepsilon_0 E. \tag{2.13}$$

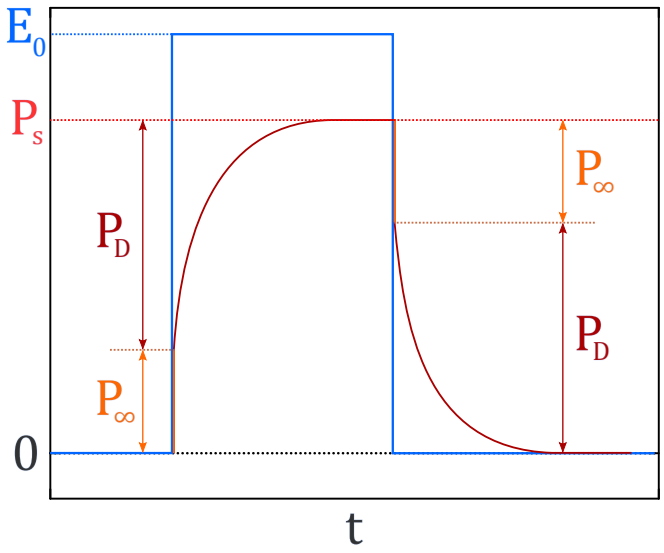

Figure 2.8.: Relaxation of sample polarization to an external field. If a stepwise increase or decrease of the electric field is applied, the fast-acting polarization mechanisms, e.g. electronic polarization, cause an instantaneous reaction of the internal polarization P_∞. The slower mechanism of dipole reorientation leads to a further increase over time $P_D(t)$. If the frequency of the external field is sufficiently low, a saturation value $P_s = P_\infty + P_D$ is reached.

For low frequencies, the dipoles can reorient to the external field quasi-instantaneously and the polarization reaches a saturation value P_s that consists of both dipole polarization P_D and high frequency contributions P_∞,

$$P_s = P_D + P_\infty = (\varepsilon_s - 1)\varepsilon_0 E. \tag{2.14}$$

For frequencies between the above limits, a dynamic response function $P(t)$ needs to be found. A basic approach by Debye [27] relies on the assumption that the differential change in polarization over time is proportional to the difference to its saturation value, which is consistent with linear response theory [26],

$$\frac{\mathrm{d}P(t)}{\mathrm{d}t} = \frac{1}{\tau_D}\left(P_s - P(t)\right). \tag{2.15}$$

Here, τ_D is the characteristic relaxation time that depends on the properties of the dipole and the system, e.g. temperature, molecular dimensions. For the above situation, the total polarization $P(t) = P_D(t) + P_\infty$ needs to be used. Then, Eq. (2.15) in combination with Eqs.

(2.13) and (2.14) results in

$$\tau_D \frac{\mathrm{d}P_D}{\mathrm{d}t} + P_D(t) = P_s - P_\infty = (\varepsilon_s - \varepsilon_\infty)\,\varepsilon_0 E(t). \tag{2.16}$$

For a periodic function $E^*(t) = E_0 \exp(i\omega t)$, the solution of this differential equation is also complex,

$$P_D^*(t) = \frac{\varepsilon_s - \varepsilon_\infty}{1 + i\omega\tau_D} \varepsilon_0 E_0 \exp(i\omega t), \tag{2.17}$$

with a complex permittivity

$$\varepsilon^*(\omega) - \varepsilon_\infty = \frac{\varepsilon_s - \varepsilon_\infty}{1 + i\omega\tau_D}. \tag{2.18}$$

Hence,

$$\varepsilon'(\omega) = \varepsilon_\infty + \frac{\varepsilon_s - \varepsilon_\infty}{1 + \omega^2\tau_D^2} \tag{2.19}$$

and

$$\varepsilon''(\omega) = (\varepsilon_s - \varepsilon_\infty)\,\frac{\omega\,\tau_D}{1 + \omega^2\tau_D^2} \tag{2.20}$$

describe the frequency dependent real and imaginary parts of the complex dielectric function for this Debye relaxation. The difference $\Delta\varepsilon = \varepsilon_s - \varepsilon_\infty$ is also referred to as 'relaxation strength'. A plot of Eqs. (2.19) and (2.20) for a given relaxation strength and time is shown in Fig. 2.9.

It should be noted that the Debye model is an idealized representation of dipolar reorientation. In many real systems, the relaxation behaviour is much more complex, e.g. when coordinated processes of dipoles are involved. The Debye model then does not adequately fit the dielectric spectra. An empirical model has been introduced by Havriliak and Negami that allows for asymmetrical and broadened relaxations [28].

2.2.5. Dipoles in Confinement

The Debye model from Sec. 2.2.4 also applies to systems of limited mobility. For dipoles in a potential energy landscape $V(\boldsymbol{x})$, where $\boldsymbol{x}$ is a generalized coordinate vector, an external electric field modifies the potential energy so that certain dipole arrangements are preferred.

As an example in one dimension, let us assume a symmetrical double-well potential and thermal activation. None of these two stable states is preferred, the occupation probability is equal and so is the stationary transition rate between them. If the two states represent two opposite orientations of dipoles, the total polarization is then zero.

When applying an electric field, the energy of the potential wells is shifted by the field energy $\Delta V = pE$ for a dipole moment p as shown in Fig. 2.10. Accordingly, the occupation

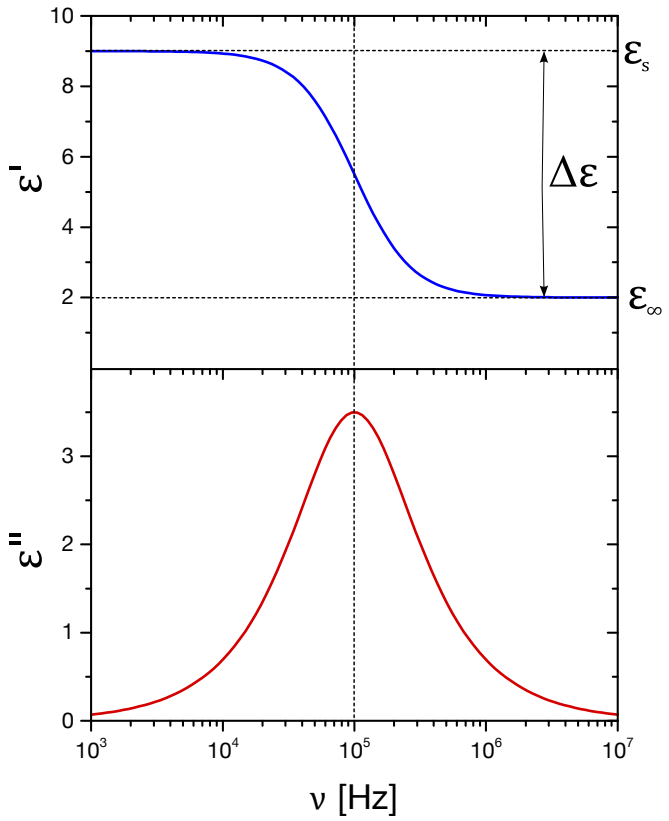

Figure 2.9.: Real and imaginary part of the permittivity for a Debye relaxation, for exemplary relaxation strength $\Delta\varepsilon = 7$ and relaxation time $\tau_D = \frac{1}{2\pi}10^{-5}$ s. The high-frequency permittivity has been chosen to $\varepsilon_\infty = 2$.

probability of the low energy state in equilibrium is higher, corresponding to a net polarization. For any initial difference from this equilibrium, it can be shown that the transition rate is a linear function of the occupation difference [26]. This is an analogous formulation of Eq. (2.15) which results in a Debye relaxation.

This consideration applies equally to an interacting ensemble of dipoles, e.g. in a liquid, and to dipoles in proximity to an interface. However, depending on the respective potential function, the equilibrium arrangement of dipoles is not necessarily the same in both cases. This can result in a difference of maximum polarisation P_D and hence the relaxation strength $\Delta\varepsilon$. Whether or not this is also the case in Vycor will be discussed in Sec. 2.3.3. Moreover, the relaxation time τ_D directly results from the transition rates and is thus critically related to the underlying potential. As a result, in nanoporous materials, the relaxation behaviour in the vicinity of the pore walls deviates from the bulk liquid [29, 30].

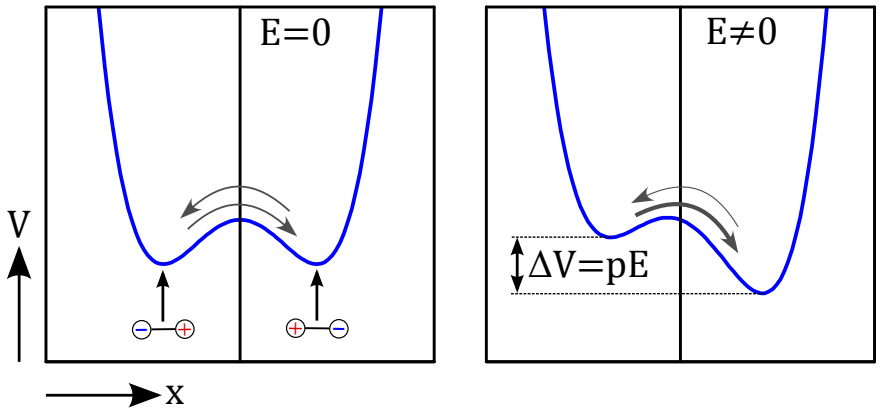

Figure 2.10.: Dipole in an external potential in one dimension. For zero electric field, the potential is assumed to have two equally stable minima. When switching on a constant field, the potential is distorted and an energy difference corresponding to the energy of dipole arrangement is introduced between both states.

2.2.6. Effective Medium Theory

Besides the previously discussed effects of microstructure, i.e. the additional interfacial polarization, and the local variation in dipole relaxation strength and frequency, there is also an inherent effect of the geometric distribution of different phases on the fields $\boldsymbol{D}$ and $\boldsymbol{E}$ inside the sample. On a microscopic scale, the shape of the inter-phase boundary and the component permittivities $\varepsilon_\mathrm{A}, \varepsilon_\mathrm{B}$ define local fields $\boldsymbol{D}(\boldsymbol{x})$ and $\boldsymbol{E}(\boldsymbol{x})$. This spatial field distribution is not accessible using macroscopic experimental techniques.

However, in many cases, only the macroscopic properties of a heterogeneous material are of interest. For static fields, an effective permittivity ε_eff can be defined that relates the spatial average of the fields,

$$\langle D \rangle = \varepsilon_\mathrm{eff}\, \varepsilon_0 \, \langle E \rangle \,. \tag{2.21}$$

Then, the definition of a static capacitance in Eq. (2.6) can be corrected by replacing the homogeneous ε with ε_eff.

For simple geometries, the effective permittivity can be modelled as a function of the component permittivities and the spatial component distribution. As an example, the Maxwell-Garnett rule analytically derives an effective permittivity for a composite of randomly distributed, spherical particles in a matrix material. Unfortunately, for unknown or complex geometries, no comparable analytic solution can be found [31, 32].

Instead of a precise value of ε_eff, one can deduct theoretical boundary values. It can be shown that the absolute limits ('Wiener bounds') of the permittivity for heterogeneous media

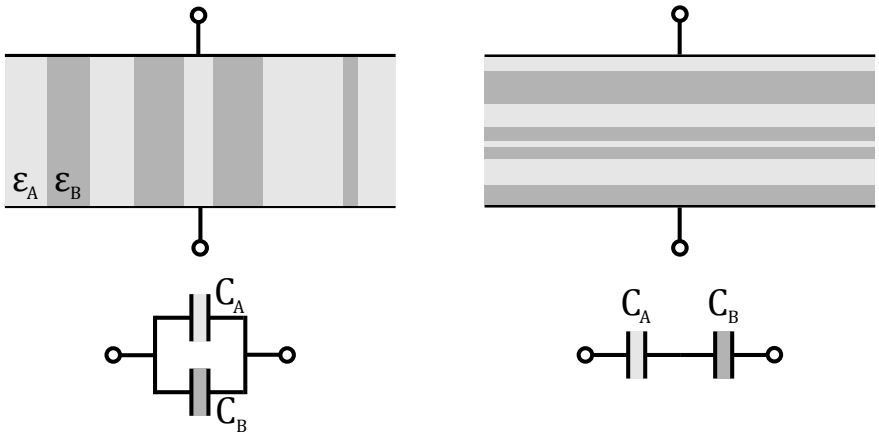

Figure 2.11.: Wiener limits for effective permittivity in heterogeneous media. The maximum and minimum effective permittivity for a two component system are defined by a layered structure perpendicular or parallel to the field vectors. This corresponds to a parallel or serial circuit of the two partial capacitances.

can be represented by a layered microstructure, as shown in Fig. 2.11. This geometry is equivalent to a discrete parallel (left) or serial circuit (right) of the individual phases weighted by the relative volume $v_A = V_A/V$ occupied by component A:

$$\varepsilon_{\text{eff,max}} = v_A\varepsilon_A + (1 - v_A)\varepsilon_B \tag{2.22}$$

and

$$\varepsilon_{\text{eff,min}} = \frac{\varepsilon_A\varepsilon_B}{v_A\varepsilon_A + (1 - v_A)\varepsilon_B}. \tag{2.23}$$

Note that these boundaries are strictly limited to static fields and purely real component permittivities ($\varepsilon'' = 0$). In good approximation, the limits will also hold for dynamic fields in a quasi-static situation ($\lambda > 2\pi\delta$) if the wavelength of the electric field $\lambda = c/\nu$ is significantly larger than structure widths δ. For nanoporous Vycor, due to the uniformity over macroscopic distances and the narrow distribution of structure widths, this condition is satisfied on the entire experimental frequency range.

For finite conductivity or dielectric losses of the components, the limits of the effective permittivity correspond to a defined region in the complex plane. The detailed construction of the region boundary is described in [32, 33]. Depending on the complex component permittivities, the real part of the effective permittivity can even exceed the Wiener limit of the real parts according to Eq. (2.22). Fig. 2.12 depicts such calculated boundaries in a model system (Vycor / ethanol+ions) using a numerical solution from [34].

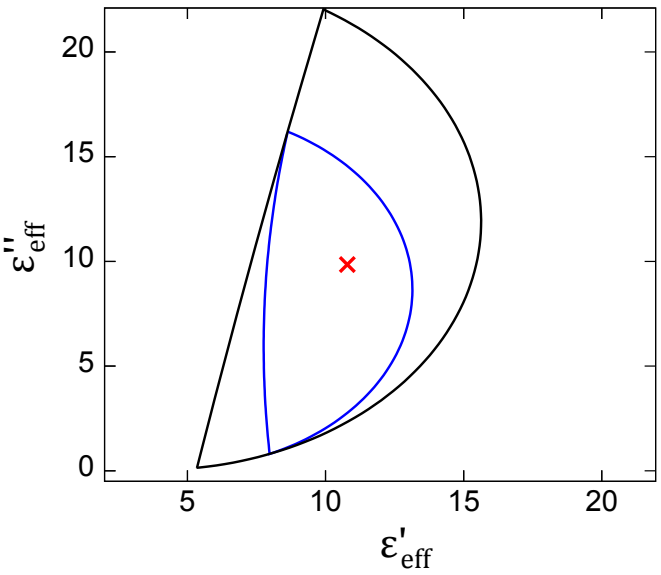

Figure 2.12.: Limiting region of the complex effective permittivity. black lines: complex Wiener bounds, blue lines: isotropic material bounds. Both regions are calculated for a composite of complex component permittivities $\varepsilon_A^* = 25.8 + i\,80$ and $\varepsilon_B^* = 3.9 + i\,0.04$, at a volume fraction $v_A = 0.275$ of component A. These values correspond to the static permittivity of ethanol with an assumed increase of the imaginary part resulting from ionic conductivity (A) and an extrapolated complex permittivity for Vycor (B). When ignoring the imaginary parts in this composite, an upper Wiener bound of $\varepsilon_{\text{eff,max}} = 9.9$ is found according to Eq. (2.22), which is exceeded by $\varepsilon'_{\text{eff}}$ in a large part of the complex region. The red cross shows a measured effective permittivity for a Vycor sample filled with ethanol in comparison, see Sec. 2.3.3.

In the context of the experiments in this work, this definition of complex limits is not suited as a theoretical model. Although some refinements resulting in smaller regions in the complex plane have been proposed for isotropic and percolating components [32], there is still a large uncertainty in the prediction. Furthermore, any model relies on explicit knowledge of the complex dielectric function of both components, which is problematic for a filled Vycor sample, since ionic contaminants critically influence the dielectric losses of the liquid phase, see Sec. 2.3.2. In order to resolve this shortcoming, Sec. 2.3.3 will introduce an empirical procedure.

2.3. Dielectric Properties of Vycor and Confined Liquids

2.3.1. Empty Vycor Matrix

The effective dielectric function of the empty porous Vycor matrix and liquid-filled sample (*vyc_iso_2*, see App. A) have been measured for a frequency range $\nu = 1\,\text{kHz}$ to $2\,\text{MHz}$ using

a setup that will be described in detail in Sec. 4.1.2. For the empty Vycor matrix, the resulting spectra are depicted in Fig. 2.13.

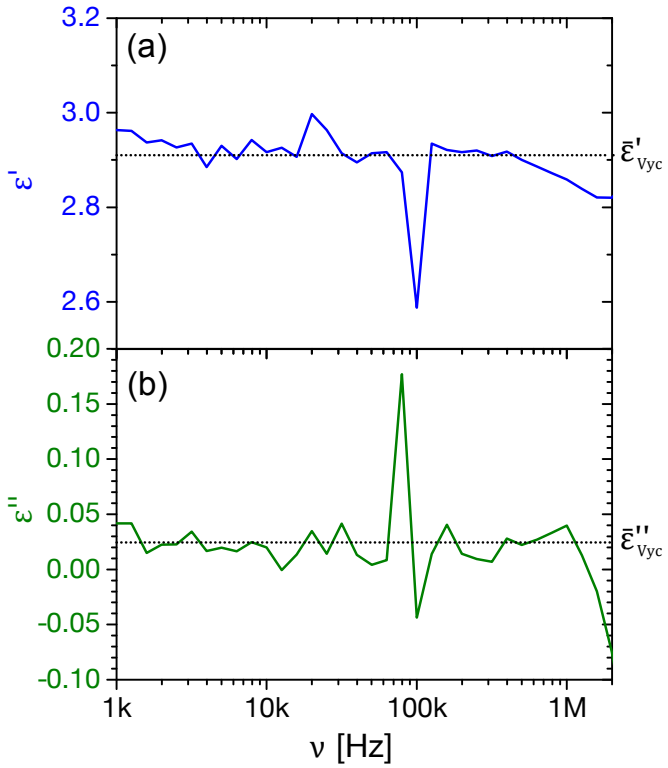

Figure 2.13.: Dielectric spectra of the empty Vycor matrix at room temperature ($T = 297\,\mathrm{K}$): (a) real part, (b) imaginary part of the complex permittivity.

In the real part of the empty Vycor matrix, a nearly constant plateau of the mean value $\bar{\varepsilon}'_{\mathrm{Vyc}} = 2.91 \pm 0.07$ was observed. The imaginary part ε'' is very small for the entire frequency range with a mean value of $\bar{\varepsilon}''_{\mathrm{Vyc}} = 0.025 \pm 0.005$. Hence, there is neither a measurable conductivity nor a relaxation process for the empty Vycor matrix in the specified frequency range. Both spectra also show some experimental limitations: The jump at $\approx 100\,\mathrm{kHz}$ is an artificial error caused by the measuring instrument and is present in every spectrum, so that this specific frequency has to be disregarded. Moreover, some negative values were recorded in the spectrum of ε''. These are a result of the uncertainty in the calibration spectra (see App. C) which is problematic for small imaginary parts. As we shall see, this problem is resolved upon filling.

2.3.2. Polar Liquids Confined to Vycor

When inserting a polar liquid into the Vycor pore space, the primary effect in the dielectric function should be a rise in the real part of the permittivity due to the additional dipole orientation polarization. If the dipole relaxation occurs above the experimental frequency range, as is expected for the n-alcohols [35], the increase $\Delta\varepsilon'$ is constant for each frequency. In the imaginary part, the observed dielectric losses then mainly depend on the conductivity of the liquid. These contributions to ε'' are a function of the frequency according to Eq. (2.12). In addition, if interfacial polarization is significant, there will be another frequency dependent increase in both spectra at lower frequencies, as sketched in Fig. 2.7.

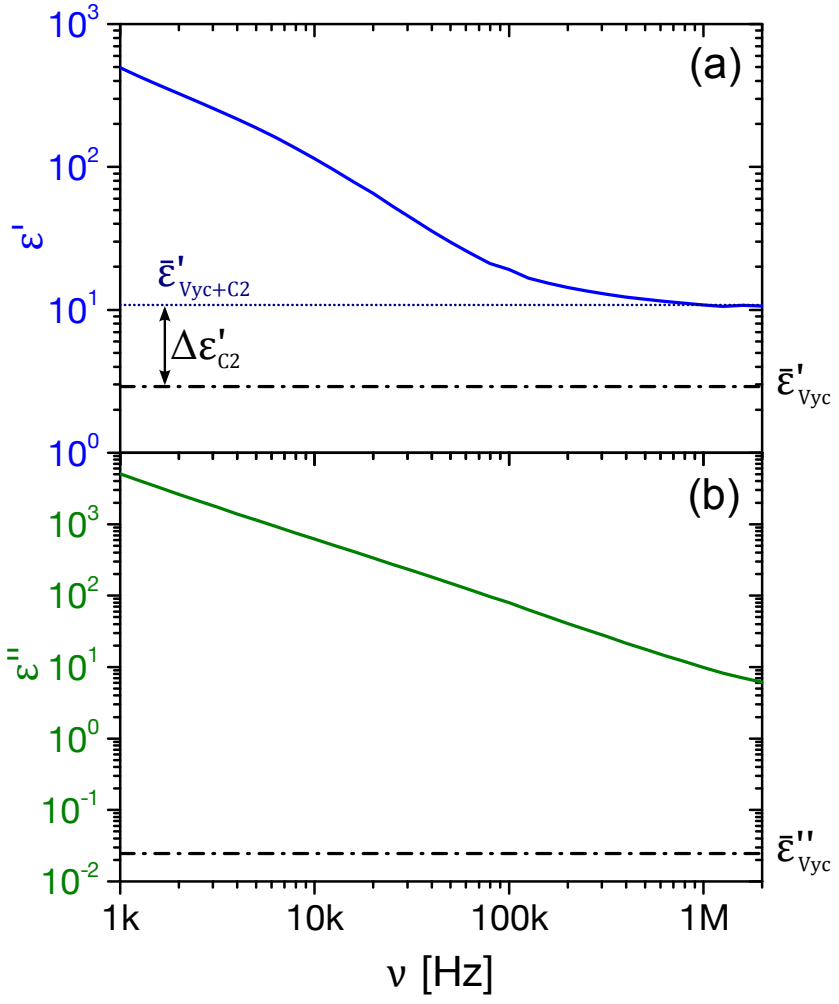

Figure 2.14.: Dielectric spectra of ethanol confined to Vycor pores at room temperature ($T = 297\,\mathrm{K}$): (a) real part, (b) imaginary part of the complex permittivity.

Fig. 2.14 depicts the measured dielectric spectra for a Vycor sample filled with ethanol (C_2H_5OH) in comparison to the plateau values $\bar{\varepsilon}'_{\text{Vyc}}$ and $\bar{\varepsilon}''_{\text{Vyc}}$ of the empty matrix. In both spectra, the measurement results confirm the above predictions:

In the real part in Fig. 2.14(a), there is a gradual, frequency dependent drop in the low frequency domain $\nu \leq 100\,\text{kHz}$. This can be identified as a continuous relaxation of the interfacial polarization at the liquid-solid interfaces within the matrix and at the macroscopic electrodes over the entire frequency range. For high frequencies $\nu \gtrsim 1\,\text{MHz}$ however, a flatter region is approached in the spectrum, which is consistent with the expected constant orientation polarization in the liquid phase and an additional small remaining contribution from interfacial effects. The mean effective permittivity for ethanol in this region amounts to $\bar{\varepsilon}'_{\text{Vyc+C2}} = 10.8 \pm 0.2$. It should be noted that despite the possibly modified relaxation properties for strongly bound dipolar molecules in the pore wall potential (see Sec. 2.2.5), neither liquid exhibited a shift of relaxation times to a measurable extent in the experiments. As the bulk relaxation frequencies for n-alcohols ($n = 10$ to 1) are expected in a range $\nu = 50\,\text{MHz}$ to $3\,\text{GHz}$ [35], this indicates that the effect of confinement induced immobilization on relaxation times is limited within an order of magnitude.

For the imaginary part, the entire spectrum is dominated by high conductivity effects which result in a nearly linear graph $\propto \nu^{-1}$ in the logarithmic plot in Fig. 2.14(b). The high absolute values of ε'' for low frequencies also conceal any peak corresponding to the relaxation of interfacial polarization observed in the real part. Using Eq. (2.12), a conductivity $\sigma_{\text{Vyc+C2}} \approx 1.6 \cdot 10^{-4}\,\Omega^{-1}\text{m}^{-1}$ could be extracted. As liquid alcohols do not conduct electrons, the conductivity is caused by other charge-carries, mainly ionic impurities. It is then proportional to the product of the concentration of ions in the liquid and their mobility. In this experiment, ethanol was inserted into the matrix from the vapour phase so that it can be concluded that the ions are already present intrinsically. Then, the addition of a liquid filling solely enhances the ionic mobility. In conclusion, the spectrum of the imaginary part of the permittivity is largely determined by the impurities in the Vycor matrix from the production process and is consequently not used for further analysis.

2.3.3. Effective Permittivity of Liquid-filled Vycor

The exact value of the effective permittivity in Vycor, in accordance to the considerations in Sec. 2.2.6, depends on the complex matrix and liquid permittivities as well as the microstructure of Vycor. Although the bulk values of both complex permittivities could theoretically be measured separately, an additional increase in the imaginary part of the liquid is observed when combining both phases due to the change in ionic mobility. Besides, the microstruc-

ture is not explicitly known. Thus, it is not possible to derive a reliable value of the effective permittivity *a priori*.

However, the results of Sec. 2.3.2 can be used to gain an empirical expression for the effective permittivity of the fully filled matrix as a function of the liquid component. This is achieved by comparing experimental real parts of effective permittivities, $\varepsilon'_{\text{eff}}(\nu = 1\,\text{MHz})$ for multiple liquids to their static bulk permittivity $\varepsilon'_{\text{bulk}}$ as reported in [36]. Fig. 2.15 depicts experimental values for different substances, including an empty matrix ($\varepsilon'_{\text{empty}} = \varepsilon'_{\text{eff}}(\varepsilon_{\text{bulk}} = 1)$).

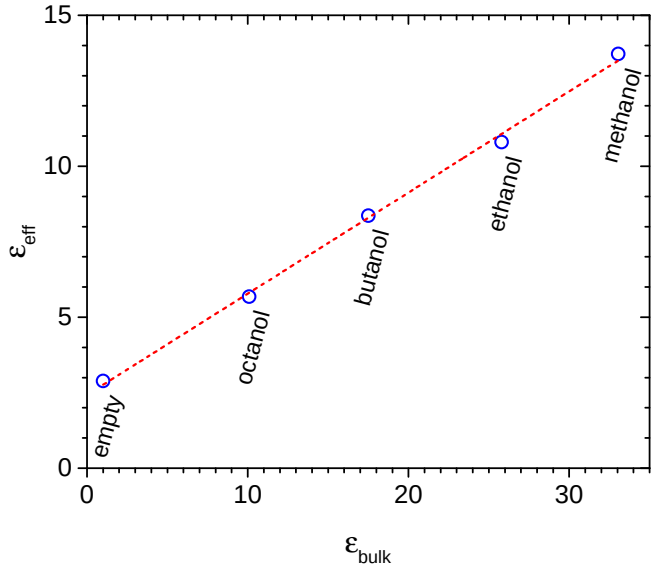

Figure 2.15.: Relation of effective permittivity of confined liquids to the bulk permittivity. Effective permittivities were measured at room temperature $T = 298\,\text{K}$ for a frequency $\nu = 1\,\text{MHz}$, where a nearly constant value of the real permittivity was observed consistently for all liquids.

Most notably, the data points in Fig. 2.15 define a linear relation

$$\varepsilon'_{\text{eff}} = \varepsilon'_{\text{empty}} + K\left(\varepsilon'_{\text{bulk}} - 1\right). \tag{2.24}$$

This is consistent with effective medium simulations of networks of interconnected pores that predict a linear relation for relative volume fractions $\Phi \geq 25\,\%$ [37]. From a linear fit, a coefficient $K = 0.34 \pm 0.01$ could be evaluated. As discussed in Sec. 2.2.6, the effective permittivity in a composite material is determined by the component permittivity, the volume fraction of the components as well as the local microstructure. Consequently, the factor K can be assumed as a product of the sample porosity Φ (assuming total filling without voids)

and an additional empirical factor α representing the influence of the field distribution,

$$\varepsilon'_{\text{eff}} = \varepsilon'_{\text{empty}} + \alpha\Phi\left(\varepsilon'_{\text{bulk}} - 1\right). \tag{2.25}$$

Using an experimental value $\Phi = 27.5\,\%$ of the sample porosity, see Sec. 4.2.1, $\alpha = 1.24\pm0.04$ could be calculated.

Note that for lossless dielectrics, Eq. (2.25) is limited to the upper Wiener bound in Eq. (2.22). A comparison between both relations can be made by identifying $\Phi = v_A$, $\varepsilon'_{\text{bulk}} = \varepsilon_A$ and $\varepsilon'_{\text{empty}} = (1-\alpha\Phi)\varepsilon_B + \alpha\Phi\cdot 1$, resulting in an inequation

$$(1-\alpha\Phi)\varepsilon_B + \alpha\Phi\varepsilon_A \leq (1-\Phi)\varepsilon_B + \Phi\varepsilon_A \tag{2.26}$$

$$\Leftrightarrow \alpha(\varepsilon_A - \varepsilon_B) \leq (\varepsilon_A - \varepsilon_B). \tag{2.27}$$

As the liquid permittivity exceeds the matrix permittivity ($\varepsilon_A > \varepsilon_B$), a value $\alpha \leq 1$ must ensue. The apparent violation by the empirical $\alpha = 1.24$ clearly shows the significant impact of the imaginary part on the liquid permittivity, as described in Sec. 2.2.6. In this case, a complex description of the limits for the effective permittivity is inevitable. Indeed, the measured complex permittivity $\varepsilon^*_{\text{eff}}$ is well within the bounds of an isotropic effective medium of component permittivities for an estimated dielectric loss coefficient in the liquid, see Fig. 2.12.

It should be noted that the ill-defined imaginary permittivity of the liquid phase renders any physical interpretation of the effective permittivity even more difficult. As discussed in Sec. 2.2.5, a reduction in the average molecular dipole moment seems very likely for a liquid in nanoporous confinement, which should result in a drop in the real part of the component permittivity and thus also in the real part of the effective permittivity. However, as the increased conductivity in the pores simultaneously modifies the imaginary part of the component permittivity, the complex boundaries with an additional uncertainty of ε''_{A} define a broad range of possible real parts for the effective permittivity. Then, only extremely strong effects resulting in a violation of complex bounds are detectable in an experimental effective permittivity. In contrast to this, the above results show an inconclusive behaviour that does neither confirm nor exclude a partial immobilization of molecules.

In summary, the high imaginary part in the permittivity of liquids confined to Vycor leads to a complex effective sample permittivity that cannot be predicted accurately by a theoretical model. This conceals any effects of local reduction in relaxation strength of confined alcohols. On the upside, an empirical linear relation results in a consistent microstructure factor for different liquids.

II

Equilibrium and Transient Gas Phase Adsorption

3 Theory of Gas Phase Adsorption

3.1. Introduction to Adsorption

The term ‘adsorption’ describes the enrichment of atoms and molecules from a gaseous or liquid phase on solid or liquid interfaces. Adsorption is a complex, multifaceted process that can feature chemical and spatial selectivity. There is a differentiation between strong, often irreversible chemical bonding (‘chemisorption’) and weak, reversible attachment of particles (‘physisorption’) depending on the value of the adsorption energy E_{ads}. For this work, only reversible adsorption from a gas phase to a solid interface will be considered. This chapter will present the theoretical framework and models needed to describe this process. Many of the concepts were taken from [38, 39].

The following nomenclature shall be used: The solid that is host to the adsorption process is referred to as ‘adsorbent’, the adsorbed particles as a collective are called ‘adsorbate’. Even in case of physisorption, the adsorbate phase usually has reduced mobility [40]. Translations on the solid surface are then limited to an activated hopping process between adsorption sites that will be discussed in Sec. 5.2.

The reason for the attraction to the interface are intermolecular forces at the solid boundary. The exact microscopic mechanisms and the strength of the interaction potential strongly depend on the surface chemistry and the adsorbate properties, often a combination of interactions is expected. The most common examples of interactions include van-der-Waals forces, electrostatic forces caused by ionic charges or polarized bonds, and hydrogen bonds, as depicted in Fig. 3.1.

The weak van-der-Waals interactions are present for every combination of adsorbate and adsorbent, even for neutral particles on saturated surfaces, e.g. noble gases on graphite. In porous Vycor glass, as discussed in Sec. 2.1.4, additional strong dipolar interactions and hydrogen bonding of the surface silanol groups are possible.

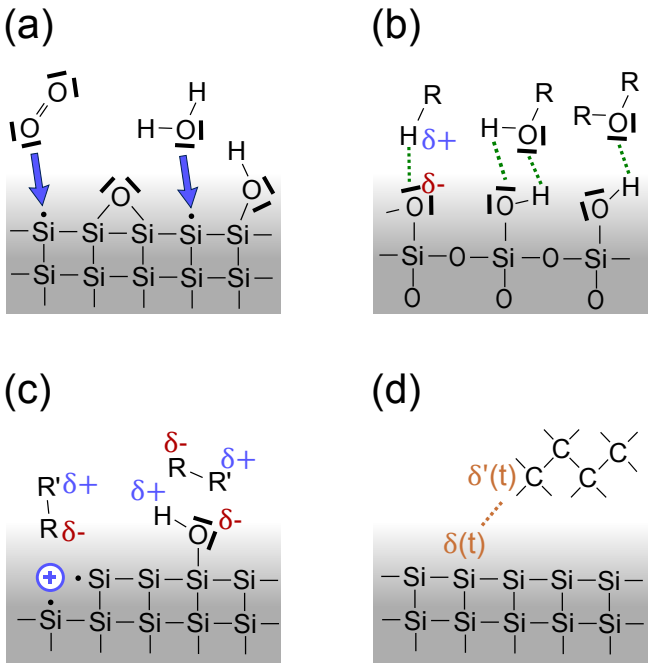

Figure 3.1.: Illustration of different surface bonds, ordered by the respective interaction strength: (a) covalent bonds that are responsible for chemisorption, (b) hydrogen bonds, (c) electrostatic interactions between ionic charges and dipoles, (d) van-der-Waals interactions.

3.2. Adsorption Thermodynamics

3.2.1. Free Energy Description of Adsorption

A possible description of adsorption thermodynamics results from the Helmholtz free energy F_{tot} of a system consisting of an adsorbent (F_s), adsorbate (F_σ) and the gas phase (F_g). Here, an adsorbent with homogeneous characteristics and an ideal gas are assumed. The notation of the adsorbed phase follows the Gibbs sorption theory as reviewed by Rouquerol et al. [39].

As an extensive state function of thermodynamics, the total free energy equals the sum of all free energies of the partial systems,

$$F_{\text{tot}} = F_s + F_\sigma + F_g. \tag{3.1}$$

The individual free energy terms in Eq. (3.1) for the three phases are given as the potentials

$$F_i = U_i - T_i S_i. \tag{3.2}$$

On the right hand side of Eq. (3.2), S_i denotes the entropy and U_i the internal energy of the phase. In a gas, F_g is a function of the temperature T_g, the volume occupied by the gas V_g, and the number of particles N_g with an internal energy

$$U_g(S_g, V_g, N_g) = T_g S_g - P V_g + \mu_g N_g. \tag{3.3}$$

This introduces the pressure P and a chemical potential μ_g. The chemical potential, implicitly, is a function of molecular concentration and thus the pressure P. Any change in free energy can be quantified by the total differential $\mathrm{d}F_g$:

$$\begin{aligned} \mathrm{d}F_g &= \mathrm{d}U_g - \mathrm{d}(T_g S_g) \\ &= T_g \,\mathrm{d}S_g - P \,\mathrm{d}V_g + \mu_g \,\mathrm{d}N_g - T_g \,\mathrm{d}S_g - S_g \,\mathrm{d}T_g \\ &= -S_g \,\mathrm{d}T_g - P \,\mathrm{d}V_g + \mu_g \,\mathrm{d}N_g. \end{aligned} \tag{3.4}$$

In the same manner, it is possible to find a total differential of free energy for the solid matrix and the adsorbate on the interface. Here, it is appropriate to introduce an interfacial energy term instead of the volume energy, which replaces PV_g with $\gamma_{s,\sigma} A_{s,\sigma}$ in Eq. (3.3). The variable $A_{s,\sigma}$ and constant $\gamma_{s,\sigma}$ denote the area and the specific interfacial energy (i.e. interfacial tension) of the unoccupied solid surface or the adsorbate covered surface, respectively. Consequently, in the total free energy differentials F_s and F_σ, the change in surface energy is accounted for by $\gamma_{s,\sigma} \,\mathrm{d}A_{s,\sigma}$:

$$\mathrm{d}F_{s,\sigma} = -S_{s,\sigma} \,\mathrm{d}T_{s,\sigma} - \gamma_{s,\sigma} \,\mathrm{d}A_{s,\sigma} + \mu_{s,\sigma} \,\mathrm{d}N_\sigma. \tag{3.5}$$

3.2.2. Equilibrium Conditions

As a consequence of the second law of thermodynamics, a closed system in thermodynamic equilibrium reaches a minimum in its free energy ($\mathrm{d}F = 0$). Although the above system is in contact to an external thermal bath, there is no energy exchanged when an equilibrium is reached. Hence, it is appropriate to apply this principle to F_{tot} in Eq. (3.1) in order to deduce an equilibrium condition.

Due to the isothermal ($T_g = T_s = T_\sigma = \text{const}$) and isosteric ($V_g = \text{const}$) conditions, the total differentials for each component simplify considerably in equilibrium. Moreover, on the interface, although there might be ongoing dynamic desorption and adsorption, the adsorbate covered area remains constant ($A_\sigma = \text{const} \Rightarrow A_s = \text{const}$). The change in free energy then solely depends on the change in the number of adsorbed particles, resulting in an equilibrium

condition

$$\frac{\partial F_{\text{tot}}}{\partial N_\sigma} = \frac{\partial F_s}{\partial N_\sigma} + \frac{\partial F_\sigma}{\partial N_\sigma} + \frac{\partial F_g}{\partial N_\sigma} = 0. \tag{3.6}$$

One can rewrite Eq. (3.6) using the continuity condition $\partial N_\sigma = -\partial N_g$:

$$\frac{\partial \left(F_s + F_\sigma\right)}{\partial N_\sigma} = \frac{\partial F_g}{\partial N_g}. \tag{3.7}$$

Using Eqs. (3.4) and (3.5), these partial differentiations correspond to chemical potentials:

$$\mu_{s+\sigma}(N_\sigma) = \mu_g. \tag{3.8}$$

Hence, in equilibrium, the combined adsorbate-adsorbent system and the gas have equal chemical potential. Note that the chemical potential of the solid matrix and the adsorbate were combined to a single effective quantity. This combined chemical potential is defined by complex surface interactions with local variations and possibly also changes if continued adsorption alters these properties, e.g. by matrix deformations [41]. Therefore, it is not easily accessible and no exact concentration of surface adsorbate can be derived from Eq. (3.8). A different modelling approach is required, see Sec. 3.3.1 and 3.3.2.

3.2.3. Non-Equilibrium Thermodynamics

In non-equilibrium, an analytic description of the free energy landscape, even for planar adsorbents is very complex, due to the large number of degrees of freedom and local variations in the system. Here, only two phenomena in non-equilibrium are introduced.

The first arises as a result from Sec. 3.2.2: In equilibrium, chemical potentials of the gas phase and the adsorbate accommodate to one another. If there is an initial imbalance in chemical potential, e.g. caused by a sudden pressure increase of the gas, an equalizing process is expected. This is the driving force of a diffusive flow into the matrix. The physics and mechanisms of this matter transport will be discussed in Sec. 5.

Second, as described above, the molecules in the adsorbate are limited in their degrees of freedom compared to molecules in the gas phase, hence the entropy decreases. On adsorption, this corresponds to a difference in internal energy. For fast processes far from equilibrium, the energy difference is detectable as a latent heat of adsorption in calorimetric measurements [42]. However, in case of slow adsorption processes, a good thermal coupling to an external reservoir ensures the continuous heat transfer and isothermal conditions can be assumed in good approximation.

3.3. Adsorption on Solid Interfaces

3.3.1. The Langmuir Model of Monolayer Adsorption

The Langmuir adsorption model is a simple model that estimates the amount of adsorbate for monolayer adsorption on a homogeneous surface with a constant number S of adsorption sites and non-interacting adsorbate particles. A review and microscopic interpretation can be found in [38].

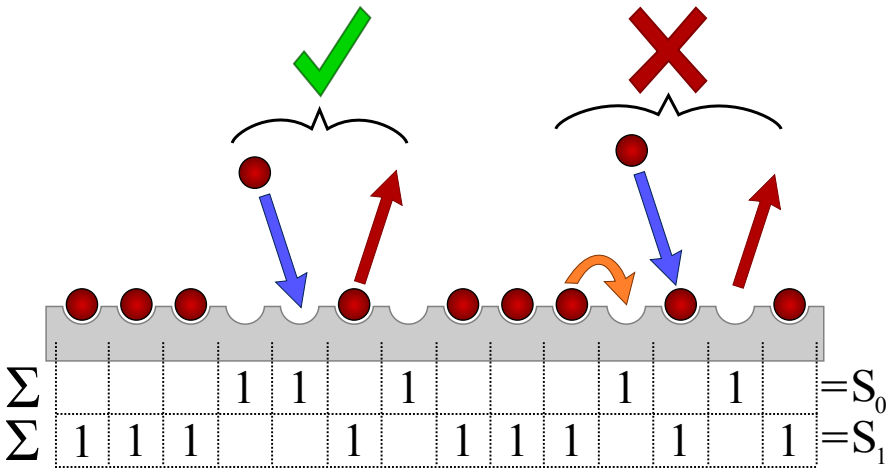

Figure 3.2.: Illustration of the Langmuir monolayer adsorption. Adsorption sites are homogeneously distributed on a model surface. Empty sites have a probability to capture an adsorbate particle, occupied sites have a probability for desorption. Other transitions are prohibited. Depending on the pressure of the surrounding gas and the properties of the combination of adsorbate/adsorbent, a relative surface coverage can be modelled, see text.

A model surface for Langmuir adsorption is depicted in Fig. 3.2. At any point, the total adsorption capacity S of this surface can be written as the sum of the vacant adsorption sites S_0 and occupied sites S_1.

The rate of adsorption ζ_{ads} is modelled using a probabilistic approach: The adsorption probability for each empty site is proportional to the number of incident adsorbate particles hitting the respective site which in turn is proportional to the total number of particles in the gas phase and thus the gas pressure. The total rate of adsorption then equals a product of the individual probability and the number of vacant adsorption spots,

$$\zeta_{\text{ads}} = k_{\text{ads}}\, P\, S_0, \tag{3.9}$$

with a constant k_{ads} containing the specific adsorption properties of the surface and the gas.

A similar relation can be found for desorption: In order to vacate a surface spot, an adsorbate particle needs to overcome an energy barrier defined by the molar adsorption energy E_{ads}. For temperatures $T > 0\,\text{K}$, the thermal activation of this process has a constant non-zero probability for every occupied site. In total, the desorption rate can be written as

$$\zeta_{\text{des}} = \underbrace{a_L \exp\left(-\frac{E_{\text{ads}}}{RT}\right)}_{k_{\text{des}}} S_1, \tag{3.10}$$

with the molar gas constant $R = 8.314\,\frac{\text{J}}{\text{mol K}}$ and a characteristic scaling factor a_L for the gas-solid combination.

In dynamic equilibrium, adsorption and desorption rates are equal. Combining Eqs. (3.9) and (3.10) and using $S_0 = S - S_1$ yields

$$\begin{aligned} \zeta_{\text{des}} &= \zeta_{\text{ads}} \\ \Leftrightarrow k_{\text{des}}\, S_1 &= k_{\text{ads}}\, P\,(S - S_1)\,. \end{aligned} \tag{3.11}$$

By rearranging Eq. (3.11), the relative surface coverage S_1/S can be expressed in terms of the pressure and a single constant:

$$\begin{aligned} \frac{S_1}{S} &= \frac{k_{\text{ads}}\, P}{k_{\text{des}} + k_{\text{ads}} P} \\ &= \frac{K_L\, P}{1 + K_L\, P}, \end{aligned} \tag{3.12}$$

with the Langmuir constant

$$K_L = \frac{k_{\text{ads}}}{k_{\text{des}}} = \frac{k_{\text{ads}}}{a_L} \exp\left(\frac{E_{\text{ads}}}{RT}\right). \tag{3.13}$$

The relative surface coverage in Eq. (3.12) is equal to a normalized molar amount of substance $S_1/S = N/N_{\text{ML}}$, with N_{ML} as the amount absorbed in the complete monolayer. For low pressures $K_L\, P \ll 1$, Eq. (3.12) is a linear relation; for $P \to \infty$, it asymptotically approaches full coverage $N/N_{\text{ML}} = 1$. As the Langmuir model does not account for adsorption exceeding this layer (e.g. bulk condensation), its application to experimental results is limited to stages of submonolayer and monolayer condensation. Then, the value of K_L is a measure of the interaction between the monolayer and the surface. A series of plots for N/N_{ML} on a constant pressure range for different K_L is depicted in Fig. 3.3.

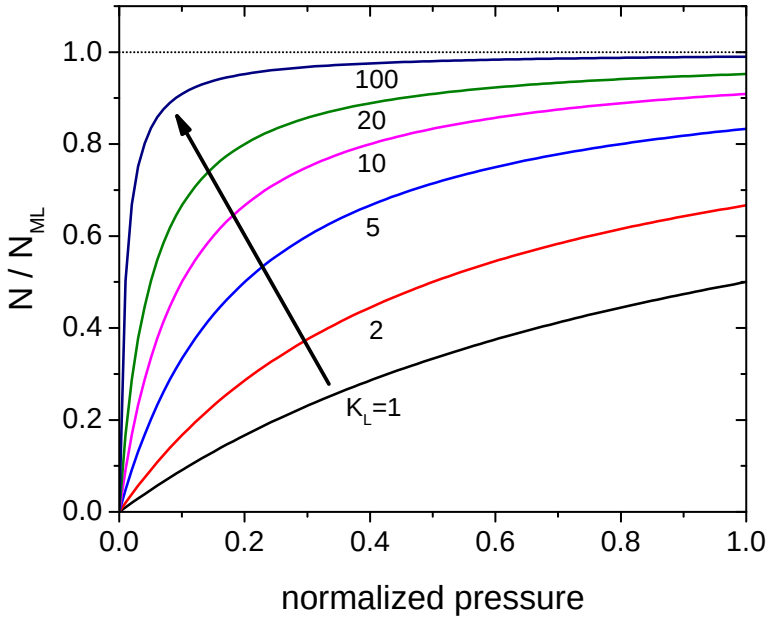

Figure 3.3.: Effect of the Langmuir constant on monolayer adsorption. The higher the values of K_L (i.e. stronger interaction potentials), see Eq. (3.13), the higher the relative monolayer coverage at a respective pressure. For high K_L, monolayer adsorption approaches a step function.

3.3.2. The BET Model of Multilayer Adsorption

In general, adsorption is not limited to a single molecular layer on the interface. If there is an attractive potential exceeding the first adsorbed layer, additional multilayer adsorption is expected.

A theory has been proposed by **B**runauer, **E**mmett and **T**eller that generalizes Langmuir adsorption for multiple layers on planar adsorbents [43, 38]. In many cases, it provides an accurate description of adsorption capability beyond the monomolecular layer. Until today, this model is used in the estimation of the monolayer capacity and the internal surface area of porous solids [44].

The BET model is based on a geometry similar to the Langmuir model with homogeneous distribution of adsorption sites on the surface. In contrast to Langmuir theory, each can be occupied multiple times. S_i then defined the number of sites holding the exactly i adsorbate particles. In layers beyond the monolayer, $i > 1$, adsorption is only permitted for sites that are occupied by $i - 1$ particles. As another model restriction, there are no direct transitions from one layer to another, only desorption and adsorption mechanisms are permitted. Moreover, desorption of multiple layers at once is also not allowed, only the outermost layer can be removed. Fig. 3.4 illustrates these rules and configurations.

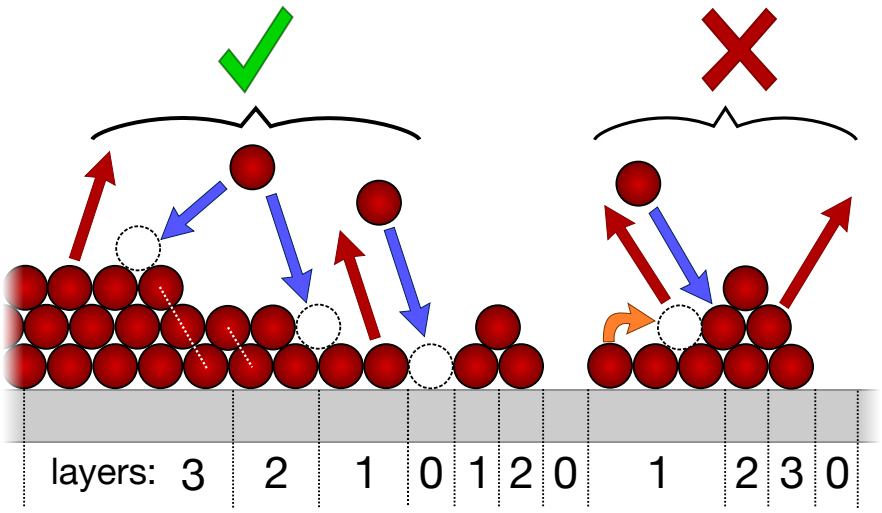

Figure 3.4.: Illustration of the BET multilayer adsorption. Adsorption sites with homogeneous distribution on the surface can be occupied multiple times. Empty sites on the surface and on preadsorbed layers have a probability to capture an adsorbate particle, but only the outermost occupied position has a probability for desorption. Direct transitions from one layer to another are prohibited.

The rate of adsorption in each layer is modelled according to the Langmuir model, see Eq. (3.9):

$$\zeta_{\text{ads},i} = k_{\text{ads},i}\, P\, S_{i-1} \tag{3.14}$$

An important simplification results from the difference in force potentials in the individual layers. Since the interaction in higher layers ($i > 1$) is primarily caused by the adsorbate, not by the solid interface, the adsorption constants are assumed equal, $k_{\text{ads},2} = k_{\text{ads},3} = \ldots = k_{\text{ads},c}$.

Desorption from the i-th layer is defined analogous to Eq. (3.10),

$$\zeta_{\text{des},i} = \underbrace{a_i \exp\left(-E_i/RT\right)}_{k_{\text{des},i}} S_i. \tag{3.15}$$

The energy of desorption E_i and the rate coefficient a_i are defined for each layer in analogy to the Langmuir model, see Sec. 3.3.1. Again, an assumption is made that the interaction potential is the equal for layers $i > 1$, so that $E_2 = E_3 = \ldots = E_c$ and $a_2 = a_3 = \ldots = a_c$. In equilibrium, this results in the following rate equations for each layer:

$$k_{\text{ads},1}\, P\, S_0 = k_{\text{des},1}\, S_1 \tag{3.16}$$

$$k_{\text{ads},c}\, P\, S_{i-1} = k_{\text{des},c}\, S_i \tag{3.17}$$

By introducing the two parameters

$$\alpha = \frac{k_{\text{ads},1}\, P}{k_{\text{des},1}} \quad ; \quad \beta = \frac{k_{\text{ads},c}\, P}{k_{\text{des},c}}, \tag{3.18}$$

the individual layer coverages can be written as

$$S_1 = \alpha S_0 \tag{3.19}$$

for the first layer and

$$S_i = \beta S_{i-1} = \beta^{i-1} S_1 = \alpha \beta^{i-1} S_0 = C \beta^i S_0 \tag{3.20}$$

for the other layers. The newly introduced constant C in Eq. (3.20) is independent of the pressure of the surrounding gas:

$$C = \frac{\alpha}{\beta} = \frac{a_c\, k_{\text{ads},1}}{a_1\, k_{\text{ads},c}} \exp\left(\frac{E_1 - E_c}{RT}\right). \tag{3.21}$$

In order to calculate the total surface coverage S_{tot}, a summation of the coverage in all layers has to be applied:

$$S_{\text{tot}} = S_1 + 2S_2 + 3S_3 + \ldots = \sum_{i=1}^{\infty} i S_i = C S_0 \sum_{i=1}^{\infty} i \beta^i = \frac{C S_0 \beta}{(1-\beta)^2}. \tag{3.22}$$

The geometric series in Eq. (3.22) converges because $\beta < 1$. This can be seen in Eq. (3.20) as the higher layer S_i has fewer molecules in it than the layer below it, S_{i-1}. Similar to the Langmuir model, a monolayer capacity is defined by the total number of possible adsorption spots on the interface:

$$S_{\text{ML}} = S_0 + S_1 + S_2 + \ldots = S_0 + C S_0 \sum_{i=1}^{\infty} \beta^i = S_0 + \frac{C S_0 \beta}{1-\beta}. \tag{3.23}$$

The relative surface coverage that can be interpreted as an averaged number of layers covering the surface is given by the quotient $S_{\text{tot}}/S_{\text{ML}}$:

$$\frac{S_{\text{tot}}}{S_{\text{ML}}} = \frac{C S_0 \beta/(1-\beta)^2}{S_0 + C S_0 \beta/(1-\beta)} = \frac{C\beta}{(1-\beta)(1-\beta+C\beta)}. \tag{3.24}$$

The final step is to identify the parameter β. This can be achieved by considering the process

of bulk condensation, i.e. a liquid-vapour interface at equilibrium vapour pressure P_0. This is equivalent to a system of i liquid layers on which adsorption and desorption are allowed at all positions S_{ML}. Hence, the equilibrium condition can be expressed in analogy to Eq. (3.17):

$$\begin{aligned} k_{\mathrm{ads},c}\, P_0 S_{\mathrm{ML}} &= k_{\mathrm{des},c}\, S_{\mathrm{ML}} \\ \Leftrightarrow P_0 &= \frac{k_{\mathrm{des},c}}{k_{\mathrm{ads},c}} = \frac{P}{\beta} \\ \Leftrightarrow \beta &= \frac{P}{P_0}. \end{aligned} \tag{3.25}$$

Because of this identity, P/P_0 is commonly used as the abscissa in plots of equilibrium adsorption, see Sec. 3.4.1. By combining Eqs. (3.24) and (3.25), the BET estimation of adsorbate amount is found,

$$\frac{N}{N_{\mathrm{ML}}} = \frac{S}{S_{\mathrm{ML}}} = \frac{C}{(1 - P/P_0)[1 + P/P_0(C-1)]} \frac{P}{P_0}. \tag{3.26}$$

A comparison of N/N_{ML} for different values of C can be found in Fig. 3.5. For strong adsorption, Eq. (3.24) reproduces a monolayer step similar to the Langmuir model, see Fig. 3.3. For weak interaction potentials ($C \to 1$), the BET model predicts a concave curve shape over the entire pressure range $P/P_0 = 0$ to 1.

For pressures $P \to P_0$, the adsorbate amount diverges in the BET theory. On one hand, this is consistent with bulk condensation. On the other hand, however, it is also a source for criticism on the model: Even for weak surface interactions and non-wetting fluids, the BET approach still predicts a comparable behaviour. Moreover, the adsorbate amount for high relative pressures is often overestimated in comparison to experimental data [45]. A probable explanation for this discrepancy are adsorbate-adsorbate interactions that have been neglected in the BET theory. A way to improve the modelling capabilities of the BET theory is to set a maximum number of layers that can be adsorbed. This however is a purely empirical method that has no theoretical justification.

3.4. Adsorption in Nanoporous Solids

3.4.1. Sorption Isotherms

As discussed in Sec. 3.3, the adsorption of mono- and multilayers of particles is directly related to the microscopic properties the interface. These concepts apply equally to planar surfaces and porous materials. In the following section, the effects of geometric confinement on ad-

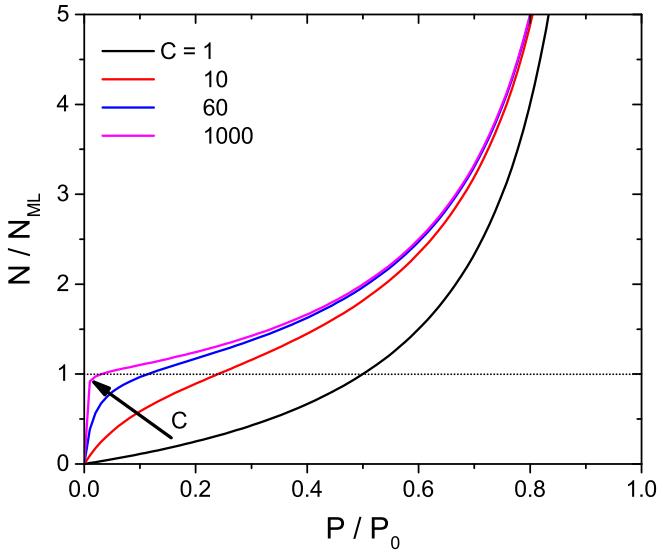

Figure 3.5.: Effect of the BET interaction constant on multilayer adsorption according to Eq. (3.26). For strong interactions ($C \gg 1$), the submonolayer and monolayer condensation are comparable to the Langmuir model. Weak interaction ($C = 1$) changes the curve shape profoundly. In all cases, the adsorbate amount diverges in the limit $P \to P_0$.

sorption will be discussed.

A widely used material characterization technique involves the measurement of a series of equilibrium adsorption situations by varying the gas pressure at constant temperature T and plotting the adsorbed amount versus the equilibrium pressure. As introduced in Sec. 3.3.2, the abscissa is usually set to a pressure normalized to the vapour pressure ($P/P_0 = 0$ to 1) and the ordinate axis is normalized to its maximum value before the bulk vapour condensation ($N/N_0 = 0$ to 1). These representations of adsorption capacities are referred to as 'sorption isotherms'.

The qualitative shape of the sorption isotherm is indicative of the material structure and the strength of molecular interactions between sorbate and sorbent. A classification has been introduced by the IUPAC [46] according to Fig. 3.6.

On planar surfaces, as discussed in Sec. 3.3.1 and 3.3.2, mono- or multilayer adsorption is expected. Depending on the interaction strength, a more or less pronounced step for low P/P_0 can be observed which is consistent to the formation of the monolayer in Langmuir theory (type I). The type II and III isotherms are similar to the BET multilayer adsorption curves, see Sec. 3.3.2 and Fig. 3.5. For strong interactions, a stage of continuous increase in N/N_0 succeeds the monolayer condensation (type II). In case of very weak interaction potentials between the surface and adsorbate, no monolayer step is observed (type III). A

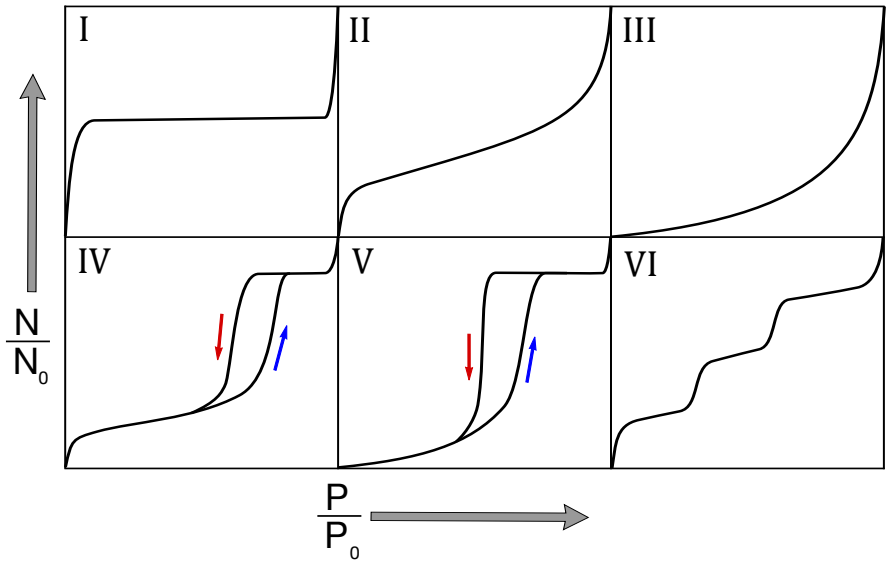

Figure 3.6.: IUPAC classification of sorption isotherms, according to [44]. For planar substrates, depending on the interaction strength, adsorption is limited to mono- or multilayer adsorption (types I, II, III). A special case is stepwise multilayer adsorption on highly ordered surfaces (VI). In mesoporous materials, additional capillary condensation and hysteresis effects are observed (types IV, V).

special case of layer condensation is depicted as type VI: For extremely uniform surfaces, e.g. graphite, coordinated layer growth can occur under certain conditions which causes stepwise adsorption in the multilayer stage.

Regarding porous materials, the sorption isotherms may deviate from the above behaviour depending on the pore size. For macropores ($d_p > 50\,\mathrm{nm}$), the surface is quasi-planar and effects of confinement are not yet noticeable, hence isotherms are mostly indistinguishable to the types I to III for planar samples. In micropores ($d_p < 2\,\mathrm{nm}$), the adsorption of a single molecular layer often leads to a complete filling, resulting in a type I isotherm with an apparently larger monolayer step.

A principal difference arises for porous materials on the mesoscopic scale, e.g. Vycor. In addition to the expected isotherm for layer growth (types I to III), a sudden condensation into the matrix is noticed on adsorption. Conversely, an inverse transition is observed during desorption, albeit at a different value of the relative pressure, giving rise to a hysteresis loop in the isotherm. This effect, due to 'capillary condensation', is characteristic for the geometric confinement in mesopores, see Sec. 3.4.2. It is present for weak (type V) and strong interaction potentials (type IV) alike.

3.4.2. Capillary Condensation and the Kelvin Equation

In contrast to the layer growth discussed in Sec. 3.3, capillary condensation is a consequence of geometric confinement rather than surface interactions and is never present for planar adsorbents. Capillary condensation in mesoporous solids induces a saturated state of maximum filling well below the bulk vapour pressure.

A simple approach to modelling this behaviour is to interpret the adsorbate layers as a liquid and to idealize the geometry of the adsorbent and the microscopic distribution of the adsorbate. Then, as proposed by William Thomson (Lord Kelvin), continuum mechanics and thermodynamics predict the breakdown of the layer condensate when a critical point is reached.

For a curved liquid interface in equilibrium to its vapour, the pressure is a function of the curvature r_C. Using the Young-Laplace equation (see Sec. 9.1.2), an altered vapour pressure $\tilde{P}$ can be calculated[1]. The resulting relation,

$$\ln \frac{\tilde{P}}{P_0} = -\frac{2\gamma_{\mathrm{lv}} V_m}{RT} \frac{1}{r_c}, \tag{3.27}$$

is known as the Kelvin equation. Here, γ_{lv} and V_m denote the surface tension and the molar volume of the liquid. For any given point on a two-dimensional surface, the radius of curvature r_c is described by the two principal curvatures (r_1, r_2),

$$\frac{1}{r_c} = \frac{1}{2}\left(\frac{1}{r_1} + \frac{1}{r_2}\right). \tag{3.28}$$

By definition, convex curvatures are counted negative ($r_c < 0$), concave curvature positive ($r_c > 0$), so that a reduction in vapour pressure $\tilde{P} < P_0$ for concave surfaces is observed. It should be noted that the Kelvin equation assumes no interactions between the capillary condensate and the solid interface. A different model approach, including an interaction potential, will be presented in Sec. 3.4.5.

Eq. (3.27) applies to both situations, capillary adsorption and desorption. The following paragraphs will describe why this results in a difference in stability and spatial distribution of different adsorbate configurations in a single cylindrical pore of radius r_0, as illustrated by Fig. 3.7.

In the layer condensation stage (1), the adsorbate layers of thickness t take the shape of a cylinder mantle with inner radius $r_i = r_0 - t$. The principal curvatures are then defined as $r_1 = r_i$ and $r_2 \to \infty$ since the pore wall runs straight in parallel to the pore axis. With Eq.

[1] For more details on the derivation, see [39].

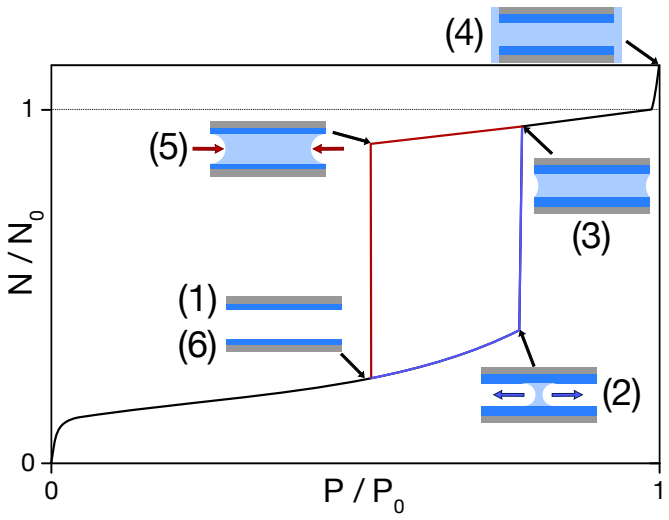

Figure 3.7.: Adsorbate amount and distribution for capillary condensation in a cylindrical pore. Formation and breakdown of the capillary condensate are discrete transitions that are defined by different interface curvatures, see text.

(3.28), this results in $r_c = 2r_i$ for every point on the surface. When more and more adsorbate covers the pore walls, r_i decreases until a critical radius r_{ads} is reached which corresponds to a critical pressure $\tilde{P}_{\text{ads}}$. The Kelvin equation can be used to predict this transition,

$$\ln \frac{\tilde{P}_{\text{ads}}}{P_0} = -\frac{\gamma V_m}{RT} \frac{1}{r_{\text{ads}}}. \tag{3.29}$$

In the process, a 'capillary bridge' forms between the adsorbate covered pore walls, i.e. a liquid filled section with a concave interface ('meniscus') on each end (2). For now, let us assume a hemispherical shape of the menisci, which is consistent with complete wetting of the adsorbed layers (contact angle $\theta = 0$). On formation, the resulting curvature of the interface is defined by $r_1 = r_2 = r_c = r_{\text{ads}}$ and was thus halved in comparison to the cylinder shape. According to the Kelvin equation, the local vapour pressure is again reduced ($\tilde{P}' < \tilde{P}_{\text{ads}}$) and a spontaneous, rapid condensation at the capillary bridge is expected. In order to reach an equilibrium configuration in the pore, either the pressure has to drop to $\tilde{P}'$ or a reduction of the meniscus curvature is required. Without changing the contact angle, the latter is only possible at the pore openings, thus a complete filling takes place (3).

On further increase of the pressure, the interfaces at the pore entrances continue to flatten, taking up a small amount of additional adsorbate. For monolithic samples, in comparison to capillary condensation in the pore volume, this effect on the macroscopic sample surface is

very limited[2]. In the limit $P \to P_0$, meniscus curvature approaches infinity ($r_c \to \infty$), i.e. bulk condensation on the exterior of the pore (4). Both, bulk condensation and the meniscus flattening are reversible on subsequent desorption.

When decreasing the pressure past the transition point of capillary condensation, $\tilde{P}_{\text{ads}}$, the menisci remain still stable. The breakdown of the hemispherical meniscus occurs for a different critical radius $r_1 = r_2 = r_c = r_{\text{des}}$, as depicted in (5). Using this curvature in Eq. (3.27), the transition condition for desorption is

$$\ln \frac{\tilde{P}_{\text{des}}}{P_0} = -\frac{2\gamma V_m}{RT} \frac{1}{r_{\text{des}}}, \tag{3.30}$$

where r_{des} and $\tilde{P}_{\text{des}}$ are defined in analogy to the adsorption case. After desorption, a residual layer condensate remains on the pore wall. Its layer thickness is equal to the value at the same point during adsorption (6).

The difference between both critical pressures $\tilde{P}_{\text{ads}}$ and $\tilde{P}_{\text{des}}$ that results only from the liquid properties and the geometric factor 2 is what defines a hysteresis loop in the sorption isotherm in the Kelvin model.

3.4.3. Metastability and Pore Blocking

So far, only capillary condensation for an idealized cylindrical pore has been considered. In real systems, complex pore geometries and a distribution of different pore sizes in a porous solid change the appearance of a sorption hysteresis critically. There are two effects that should be discussed in case of Vycor glass.

The first is metastability of the adsorbed multilayer. In Fig. 3.7, there is a segment of the adsorption branch, (1) $\to$ (2), in coexistence to a segment on the plateau before desorption, (3) $\to$ (5). This contradicts classical thermodynamics, stating that there is only one global minimum of free energy defined by the surface chemical potential. In analogy to the consideration in Sec. 3.2, the adsorbate distribution should approach a defined state in the limit $t \to \infty$. As is expected from the energy balance for adsorption, this should be a complete filling of the pores. However, in order to overcome the point of capillary adsorption, an activation is needed. The adsorbed wall layers thus remain in metastability until the transition is triggered. As an example, delayering of an argon multilayer to capillary condensate has been observed in mesopores on cooling [47].

In an experimental context, this is important to consider: Although the reproducibility of

[2]The saturation plateau in real sorption isotherms often exhibits a slight positive slope due to bulk-condensation on defects of the macroscopic surface.

sorption isotherms suggests large life times of metastable layers, the observed adsorption isotherm can possibly be influenced by the time of measurement, which introduces uncertainty into the adsorption branch.

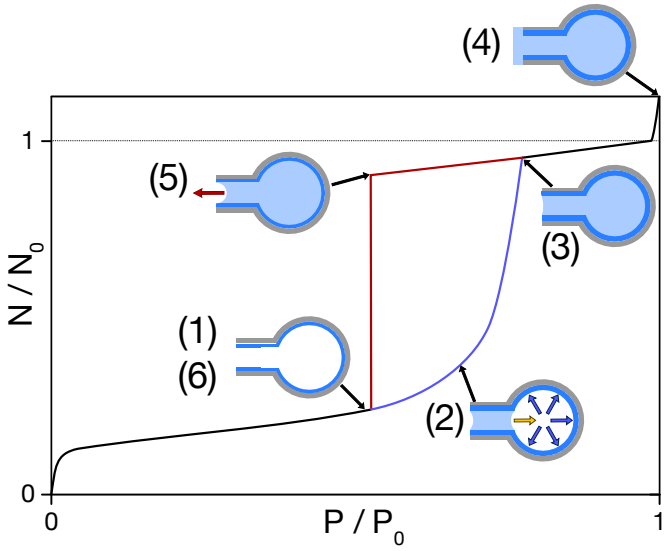

Figure 3.8.: Pore blocking in ink-bottle pores. On capillary adsorption, the meniscus can rearrange to fill the cavity. However, in contrast to cylindrical pores, the desorption transition for the spherical section of large curvature is determined by the smaller curvature at the pore entrance. As a consequence, the isotherm is asymmetrical in adsorption and desorption direction.

The second important phenomenon is pore blocking as a consequence of a distribution of pore radii. During desorption, parts of the pore space apparently contain a stable capillary condensate even though they would individually transition to a layer condensate.

A model system for this effect are ink-bottle pores: A spherical pore volume shall be connected to the outside only by a single pore neck of smaller diameter, see Fig. 3.8. On adsorption, layer condensate covers the pore homogeneously (1). The critical pressure for capillary condensation in the pore neck is lower than in the spherical section, a capillary bridge thus plugs this part of the pore (2). However, when raising the pressure, the adsorbate can rearrange by a dynamic desorption-adsorption mechanism, so that the cavity is filled gradually (3). On the saturation plateau and during bulk condensation, the pore is filled completely (4). As for desorption, the large internal cavity is blocked for desorption by the smaller pore neck. The transition point for the entire pore is then determined by the small pore radius (5).

For more complex networks, it has to be noted that the pore connectivity largely influences the magnitude of pore blocking in networks. For porous Vycor glass, in contrast to parallel pore arrays, it has been shown that even in the stage of capillary condensation ($N/N_0 > 0.4$),

there are still connected networks of empty pores [48, 49]. The extent of this percolation can in turn be used to estimate the pore connectivity [50].

As a result of both effects, the hysteresis loop in many porous materials is asymmetrical for adsorption and desorption ('H2 hysteresis' [46]).

3.4.4. Calculating Pore Size Distributions

Application of the Kelvin Equation

One of the goals in measuring adsorption isotherms is to gain information on internal pore structure. Due to the geometric origin of capillary condensation, the Kelvin equations (3.29) and (3.30) are a well suited basis for the experimental determination of a pore size distribution in porous solids.

In real pore networks, the total sorption isotherm can be interpreted as a superposition of partial isotherms for different radii weighted by a pore volume distribution function $v(r)$ or pore width distribution function $w(r)$. At each pressure step for capillary adsorption or desorption, a certain partial volume of pores fills or empties. Assuming cylindrical pores, Eqs. (3.29) and (3.30) relate the reduced pressures P/P_0 to radii of curvature r_K (as r_{ads} or r_{des}, respectively) for given sections of the isotherm. The partial volume for a specific radius $v(r_K)$ is proportional to the local change in adsorbate $\mathrm{d}(N/N_0)$ over the pressure range $\mathrm{d}(P/P_0)$,

$$v(r_K) = K \left. \frac{\mathrm{d}\frac{N}{N_0}}{\mathrm{d}\frac{P}{P_0}} \right|_{r_K}, \tag{3.31}$$

with a scaling coefficient K. By using numerical differentiation of experimental isotherms and by introducing the norm

$$\int_{r=r_{\text{min}}}^{r_{\text{max}}} v(r_K)\,\mathrm{d}r_k = 1, \tag{3.32}$$

$v(r_K)$ reflects the relative distribution of volume as a function of the Kelvin radius r_K. For experimental data, the boundaries r_{min} and r_{max} are chosen to include only the mesoscopic range of the respective branch of the hysteresis. Hence, it is ensured that other contributions to adsorption, e.g. multilayer adsorption and finite slope in the saturation plateau, are not misinterpreted as capillary condensation. Usually, for the Vycor samples in this work, the range of the normalization was limited from $r_{\text{min}} \approx 1.5\,\text{nm}$ to $r_{\text{max}} \approx 7\,\text{nm}$.

The pore volume distribution $v(r_k)$ can be divided by the cross-sectional area of the pore, $A = \pi r_K^2$, which yields a pore size distribution $w(r_K)$. This is often applied for ordered porous

materials, when pores are modelled to exhibit a constant radius over their entire length. In disordered media, e.g. Vycor glass, the volume distribution $v(r_k)$ is expected to give a better representation of pore widths, since the assumption of cylindrical cross-sections is only a good approximation for finite sections of the pores.

Additional Multilayer Thickness

Due to layer adsorption, as shown in Fig. 3.7, the Kelvin radius determined by Eqs. (3.29) and (3.30) needs to be corrected for the thickness $t(P/P_0)$ of the adsorbed layer in order to derive a pore radius r_0,

$$r_0 = r_K + t(P/P_0). \tag{3.33}$$

In principle, Eq. (3.26) from the BET theory could be restated in terms of a layer thickness, however an overestimation of $t(P/P_0)$ is expected, see Sec. 3.3.2. Many empirical equations have been proposed that relate the vapour uptake to the reduced vapour pressure P/P_0 [51, 52]. In order to derive thickness equations for a multilayer, the general strategy is to apply data obtained for planar substrates with comparable surface chemistry to the isotherms for a porous material, assuming uniform surface coverage for the adsorbate layer. Then, a layer thickness $t(P/P_0)$ can be expressed as a fit function of experimental data.

A versatile empirical model has been proposed by Halsey [53], which is suited to produce type I-III isotherms and also shows a quantitative agreement to experimental data for planar substrates. In its general form, it is now known as the Frenkel-Halsey-Hill (FHH) isotherm. It can also be stated in terms of a layer thickness [54],

$$t(P/P_0) = a \left(\frac{5}{\ln(P_0/P)} \right)^{\frac{1}{b}}. \tag{3.34}$$

For every combination of temperature, adsorbate and sorbent, the model parameters a and b amount to different values. From a theoretical standpoint, a corresponds to a distance between particles in the sorbate that can also be quantified in X-ray diffraction experiments. b is a characteristic exponent related to the intermolecular force potential: Higher values of b indicate strong but short-ranged adsorption resulting in a tendency to avoid multilayers.

Interestingly, for nitrogen, the interaction exponent b was determined as rather robust for many sorbents [55]. This is one of the reasons why the standard characterization isotherm of porous media is carried out with nitrogen at its boiling temperature $\approx 77\,\mathrm{K}$. For this standard

isotherm, the layer thickness can be calculated to

$$t(P/P_0) = 0.354\,\mathrm{nm} \cdot \left(\frac{5}{\ln(P/P_0)}\right)^{\frac{1}{3}}. \tag{3.35}$$

The BJH model

On capillary adsorption and desorption in real systems, the change in the amount of adsorbate is also partially caused by the thickening and thinning of the multilayer upon adsorption and desorption. For a distribution of different pore sizes, this is limited to the pores that are not filled by capillary condensate. This has been recognized by Barrett, Joyner and Halenda as a source of error in the calculation of pore size distributions when relying on Eq. (3.31) [56].

A computational model ('BJH model') has been suggested. It incorporates a fundamental Kelvin equation approach with additional empirical thickness equations for the multilayer that are modelled after adsorption data on planar substrates in order to correct the local slope in the sorption isotherm. However, as we shall see in Sec. 4, the multilayer growth is often negligible in comparison to the impact of capillary condensation. In this case, the BJH model offers no additional precision and is thus rejected in pore size analysis.

Limitations and Discussion

The Kelvin model, despite its numerous simplifications and shortcomings, is still a very common technique to calculate pore size distributions in pore networks. However, there are some points that indicate a critical model failure under certain conditions:

- Continuum mechanics break down on the length scale of micropores.
- The implicit assumption of cylindrical shape fails for complex pore morphologies.
- Multilayer thickness is only empirically derived from planar substrates. Interaction potentials are different in cylindrical geometry.
- For strong adsorbate-wall interactions, the curvature varies along the meniscus.

Many of these limitations result from ignoring the adsorbate-wall interactions and the simplified geometry in the Kelvin model. There has been quite some work regarding the applicability of the Kelvin equation in different systems [57, 58]. A general agreement is that the Kelvin equation is a good approximation in mesoporous samples with pore radii $r_0 > 3\,\mathrm{nm}$, but the

calculated distribution functions in the range $< 3\,\mathrm{nm}$ are to be taken as mostly qualitative estimates. If, however, microporosity plays a large role, any pore size calculation based on the Kelvin equation does only reflect parts of the total pore space.

It should also be mentioned that experimental Kelvin pore size distributions can differ between capillary adsorption and desorption. This effect can be attributed to both metastability and pore-blocking effects, see Sec. 3.4.3, as well as a model weakness by oversimplifying the pore geometry. In many situations, this begs the question which one of the two distribution functions is more accurate. The standard isotherm in the BJH approach always focusses on the desorption branch, reasoning that hemispherical menisci, which the Kelvin equation assumes for desorption, are robust for geometric variations of the pore walls. However, in the case of a complex pore network, as is present in Vycor glass, it can also be justified to reject the desorption data, due to the effect of pore-blocking. A comparison for an experimental nitrogen isotherm in Vycor will be made in Sec. 4.2.3.

3.4.5. Advanced Modelling of Sorption Isotherms

The Model of Saam and Cole

The idea of the Saam-Cole (SC) model is to unify layer and capillary condensation by modelling the film stability in terms of a pore geometry and an adsorbate-wall interaction potential. The original work of Saam and Cole [59] described adsorption of helium in cylindrical pores using a Lennard-Jones interaction potential. The condition for capillary condensation in SC theory is a critical capillary wave excitation in the adsorbed helium films. Depending on the interaction strength and the pore radius, a model isotherm is found, exhibiting the characteristics of cylindrical pores as depicted in Fig. 3.7. In a system of pores with different radii, a weighted summation of model isotherms is applied (using the same interaction potential). By choosing an appropriate weighting function $w(r_0)$, i.e. the model pore size distribution, a match to experimental data can be achieved.

The main advantage of the SC theory is that it is based on microscopic dynamics and interactions rather than macroscopic thermodynamic properties. On one hand, this leads to more accurate predictions of the layer thickness, and on the other hand, the model is expected to hold for slightly smaller pores. While the SC model was conceived for van-der-Waals forces, the interaction potential can also be adapted to different types of adsorbate-wall interactions. However, by introducing this new degree of freedom, there is even more uncertainty in the resulting pore size distributions. Furthermore, some of the geometric assumptions from the Kelvin equation are still present in the SC theory, namely the cylindrical pore geometry and

the treatment of the pore network as a superposition of independent pores. Especially the latter is still problematic when confronted with experimental data exhibiting pore blocking effects.

In conclusion, the SC model is an alternative description of capillary condensation to the classical Kelvin equation. Due to the higher number of assumptions in the model, the uncertainty in the pore size distribution is comparable or larger than in the Kelvin approach, especially for complex interactions. Hence, it will not be used in this work

Non-Local Density Functional Theory

The density functional theory (DFT) describes the distribution of adsorbate in a pore system in terms of a local density $\rho(\boldsymbol{r})$ with a coordinate vector $\boldsymbol{r}$ as the distance to the pore wall in generalized coordinates. From statistical mechanics [60, 39], the grand potential Ω for a single pore can be expressed as

$$\Omega\left[\rho(\boldsymbol{r})\right] = F\left[\rho(\boldsymbol{r})\right] + \int_V \rho(\boldsymbol{r})\left[U_{\text{ext}}(\boldsymbol{r}) - \mu\right]\,\mathrm{d}\boldsymbol{r}. \tag{3.36}$$

Here, $F\left[\rho(\boldsymbol{r})\right]$ is the Helmholtz free energy functional for both the gas and the adsorbate that also contains the particle-particle interactions in the adsorbed phase. U_{ext} is an external force potential resulting from adsorbate-wall interactions and μ is the chemical potential. In an equilibrium state, a density profile results in principle from the minimization of the grand potential at constant μ, V and T. Here, model assumptions need to be made from the treatment of the molecular interactions: Two different potential functions need to be assumed for adsorbate-adsorbate and adsorbate-wall interactions. Most commonly, pairwise Lennard-Jones interaction potentials and/or hard-sphere repulsion are chosen, with mean-field approximations at long ranges. One of the main problems, however, is then found close to the pore walls, as this approach cannot accurately reproduce an inhomogeneous distribution on such small scales.

Due to this shortcoming, 'non-local' variants of the density functional theory (NLDFT) utilize short-range smoothing approximations and weighting functions to predict a fluid density in a pore [61]. Then, in the hysteresis region of the isotherm, there are two local minima of Ω: A (metastable) state with lower mean density as a local minimum and a global minimum as the stable, liquid filled state. These results correspond to the well-known adsorption states in a pore: layer condensation and capillary condensation. The potential functions for both states are equal at the desorption transition and a stability limit of the metastable layer can be

observed that coincides with the adsorption branch of the isotherm.

It is also possible to use NLDFT in the calculation of pore size distributions: An integration of $\rho(\boldsymbol{r})$ over the pore volume gives an amount of substance N so that the isotherm of a single pore can be calculated for given model parameters (interaction potentials, temperature, pore size). Based on a database of model isotherms for different pore sizes r_0 (kernel), a weighting function $w(r_0)$ can be determined by a mathematical regression method that relates the individual contributions to the integral adsorption in a pore system. $w(r_0)$ then corresponds to the pore size distribution. Here, one of the key advantages of NLDFT is the incorporation of microporosity into the isotherm kernel.

Although the modelling is fundamentally different, a good quantitative match of pore size distributions from NLDFT and the Kelvin equation has been found for mesoporous materials. This is especially true in ordered porous materials [61], but even in the complex pore geometry of Vycor within an error margin of $10\,\%$ for pore radii $r_0 > 3\,\mathrm{nm}$ [62].

4 Experimental Study of Equilibrium Adsorption

4.1. Experimental Setup

4.1.1. Manometric Isotherm Measurement

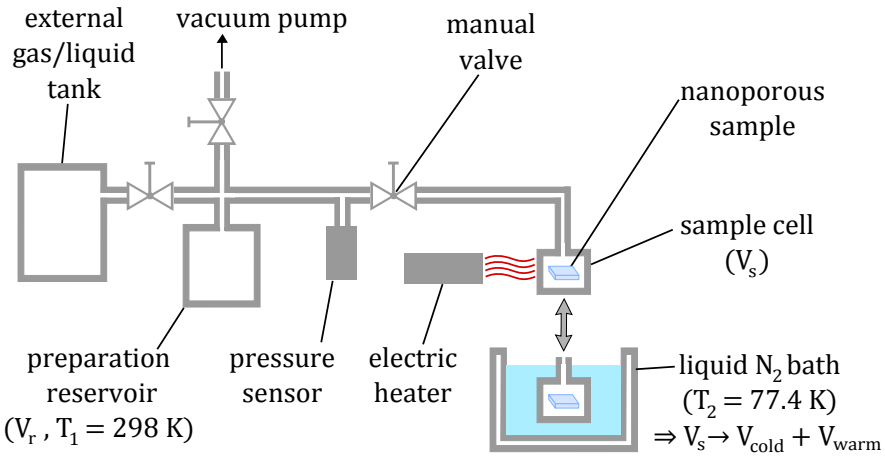

Figure 4.1.: Experimental setup for equilibrium adsorption. The individual components and a typical experiment are described below. The sample cell is exchangeable so that an additional dielectric measurement can be performed *in situ*, see Sec. 4.1.2.

The sorption isotherm experiments were carried out using a manometric evaluation of the amount of adsorbate, see Fig. 4.1. The basic setup consists of a closed gas distribution system that is split into a reservoir of volume V_r and a sample cell of volume V_s that holds the porous material[1]. The pressure in the preparation reservoir can be measured using a capacitive pressure transducer *MKS Baratron*. Both recipients are separated by a manual valve. For nitrogen isotherms, the sample cell can be submerged in a liquid nitrogen bath at boiling temperature. Accordingly, the vapour pressure is then $P_0 \approx 1000\,\mathrm{mbar}$.

Prior to an experiment, the sample cell is evacuated with a turbomolecular pump and heated to temperatures $T > 250\,^{\circ}\mathrm{C}$ by an external heater for a prolonged time, so that the residual water monolayer in Vycor is removed (see Sec. 2.1.4).

For a sorption step, a defined gas pressure P_1 can be prepared in V_r. On opening the valve,

[1] For isotherm experiments without additional dielectric spectroscopy, no gold electrodes were applied to the sample, see Sec. 2.1.3

an equilibrating adsorption or desorption process is initiated that results in a gradual pressure change whose kinetics will be discussed in Sec. 6.1. Once a stable equilibrium is reached, the valve is closed again and the pressure P_2 is measured. The pressure difference before and after the relaxation corresponds to an amount ΔN that is transferred into the sample cell according to the ideal gas equation

$$\Delta N = \frac{V_r}{RT_1}(P_1 - P_2). \tag{4.1}$$

The transferred amount ΔN can be split up into a contribution to the gas phase (ΔN_g) and to the adsorbate (ΔN_σ),

$$\Delta N = \Delta N_g + \Delta N_\sigma. \tag{4.2}$$

The total amount of substance in the gas phase N_g can be calculated for every measured point from the equilibrium pressure P_2, again using the ideal gas equation. In this setup, V_s splits into a partial volume at liquid nitrogen temperature V_{cold} and another part at room temperature V_{warm} due to the connections outside the nitrogen bath.[2] The difference between two consecutive equilibrium states corresponds to $\Delta N_{g,i} = N_{g,i} - N_{g,i-1}$. Then, ΔN_σ can be calculated according to Eq. (4.2). Due to the recursive condition for $\Delta N_{g,i}$, the pressure inside the sample cell has to be tracked continuously throughout the entire experiment and any leakage into the sample cell has to be avoided.

4.1.2. Dielectric Measuring Extension

The setup shown in Fig. 4.1 can also be modified for additional *in situ* dielectric spectroscopy. For this purpose, a different sample cell, described with technical details in [63], has been attached to the preparation volume. A cross-section of this dielectric setup is depicted in Fig. 4.2.

The sample (area A, thickness d) is fixed in an external, circular plate capacitor (diameter $13\,\mathrm{mm}$) that exceeds the sample dimensions. As the sputter coated gold electrodes are directly applied to the matrix material, there are no air gaps or slits that could influence the total sample capacitance. However, as indicated in the inset of Fig. 4.2, the connection between the capacitor and the sample electrodes is by no means a hermetic seal. Due to the finite surface roughness a gas flow is expected in the interspace. The gold coating also does not hinder gas flow into the sample from these sides, as the sputter deposited layer exhibits a large porosity.

A frequency response analyser (FRA) is connected to the capacitor plates. The measuring devices consist of a *Solartron SI 1255 FRA* with the *Solartron 1296 dielectric interface extension*

[2] All volume values were determined experimentally at room temperature and liquid nitrogen temperature.

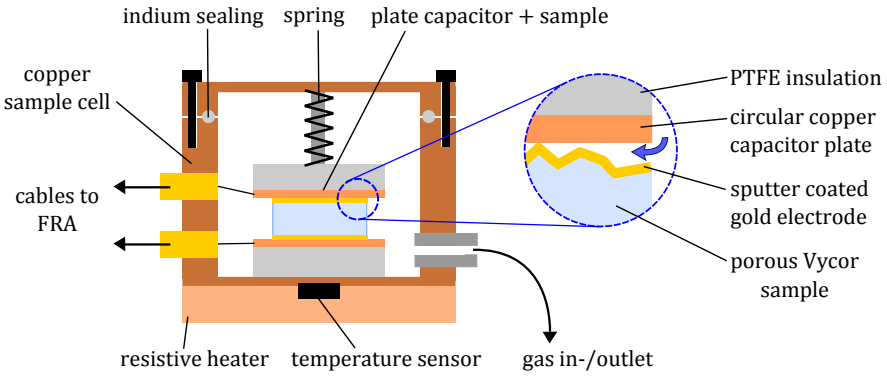

Figure 4.2.: Experimental extension for dielectric sorption isotherm measurement. Instead of the simple cell only holding the porous sample, this sample cell can be used as a replacement in the gas distribution system in Fig. 4.1. Here, the porous sample is fixed inside a defined capacitor geometry which allows a precise dielectric measurement without stray field contributions. The dielectric sample cell can be evacuated and heated, although the maximum temperature cannot exceed 320 K due to technical limitations.

that both generate a signal and interpret the response in terms of the complex impedance for a given frequency. By executing this measurement over a range $\nu = 1\,\mathrm{kHz}$ to $10\,\mathrm{MHz}$ and repeating this frequency sweep periodically, a time-dependent dielectric spectrum can be recorded. The measured signal is saved by the proprietary software as a real and imaginary part of the total connected complex impedance.

$$\tilde{Z}^*(\nu) = \tilde{Z}'(\nu) + i\tilde{Z}''(\nu). \tag{4.3}$$

At first, this signal contains the sample impedance as well as the parasitic line impedance and stray field capacitance of the fixture. By performing two calibration measurements with a defined calibration capacitance and with a short circuit, the parasitic contributions can be removed, see App. C. The resulting impedance signal $Z^* = Z' + iZ''$ then only reflects the sample capacitance C^*,

$$Z^* = \frac{1}{i\omega C^*}. \tag{4.4}$$

The real and imaginary capacitance and hence the sample permittivity can be calculated readily, using the geometric capacitance $C_0 = \varepsilon_0 A/d$,

$$C' = \varepsilon'\varepsilon_0 C_0 = \frac{1}{2\pi\nu}\frac{-Z''}{(Z')^2 + (Z'')^2}, \tag{4.5}$$

$$C'' = \varepsilon''\varepsilon_0 C_0 = \frac{1}{2\pi\nu}\frac{Z'}{(Z')^2 + (Z'')^2}. \tag{4.6}$$

4.2. Nitrogen Isotherm Characterization of Vycor

4.2.1. Sorption Isotherm and Porosity

The different Vycor samples used in this work were characterized in an adsorption isotherm with nitrogen at $\approx 77.4\,\mathrm{K}$, in accordance to the BJH standard conditions [56]. At this temperature, the bulk vapour pressure of nitrogen amounts to $P_0 \approx 1000\,\mathrm{mbar}$.

Fig. 4.3 shows the equilibrium sorption isotherm for Vycor sample *vyc_iso_1* (see App. A) that was calculated using the manometric method described in Sec. 4.1[3].

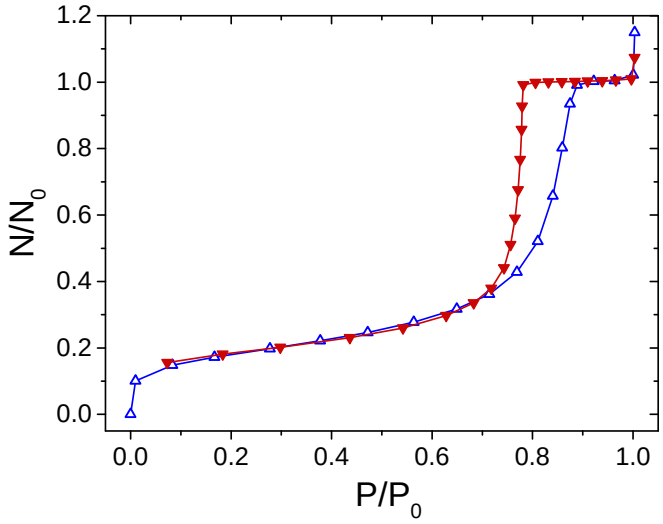

Figure 4.3.: Nitrogen sorption isotherm for sample characterization for sample *vyc_iso_1*, see App. A. △: adsorption, ▼: desorption. From the sorption isotherm, the sample porosity, pore size distribution and other properties can be quantified, see text.

The resulting isotherm curve shows a great match to type IV isotherms, as introduced in Sec. 3.4.1. The prominent, asymmetrical hysteresis loop exhibits a very steep drop for the desorption, whereas during adsorption, the capillary condensation is spread over a wider pressure range. This is consistent with a H2(a) hysteresis loop that results from pore blocking [44].

As a result of the heat treatment prior to the experiment (see Sec. 4.1.1), no residual water is expected in the pores. The sample porosity is thus determined by the maximum molar amount of adsorbate N_0 on the saturation plateau,

$$\Phi = \frac{V_m N_0}{V_{\text{sample}}}, \tag{4.7}$$

[3] No additional dielectric measurement has been performed due to the low relative permittivity and thus the limited resolution for nitrogen.

where V_m is the molar volume of liquid nitrogen and V_{sample} is the macroscopic volume of the porous sample. For the above isotherm, the porosity amounts to $\Phi = 27.5 \pm 0.5\,\%$, other Vycor samples exhibited porosities up to $32.3 \pm 0.5\,\%$. These values are in very good agreement to the material specifications [4].

4.2.2. Multilayer Condensation

Fig. 4.3 exhibits a multilayer condensation stage for a range of $P/P_0 \approx 0$ to 0.7. In terms of adsorbate, a maximum value of $N/N_0 \approx 0.3$ can be attributed to the adsorbed multilayer. Using the BET model introduced in Sec. 3.3.2, a fit of the multilayer adsorption equation, Eq. (3.26), has been applied to the layer condensation stage.

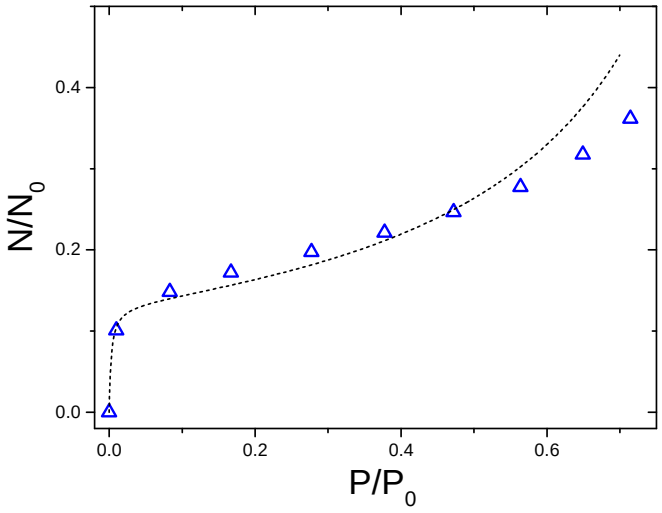

Figure 4.4.: BET fit of equilibrium nitrogen adsorption data in the layer condensation stage. The monolayer step and low pressure layer condensation stage are well described by a BET multilayer growth according to Eq. (3.26) for fit parameters $N_{\text{ML}}/N_0 = 0.132 \pm 0.04$ and $C \approx 350$. For higher pressures, the BET model deviates from the experimental data.

The resulting BET isotherm in Fig. 4.4 fits the initial layer condensation but slightly overestimates the adsorption for higher relative pressures, as expected from the model weaknesses, see Sec. 3.3.2. However, a monolayer capacity $N_{\text{ML}}/N_0 = 0.132 \pm 0.04$ could be derived from the above fit. As for the BET interaction constant, only an order of magnitude estimation $200 < C < 500$ is possible due to the lack of points in the monolayer stage for very low pressures. In conjunction with the isotherm shape, this is consistent with moderately strong pore wall interactions [44].

4.2.3. Pore Volume Distributions

The pore volume distributions $v(r_0)$ have been calculated for the adsorption and desorption branches using the respective Kelvin equation with an additional wall layer correction by Eq. (3.35), as described in detail in Sec. 3.4.4. Results are depicted in Fig. 4.5.

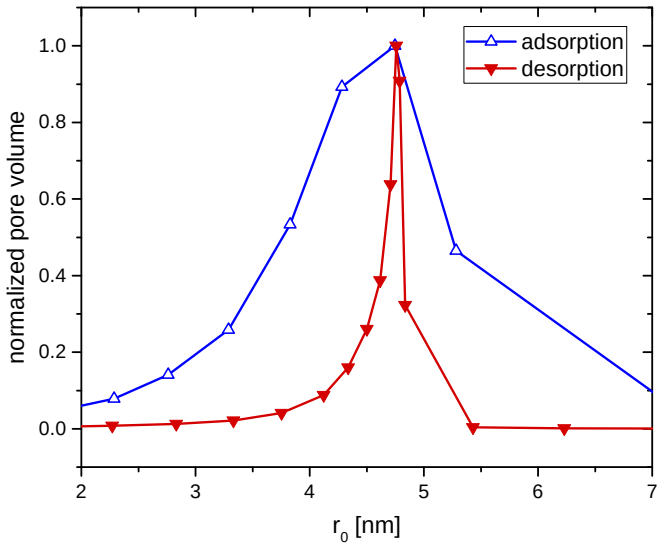

Figure 4.5.: Normalized pore volume distribution for Vycor, extracted for the adsorption and desorption branch of the isotherm in Fig. 4.3, respectively. Note that both plots are normalized to a maximum value of 1 instead to the integral norm introduced in Eq. (3.32) for better comparison.

As expected from the isotherm shape, the most frequent pore radii are found in the low mesoporous range, with an equal maximum value of $r_{0,\mathrm{max}} \approx 4.75\,\mathrm{nm}$ for both distributions. A rapid decline of the distribution functions is observed towards both smaller and larger radii, which is consistent with the expectation of uniform structure sizes resulting from the spinodal decomposition in the Vycor production process, see Sec. 2.1.2. When calculating the average radius of both distributions numerically,

$$\langle r_0 \rangle = \int r_0 v(r_0)\,\mathrm{d}r_0, \tag{4.8}$$

a similar value is found: $\langle r_0 \rangle_{\mathrm{ads}} = 4.5\,\mathrm{nm}$, $\langle r_0 \rangle_{\mathrm{des}} = 4.55\,\mathrm{nm}$. This can be interpreted as a model success of the Kelvin equation with the additional Halsey wall layer, as it accurately predicts the same mean transition point for capillary condensation and capillary desorption. In addition, this match also confirms that the cylindrical pore geometry that has been assumed implicitly is a valid simplification for Vycor.

However, both distributions exhibit qualitative differences. For adsorption, a broader distribution of pore radii is observed, whereas the desorption branch yields a distinct peak of pore sizes. The differences in both distributions can be attributed to effects discussed in Sec. 3.4.4: The cumulated weaknesses of the Kelvin equation and its model simplifications, along with inherent metastability for adsorption as well as pore-blocking and network effects for desorption, manifest in the calculated pore volume distributions.

In conclusion, the pore size distribution confirms the expectations of a mesoporous network. Due to the great match of average pore radii, the Kelvin equation with cylindrical pore geometry is regarded as an adequate modelling in Vycor. However, the pore volume distribution functions as a whole deviate for ad- and desorption and will not be used for quantitative statistics. From now on, a mean pore radius $r_0 = 4.5 \pm 0.2\,\mathrm{nm}$ will be used for this sample. The same qualitative results could be obtained for the other samples in this work. A quantitative reference of the respective values of r_0 and Φ can be found in App. A.

4.3. Equilibrium Adsorption of 1-Butanol

4.3.1. Outline

An experimental study of adsorption of 1-butanol (C_4H_8OH) was conducted on a thin Vycor sample (*vyc_iso_1*, see App. A), the properties of which have been characterized in Sec. 4.2. First results have been reported in [64]. Over the course of the experiment, a sorption isotherm for butanol is measured for incremental filling steps in adsorption direction and subsequent analogous desorption. The resulting isotherm curve should give an exemplary insight on particle-wall interactions for alcohols. By using dielectric and manometric measurement in parallel, it is another goal of this experiment to derive an empirical relation between the relative filling and the effective permittivity of the sample.

4.3.2. Manometric Measurement and Complications

In contrast to nitrogen adsorption that requires cooling of the sample to achieve significant condensation, 1-butanol is liquid at room temperature ($T = 298\,\mathrm{K}$) with a saturation vapour pressure of $P_0 = 8.5\,\mathrm{mbar}$. Due to the lower absolute pressures, a much higher resolution was required in the pressure measurement. Furthermore, for each step of the isotherm, an equilibrium was typically reached after $24\,\mathrm{h}$, in comparison to minutes for nitrogen adsorption[4]. Hence, great care was taken that leakage from the outside was minimal $\Delta P/t < 5\,\frac{\mu\mathrm{bar}}{\mathrm{d}}$.

[4] An in-depth analysis on the dynamics of the uptake process can be found in Sec. 6.1.

However, during the experiment, another parasitic effect had far more consequences on the quality of the recorded data: After the preparation of a defined pressure P_r in the preparation volume, a gradual drop over time has been observed, see Fig. 4.6(a). This was attributed to a finite condensation of butanol on the walls due to small temperature fluctuations in the laboratory.

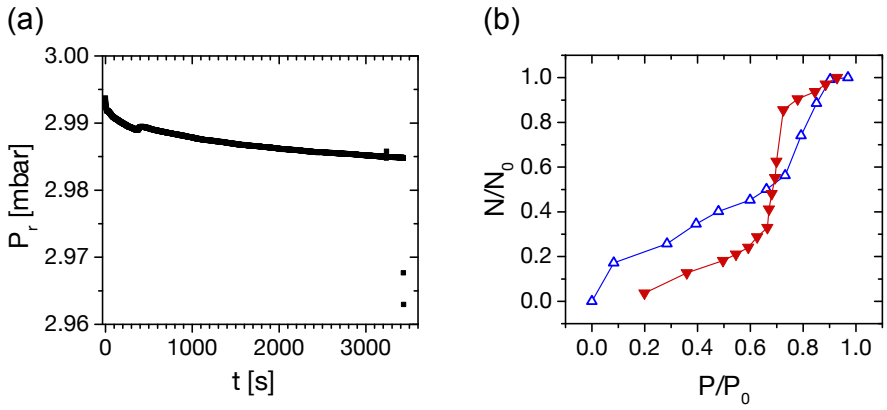

Figure 4.6.: Erroneous manometric isotherm measurement for 1-butanol. (a) While preparing an incremental filling step, the pressure gradually drops, indicating non-zero adsorption in the bulk volume. (b) This error accumulates over the course of the entire isotherm measurement. The resulting adsorption and desorption curves were thus discarded.

As this additional adsorbate phase is undetectable via a simple pressure measurement, it is erroneously ignored when calculating the amount adsorbed using the method described in Sec. 4.1.1. Due to the low absolute pressures, this uncertainty in ΔN is significant for every single point. Moreover, since the amount of substance is tracked over the course of the experiment, this error accumulates with the number of pressure steps, resulting in a growing uncertainty. As a result, the normalized manometric sorption isotherm for adsorption and desorption deviate strongly from one another, see Fig. 4.6(b). However, the qualitative shape of a sorption isotherm for mesoporous samples is still present to a certain degree in both, adsorption and desorption curves, albeit masked by a very large slope in the layer condensation stage.

The impact of the additional condensation on macroscopic surfaces is quantifiable through the normalization N_0 in Fig. 4.6(b). The measured maximum amount of $N_0 = 1.26\, N_{0,\text{theo}}$ shows significant deviations from the expected value $N_{0,\text{theo}} = \Phi V_{\text{sample}}$.

In summary, the manometric results for N/N_0 have to be disregarded in light of the experimental problems. It should be noted though that the measurement of the equilibrium pressure is still accurate, hence it can be used for a dielectric sorption isotherm.

4.3.3. Dielectric Measurement of Filling

The advantage of a dielectric measurement of adsorption in comparison to the manometric method is that it directly detects a signal resulting from the relative filling fraction, $\varepsilon^*_{\text{eff}}(N/N_0)$ at any time without the need to track a quantity (e.g. pressure) over the entire experiment. This should remedy the problems discussed in Sec. 4.3.2. Since the relationship between relative filling and dielectric properties should have been probed by comparing with a manometric isotherm, a different strategy is needed to convert the measured effective permittivity into a relative filling of the pores.

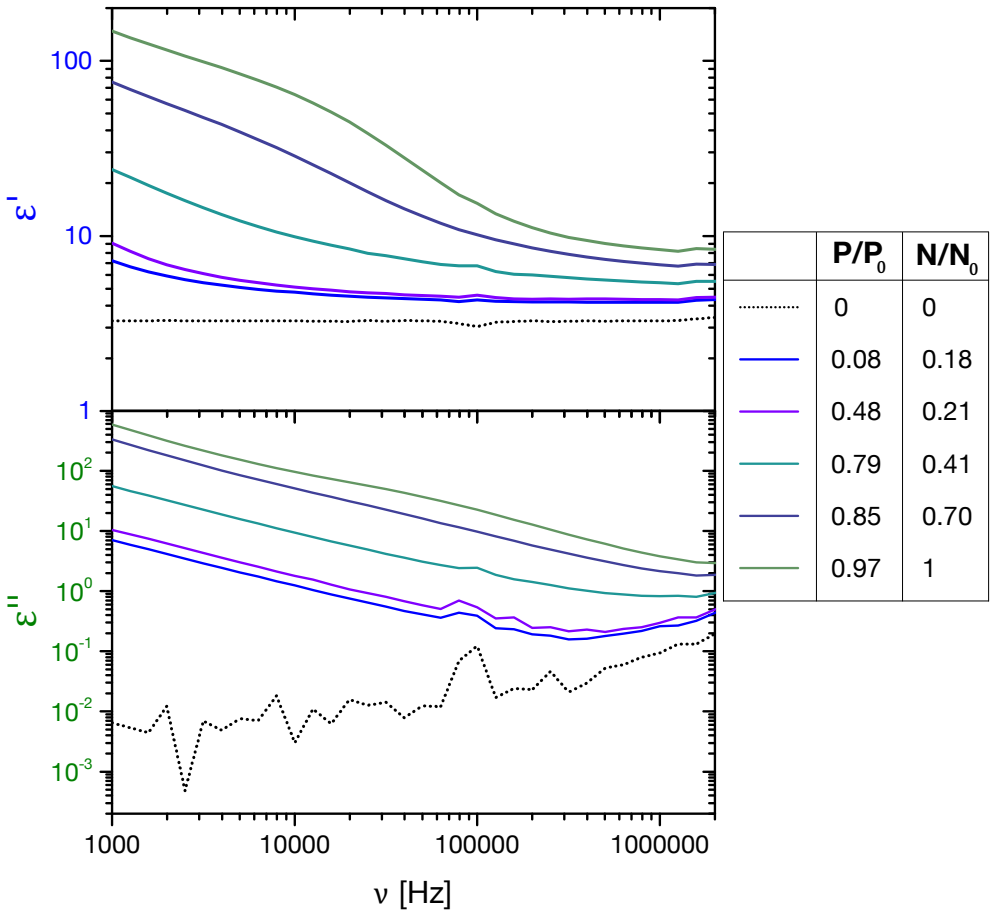

Figure 4.7.: Dielectric Spectra of Vycor at room temperature for different partial fillings with 1-butanol for adsorption direction in comparison to the empty matrix. Values for N/N_0 have been calculated using Eq. (4.10) and were normalized to the maximum value, see Sec. 4.3.4.

The dielectric spectra for some equilibrium fillings of 1-butanol in Vycor are shown in Fig. 4.7. By examining the spectrum of the imaginary part, it can be asserted that low frequency

effects (conductivity, interfacial polarization) are the dominant sources for dielectric losses, which are mainly caused by ionic impurities on the solid interface. As these do not primarily reflect the amount of 1-butanol added, the imaginary part is discarded as an indicator for relative filling.

In the real part $\varepsilon'_{\text{eff}}$, a continuous increase due to interface polarization is visible in the low frequency domain. For higher frequencies, analogous to the results for the fully filled matrix in Sec. 2.3.2, the spectrum exhibits a flat region that increases in value with the amount of adsorbate. In line with the discussion of fully filled Vycor in Sec. 2.3.3, the difference in effective permittivity of this state and an empty matrix can be attributed to the orientation polarization of the additional liquid.

In analogy to Sec. 2.3.3, this contribution is assumed as the product of the difference in bulk permittivity, the volume fraction (v_{C4}) and a microstructure factor (α). In contrast to Eq. (2.25), the volume fraction is defined by the porosity multiplied by the relative filling $v_{\text{C4}} = \Phi N/N_0$. Then, we can rewrite Eq. (2.25) as

$$\varepsilon'_{\text{eff}}(N/N_0) = \varepsilon'_{\text{eff,empty}} + \left(\varepsilon'_{\text{bulk,C4}} - 1\right) \Phi \frac{N}{N_0} \alpha(N/N_0). \tag{4.9}$$

Here, the microstructure parameter has been assumed as a function of relative pore filling, $\alpha(N/N_0)$. It is this function that was expected as an empirical result from the comparison of dielectric and manometric methods. However, since these results could not be obtained experimentally, a reasonable approximation has to be applied. A first assumption is to use the constant $\alpha = 1.24$ that has been measured in Sec. 2.3.3 for a filled matrix. The quality of this approximation for other adsorbate distributions will now be discussed for the different condensation stages.

During multilayer condensation, the adsorbate layers take the shape of the pore walls, thus mimicking the interface of the filled matrix. As for the additional interface between the adsorbate and the empty parts of the pore space, the same microstructure applies in good approximation with a small uncertainty due to the added constriction of the pore. Still, only a small error should result from the simple approximation in layer condensation.

As for capillary condensation and desorption, there are small incremental changes to the distribution of electric fields each time a new capillary bridge forms, collapses or coalesces with another one within the pore network. However, because of the large slope in the sorption isotherm, the structural changes coincide with a large increase or decrease in N/N_0. The effect on permittivity is therefore mitigated.

In summary, a simple dependence on relative pore loading can be used as a first order

approximation, although it will result in an error for the capillary condensation stage. The relative adsorbed amount in equilibrium can then be calculated by rearranging Eq. (4.9),

$$\frac{N}{N_0} = \frac{\varepsilon'_{\text{eff}} - \varepsilon'_{\text{eff,empty}}}{\Phi\alpha\left(\varepsilon'_{\text{C4,bulk}} - 1\right)} = \frac{\Delta\varepsilon'_{\text{eff}}(N/N_0)}{\Delta\varepsilon'_{\text{max,theo}}}. \tag{4.10}$$

4.3.4. Sorption Isotherm

With Eq. (4.10), a relative filling N/N_0 has been calculated from the equilibrium permittivity at $\nu = 1\,\text{MHz}$. Instead of using the theoretical maximum in the denominator on the right hand side of Eq. (4.10), it is also possible to normalize the results to a range 0 to 1 by using the experimental maximum permittivity $\Delta\varepsilon'_{\text{max}} = \varepsilon'_{\text{max}} - \varepsilon'_{\text{eff,empty}} = 5.08$. Then, by comparing to the theoretical increase,

$$\Delta\varepsilon'_{\text{max}} = \alpha\left(\varepsilon'_{\text{C4,bulk}} - 1\right)\tilde{\Phi}, \tag{4.11}$$

an apparent porosity $\tilde{\Phi} = 24.8\,\%$ can be calculated using $\alpha = 1.24$ as determined experimentally in Sec. 2.3.3. The fact that $\tilde{\Phi}$ is smaller than the characterized value from nitrogen sorption ($\Phi = 27.5\,\%$) indicates incomplete removal of the adsorbed water monolayer. This was expected due to the limited heating temperature during evacuation. An equivalent layer thickness t_{pre} can be derived, assuming homogeneous distribution in cylindrical pores of uniform radius r_0:

$$\frac{\tilde{\Phi}}{\Phi} = \frac{(r_0 - t_{\text{pre}})^2}{r_0^2}. \tag{4.12}$$

In this experiment, $t_{\text{pre}} = 0.23\,\text{nm}$ could be calculated, which is in very good agreement with molecular dimensions of water as well as MD simulation results of bound water layers [65]. The uncertainty in pore radius resulting from this preadsorbed layer will be further discussed in the analysis of the properties of the layer condensate in Sec. 4.3.5.

When plotted as a function of the measured equilibrium pressure, as depicted in Fig. 4.8, the normalized increase in permittivity produces a type IV isotherm, similar to the results from nitrogen characterization. The following characteristic features are worth noting:

- Initial step occurs for small pressures below the first data point $P/P_0 < 0.08$.
- The flat layer condensation stage shows no significant multilayer adsorption.
- For capillary condensation, the hysteresis shape shows a good match to the results from nitrogen characterization: spread out rise on adsorption, almost vertical drop on desorption.

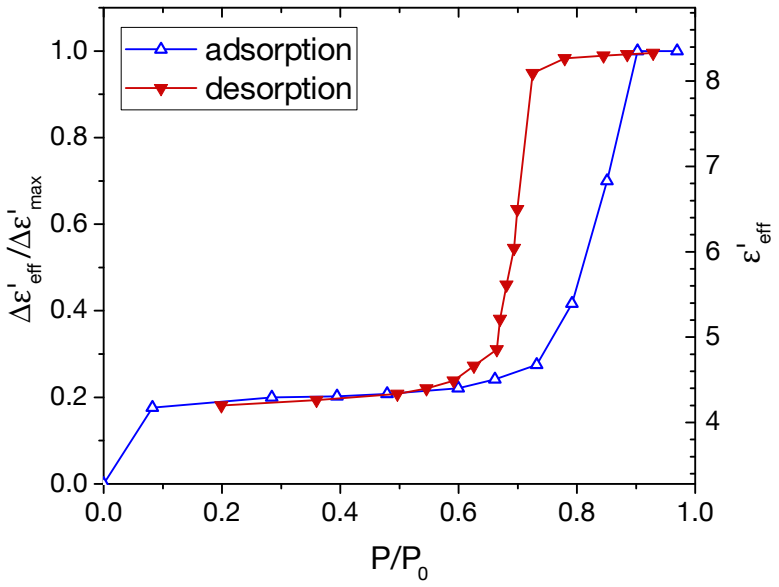

Figure 4.8.: Sorption isotherm for 1-butanol in Vycor, as resolved by dielectric spectroscopy, see text.

- The plateau of total filling is achieved for a pressure $P/P_0 \approx 0.9$. No additional uptake is detected on continued pressure increase.

These properties of the sorption isotherm can also be compared to results in literature. Jones and Wade [66] studied equilibrium sorption of a series of alcohols featuring 1-butanol using gravimetric methods in porous Vycor with comparable pore radius $r_0 = 3\,\mathrm{nm}$. In their experiments, as depicted in Fig. 4.9, they observed a strong and very localized monolayer step of matching height for low pressures $P/P_0 < 0.03$ followed by a very flat layer condensation domain, indicating no multilayer adsorption. Moreover, the shape of their capillary condensation hysteresis exhibited the same asymmetric H2(a) characteristics.

The perfect agreement between this experiment and the reported data clearly shows that the dielectric measurement along with the approximation of linear filling dependency is accurate within the experimental uncertainties. Hence, the normalized permittivity in Eq. (4.10) and N/N_0 can be used interchangeably.

4.3.5. Monolayer Adsorption

When interpreting the layer condensation stage as a monolayer growth, it is appropriate to apply the Langmuir model. A dimensionless fit of Eq. (3.12) as $N/N_{\mathrm{ML}}(P \to P/P_0)$ has been applied to the pressure range $0 < P/P_0 < 0.6$ for adsorption data, see Fig. 4.10.

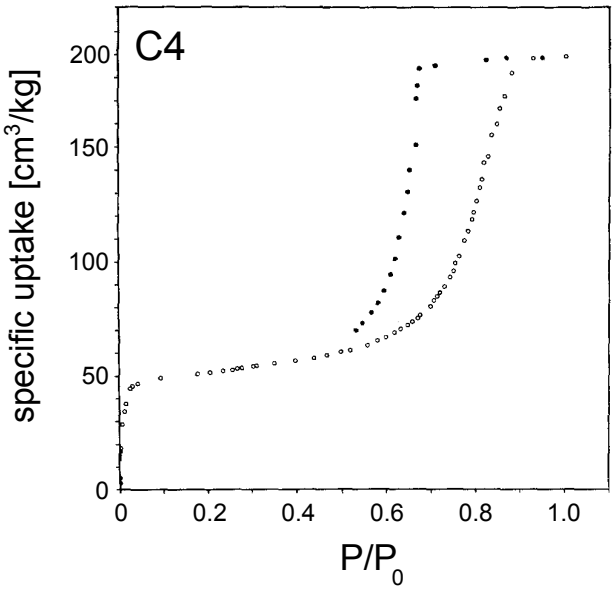

Figure 4.9.: Gravimetric sorption isotherm for 1-butanol in Vycor ($r_0 = 3\,\mathrm{nm}$), redrawn from [66].

The resulting monolayer capacity amounts to $N_{\mathrm{ML}}/N_0 = 0.219$. Similar to the BET fit of nitrogen adsorption, see Sec. 4.2.2, the Langmuir constant is only known with a large margin of error due to the lack of points for very low fillings, $K_L = 50 \pm 10$.

The thickness of the adsorbed layer can be estimated from the relative pore volume occupied by adsorbate N/N_0,

$$N/N_0 = \frac{V_{\mathrm{ads}}}{V_{\mathrm{pore}}}. \tag{4.13}$$

Assuming cylindrical pore geometry and a single pore radius r_0 and homogeneous adsorption, the adsorbate layers take the shape of the cylinder wall with a layer thickness $t(N/N_0)$, so that the right hand side of Eq. (4.13) can be rewritten as

$$\frac{V_{\mathrm{ads}}}{V_{\mathrm{pore}}} = \frac{r_0^2 - (r_0 - t(N/N_0))^2}{r_0^2}. \tag{4.14}$$

Combining Eqs. (4.13) and (4.14) then yields

$$t(N/N_0) = r_0 \left(1 - \sqrt{1 - \frac{N}{N_0}}\right). \tag{4.15}$$

According to this relation, a Langmuir monolayer thickness of $t_{\mathrm{ML}} = 0.52 \pm 0.10\,\mathrm{nm}$ is ob-

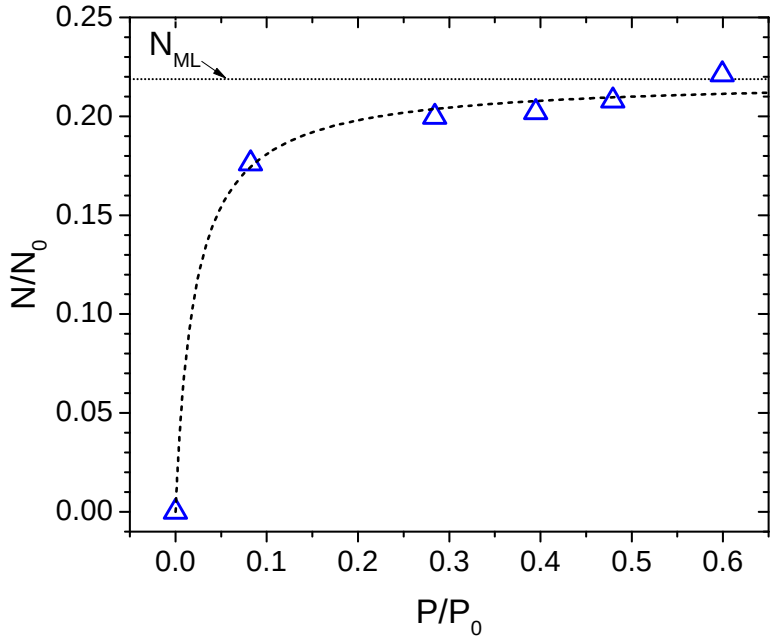

Figure 4.10.: Langmuir fit for the 1-butanol monolayer condensation. The steep increase at very low pressures is a characteristic of strong adsorption. A Langmuir constant $K_L = 50 \pm 10$ could be extracted

tained without considering the pre-adsorbed water. This value is in the range of the molecular dimensions for 1-butanol (418 to $904\,\mathrm{pm}$, see App. B). The high uncertainty in the layer thickness corresponds to the reduced apparent porosity for the butanol measurement. If interpreted as a residual water monolayer, the preadsorbed layer thickness $t_{\mathrm{pre}} = 0.23\,\mathrm{nm}$ estimated above and t_{ML} add up to a total wall layer of thickness $t_{\mathrm{ML+H_2O}} = 0.75 \pm 0.10\,\mathrm{nm}$

Using the Frenkel-Halsey-Hill equation, a molecule-wall interaction exponent for 1-butanol can be quantified. By converting the experimental data to a layer thickness $t(P/P_0)$ for each point of the layer condensation stage using Eq. (4.15), a fit of Eq. (3.34) can be applied. Equivalently, a plot of $\ln\left(t(P/P_0)\right)$ over $\ln\left(\frac{5}{\ln(P_0/P)}\right)$ yields a linear relation of slope $1/b$, as depicted in Fig. 4.11.

For the experimental data, $b = 6 \pm 0.5$ was observed. In comparison to the value $b = 3$ that was used for nitrogen in Eq. (3.35), this indicates a much stronger interaction of the butanol molecules with the pore walls which is consistent with the difference in the shape of both isotherms, i.e. flat layer condensation domain (1-butanol) vs. multilayer growth (N_2). Furthermore, this value is in agreement with results for other strong adsorbates on polar surfaces [53].

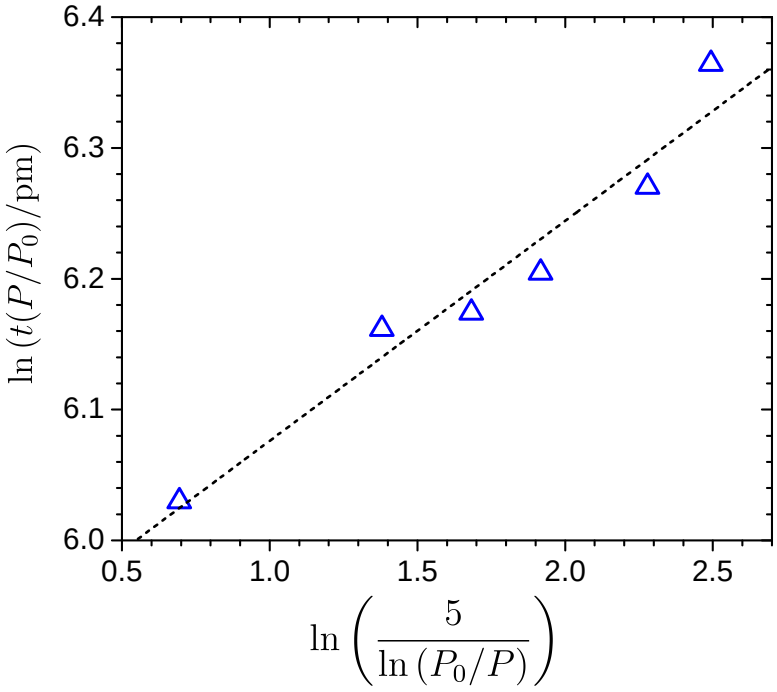

Figure 4.11.: Frenkel-Halsey-Hill plot of 1-butanol monolayer condensation. From the slope in this plot, an FHH interaction exponent $b = 6$ could be extracted according to Eq. (3.34).

4.3.6. Capillary Condensation

In analogy to the method for pore size characterization (see Sec. 4.2.3), a pore volume distribution has been calculated for the desorption branch in the capillary condensation hysteresis loop that has been studied with higher resolution than the adsorption branch. The results, as a function of the Kelvin radius r_K can be found in Fig. 4.12.

The normalized pore volume shows comparable characteristics to Fig. 4.5, although the distribution is wider than for nitrogen. However, an important difference is seen in the absolute values of Kelvin radii: The maximum of the pore volume distribution is found at $r_{\mathrm{K,max}} = 5.05\,\mathrm{nm}$[5]. Assuming a constant wall layer thickness t_{ML} due the monolayer adsorbate in addition to the Kelvin radius, the maximum position yields an apparent pore radius of $\tilde{r}_0 = 5.6\,\mathrm{nm}$, which is significantly higher than the radius from the sample characterization ($r_{0,\mathrm{max}} = 4.75\,\mathrm{nm}$).

Two possible explanations can be given for the deviation of the Kelvin radius: On one hand, a model error of the Kelvin equation for strong particle-wall interactions is expected

[5]Because of the uncertainty in the dielectric model discussed in Sec. 4.3.3, only the maximum value will be used

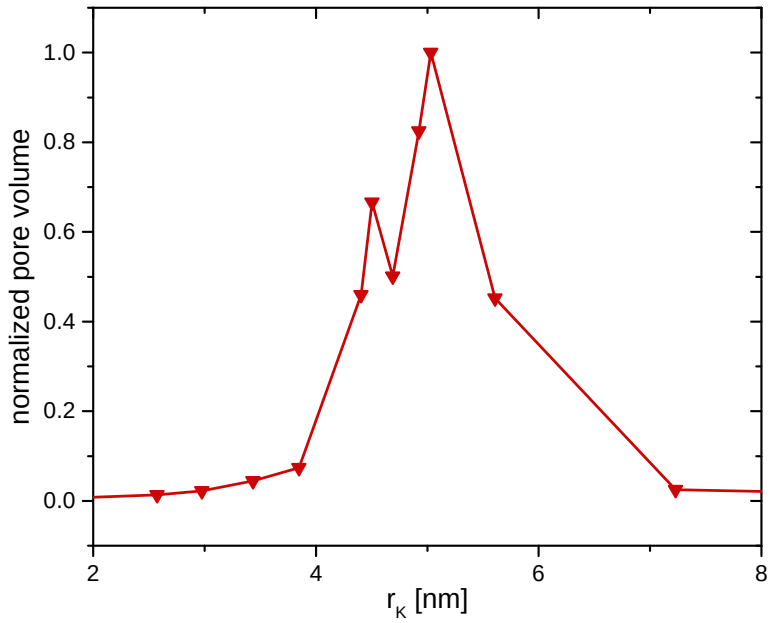

Figure 4.12.: Pore volume distribution of the 1-butanol desorption branch as a function of the Kelvin radius (calculated for a contact angle $\theta = 0$). For the data point at $r_K \approx 4.5\,\mathrm{nm}$, a small temperature fluctuation was observed, this small experimental error results in an artificial secondary peak.

that could result in a different meniscus curvature. On the other hand, a finite contact angle θ between the menisci and the monolayer condensate would also result in a larger Kelvin radius, as depicted in Fig. 4.13(a).

So far, it has been assumed that the capillary condensate has a hemispherical meniscus. This is justified for most multilayer systems, where the layer condensate has liquid-like properties. However, for strong interactions with the pore surface and a monomolecular adsorbate layer, this is not guaranteed.

Due to the directional H-bonds of 1-butanol to the silica interface, we expect a preferred orientation of molecules in the vicinity of the pore walls, as observed for water in simulations [67]. Then, the interaction to the next layer of molecules in the liquid is critically modified, see Fig. 4.13(b) and (c). The result is an interfacial tension between both layers, even though they consist of the same molecular species. This effect, known as autophobicity, can be observed experimentally for many strongly interacting adsorbates [68, 69]. It is especially prominent on high energy surfaces like silica [70].

In order to quantify the contact angle, Eq. (3.33) can be easily modified, since the liquid

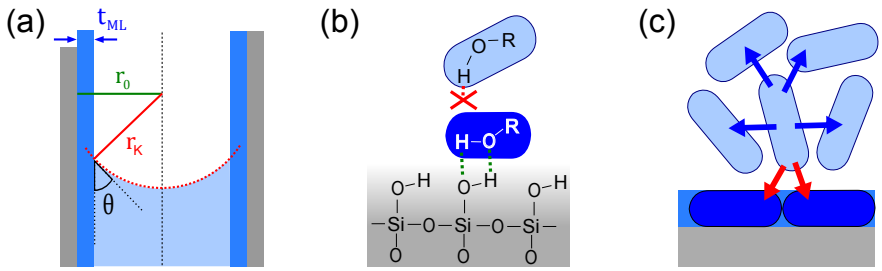

Figure 4.13.: Illustration of autophobicity of n-alcohols to an adsorbed monolayer. (a) In adsorption experiments, there is often a finite contact angle between the capillary bridge and the layer adsorbate. (b) The reason behind this are the strong interactions of the monomolecular layer to the surface, here: H-bonds. (c) As the mobility of the molecules on the interface is limited and a strong H-bond is already formed with the silica surface, the intermolecular interactions to the next layer of liquid molecules are modified.

interface still exhibits the shaped of a spherical segment. A factor $\cos\theta$ can be introduced:

$$r_0 = r_K \cos\theta + t(P/P_0). \tag{4.16}$$

If we assume r_0 as the pore radius from the N_2-isotherm characterization, $r_K = r_{\mathrm{K,max}}$ from the Kelvin radius distribution for butanol and $t(P/P_0) = t_{\mathrm{ML}}$ as the butanol monolayer thickness, a contact angle of $\theta = 38 \pm 4°$ for the butanol menisci can be calculated. This indicates a significant autophobicity of butanol in nanopores, while the capillary bridge still readily wets the layer adsorbate.

The same effect was reported by Jones and Wade in smaller nanopores [66]. In their experiments for Vycor with 3 nm pore radius, a contact angle of $\theta = 59°$ was measured along with a comparable monolayer thickness $t_{\mathrm{ML}} \approx 600\,\mathrm{pm}$. This could be indicative of a geometric dependence of the autophobicity on the surface curvature. Furthermore, the surface chemistry seems to play a critical part for autophobicity: In experiments of alcohol adsorption to planar alumina surfaces by Barto et al. a value of $\theta = 50°$ to $80°$ has been derived for 1-butanol [71].

5 Theory of Diffusive Transport in Nanopores

5.1. Elementary Theory of Diffusion

5.1.1. Introduction

As a part of the results from the considerations in Sec. 3.2, an equilibrating thermodynamic process was predicted based on an imbalance in the chemical potential μ. It was Einstein [72] who recognized that a gradient in chemical potential $\nabla\mu$ is the driving force for molecular transport, which is counteracted by friction forces. These in turn depend on the interactions of the involved particle ensemble. In this way, the diffusive transport of matter reflects the microscopic properties of a system. An in-depth review of the theoretical framework can be found in [73], where many of the following concepts have been taken from.

5.1.2. Transport Diffusion and Self-Diffusion

In one dimension, a balance of forces according to Einstein's theory of diffusion results in

$$fv = -\frac{\mathrm{d}\mu}{\mathrm{d}x}, \tag{5.1}$$

where f is a friction coefficient and v denotes the relative velocity of a particle. At a local molar concentration c of particles, a molar flux density $J = vc$ is expected that is referred to as 'transport diffusion'. As a function of the concentration, the gradient of chemical potential is usually oriented in parallel to a concentration gradient, as is the case on adsorption in a monolithic mesoporous sample. Then, transport diffusion can be described using Fick's model [74]. Sec. 5.1.3 will give a theoretical framework that relates the flow to a concentration gradient for a transport diffusivity constant D.

Another instance of diffusion results from the statistical mechanics of particles in a fluid of uniform density. A random, spontaneous molecular movement, i.e. Brownian motion, is observed for finite temperatures due to a statistical velocity distribution. On interaction with other particles, momentum is exchanged arbitrarily and the motion is redirected. The result is a so-called 'random walk' of particles within the fluid. However, in an ensemble of particles,

the statistical mean square displacement $\left\langle r^2(t) \right\rangle$ from the starting point is a linear function of time,

$$\left\langle r^2(t) \right\rangle = 6\hat{D}t, \tag{5.2}$$

with a diffusivity constant $\hat{D}$. This statistical motion of particles is also known as 'self-diffusion', as it is an inherent property of the medium without external stimuli. The self-diffusivity $\hat{D}$ depends on the friction forces in the fluid. For liquids, they can be identified as viscous drag according to the Stokes-Einstein relation. Similarly, the self-diffusivity for pure gases in the hydrodynamic limit can be derived from kinetic gas theory for an infinite medium,

$$\hat{D} = \frac{1}{3}\bar{v}_{\text{th}}\lambda, \tag{5.3}$$

where λ is the mean free path of particles, see Eq. (5.9), and $\bar{v}_{\text{th}}$ denotes the mean thermal velocity of the Maxwell-Boltzmann distribution:

$$\bar{v}_{\text{th}} = \sqrt{\frac{8RT}{\pi M_m}}, \tag{5.4}$$

with the molar mass M_m of the gas particles. Due to the compressibility of gases, the mechanisms of particle interaction change, which will be discussed in Sec. 5.2. Thus, the self-diffusivity in nanoporous media is much more complex than Eq. (5.3) suggests.

In conclusion, self diffusion and transport diffusion are generally different processes that should not be confused with one another. While transport diffusion is always correlated to a net transport of matter and a driving force, self-diffusion is also present for a fluid in an equilibrium. In general, both processes exhibit different diffusivities ($\hat{D} \neq D$). With regard to the experiments in this work, the diffusivity constants correspond to transport diffusivities, as they result from a molecular flow.

5.1.3. Fick's Laws of Diffusion

The first theoretical model of transport diffusion flow has been derived by Adolf Fick in the middle of the 19$^{\text{th}}$ century as a purely phenomenological description. A review of the model can be found in [73]. At the time, it has been established experimentally that a concentration imbalance in a gas mixture is spontaneously reduced in favour of a uniform distribution of the individual components, as depicted in Fig. 5.1.

In analogy to heat transfer, a diffusion flux $\boldsymbol{J}$ can be defined that is proportional to the gradient of the concentration c:

$$\boldsymbol{J} = -D(c)\nabla c, \tag{5.5}$$

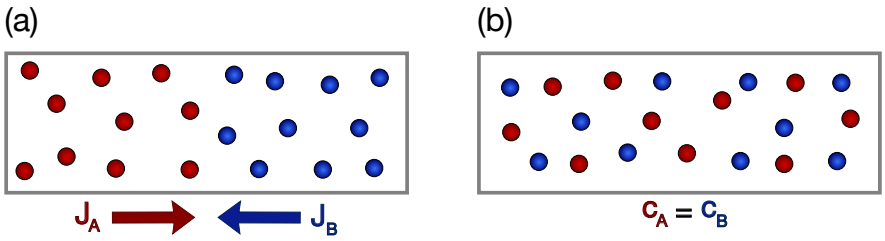

Figure 5.1.: Phenomenology of diffusion in a mixture of two gases. Any given concentration difference is reduced over time by a spontaneous flow of particles. In an equilibrium state, the concentration throughout the entire bounding volume is equal for both components.

where the coefficient $D(c)$ is the transport diffusivity. Eq. (5.5) is known as Fick's first law of diffusion. In gases, the concentration can also be expressed by a partial pressure P_i for the i-th component. For a one-dimensional case, Eq. (5.5) then results in

$$J_i = -\frac{D}{RT}\frac{\partial P_i}{\partial x}. \tag{5.6}$$

Eq. (5.6) requires isothermal conditions $T = \text{const}$, as is the case in the experiments for this work.

As a result of the flow of particles, the local concentration changes over time. Due to the conservation of particles, a continuity equation has been formulated as Fick's second law:

$$\frac{\partial c}{\partial t} = -\nabla \boldsymbol{J} = \nabla \left(D(c) \nabla c \right). \tag{5.7}$$

For a constant diffusivity, Eq. (5.7) further simplifies to

$$\frac{\partial c}{\partial t} = D \Delta c, \tag{5.8}$$

with the Laplace operator Δ. By solving the partial differential equations resulting from Eq. (5.7) or Eq. (5.8), a concentration profile $c(\boldsymbol{x}, t)$ can be calculated for specific boundary and initial conditions. For some conditions and simple geometries, an analytical description can be found, as will be shown in Sec. 5.3.

5.2. Diffusion Mechanisms in Mesopores

5.2.1. Principles of Gas Transport

A large part of diffusive matter transport in mesopores can be attributed to the gas phase. Eq. (5.6) predicts a diffusion flow caused by a gradient in the partial pressure of a gas. As opposed to liquids, where in most cases the incompressible Navier-Stokes equation is an accurate description of flow processes (see Sec. 7.1.1), the compressibility has to be taken into account for gas flow. As we shall see, this introduces significant complications.

In contrast to liquids that contain interacting molecules in close proximity, an ensemble of gas particles can only exchange energy and momentum by statistical particle collisions. These can occur either with other gas particles or the bounding geometry with different relative importance depending on the density of the gas. For ideal gases consisting of spherical gas particles of van-der-Waals radius r_A, the mean free path between particle-particle collisions can be derived using kinetic gas theory from the particle density $n = N/V$ and the effective collision cross-section for interactions, $\sigma = \pi(2r_A)^2$. If particle velocities exhibit Maxwell-Boltzmann distribution, the mean free path is given by

$$\lambda = \frac{1}{\sqrt{2}n\sigma} = \frac{1}{\sqrt{2}}\frac{k_B T}{P}\frac{1}{\pi(2r_A)^2}. \tag{5.9}$$

On dilution of a gas, i.e. on lowering the mean pressure P, the rate $\zeta_{\text{p-p}}$ of inter-particle collisions is reduced. If the mean free path is comparable to the distance between geometric boundaries, e.g. the width of a mesopore, particle-wall collisions at a rate $\zeta_{\text{p-w}}$ govern the behaviour of the gas. For cylindrical flow channels of radius r_0, a dimensionless Knudsen number Kn can be defined that indicates the degree of rarefaction in a gas:

$$\text{Kn} = \frac{\zeta_{\text{p-w}}}{\zeta_{\text{p-p}}} = \frac{\lambda}{2r_0}. \tag{5.10}$$

Based on this definition, one can distinguish three regimes for gas transport [75]:

Hydrodynamic regime: $\text{Kn} < 0.1$

Transition regime: $0.1 \leq \text{Kn} < 10$

Knudsen diffusion regime : $10 \leq \text{Kn}$

Fig. 5.2 shows the different transport mechanisms in the limiting cases of low (a) and high Kn (b), the physical properties of which will be discussed in the following sections.

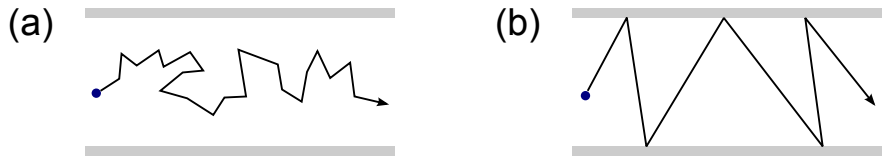

Figure 5.2.: Gas flow mechanisms for different flow regimes. (a) Low-Kn hydrodynamic continuum flow. (b) High-Kn Knudsen flow determined by interactions with the geometric boundary.

5.2.2. Hydrodynamic Gas Flow

In the limit of dense gases, the particle-wall collisions can be neglected in good approximation. Particle-particle collisions are the only way to exchange momentum and energy between gas particles, as indicated in Fig. 5.2(a). The transport of gas molecules resulting from a difference in pressure is then described by continuum fluid mechanics. The Navier-Stokes equation, which will be introduced in detail in Sec. 7.1.1 applies to the flowing gas and thus for one-dimensional pressure gradients $\mathrm{d}P/\,\mathrm{d}x$ in cylindrical geometry, Hagen-Poiseuille flow is expected,

$$\dot{V} = -\frac{\pi r_0^4}{8\eta}\frac{\mathrm{d}P}{\mathrm{d}x}, \tag{5.11}$$

where η denotes the dynamic viscosity of the gas. As an equivalent formulation to shear stress between fluid layers, Maxwell's kinetic gas theory predicts a tangential momentum transfer between gas particles that results in a definition of a viscosity for gases,

$$\eta = \frac{1}{3} n m \bar{v}_{\mathrm{th}} \lambda, \tag{5.12}$$

with n denoting the particle density, m the particle mass, and $\bar{v}_{\mathrm{th}}$ the mean thermal velocity from Eq. (5.4). The volumetric flow rate $\dot{V}$ in Eq. (5.11) can then be related to a molar flow rate $\dot{N}$,

$$\dot{V} = \frac{\mathrm{d}V}{\mathrm{d}N}\frac{\mathrm{d}N}{\mathrm{d}t} = \frac{RT}{P}\dot{N}. \tag{5.13}$$

The average flux for the flow channel is then given by

$$J = \frac{1}{\pi r_0^2}\frac{\mathrm{d}N}{\mathrm{d}t} = -\frac{P r_0^2}{8\eta RT}\frac{\mathrm{d}P}{\mathrm{d}x}. \tag{5.14}$$

Comparing Eq. (5.14) to Fick's first law for gases, Eq. (5.6), a transport diffusivity for this viscous flow can be identified as

$$D_{\mathrm{vis}} = \frac{P r_0^2}{8\eta}. \tag{5.15}$$

It should be noted that for $0.01 \leq \mathrm{Kn} < 0.1$, Eq. (5.14) needs to be corrected by applying a slip boundary condition when solving the Navier-Stokes equation. The finite velocity at the pore walls directly results from the thermodynamics of the Knudsen layer, i.e. a layer of thickness λ from the pore walls [11]. Effects of slip flow in the context of liquid flow will also be discussed in Sec. 7.1.3.

5.2.3. Knudsen Diffusion

In the limit for dilute gases ($\mathrm{Kn} > 10$), particle-particle collisions can be omitted. The only remaining collision mechanism are particle-wall collisions, as depicted in Fig. 5.2(b).

In the process, the gas molecules are reflected by the pore walls in a diffuse manner, so that the momenta before and after collision exhibit no correlation. This loss of orientation is a consequence of short-time adsorption and subsequent desorption from the surface [76]. A diffuse reflection of gas particles is expected, resulting in an angular probability according to Lambert's cosine law, $p(\phi) \propto \cos\phi$, with an angle ϕ to the surface normal.

From the momentum balance in kinetic gas theory, Knudsen calculated the diffusivity in a cylindrical pore of radius r_0 [77],

$$D_{\mathrm{Kn}} = \frac{2}{3} r_0 v_{\mathrm{th}}. \tag{5.16}$$

Obviously, this Knudsen diffusivity is independent of the mean pressure as well as the pressure gradient in the pore. Moreover, the dependence on temperature and the molar mass of diffusing particles is also weak ($D_{\mathrm{Kn}} \propto \sqrt{T/M_m}$). Accordingly, the Knudsen diffusivities for alcohol molecules of chain lengths $n = 4$ and $n = 10$ at room temperature only differ by $45\,\%$ despite a large difference in molecular dimensions.

The Knudsen diffusivity depends on the pore geometry and hence is a function of the amount of adsorbate in a pore. In the presence of pre-adsorbed layers of thickness $t(N/N_0)$ according to Eq. (4.15), the diffusivity is reduced to

$$D_{\mathrm{Kn}}(N/N_0) = \frac{2}{3} \left(r_0 - t(N/N_0)\right) v_{\mathrm{th}} \tag{5.17}$$

Due to the stochastic nature of the transport and collisions in the Knudsen mechanism, the self-diffusivity and transport diffusivity are in good approximation equal. However, simulations revealed that this is only observed for perfectly smooth pores [78]. In case of rough pore walls, the self-diffusivity is reduced considerably due to local variations, while the transport diffusivity shows no strong dependence. This will be revisited in the context of the tortuosity factor in a porous network, see Sec. 5.3.2.

5.2.4. Gas Flow in the Transition Regime

A very interesting domain of gas flow is found for a transition between viscous flow and Knudsen diffusion. Here, the assumptions of Secs. 5.2.2 and 5.2.3 break down in that both particle-particle and particle-wall collisions need to be considered for momentum transfer.

As a general rule, the diffusivity in the transition region is reduced in comparison to pure Knudsen diffusion but also compared to viscous flow in the hydrodynamic regime, resulting in a minimum of gas throughput. In order to derive an analytical description of flow for these conditions, one needs to find a solution of the Boltzmann equation. In most practical cases, this is impossible due to the complexity of the collision integral therein.

Most attempts to bridge this gap in flow rate modelling between the two above descriptions are based on a weighted superposition of mechanisms and empirical studies. Based on a linearized representation of the Boltzmann equation and on molecular dynamics simulations of flow profiles, a unified model has been developed by Beskok and Karniadakis that accurately predicts flow rates for pure gases over a large range of Kn for different flow geometries [77].

5.2.5. Intermolecular diffusion

For gas mixtures of components A and B, the additional momentum exchange due to interspecies collisions has to be considered. By applying Chapman-Enskog theory [79, 80], a diffusivity

$$D_{\mathrm{AB}} = \frac{3}{8\sqrt{\pi}} \frac{(k_B T)^{3/2} M_{\mathrm{AB}}^{-1/2}}{P d_{\mathrm{AB}}^2 \Omega(\epsilon_{\mathrm{AB}})} \tag{5.18}$$

can be derived for this process. This diffusivity applies equally to the transport of either component. Accordingly, the index AB indicates a mean parameter for the mixture. In detail, d_{AB} denotes the arithmetic mean of hard-sphere collision diameters, M_{AB} denotes the harmonic mean of particle masses for both components. The value of the collision integral $\Omega(\epsilon_{\mathrm{AB}})$ depends on the geometric mean of Lennard-Jones parameters ϵ_{AB} for both gases.

The Chapman-Enskog diffusivity scales as a function of P^{-1} in the hydrodynamic regime. However, in the limit for dilute gases, the diffusivity of each component corresponds to Knudsen diffusion and the intermolecular diffusivity vanishes. For gas mixtures in the transition regime, Scott and Dullien derived an approximation for an apparent diffusivity D_{trans} that results from the Knudsen diffusivity of the respective gas and the intermolecular diffusivity [81],

$$\frac{1}{D_{\mathrm{trans}}} = \frac{1}{D_{\mathrm{Kn,A}}} + \frac{1}{D_{\mathrm{AB}}}. \tag{5.19}$$

5.2.6. Surface Diffusion

So far, only diffusion in the gas phase has been considered for molecular transport on adsorption. However, the additional sorbate layer on the interfaces also impacts matter transport. For any concentration imbalance along the walls, there are equal variations of the local chemical potential of the adsorbate, $\mu_\sigma(c)$. A gradient in this potential then drives a transport diffusion inside the adsorbed ensemble.

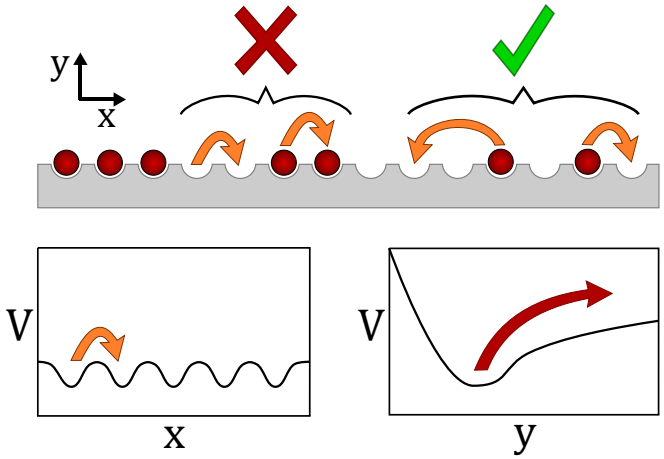

Figure 5.3.: Illustration of surface diffusion and surface potentials. Here, a one-dimensional diffusion is depicted including sketched interaction potentials. For an adsorbate particle, depending on the surface chemistry, the energy barrier to neighbouring sites can be lower than for desorption. Then, the activated transition between potential wells is another means of diffusion. Besides the obvious self-diffusion, there is also a net transport if a concentration gradient is assumed in the adsorbate.

Microscopic models of this surface diffusion describe the diffusion flux as an activated hopping process in the potential landscape of the interface. For one dimension, this is illustrated in Fig. 5.3. In case of physisorption, the adsorbed particles are not fixed in place. They can overcome the energy barrier between neighbouring potential wells on the surface for a thermal activation without complete desorption. If only jumps from occupied to vacant sites are allowed, this hopping mechanism, even for non-interacting adsorbate particles, results in a net flow from a zone of higher adsorbate concentration to a lower concentration.

A basic model [73] treats adsorption sites as equidistant points on a two-dimensional square lattice. The resulting transport diffusivity then solely depends on the distance of adsorption sites d and the hopping rate ζ_H that is determined by the temperature and the adsorption strength.

$$D_S = \zeta_H d^2 \tag{5.20}$$

Although this diffusivity seems independent of the number of particles in the adsorbate layer, both ζ_H and d can be modelled implicitly as functions of the layer occupation. In real situations, the complexity of the interface potential, the distribution of adsorption sites and the molecular interactions in the adsorbate all have to be considered.

A refined model has been introduced by Reed and Ehrlich [82], which takes into account the repulsive interaction between adsorbate particles. Then, surface diffusivity in a monomolecular layer is a function of fractional loading. For low surface occupation, the hopping rate and thus the diffusivity is limited by the number of particles in the adsorbate layer. As the population grows, so does the probability of a successful hopping. The repulsion between particles further enhances the diffusivity. For high loadings though, the lack of vacant adsorption sites limits the process again and diffusivity drops off. Hence, a global maximum of surface diffusivity is expected at a surface coverage $0 < N/N_{\mathrm{ML}} < 1$ [73].

5.2.7. Liquid Capillary Flow

The last important mechanism for molecular transport is only present at very high pore loadings, when capillary condensation sets in. On formation of a capillary bridge, the pore is effectively sealed for gas phase diffusion from one end to another. Matter transport to the closed off end of the pore can then only be achieved by other mechanisms.

One of these is added by the capillary bridge itself: The concave menisci act as quasi infinite sinks for adsorbing particles and a spreading of the capillary bridge is expected due to capillary forces. The dynamics of spontaneous capillary flow will be a central subject of part III. For now, it should be noted that transport is critically modified when capillary condensation sets in.

5.2.8. Total Pore Transport Diffusivity

All the above diffusion mechanisms need to be considered when trying to quantify molecular transport in a cylindrical nanopore. An analogy to electric circuits illustrates the diffusion resistance caused by individual transport mechanisms [73]. As depicted in Fig. 5.4, the combined intermolecular and Knudsen diffusivity according to Eq. (5.19), the surface diffusion, and a viscous flow contribution (for transition flow) are three independent resistances in a parallel circuit[1].

In the limit for dilute gases, the intermolecular and viscous mechanisms can be neglected, resulting in a simplified pore transport only by Knudsen and surface diffusion. For station-

[1] Here, it is assumed that no capillary condensation takes place.

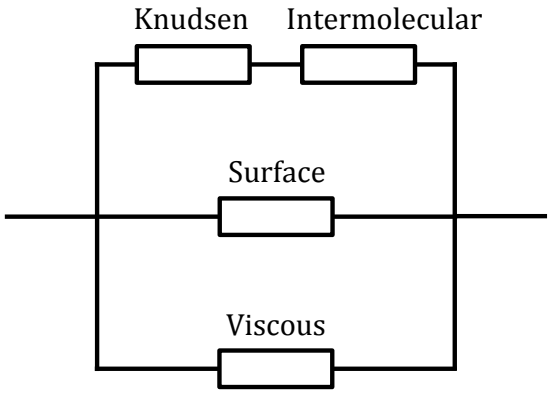

Figure 5.4.: Combined diffusion resistance in a cylindrical mesopore. The total resistance of this equivalent circuit defines the diffusivity of a mesopore in the layer condensation stage. Note that each individual resistance is a function of molecular concentration in the gas phase and/or in the adsorbate.

ary diffusion, i.e. constant concentration gradient and flow, both mechanisms add up to the stationary pore diffusivity D_P^* in a weighted superposition. The weights are determined by the relative amount of particles in the gas phase (N_g/N) and in the adsorbate ($N_\sigma/N = (1 - N_g/N)$),

$$D_P^* = \frac{N_g}{N} D_{\mathrm{Kn}} + \left(1 - \frac{N_g}{N}\right) D_S, \tag{5.21}$$

where $N = N_g + N_\sigma$ is the total number of particles in the pore.

It should be noted that the individual diffusivities in (5.21) are functions of the relative pore filling. For D_S, a direct occupation dependence in the adsorbate layer was discussed in Sec. 5.2.6. Knudsen diffusion varies with the thickness of the adsorbed layer, see Eq. (5.17). While in a stationary case, this results in constant diffusivities, the total pore diffusivity in transient situations is a complicated function of the concentration of adsorbate $D(c)$, resulting in a nonlinear form of Fick's second law (Eq. (5.7)).

In order to simplify this problem, the individual diffusivities are usually assumed constant for small concentration variations, i.e. incremental steps in adsorbate. While this is an appropriate approximation for small changes in the layer condensation stage for isotherms, it is much less suited for experiments probing transient filling dynamics for a large $\Delta N/N_0$. Moreover, a critical change in transport mechanism occurs upon capillary condensation in the pore, as described in Sec. 5.2.7. The application of the above model and equations is thus limited to the layer condensation stage. This will be discussed further in Sec. 6.

5.3. Modelling Diffusivity in Mesoporous Solids

5.3.1. Effective Diffusivity of Porous Solids

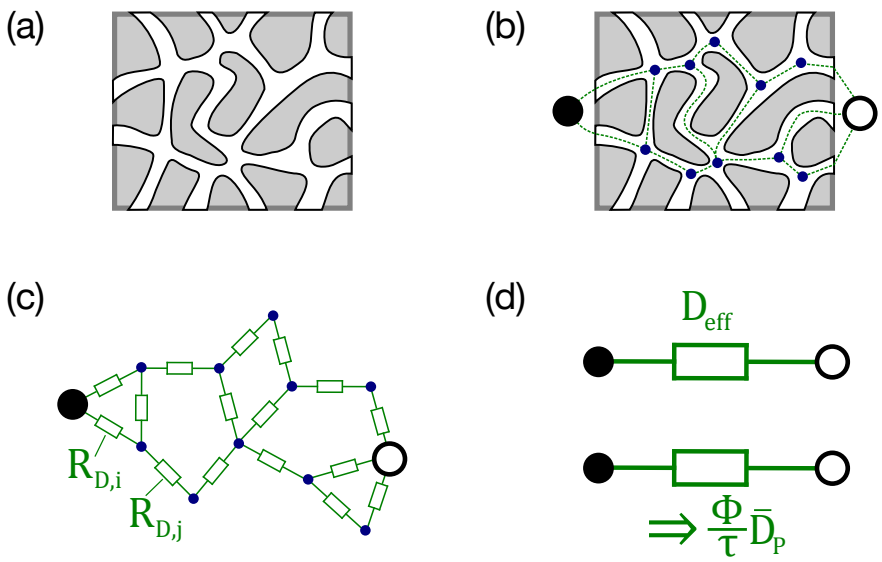

Figure 5.5.: Diffusion resistance in Vycor pore networks. (a) Vycor contains an interconnected network of meandering pores with different lengths and widths. (b) In order to find the diffusion resistance between two points (● and ○) in the network, pore intersections can be interpreted as nodes (blue dots), pores as connections between nodes. (c) This abstract network constitutes a resistor circuit with different diffusional resistances. (d) Instead of a network resistance (network diffusivity), an effective diffusivity can be defined for the geometric space occupied by the porous sample. Due to the uniformity of the Vycor network, D_{eff} is assumed to be a constant over macroscopic distances, resulting from a mean pore diffusivity $\bar{D}_P$, see Sec. 5.3.2.

The structure of the pore space in mesoporous materials defines a complex network of pore diffusion resistances, as illustrated in Fig. 5.5. In contrast to the ideal cylindrical geometry assumed for the above diffusivities, the network branches exhibit significant variation in shape, size and length between nodes in the network. Hence, a diffusion resistance of the network cannot be calculated directly.

Many experiments regarding transport in porous materials rely on the measurement of macroscopic flow rates. Similar to effective medium theory for dielectric properties, see Sec. 2.2.6, an effective diffusivity D_{eff} for a porous sample (matrix + pores) can be introduced as a practical parameter [73]. As diffusion is limited to the porous space, the effective diffusivity is related to the pore network diffusivity D_{NW} by the porosity Φ:

$$D_{\text{eff}} = \Phi D_{\text{NW}}. \tag{5.22}$$

5.3.2. Tortuosity

It is a general assumption that the diffusivity in pore networks is in some way related to the diffusivity in an average pore of the network, $\bar{D}_P(\langle r_0 \rangle)$. The ratio between the network diffusivity and the mean pore diffusivity defines a factor

$$\tau = \frac{\bar{D}_P}{D_{\mathrm{NW}}} = \Phi \frac{\bar{D}_P}{D_{\mathrm{eff}}}, \tag{5.23}$$

which is called the 'tortuosity' of the pore network. Since Vycor is reasonably uniform over macroscopic distances, τ is expected to be a constant for macroscopic samples.

By its definition, τ can also be interpreted as a factor relating the diffusivity of an array of uniform parallel pores and a pore network. In a three-dimensional, interconnected arrangement of pores with equal partitions oriented in parallel to the three coordinate axes (see Fig. 5.6(a)), the diffusivity in x, y, and z-direction is defined by a third of the pore space, hence $\tau = 3$ is expected. This value is also a rough estimate for random isotropic networks.

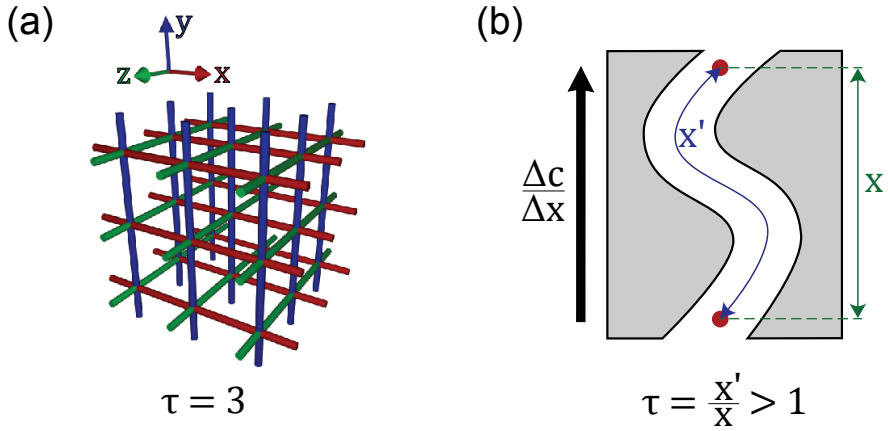

Figure 5.6.: Topological and morphological origin of the tortuosity. (a) In pore networks, the tortuosity factor is primarily determined by interconnectivity and network structure. As an example, the depicted interconnected pore lattice results in $\tau = 3$ for transport in parallel to one of the coordinate axes. (b) The meandering pore geometry further increases the tortuosity.

In addition to the network properties, the individual pore morphologies also influence the value of the tortuosity due to an effective prolongation of diffusion paths as illustrated in Fig. 5.6(b). In a single meandering pore with constant radius, the tortuosity corresponds to the ratio of pore length and distance covered in direction of the concentration gradient, $\tau = x'/x$. This effect is also expected to a certain degree for the entire pore network.

Combining both partial contributions to the tortuosity, a value $\tau > 3$ is expected for Vy-

cor. In order to determine τ experimentally, the pore diffusivity and the effective diffusivity need to be known independently. In the Knudsen regime, the pore diffusivity is given by Eq. (5.21). This relation simplifies further for non-adsorbing gases (e.g. He at $T \gg 4\,\mathrm{K}$), since all particles are in the gas phase, $N = N_g$. By measuring an effective transport diffusivity of a membrane and calculating the mean Knudsen diffusivity with Eq. (5.16), a value of $\tau = 3.6$ could be determined for Vycor [83, 49]. A similar value ($\tau = 3.2$) has been observed in other mesoporous silica membranes [84].

Lin et al. used a SANS self-diffusivity measurement in Vycor and observed a range of tortuosities $\tau = 3.4$ to 4.2 [85]. The above experimental value shows a good match to these results. If one recalls the comparison of Knudsen transport and self-diffusivity in Sec. 5.2.3, this indicates that pore wall roughness has little significance in Vycor.

However, it should be noted that the notion of a constant tortuosity breaks down when capillary condensation is considered. As more and more pores are blocked by capillary bridges, parts of the pore space can be cut off from the outside gas phase, effectively changing the network topology, as illustrated in Fig. 5.7. It is thus expected that the contribution of gas diffusion to the effective diffusivity is reduced.

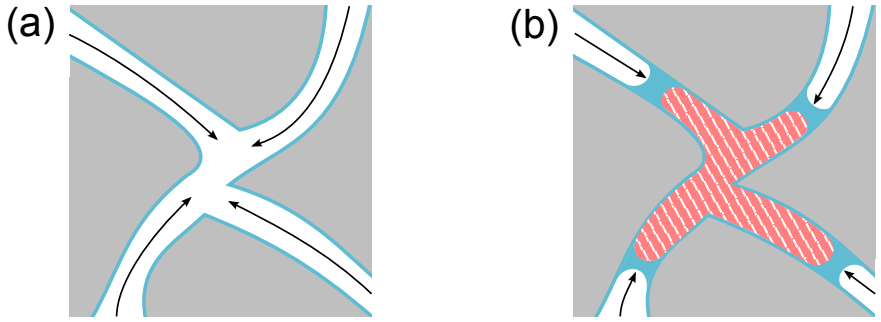

Figure 5.7.: Effect of capillary condensation on pore network structure. (a) For layer condensation, the entire pore space can be reached by diffusing gas. (b) As more and more capillary bridges form in the pores, the pore network is partially cut off from the outside. Transport in these regions is limited to secondary mechanisms, changing the structure of the network.

5.3.3. Geometric Model for Parallel-Sided Slabs

With the above definition of an effective diffusivity D_{eff}, the process of vapour uptake into a Vycor sample reduces to a problem of solving Fick's second law in Eq. (5.8) for appropriate geometric, initial and boundary conditions.

In case of the Vycor samples in this work, an analytical solution of the diffusion equation

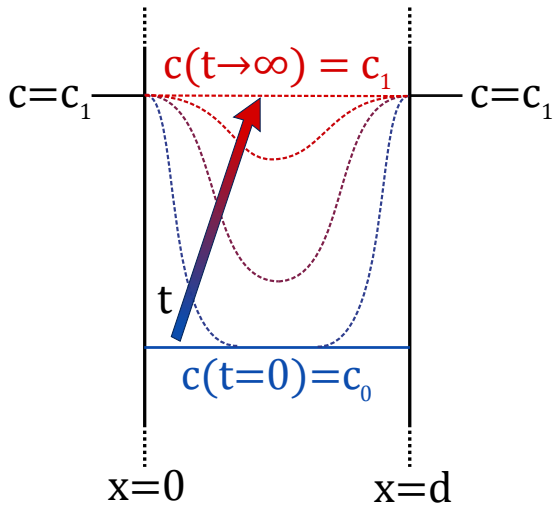

Figure 5.8.: Geometric model for diffusion into Vycor slabs. The sample are assumed as infinitely large, with a constant concentration on the boundaries. For this model, the concentration profile on the inside can be calculated using the diffusion equation (Fick's second law, Eq. (5.8)). Note that concentration profiles in this figure are qualitative representations, for illustration purposes only.

has been derived by Crank [74] as illustrated in Fig. 5.8. The geometric model consists of an infinitely large sheet limited by two parallel planes at a distance d. Then, the concentration profile is one-dimensional, since effects of the sample edges are neglected. The concentration distribution inside the sample is assumed uniform at first, $c(t = 0, 0 < x < d) = c_0$, the surface concentration on both sides is kept constant at all times, $c(x = 0) = c(x = d) = c_1$. Again, the latter is only a good approximation for small changes in the amount adsorbed. This initial concentration distribution results in the following evolution over time,

$$\frac{c(x,t) - c_0}{c_1 - c_0} = 1 - \frac{4}{\pi} \sum_{n=0}^{\infty} \frac{(-1)^n}{2n+1} \exp\left[-\frac{D_{\text{eff}}(2n+1)^2\pi^2 t}{d^2}\right] \cos\frac{(2n+1)\pi x}{d}. \tag{5.24}$$

Here, the infinite series results from an expansion into a trigonometric series during the solution. The concentration profile $c(x,t)$ on its own cannot be compared to the experimental results, however, when integrated over the sample volume, a mass or molar uptake can be calculated. Likewise, it is also best expressed as a normalized difference $\Delta N(t)/\Delta N_\infty$, where $\Delta N(t) = N(t) - N(t = 0)$ and ΔN_∞ corresponds to the maximum difference for a uniform increase in concentration in the entire sample volume, as seen for large times, $c(t \to \infty, 0 < x < d) - c(t = 0, 0 < x < d) = c_1 - c_0$. Then, the following uptake equation

for transient stepwise adsorption is found:

$$\frac{\Delta N(t)}{\Delta N_\infty} = 1 - \sum_{n=0}^{\infty} \frac{8}{(2n+1)^2\pi^2} \exp\left[-\frac{D_{\text{eff}}(2n+1)^2\pi^2 t}{d^2}\right]. \tag{5.25}$$

This is the basis for comparison with experimental uptake curves.

5.3.4. Relation of Transient Diffusivity to Pore Diffusivities

In transient adsorption experiments, the effective diffusivity for the macroscopic sample can be used to calculate a mean pore diffusivity as well as the partial contributions of gas and surface diffusion. In order to derive a relation between D_{eff} and the component diffusivities, it is assumed that both diffusion processes are independent and localized in the respective phase: Gas flow is limited to the free pore space, surface diffusion occurs in the combined volume of the solid and the adsorbate. This is equivalent to the formulation of Costa et al. [86]. Accordingly, one can define the concentrations of the gas phase c_g and the adsorbate phase c_σ to

$$c_g = \frac{N_g}{V_g} = \frac{N_g}{\Phi' V_s} \tag{5.26}$$

and

$$c_\sigma = \frac{N_\sigma}{V_\sigma} = \frac{N_\sigma}{V_s - V_g} = \frac{N_\sigma}{V_s\,(1-\Phi')}. \tag{5.27}$$

Here, V_s denotes the macroscopic sample volume and $\Phi' = \Phi\,(1 - N/N_0)$ is the modified porosity of a sample upon constriction by the additional adsorbate. The latter is assumed constant over the course of a transient process, which is consistent with the assumption of small changes in the amount adsorbed from Sec. 5.3.3. As the total molar amount is $N = N_g + N_\sigma$, the total concentration in the sample $c = N/V_s$ can be written as

$$c = \Phi' c_g + \left(1 - \Phi'\right) c_\sigma. \tag{5.28}$$

By this definition, c corresponds to a macroscopic concentration for which the effective diffusivity D_{eff} is defined. Any derivative of the total concentration can be described by a sum

of derivatives of the partial contributions, e.g. for a time-derivative,

$$\begin{aligned}\frac{\partial c}{\partial t} &= \Phi' \frac{\partial c_g}{\partial t} + \left(1-\Phi'\right) \frac{\partial c_\sigma}{\partial t} \\ &= \Phi' \frac{\partial c_g}{\partial t} + \left(1-\Phi'\right) \underbrace{\frac{\partial c_\sigma}{\partial c_g}}_{:=K(N/N_0)} \frac{\partial c_g}{\partial t} \\ &= \left(\Phi' + \left(1-\Phi'\right) K\right) \frac{\partial c_g}{\partial t}. \end{aligned} \tag{5.29}$$

In the last step of the calculation, it has been exploited that both concentrations are related to one another. While only strictly true in equilibrium, this can be applied to transient processes assuming that the time scale for adsorption is much smaller than for diffusion. The parameter K results directly from the local slope of the measured sorption isotherm, when rescaling the axes according to the transformations

$$\frac{P}{P_0} \rightarrow c_g = \frac{P_0}{RT}\frac{P}{P_0} \tag{5.30}$$

and

$$\frac{N}{N_0} = \frac{N_g + N_\sigma}{N_0} \rightarrow c_\sigma = \frac{\frac{N}{N_0} - c_g\left(1-\frac{N}{N_0}\right)\frac{M_m}{\rho_{\text{liq}}}}{\underbrace{\left(1-\Phi\left(1-\frac{N}{N_0}\right)\right)}_{\Phi}\frac{M_m}{\rho_{\text{liq}}}}, \tag{5.31}$$

using $N_0 = \Phi V_s \rho_{\text{liq}}/M_m$ with the liquid density ρ_{liq} and molar mass M_m of the adsorbate in the conversion for c_σ. In the stages of strongest ad-/desorption in the isotherm, the value of K is very large, whereas in the flat multilayer domain, K is smaller by orders of magnitude.

In order to describe the dynamics in both diffusing phases, two separate diffusion equations according to Fick's second law can be defined, see Eq. (5.8). Here, an additional term T_g or T_σ accounts for the change in concentration due to the transition of particles into the gas phase (index g) and into the adsorbate phase (index σ):

$$\frac{\partial c_g}{\partial t} = D_g \frac{\partial^2 c_g}{\partial x^2} + T_g, \tag{5.32}$$

$$\frac{\partial c_\sigma}{\partial t} = D_\sigma \frac{\partial^2 c_\sigma}{\partial x^2} + T_\sigma. \tag{5.33}$$

Note that the diffusivities D_g and D_σ have been assumed constant during the diffusion process, as discussed in Sec. 5.2.8.

Since the transition of molecules from one phase to another involves the same molar amount

($\frac{\partial N_g}{\partial t} = -\frac{\partial N_\sigma}{\partial t}$), the transfer terms T_g and T_σ are interdependent. Using Eqs. (5.26) and (5.27), they can be related as

$$T_g = -\frac{1-\Phi'}{\Phi'} T_\sigma. \tag{5.34}$$

With this identity, Eqs. (5.32) and (5.33) can be combined to

$$\frac{\partial c_g}{\partial t} = D_g \frac{\partial^2 c_g}{\partial x^2} + \frac{1-\Phi'}{\Phi'} \left(D_\sigma \frac{\partial^2 c_\sigma}{\partial x^2} - \frac{\partial c_\sigma}{\partial t} \right). \tag{5.35}$$

By introducing $\partial c_\sigma = K \partial c_g$, this can be further simplified,

$$\frac{\partial c_g}{\partial t} = \frac{D_g + K \frac{1-\Phi'}{\Phi'} D_\sigma}{1 + K \frac{1-\Phi'}{\Phi'}} \frac{\partial^2 c_g}{\partial x^2}. \tag{5.36}$$

Using the transformation for the differentiations according to Eq. (5.29), Eq. (5.36) can be reformulated as a macroscopic diffusion equation:

$$\frac{\partial c}{\partial t} = \underbrace{\frac{\Phi' D_g + K\left(1-\Phi'\right) D_\sigma}{\Phi' + K\left(1-\Phi'\right)}}_{D_{\text{eff}}} \frac{\partial^2 c}{\partial x^2}. \tag{5.37}$$

A transient effective diffusivity can be identified,

$$D_{\text{eff}} = \frac{\Phi' D_g + K\left(1-\Phi'\right) D_\sigma}{\Phi' + K\left(1-\Phi'\right)}. \tag{5.38}$$

Analogous to the definition in Sec. 5.3.2, D_{eff} can be related to the mean transient pore diffusivity D_P using Eq. (5.23).

$$D_P = \frac{\tau}{\Phi} D_{\text{eff}} = \frac{\tau}{\Phi} \frac{\Phi' D_g + K\left(1-\Phi'\right) D_\sigma}{\Phi' + K\left(1-\Phi'\right)} \tag{5.39}$$

Then, the diffusivities D_g and D_σ can be identified with the respective quantities of a cylindrical pore. Here, the adsorbate contributes solely by surface diffusion, $D_\sigma = D_S$ as defined in Sec. 5.2.6. In contrast to this simple equality, D_g contains Knudsen, intermolecular and viscous contribution, depending on the gas rarefaction. A simple form is found in the limit for high Knudsen numbers Kn, where only the Knudsen mechanism $D_g = D_{\text{Kn}}$ prevails. This results in a simple relation between the macroscopic transient diffusivity and partial mechanisms in a cylindrical pore,

$$D_P = \frac{\tau}{\Phi} \frac{\Phi' D_{\text{Kn}} + K\left(1-\Phi'\right) D_S}{\Phi' + K\left(1-\Phi'\right)}. \tag{5.40}$$

6 Transient Sorption Experiments

6.1. Kinetics of Sorption Isotherm Experiments

6.1.1. Outline

As a part of the 1-butanol sorption experiments in Sec. 4.3, the uptake kinetics in non-equilibrium were measured in the process of determining an equilibrium adsorption state for each point of the isotherm, see [64]. In line with the results of Sec. 4.3.3, the real part of the dielectric permittivity at $\nu = 1\,\mathrm{MHz}$ can be used as a measurement for momentary filling of the sample $N(t)/N_0$. Over the course of an ad-/desorption point, a continuous in-/decrease of total filling can be observed.

By applying the theoretical model of Sec. 5.3 to experimental uptake curves, it is possible to quantify the transport diffusivity of the Vycor pores for different filling steps. The goal is to compare the contributions of different diffusion mechanisms in the pores in order to gain insight on the total transport process of strongly adsorbing molecules.

Both, the adsorption and desorption directions have been studied, the results are separated for both experimental parts into the following two sections, followed by a comparison.

6.1.2. Kinetics for Adsorption

Exemplary adsorption kinetics for points in different stages of the isotherm are depicted in Fig. 6.1. Besides the adsorption plateau for high relative pressures (d), all isotherm points show a similar time evolution of the amount adsorbed: Starting from the initial permittivity $\varepsilon(t = 0)$, a continuous increase is observed that is initially very fast and slows down over time until the permittivity approaches the equilibrium value $\varepsilon'(t \to \infty)$. As depicted, the times to reach an equilibrium state vary by several orders of magnitude: In the monolayer (a) and the capillary condensation stages (c), the equilibration takes much longer than for the layer condensation (b). This is also consistent with experimental observations for other isotherm measurements.

In contrast to any other step, when reaching the plateau of total filling $N/N_0 = 1$, an abrupt transition to the filled state was observed rather than a gradual approach, see the arrow in Fig. 6.2. In comparison to similar uptake curves for spontaneous imbibition, see Sec. 10.2, this could indicate a contribution by a liquid capillary flow.

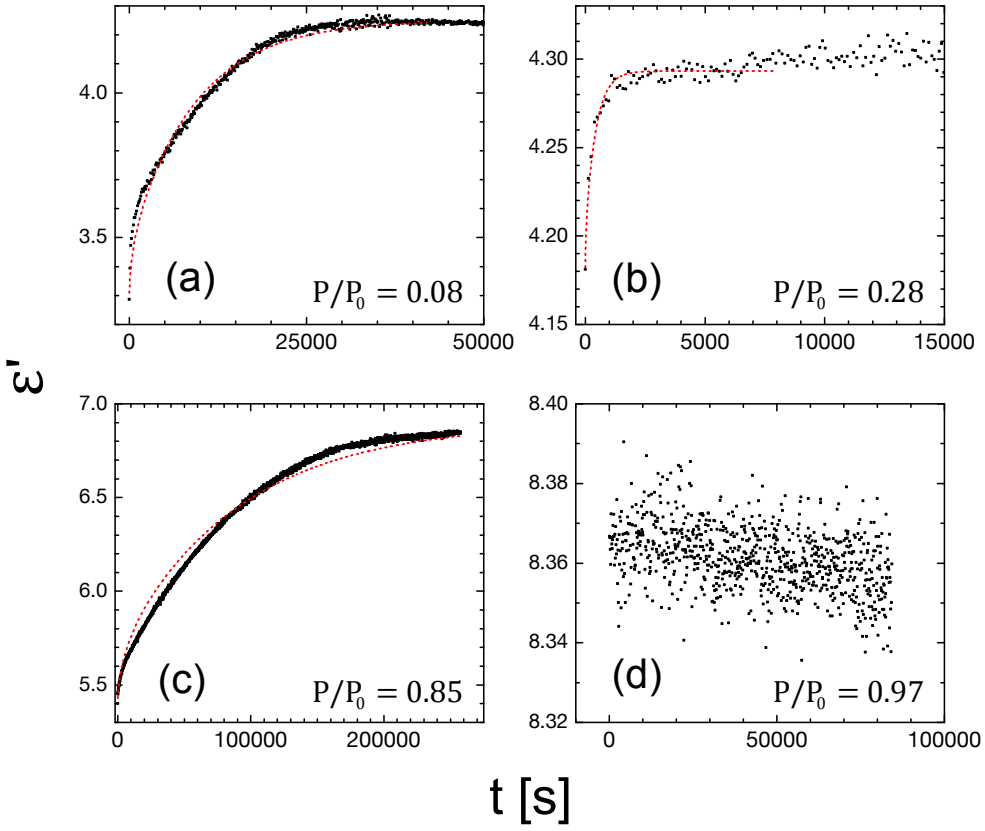

Figure 6.1.: Comparison of adsorption kinetics for incremental isothermal adsorption steps for 1-butanol. (a) monolayer step, (b) layer condensation, (c) capillary condensation, (d) plateau. Note the different magnitudes of time required for reaching the equilibrium state. For suited data points (a-c), a fit using Eq. (6.2) has been applied to the data, displayed as red dashed lines.

For quantitative analysis, a normalized permittivity can be defined that corresponds to the normalized filling $\Delta N(t)/\Delta N_\infty$ from Eq. (5.25),

$$\frac{\Delta\varepsilon'(t)}{\Delta\varepsilon'_\infty} = \frac{\varepsilon'(t) - \varepsilon'(t=0)}{\varepsilon'(t\to\infty) - \varepsilon'(t=0)} = \frac{\Delta N(t)}{\Delta N_\infty}. \tag{6.1}$$

Accordingly, the momentary permittivity $\varepsilon'(t)$ is described by

$$\varepsilon'(t) = \varepsilon(t=0) + \Delta\varepsilon'_\infty \frac{\Delta N(t)}{\Delta N_\infty} \tag{6.2}$$

A non-linear curve fit can be applied to the experimental data as described by a combination of Eqs. (6.2) and (5.25). For computational purposes, the summation in Eq. (5.25) has been limited to the orders $n = 0$ to 9. In terms of fit parameters, the diffusion geometry d can be

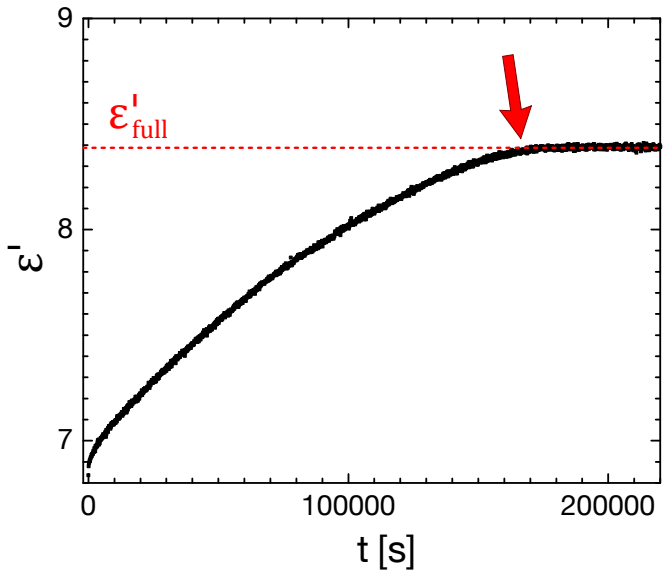

Figure 6.2.: Adsorption kinetics for 1-butanol at the saturation plateau. The arrow indicates an abrupt transition to the filled state instead of an asymptotic approach, unlike any other uptake curve.

identified as the constant sample thickness; the initial value $\varepsilon'(t = 0)$ as well as the increase $\Delta\varepsilon'_\infty$ are extracted directly from the measured kinetics. This reduces the free parameters to the effective diffusivity D_{eff} only.

Fit results are depicted as red dashed lines in Fig. 6.1. For the most part, the curves show a good match to the experimental data. The largest deviations of the fits are observed for large uptakes of adsorbate, i.e. monolayer step and capillary condensation.

Note that due to thermal fluctuations and the general precision in the measurement, there is considerable noise in the signals. This is most prominent in kinetics featuring only a small total increase $\Delta\varepsilon'_\infty$, mainly for layer condensation after the monolayer step, see Fig. 6.1(b). The fits for these data points were tailored to the first stage of the kinetics only, where the largest changes were measured. Any delayed effects, e.g. due to collapsing metastable layer condensate, will be neglected in the process. Fig. 6.3 shows the resulting effective diffusivities in relation to the relative pressure and the amount of adsorbate.

For the mentioned data points of large increase in adsorbate, the validity of the applied model has to be discussed: On one hand, the diffusivity and the outside pressure may shift significantly, resulting in an error in the solution of the geometric diffusion model. On the other hand, as capillary bridges form in the matrix, they present new sinks for the uptake of adsorbate in the matrix, influencing the concentration gradients on small length and time-scales. Thus, the above values of D_{eff} for capillary condensation should only be considered

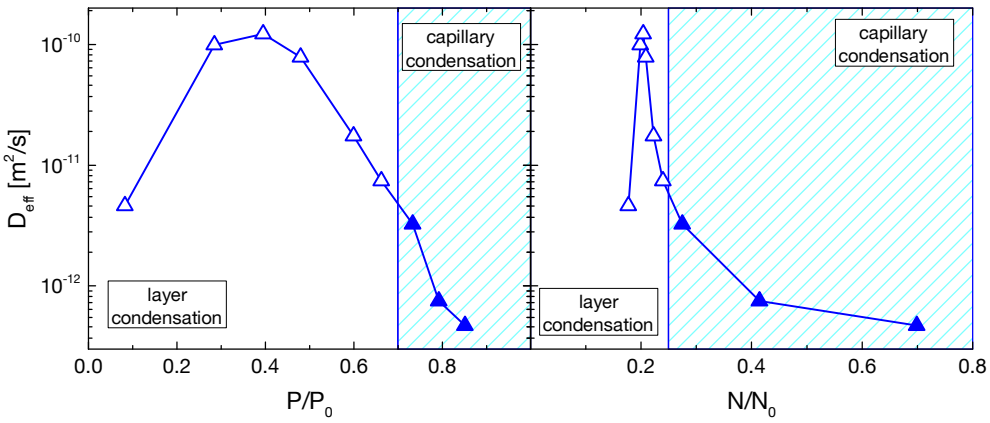

Figure 6.3.: Effective diffusivities for 1-butanol adsorption data, as a function of the normalized pressure (left) and relative amount of adsorbate (right). Uncertainties resulting from the fit to kinetics curves are in the order of symbol sizes.

as a practical estimate in an experimental context, e.g. to indicate the time scale on which an equilibrium is reached.

According to Eq. (5.9), the mean free path for butanol molecules (van-der-Waals radius $r_A \approx 255\,\mathrm{pm}$, see App. B) for laboratory conditions $T = 298\,\mathrm{K}$ and at saturation pressure $P = P_{0,\mathrm{C4}} = 8.5\,\mathrm{mbar}$ amounts to $\lambda_{\mathrm{C4}} \approx 3.6\,\mu\mathrm{m}$. A lower boundary estimate for the Knudsen number in the experiment can be derived using Eq. (5.10), assuming that the Vycor pores are completely empty with a radius $r_0 = 4.5\,\mathrm{nm}$. This results in a value $\mathrm{Kn}_{\mathrm{C4,min}} \approx 400$. Hence, the limit of dilute gasses is justified for all points of the isotherm and the model of Sec. 5.3.4 can be applied.

Using Eq. (5.39), a modified transient pore diffusivity D'_P can be calculated from D_{eff},

$$\begin{aligned} D'_P &= \frac{\Phi}{\tau} D_P \left[\Phi' + K\left(1-\Phi'\right)\right] \\ &= D_{\mathrm{eff}} \left[\Phi' + K\left(1-\Phi'\right)\right]. \end{aligned} \tag{6.3}$$

Values for D'_P were calculated for all data points of the effective diffusivity and results are shown in Fig. 6.4(a). By equally rearranging Eq. (5.40), D'_P can in turn be easily compared to the weighted partial contributions of individual diffusion mechanisms:

$$\underbrace{\frac{\Phi}{\tau}\left[\Phi' + K\left(1-\Phi'\right)\right] D_P}_{D'_P} = \Phi' D_{\mathrm{Kn}} + K\left(1-\Phi'\right) D_S. \tag{6.4}$$

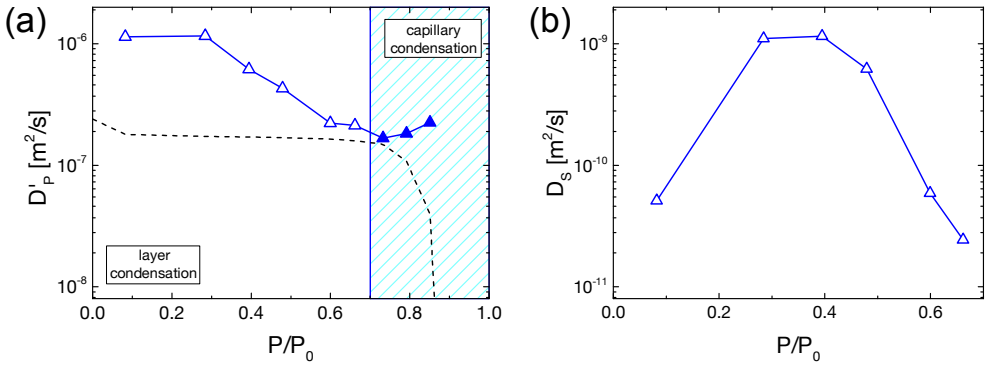

Figure 6.4.: Transient pore diffusivities and surface diffusivities upon adsorption of 1-butanol. (a) Transient pore diffusivities (△, ▲) in comparison to partial Knudsen contributions (dashed line). (b) Calculated surface diffusivities for layer condensation.

For the layer condensation stage, a quantitative comparison can be made using the right side of Eq. (6.4). Here, the first summand can be calculated with the theoretical Knudsen contribution $D_{\mathrm{Kn}}(N/N_0)$ using Eqs. (5.17) and (4.15),

$$\Phi' D_{\mathrm{Kn}}(N/N_0) = \Phi' \frac{2}{3} r_0 v_{\mathrm{th}} \sqrt{1 - N/N_0}. \tag{6.5}$$

This variable Knudsen diffusivity is depicted as a black dashed line in Fig. 6.4(a) in comparison to the experimental pore diffusivities D'_P. For all points in the layer condensation regime, the experimental values are significantly higher than the predicted values of this Knudsen mechanism. This confirms that surface diffusion is important to consider in this strongly adsorbed configuration.

As for the hysteresis region, the values for D'_P have been calculated as a qualitative indicator only. Since capillary condensation inevitably leads to gradual blocking in the pore network, it was expected that the tortuosity τ is increased in the process. Then, the calculated pore diffusivity should be reduced, see Eq. (6.4). Contrary to these considerations, the capillary condensation stage depicted in Fig. 6.4(a) exhibits an increase of pore diffusivity. Putting model errors aside, an enhanced transport could be interpreted as an additional flow mechanism. This is consistent with the likely contribution from spontaneous flow of capillary bridges that has been introduced in Sec. 5.2.7.

For the layer condensation stage, the difference to the theoretical Knudsen value can be directly evaluated to a surface diffusivity D_S using Eqs. (6.4) and (6.5),

$$D_S = \frac{D'_P - \Phi' D_{\mathrm{Kn}}(N/N_0)}{K(1 - \Phi')}. \tag{6.6}$$

Results for the layer condensation stage of 1-butanol are shown in Fig. 6.4(b) as a function of the relative pressure. A variation of surface diffusivity of approximately an order of magnitude is found with a clear maximum in a range between $P/P_0 = 28$ to $40\,\%$. In accordance to the surface diffusion model in Sec. 5.2.6, this can also be interpreted as a hopping probability in the surface layer. Thus, these results indicate that the particle mobility is maximized for nearly complete occupation ($N/N_0 \approx 20\,\%$), which suggests that repulsive forces between adsorbate particles increase the probability of hopping at high occupation densities. However, when further increasing the population in the surface layer, mobility is reduced due to the lack of vacant adsorption sites.

6.1.3. Kinetics for Desorption

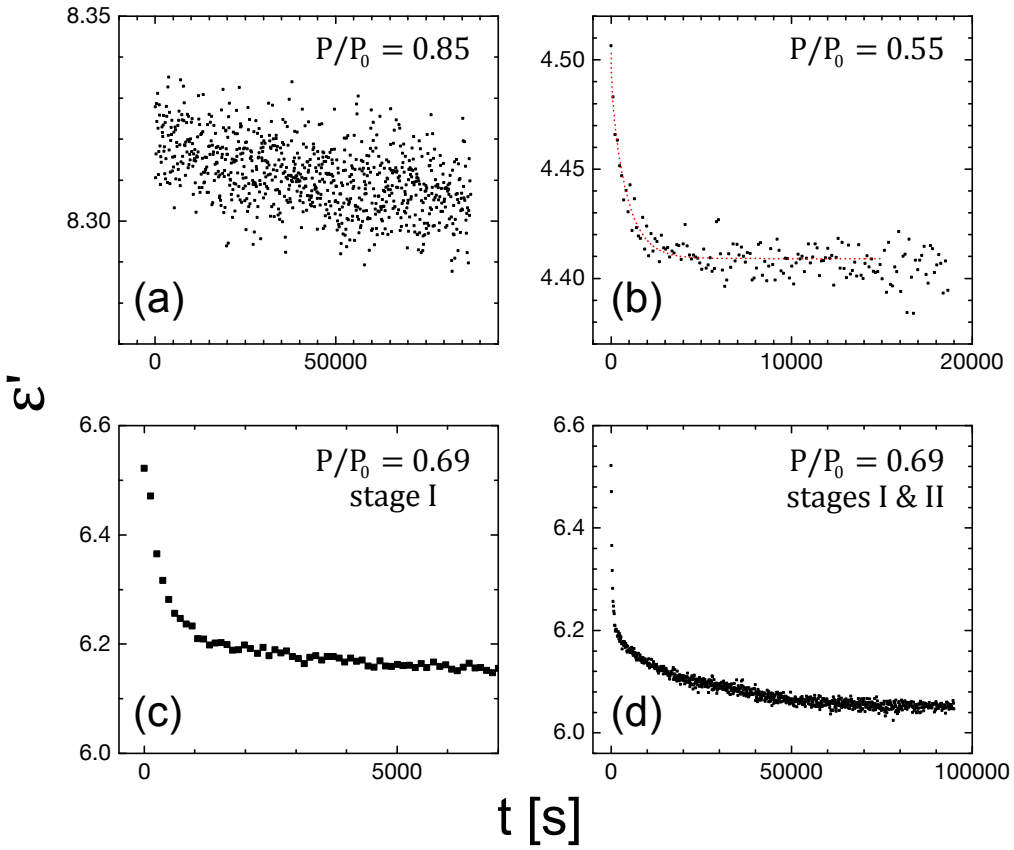

Figure 6.5.: Comparison of desorption kinetics for incremental isothermal desorption steps for 1-butanol (a) plateau region, (b) layer condensation stage, (c)-(d) capillary desorption. A fit using Eq. (6.2) has been applied to the layer condensation data, displayed as the red dashed line.

The kinetics of desorption were measured analogous to adsorption. The resulting uptake curves depicted in Fig. 6.5 share many similarities with adsorption: In the layer stage (b), equilibrium is reached substantially faster than for capillary desorption (d); on the plateau (a), only minor desorption is measured.

However, a peculiar difference to adsorption was observed for the kinetics data during capillary desorption, which all exhibit a characteristic two-stage desorption, see Fig. 6.5. After a very fast initial drop (c), dynamics slow down considerably while still approaching equilibrium (d). A possible reason for this behaviour is a combination of two different desorption mechanisms, which will be elucidated below.

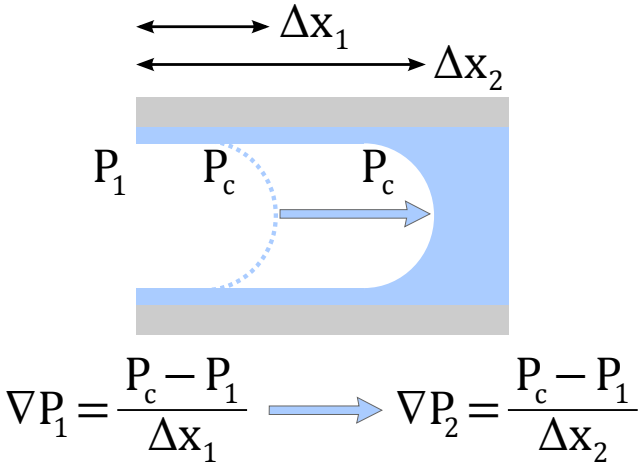

Figure 6.6.: Effect of receding menisci on pressure gradients. During the initial phase of capillary desorption, the liquid interfaces in the sample recede over time. In this varying geometric situation, the driving pressure gradient is dynamically shifted over time. The consequence is a failure of the geometric diffusion model.

Due to a difference in distribution of the adsorbate, a critical failure ensues for the geometric diffusion model during capillary desorption. In contrast to capillary adsorption, when capillary bridges form throughout the entire sample volume, desorption is limited to a smaller number of liquid interfaces that are accessible from the outside. This is a consequence of pore blocking effects, see Sec. 3.4.3. In this situation, the pressure gradient that drives the diffusive flux is critically determined by the interface position, see Fig. 6.6. It is likely that this collapse of capillary condensate governs the first stage of desorption kinetics in Fig. 6.5(c). Then, the second stage of dynamics can be interpreted as delayed effects in the filled pore network, e.g. partial desorption on dynamic redistribution of adsorbate. Hence, as both of these effects are not quantifiable without any knowledge of spatial distribution of the adsorbate, the capillary desorption data has not been included in quantitative analysis.

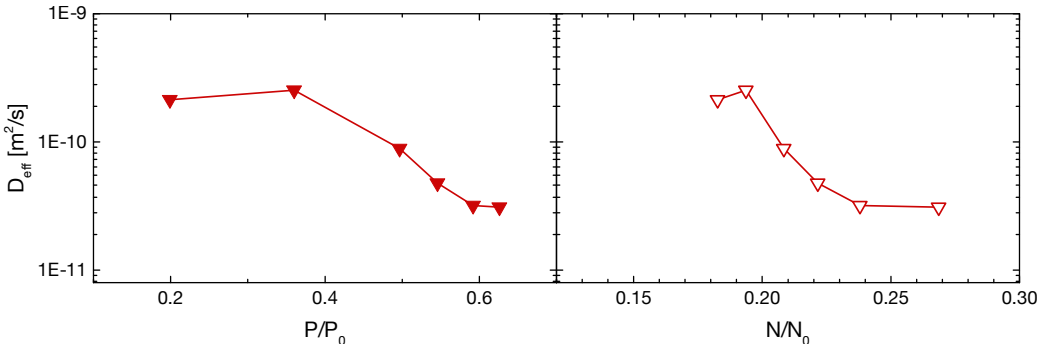

Figure 6.7.: Effective diffusivities for 1-butanol desorption data in the layer condensation regime, as a function of the normalized pressure (left) and relative amount of adsorbate (right). Uncertainties of the fit are in the order of symbol sizes.

For the layer condensation stage, the same theoretical models apply to transport during adsorption and desorption. Based on the previous assumptions of constant diffusivity, no pressure change on the outside and constant flow geometry, the results from stepwise desorption can be analysed analogous to the adsorption measurement. Fig. 6.7 shows the effective diffusivities for desorption in the layer regime that were extracted using a curve fit of Eq. (6.2).

The effective diffusivities show the same qualitative behaviour as the results from adsorption with a maximum of diffusivity at $N/N_0 \approx 0.2$. Analogous to adsorption, the transient pore diffusivities D'_P and partial Knudsen contributions were calculated using Eqs. (6.4) and (6.5), as shown in Fig. 6.8(a).

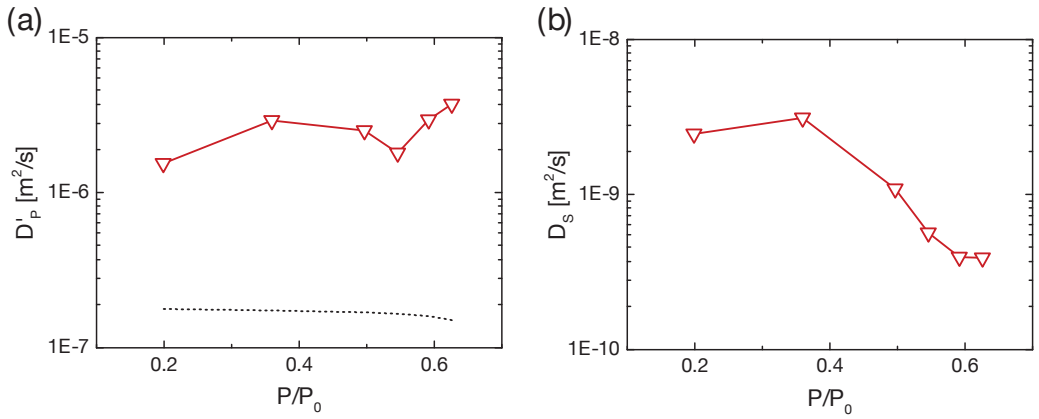

Figure 6.8.: Transient pore diffusivities and surface diffusivities upon desorption of 1-butanol. (a) Transient pore diffusivities in comparison to partial Knudsen contributions (dashed line). (b) Calculated surface diffusivities.

Again, the pore diffusivity shows an enhanced transport for the entire layer condensation stage when compared to the simple Knudsen diffusion. This is interpreted as an additional surface diffusivity which was evaluated using Eq. (6.6). The results, as displayed in 6.8(b) show a remarkable qualitative match to the adsorption results, with a maximum at $P/P_0 = 0.36$ and a drop towards higher pressures that is consistent with the interpretation of a reduced mobility in a completely filled monolayer, see Sec. 6.1.2.

6.1.4. Summary and Discussion

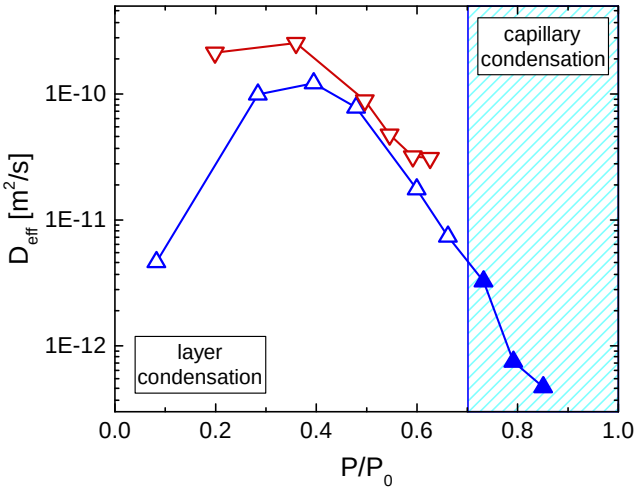

Figure 6.9.: Comparison of effective diffusivities for adsorption and desorption of 1-butanol (blue △: adsorption, red ▽: desorption).

The kinetics for adsorption and desorption indicate the same qualitative and quantitative behaviour for a wide range of relative pressures. When comparing effective diffusivities for both directions of sorption, see Fig. 6.9, the data for both layer condensation stages shows an agreement for most data points. This indicates that the layer adsorption and desorption is correlated with the same transport characteristics in the matrix, as is expected due to the reversible character of this process. Though, the small but systematical deviations for ad- and desorption, especially for lower pressures could indicate a potential model weakness, e.g. the failing assumptions of constant diffusivity and outside concentration.

These results show a great match to the experimental work of Valiullin et al. [87, 88] who conducted PFG-NMR experiments on the self-diffusivity of non-polar adsorbates in Vycor. In their experiments, the same qualitative behaviour and a comparable position of the maximum in self-diffusivity was observed, which indicates that self- and transport diffusivity in the layer

condensation stage are closely related.

In the capillary condensation stage, where the geometric diffusion model is strictly invalid, the adsorption kinetics still exhibit the same characteristics as the layer condensation stage, see Fig. 6.1. Then, it is technically possible to apply the same quantitative analysis which yields estimates of the sample transport diffusion coefficient. On the contrary, pore blocking and the resulting difference in adsorbate distribution induce a difference in dynamics during capillary desorption that manifests as a two-stage desorption process. These dynamics however are not quantifiable without additional experimental methods probing the adsorbate distribution.

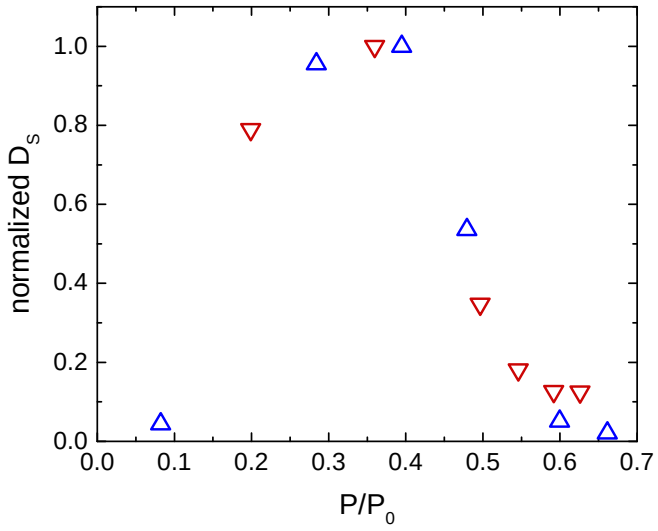

Figure 6.10.: Comparison of normalized surface diffusivities for adsorption and desorption of 1-butanol (blue △: adsorption, red ▽: desorption).

Furthermore, by comparing transient pore diffusivities to the partial contribution of different mechanisms, it has been shown that transport in the pore network consists of both a gas flow in the empty pore space as well as an additional surface diffusion which has significant impact on total transport. The surface diffusivity has been quantified for both directions independently, assuming a pure Knudsen mechanism in the gas phase. Fig. 6.10 shows a comparison of normalized values, revealing a great match of both directions. A maximum of surface diffusivity has been observed at $P/P_0 \approx 0.4$, corresponding to pore loading $N/N_0 \approx 0.2$. For higher or lower surface occupation, the diffusivity exhibits a steep drop. In a microscopic interpretation, this maximum of hopping mobility for near-complete occupation in the adsorbate layer suggests a strong additional contribution of repulsive forces between adsorbate particles.

6.2. Spontaneous Vapour Filling Dynamics

6.2.1. Outline

Besides the stepwise adsorption experiments, the vapour uptake dynamics were also studied for complete filling of Vycor with n-alcohols. In these experiments, empty samples were exposed to a saturated vapour atmosphere over a liquid. At room temperature, this leads to a spontaneous adsorption inside the Vycor matrix $N/N_0 \rightarrow 1$ and associated transport diffusion through the gaseous phase. Although this process is of great interest in many experimental situations, e.g. in comparison to spontaneous imbibition, see Sec. 11, there is a striking absence of reported data in literature.

Partly, this can be attributed to the complex dynamics of this non-equilibrium process: As discussed in Sec. 5.2.8, a large increase in concentration causes considerable changes to the diffusivity inside the pores, resulting in a non-linear form of the diffusion equation. Moreover, as a result of the continuous local formation of capillary bridges during this uptake process, the pore network structure is also gradually modified. Hence, the assumptions of the theoretical model in Sec. 5.3 fail for this type of experiment.

The goal of this work is to conduct a qualitative study of this process with special focus on the time evolution of the uptake rates. Later on, the quantitative impact of vapour phase filling will be assessed in comparison to a spontaneous liquid uptake and a hybrid model for a combined uptake can be derived, see Sec. 11.

6.2.2. Experimental Procedure

The experiments were carried out in the imbibition setup that will be described in detail in Sec. 10.1.1. The sample is suspended in a closed system containing a liquid reservoir and is connected to an impedance analyser. When starting an uptake experiment, a small amount of liquid is inserted into the sample chamber and partially evaporates until a saturated atmosphere is reached. In this situation, the diffusion flow through the macroscopic gas phase is the only mechanism for molecular transport.

In accordance to the conditions during imbibition experiments (see Sec. 10.1.1), a protective He-atmosphere ($P_{\mathrm{He}} = 800\,\mathrm{mbar}$) was inserted. On one hand, this allows to consistently recreate a defined total pressure for different P_0 of the liquids in order to ensure comparability of results. On the other hand, this also simulates the ambient air pressure in a non-controlled environment without breaking the seal of the sample chamber and risking contamination. Since helium does not exhibit significant condensation at room temperature, co-adsorption is not expected. The only consequence of the additional gas is then a slight change in diffusion

dynamics, which will now be discussed.

Due to the higher total pressure, the Knudsen number in Vycor reaches the transition regime (Kn ≈ 5) and the considerations of Sec. 5.2.5 have to be applied. An order of magnitude estimation using Eq. (5.18) with typical molecular geometries and $\Omega \approx 1$ yields an intermolecular diffusion $D_{\mathrm{AB}} \sim 10^{-5}\,\mathrm{m^2/s}$ while the respective Knudsen diffusivities according to Eq. (5.16) are in the range of $D_{\mathrm{Kn}} \approx 10^{-7}$ to $10^{-6}\,\mathrm{m^2/s}$. Thus, intermolecular diffusions results only in a small reduction in gas phase diffusivity of $10\,\%$ in the worst case, see Eq. (5.19). Dynamics inside the pores should therefore be comparable to the low-Kn limit.

There is also the possibility that a concentration gradient of alcohol arises in the bulk vapour phase, since intermolecular diffusion is significant. Considering an electrical analogy, a serial circuit of diffusion conductances for the bulk vapour phase and the porous sample determines the total diffusion flux into the sample. For an order of magnitude estimation, each conductance in this serial circuit as well as the total conductance can then be estimated from the ratio of the individual diffusivity and the distance covered,

$$\frac{d_{\mathrm{serial}}}{D_{\mathrm{serial}}} = \frac{d_{\mathrm{sample}}}{D_{\mathrm{sample}}} + \frac{d_{\mathrm{gas}}}{D_{\mathrm{gas}}}. \tag{6.7}$$

For the porous sample, a typical effective transient diffusivity for 1-butanol from Sec. 6.1.2 can be assumed ($D_{\mathrm{sample}} = 1 \cdot 10^{-10}\,\mathrm{m^2/s}$), which is approximately five orders of magnitude below the intermolecular diffusivity ($D_{\mathrm{gas}} \sim 1 \cdot 10^{-5}\,\mathrm{m^2/s}$) in the bulk gas phase. Then, even though the distance from the liquid reservoir to the sample ($d_{\mathrm{gas}} \sim 1\,\mathrm{cm}$) is significantly larger than the sample thickness ($d_{\mathrm{sample}} \sim 1\,\mathrm{mm}$), the contribution of the bulk gas phase in Eq. (6.7) is still negligibly small. Thus, in analogy to an electrical voltage divider, the concentration gradient in the bulk phase is small compared to the gradient in the sample and therefore not decisive for total transport.

Nevertheless, it is expected that the sample geometry has a critical impact on kinetics. To ensure comparable results for the different liquids, a single sample (*vyc_im_1*, see App. A) was reused over the course of the series of experiments. By utilizing the cleaning technique introduced in Sec. 2.1.4, the organic liquids could be completely removed from the matrix which was confirmed in the dielectric spectra at the beginning of each experiment.

As sketched in the inset of Fig. 6.11, the electrodes in these experiments cover only a part of the sample surface, which will be motivated in Chapter 11. This results in a gradual uptake of vapour in the stray field on one side of the sample capacitor. Though, if the uptake dynamics are equal throughout the entire sample volume, normalized changes $\Delta\varepsilon'/\Delta\varepsilon'_{\mathrm{max}}$ are still free from stray field effects, see Sec. 11.3.1 for a derivation. In accordance to considerations from

equilibrium adsorption in Sec. 4.3.3, these define a relative filling fraction f of the pore space,

$$f = \Delta\varepsilon'/\Delta\varepsilon'_{\mathrm{max}} \tag{6.8}$$

6.2.3. Results and Discussion

An exemplary uptake curve for 1-heptanol ($C_7H_{15}OH$) is depicted in Fig. 6.11. Three stages of different dynamics can be identified: The fastest uptake is observed at the very beginning of the first stage (I). Over time, dynamics gradually slow down and approach a constant slope. This linear stage (II) is observed over a large timespan. The final stage (III) shows another increase in uptake rate, until an abrupt transition to the filled state is observed.

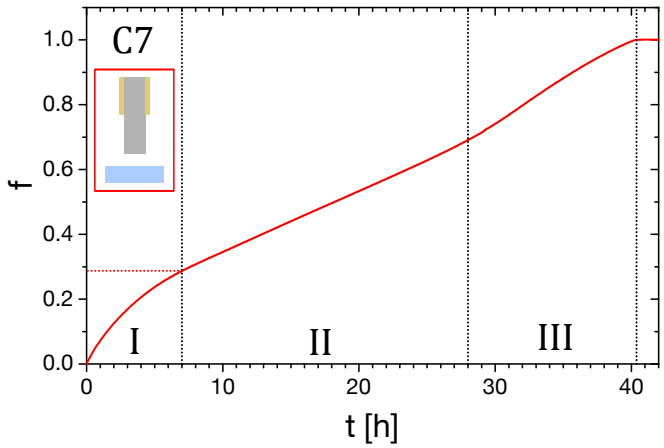

Figure 6.11.: Vapour filling kinetics for 1-heptanol at room temperature ($T = 294\,\mathrm{K}$). The spontaneous uptake over time shows three stages of qualitatively different dynamics. Also see Fig. 6.12 on the distinction of the three stages.

According to diffusion theory, the steep increase at the beginning of the experiment indicates that the surface concentration on the outside of the sample reaches its maximum value quasi-instantaneously [74], which is consistent with the expectation that intermolecular diffusion in the bulk vapour is not the determining mechanism. To further back up this interpretation, it should also be noted that the outside diffusivity is constant in good approximation, so that any variation of dynamics originates from effects inside the sample. Hence, the rapid changes at the beginning of stage I indicate a shift in transport properties up to a relative filling of $N/N_0 \approx 0.3$. Two possible reasons for this can be given: The variable surface diffusivity declining for a complete monolayer, as shown for 1-butanol in Fig. 6.10, and the onset of

capillary condensation in smaller pores altering the pore network topology, see Sec. 5.3.2.

The slope of the uptake curve in Fig. 6.11 is proportional to the molecular flow rate into the sample. A time-derivative of the relative filling is displayed in Fig. 6.12. Here, stage II of the experiment is characterized by a nearly constant value as indicated by the dashed line. This is equivalent to a stationary diffusion. According to Fick's first law in Eq. (5.6), a constant diffusion flux results from a constant product of pressure gradient and transport diffusivity for any given time. This is a remarkable result, considering that the effective diffusivity in the porous matrix in equilibrium experiments exhibited large variations as a function of relative filling, see Sec. 6.1.2 and Fig. 6.3.

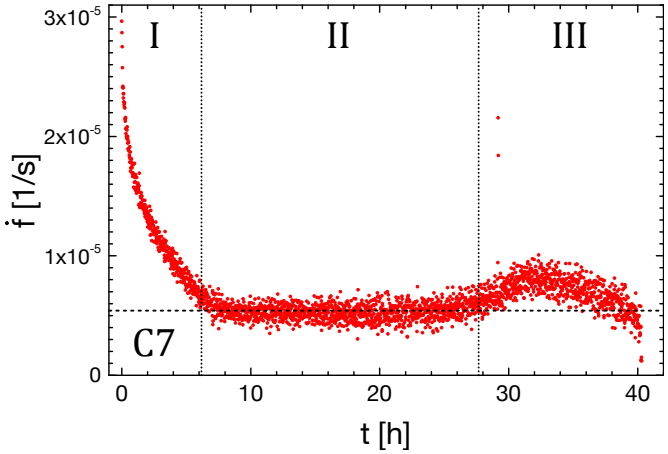

Figure 6.12.: Vapour uptake rates of 1-heptanol. The numerical derivative of the uptake curve reveals a linear uptake during stage II.

A possible microscopic reason for this behaviour is the nearly constant pressure at the capillary bridges: Assuming homogeneous distribution of filled pore sections in the sample volume and constant pore network geometry (no dynamic cutoff of pore space from the outside vapour phase by the formation of capillary bridges), the total pressure gradient is expected as nearly constant on filling, which in turn drives a constant diffusion flux through the empty parts of the pore network. This pressure should in principle be determined by the Kelvin equation, Eq. (3.30) and scale for different liquid parameters accordingly. However, the pressure gradient and diffusivity cannot be quantified separately, mainly due to the unknown spatial distribution of adsorbate.

The start of stage III is defined by a gradual acceleration in uptake dynamics, see Fig. 6.12, which is interpreted as a shift in the transport mechanism inside the pore network. As more and more capillary bridges form inside the matrix, diffusive transport is enhanced by the

additional spontaneous liquid flow of capillary bridges, see Sec. 5.2.7. At a certain point of filling, as more and more pores are blocked for the outside vapour due to dynamic formation of capillary condensate, this contribution is dominant for total transport. As we shall see in Sec. 11, the dynamics of this final stage show a good qualitative agreement to spontaneous capillary filling, confirming this hypothesis. Furthermore, the transition to the filled state is abrupt, also indicating liquid flow in contrast to asymptotic approaches by gas diffusion.

Vapour filling experiments have been conducted for a series of n-alcohols ($n = 4$ to 10). Results are shown in Fig. 6.13. For butanol, the most volatile liquid probed, the sample is filled in $\approx 3\,\mathrm{h}$, which is comparable to the time scale for spontaneous capillary rise, see Sec. 10. Notably, the process of total filling through the vapour phase is much faster than reaching an equilibrium in stepwise adsorption, especially in the adsorption branch of the hysteresis, see Sec. 6.1.2. Valiullin et al. attributed this slow approach to equilibrium to gradual, thermally activated rearrangement of the adsorbate inside the Vycor pore space [88]. For the dynamics of complete vapour filling, this small effect seems to be overshadowed by the constant influx of additional adsorbate.

The times to achieve complete filling increase by more than two orders of magnitude from butanol (C4) to decanol (C10). This relative increase can be compared to the estimated scaling of diffusive flux: On one hand, the Knudsen diffusivity inside the pores only weakly depends on the molar mass of the particles ($\propto M_m^{-0.5}$). On the other hand, the respective vapour pressures of C4 and C10 amount to $850\,\mathrm{Pa}$ and $1.18\,\mathrm{Pa}$, the pressure gradients should scale accordingly. This scaling behaviour of the pressure gradient is in agreement with the experimental time scales.

For all alcohols, the kinetics feature the principal dynamics discussed in Sec. 6.2.3. However, the individual stages vary in relative importance when comparing the different substances. Smaller chain lengths $n < 7$ exhibit less defined stages I and III as well as a more pronounced stationary diffusion stage II. Conversely, for longer chain lengths $n > 7$, stages I and III are relatively longer.

As for stage I, the different extent is potentially related to a different relative importance of surface diffusion for total transport. While the gas phase diffusion flux critically depends on the vapour pressure and the resulting pressure gradient, see Eq. (5.6), the surface diffusion is determined by molecular interactions and surface properties. These are expected to show fewer variations for all alcohols, so that a nearly constant contribution ensues. In case of short chain lengths, the large diffusion flux within the gas phase thus dominates the total uptake behaviour of the first phase. In contrast to this, long-chain alcohols exhibit a significant additional transport by surface diffusion at first. When a complete monolayer coverage is

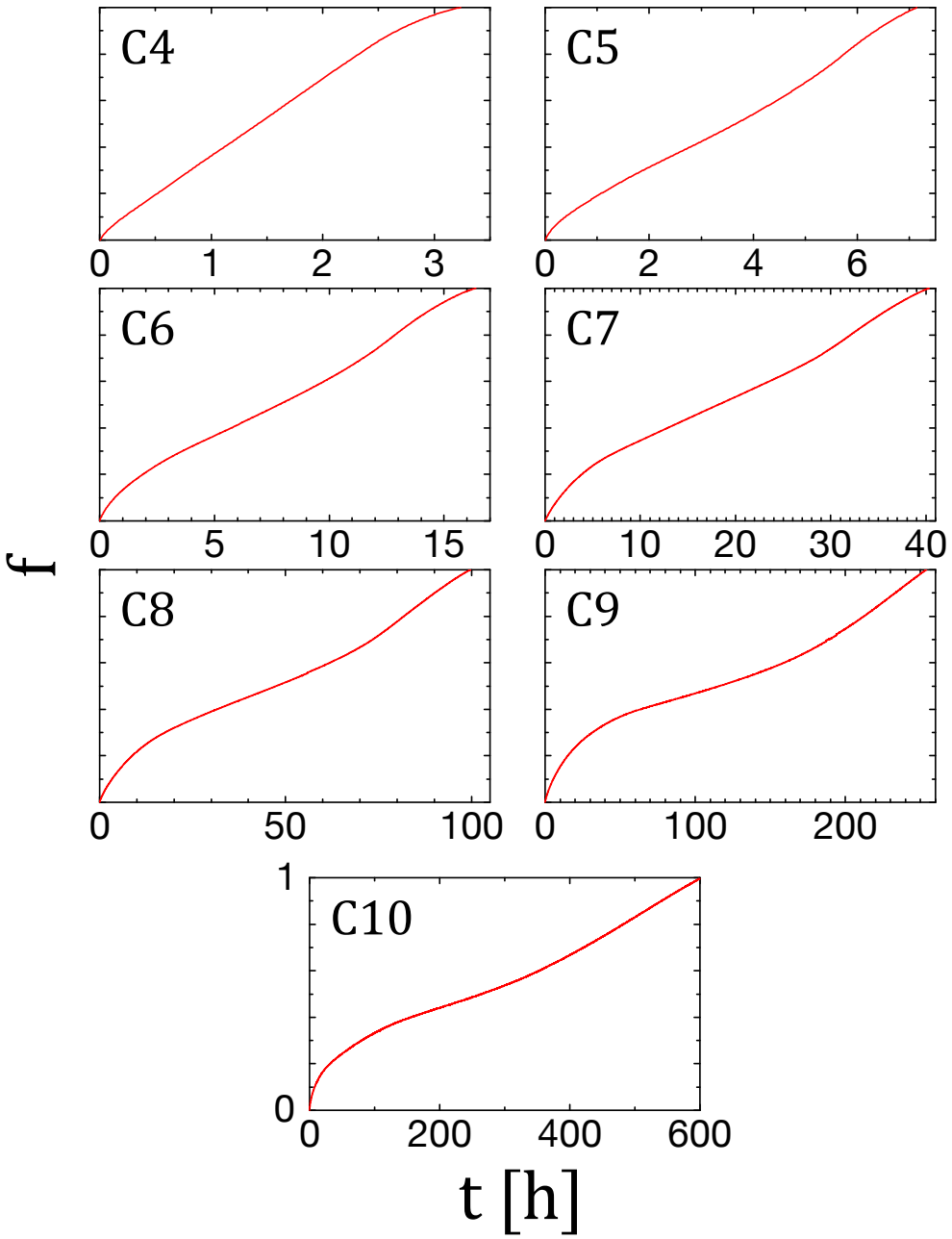

Figure 6.13.: Comparison of vapour uptake rates for n-alcohols. The y axis for each plot is normalized to $[0, 1]$. Depending on the liquid, the individual stages I-III are more or less pronounced in the uptake curves. Also note the critical change in the time scale for the different alcohols involved.

achieved, only the gas phase diffusion remains, resulting in a reduction of total uptake rate. This interpretation is consistent with the observed steps and the approach to a constant diffusion flux in stage I for all alcohols.

Since stage III is supposedly related to liquid transport, the more discernible appearance for long-chain alcohols indicates a larger relative contribution from this mechanism to transport. Again, this is expected as gas-phase diffusion has a smaller overall impact due to the low vapour pressures. A remarkable similarity between all alcohols is the relative filling at the onset for stage III, which is found consistently[1] at $N/N_0 \approx 0.6$. This hints to a critical change in the transport properties for this specific relative filling. As it is independent of the liquid substance, a relation to the pore network properties is suspected, i.e. partial cutoff of pore space, percolation threshold for capillary bridges. Further investigation of this transition in dynamics is needed.

As no analytical description of the total uptake process is possible without specific information on the geometry of the pore network and a relation for the variable diffusivity with the additional adsorbate upon filling, computer simulations could provide an additional insight into this phenomenon. Here, it would be very interesting to compare experimental result with molecular dynamics simulations or comparable deterministic methods for model pore networks that result in a dynamic distribution of molecules. This would offer a means to evaluate the formation of capillary condensate and resulting network alterations as well as the relative flows in the liquid, gas and adsorbate phase, which should be able to test the hypotheses made above.

[1] with the exception of 1-butanol exhibiting no prominent stage III at all

III

Driven and Spontaneous Flow of Liquids in Nanopores

7 Theory of Nanoscale Liquid Flows

7.1. Liquid Transport Equations

7.1.1. The Navier-Stokes Equations for Incompressible Fluids

The basic description of liquid transport on macroscopic scales results from elementary principles of continuum mechanics [89]. In general, fluids are modelled as a mass density distribution, $\rho(\boldsymbol{x}, t)$ exhibiting a local velocity field $\boldsymbol{v}(\boldsymbol{x}, t)$. Then, the product $\boldsymbol{J}(\boldsymbol{x}, t) = \rho(\boldsymbol{x}, t)\boldsymbol{v}(\boldsymbol{x}, t)$ constitutes a mass flux density inside the liquid. Due to the condition of mass conservation, a continuity equation can be formulated as

$$\nabla \boldsymbol{J} = \nabla(\rho \boldsymbol{v}) = \boldsymbol{v}\nabla\rho + \rho\nabla\boldsymbol{v} = -\frac{\partial \rho}{\partial t}. \tag{7.1}$$

In contrast to gas flow, liquids are in good approximation incompressible, hence the mass density ρ is a constant for all times and volume elements, resulting in a simplified form of Eq. (7.1),

$$\nabla \boldsymbol{v} = 0. \tag{7.2}$$

The product $\rho\boldsymbol{v}$ is also equal to a local momentum density $\boldsymbol{p}/V$ of the fluid. In a volume element, changes of this quantity either require a momentum transfer from the surroundings by convection or a net force acting on the liquid. According to Newtonian mechanics, this can be expressed as a momentum conservation law,

$$\frac{\mathrm{d}(\rho \boldsymbol{v})}{\mathrm{d}t} = \rho \left[\frac{\partial \boldsymbol{v}}{\partial t} + (\boldsymbol{v} \cdot \nabla)\boldsymbol{v} \right] = \boldsymbol{f}. \tag{7.3}$$

The force term f corresponds to a density of forces and consists of a superposition of volume forces, e.g. gravitational forces, and surface forces due to a stress tensor between finite fluid elements. This stress tensor is a key difference to gas flows covered in Sec. 5.2: Due to the close proximity of liquid molecules, interactions occur at all times in constrast to a limited interaction on collisions. The resulting internal force on a liquid element splits into normal forces caused by a pressure gradient ∇P as well as viscous forces due to shear stress between neighbouring fluid elements moving with different velocities, which defines a dynamic viscosity η.

Here, only Newtonian liquids with a constant η shall be considered. Using the appropriate form of the individual force terms yields the incompressible Navier-Stokes equation

$$\rho\frac{\partial \boldsymbol{v}}{\partial t} + \rho(\boldsymbol{v}\cdot\nabla)\boldsymbol{v} = -\nabla P + \eta\nabla^2\boldsymbol{v} + \boldsymbol{f}'. \tag{7.4}$$

Here, $\boldsymbol{f}'$ denotes a vector containing the external volume forces. The Navier-Stokes equation as a non-linear partial differential equation can be solved analytically for some initial, boundary conditions and force terms. Depending on the flow specifications, Eq. (7.4) can be further simplified, see Sec. 7.1.2.

7.1.2. Hagen-Poiseuille Flow in Cylindrical Channels

An exact solution of the Navier-Stokes equation can be derived for stationary, pressure driven flow in cylindrical pipes of radius r_0 by applying appropriate assumptions and boundary conditions. Fig. 7.1 depicts this flow geometry.

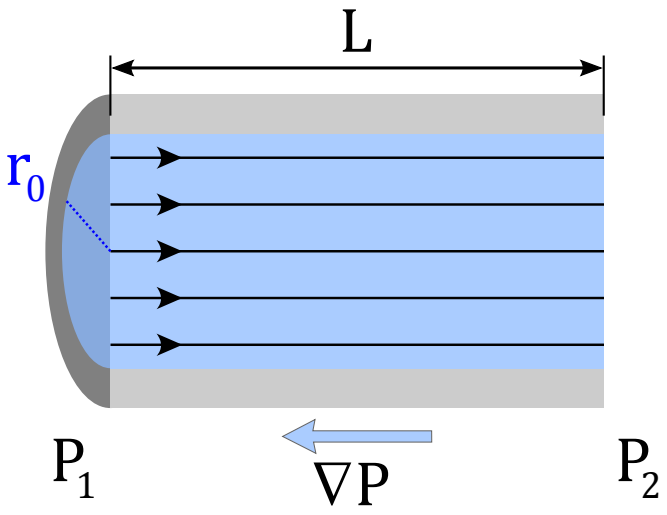

Figure 7.1.: Cross-section of a flow geometry in Hagen-Poiseuille flow. A laminar flow through a cylindrical pore of length L and radius r_0 is driven by an axial pressure gradient ∇P.

The impact of gravity is usually negligible, which is particularly reasonable on micro- and nanoscopic scales. Thus, if no other external forces are expected, the volume force term in Eq. (7.4) can be omitted ($f' = 0$). Moreover, the Reynolds number Re, which is an indicator of turbulence in the flow, also scales with the system dimension. In a nanopore, usually $\mathrm{Re} \ll 1$ can be assumed and laminar flow without turbulences prevails. This enormously simplifies the liquid flow to a linear motion of fluid elements, as illustrated in Fig. 7.1.

In a stationary, fully developed state of flow, the velocity vector field is constant over time and along the pore axis: $\frac{\partial \boldsymbol{v}}{\partial t} = 0$, $\frac{\partial \boldsymbol{v}}{\partial z} = 0$, in cylinder coordinates (r, ϑ, z). Then, only the axial component of the velocity remains as a variable $\boldsymbol{v} = (0, 0, v_z)$. Furthermore, due to the axial symmetry of the problem, it can only depend on the radial position, $v_z = v_z(r)$.

The Navier-Stokes equation, Eq. (7.4), can be rewritten for this situation, since the inertial terms on the left side vanish completely in the steady state:

$$\nabla P = \eta \nabla^2 \boldsymbol{v}. \tag{7.5}$$

This equality of a pressure gradient and viscous forces determines the Poiseuille flow. Eq. (7.5) results in three component equations, two of which lead to the condition $\frac{\partial P}{\partial r} = \frac{1}{r}\frac{\partial P}{\partial \vartheta} = 0$ that limits the pressure gradient to an axial direction. The third equation results in a condition for the velocity profile,

$$\frac{\partial P}{\partial z} = \frac{1}{r}\frac{\partial}{\partial r}\left(r\frac{\partial v_z}{\partial r}\right). \tag{7.6}$$

This equation can be solved by integration given that boundary conditions are defined. One of these directly results from the axial symmetry, $\frac{\partial v_z(r=0)}{\partial r} = 0$. The second condition is determined by the velocity at the walls, which is usually assumed to the 'no-slip' boundary condition $v_z(r = r_0) = 0$ in macroscopic geometries. This can be interpreted as the outermost liquid layer sticking to the static interface. Then, a parabolic velocity profile is found,

$$v_z(r) = \frac{1}{4\eta}\frac{\partial P}{\partial z}\left(r^2 - r_0^2\right), \tag{7.7}$$

which is also depicted in Fig. 7.2(a). Since incompressible fluids result in a linear pressure drop along the flow channel, the pressure gradient can be replaced by the pressure difference $\Delta P = P_1 - P_2$ applied over the length L. The volumetric flow rate $Q = \dot{V}$ in this geometry results from the integration of Eq. (7.7) over the pore cross-section:

$$Q = \frac{\pi}{8\eta}\frac{\Delta P}{L} r_0^4. \tag{7.8}$$

This constitutes the classical Hagen-Poiseuille flow rate equation and is equivalently found as the transport equation of gases in the dense limit, see Sec. 5.2.2. Notably, as this flow rate scales to the fourth power of the radius r_0, the liquid throughput in nanoporous solids is reduced substantially and dynamics on the nanoscale exhibit substantially larger time-scales, e.g. spontaneous imbibition, see Sec. 9.

In light of the continuum approach in the derivation of Eq. (7.8), it should be discussed

whether this is an adequate description of flows in the order of 1 to 10 nm. The Navier-Stokes equation implicitly relies on the fact that infinitesimal volume elements still contain a large number of fluid molecules, so that the definitions of continuum properties such as density and viscosity are reasonable. Contrary to this, nanoscopic flow geometries are comparable to typical molecular dimensions: 1-butanol has an approximate van-der-Waals radius of $r_A = 255\,\mathrm{pm}$, which amounts to $\approx 5\,\%$ of the Vycor pore radius. Although this means that only an order of tens of molecular layers partakes in total flow, experimental transport rates in nanopores match the expectation for scaled macroscopic theory [90]. Viscosity in particular has been observed to be robust on small length scales down to $\approx 3.5\,\mathrm{nm}$ [91, 92].

7.1.3. Slip Flow

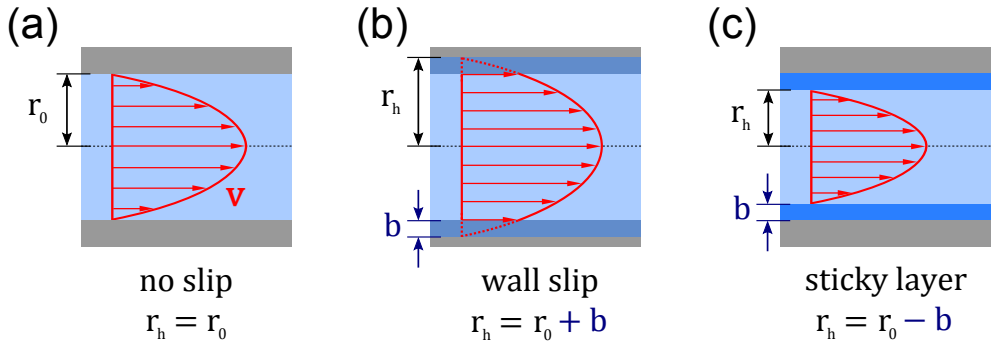

Figure 7.2.: Illustration of different boundary conditions in pipe flow. (a) no-slip boundary condition, (b) finite velocity slip on the walls, (c) sticking wall layer of finite thickness reduces pipe radius.

In nanofluidics, effects in the boundary layer closest to the solid interface have a significant influence on total flow in the pore. Depending on the specific interaction between molecules in the liquid and the pore wall, two different phenomena on the interface are observed: In systems with limited wetting or partial fluid repulsion due to a low specific interaction potential, the flow velocity is greater than zero on the interface [93, 94]. Conversely, for strongly interacting fluids, an immobilization of a finite layer and thus a constriction of the flow geometry is expected [95]. For the flow of n-alcohols in Vycor, the second case is expected as a consequence of the monolayer strongly adhering to the pore walls, as found in Sec. 4.3.5.

These effects in the velocity profile can be incorporated into a slip boundary condition

$$v_z(r_0 + b) = 0, \tag{7.9}$$

where b is the slip length as illustrated in Fig. 7.2(b)-(c). For sticking wall layers, b is negative,

for finite slippage of the wall layer, b is positive.

Then, Eqs. (7.7) and (7.8) can be corrected by simply replacing r_0 with the corrected 'hydraulic' radius $r_h = r_0 + b$,

$$Q = \frac{\pi}{8\eta}\frac{\Delta P}{L}(\underbrace{r_0 + b}_{r_h})^4. \tag{7.10}$$

Due to the scaling to the fourth power of the radius, the effect in flow rate is detectable in flow experiments on the microscale [96, 97].

7.2. Liquid Flow in Porous Solids

7.2.1. Network Model for Liquid Flow

Pressure driven liquid flow and diffusion inside a nanoporous solid are closely related phenomena. This was already shown in Sec. 5.2.2, where hydrodynamic gas flow was described using a Hagen-Poiseuille flow equation and a viscous diffusivity could be defined according to Eq. (5.15).

This analogy in transport can be exploited for liquids: The concept of a tortuosity factor introduced in Sec. 5.3.2, which relates a complex network to an idealized situation of independent pores, applies equally to liquids. Given that a nanoporous solid has a constant cross-sectional area along the flow direction, the total flow rate can be expressed as the combined flow of N parallel, straight, and identical pores with the mean pore geometry,

$$Q_{\text{eff}} = \frac{N}{\tau}\bar{Q}_{\text{pore}}. \tag{7.11}$$

As a parameter that only results from the pore network topology and pore morphology, τ is expected to be constant and equal to the value introduced for transport diffusion in Sec. 5.3.2, $\tau = 3.6$. For the assumed constant cross-sectional area A of a porous sample, the number of pores N is determined by the volume porosity Φ and the mean pore radius r_0,

$$N = \frac{\Phi A}{\pi r_0^2}. \tag{7.12}$$

Combining Eqs. (7.11) and (7.12) and using the slip flow rate from Eq. (7.10) yields the total flow rate in nanoporous solids

$$Q_{\text{eff}} = \frac{\Phi}{8\tau}\frac{\bar{r}_h^4}{r_0^2}\frac{A}{\eta}\frac{\Delta P}{L}, \tag{7.13}$$

with L denoting the length of the macroscopic sample in the direction of the flow and $\bar{r}_h$ as

the mean hydraulic radius of the pore ensemble.

7.2.2. Darcy's Law

A phenomenological formulation of flow through porous media originates from the empirical proof that the flow rate scales linearly with the applied pressure difference ΔP. Then, a single parameter κ characterizes the liquid throughput in a porous solid of a defined geometry (cross-sectional area A and length L in flow direction) according to Darcy's law,

$$Q = \frac{\kappa A \Delta P}{\eta L}. \tag{7.14}$$

This so-called 'hydraulic permeability' κ can be determined experimentally, even for complex pore shapes and network topologies [98].

By comparison with the previous considerations, Hagen-Poiseuille flow in tortuous, cylindrical pores is a special case of Darcy's law. The hydraulic permeability can then be extracted from Eq. (7.13),

$$\kappa_{\mathrm{HP}} = \frac{\Phi}{8\tau} \frac{\bar{r}_h^4}{r_0^2}. \tag{7.15}$$

8 Stationary Flow Experiments with n-Alcohols

8.1. Outline

As shown in the previous chapter, the stationary flow in porous media reflects both the microscopic flow geometry (hydraulic radius) as well as the characteristic properties of the pore network (porosity, tortuosity). When applying a constant pressure difference to a fixed flow geometry of a porous solid under controlled conditions, a constant volumetric flow rate is expected over time. When using Darcy's law as a description of flow, see Eq. (7.14), the only free parameter is the hydraulic permeability of the matrix. Due to the cylindrical pore geometry and known matrix parameters Φ, r_0 and τ of Vycor, Eq. (7.15) provides an insight into the hydraulic radius which in turn depends on microscopic interactions on the pore walls.

In this chapter, different n-alcohols are compared as flowing liquids ($n \in \{4, 6, 8, 10\}$). Due to H-bonding to the hydrated silica surface, the n-alcohols exhibit strong interactions with the solid pore walls, which should then result in a negative slip length and a reduced overall permeability that is detectable in the flow rate. Another goal in these experiments is to test whether the hydraulic permeability shows systematic variations with the flow rate, which would indicate a reaction of the wall layer to the shear stress exerted by the liquid phase.

Some of the experiments shown were also covered in [99], but due to an erroneous pore size determination, the interpretation needs to be corrected.

In addition to the flow rate measurement, dielectric spectroscopy can be performed on the porous solid containing the flowing liquid. Here, the goal is to detect whether the flow impacts the dielectric spectra, e.g. due to flow-induced inhibition of dipole reorientation in the pore volume or on the pore walls.

8.2. Experimental Methods

8.2.1. Forced Throughput Apparatus

The experimental study of pressure driven flow was carried out in a custom design, high-pressure setup as depicted in Fig. 8.1, see also [99]. The basic functionality of this appar-

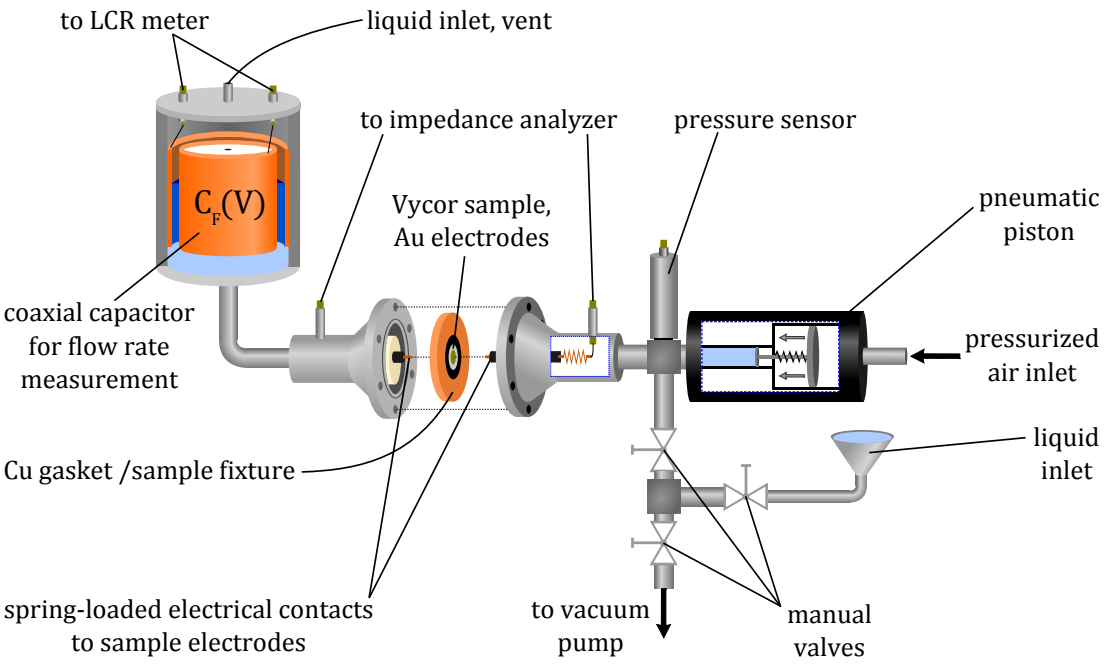

Figure 8.1.: Setup for forced throughput experiments, see text for a detailed description. In order to ensure thermal stability, the setup is enclosed in a thermally insulating box when in use.

atus comprises pressure generation and measurement on the inlet (high-pressure) side which causes drainage of liquid into the outlet (low-pressure) side via a nanoporous Vycor membrane. The outlet is kept on ambient pressure so that a constant pressure gradient can be maintained. The flow rate is measured by tracking the absolute amount of liquid on the low-pressure side. Moreover, the setup features an additional electric contacting for *in-situ* dielectric spectroscopy on the porous sample.

Due to the low hydraulic permeability of nanoporous solids, considerable pressure gradients are needed to ensure a measurable flow rate. A pneumatic piston of type *Kostyrka 1410.30* is used to generate the driving pressures by translating a supplied input pressure of compressed air into a 17 times amplified output pressure of up to 100 bar on a liquid reservoir on the high-pressure side. This liquid pressure was continuously monitored using a capacitive, relative pressure sensor. As found for a similar setup used by Gruener [48], the separation of pressurized gas and liquid is crucial to prevent gas dissolution and subsequent precipitation on the low pressure side, which artificially increases the volume flow rate. In order to avoid the same effect for entrapped air bubbles, the high-pressure side can be evacuated to pressures $< 1\,\mathrm{mbar}$ prior to liquid insertion. As for the dissolved gases in the alcohols, the concentrations are in an equilibrium state for ambient pressures, so that precipitation at

higher pressures should not occur.

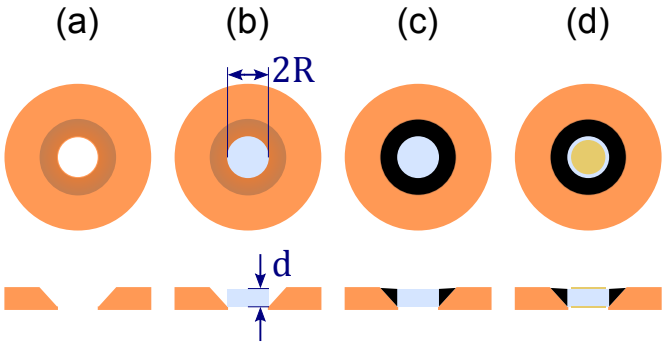

Figure 8.2.: Sample preparation for forced throughput experiments. Top view and cross-section. (a) sample fixture is copper gasket between the high and low pressure sides, (b) cylindrical Vycor sample (radius $R = 7\,\mathrm{mm}$, variable depth d, see App. A) is mounted in the bore hole, (c) sample is fixed and sealed with epoxy resin, (d) with sputter coated circular gold electrodes.

The cylindrical porous sample (radius $R = 7\,\mathrm{mm}$, variable depth $d \approx 2$ to $6\,\mathrm{mm}$, see App. A) is placed as the connecting membrane between the high and low pressure sides as depicted in Fig. 8.2. Samples are mounted within a tapered bore hole in a copper gasket and subsequently encapsulated with epoxy resin *Stycast 2850 FT*, leaving only the parallel, circular faces open. This ensures a tight sealing of the sample sides under the extreme pressure conditions as well as no liquid leakage through macroscopic slits[1]. In this geometry, liquid only passes through the porous cylinder axially, the sample cross-section is constant along the flow direction and Darcy's law applies, see Sec. 7.2.2.

By sputter coating concentric, circular gold electrodes to the parallel faces of the sample, a plate capacitor is formed for dielectric spectroscopy, see Fig. 8.2. As mentioned in Sec. 2.1.3, the sputter coated layer does not hinder liquid flow into the porous sample. Both capacitor plates are contacted to outside connections and an impedance analyzer *Agilent 4294* is used to periodically measure a complex impedance spectrum for a frequency range from $\nu = 1\,\mathrm{kHz}$ to $2\,\mathrm{MHz}$.

The low-pressure outlet side consists of a liquid recipient with an integrated cylindrical, coaxial capacitor (inner plate radius $r_i = 39.0\,\mathrm{mm}$, outer plate radius $r_o = 39.5\,\mathrm{mm}$, height $h = 60\,\mathrm{mm}$). A volume flow through the porous membrane then pushes liquid into the interstitial plate space. The increase in capacitance resulting from the higher dielectric constant of the liquid is measured in a fixed time interval using an external LCR meter *Hameg HM8118* at $\nu = 200\,\mathrm{kHz}$ with an accuracy of $\pm 0.01\,\mathrm{pF}$. Due to the high relative permittivity of the li-

[1] This was assessed experimentally by replacing Vycor with a solid cylinder, resulting in no measurable flow rates.

quids used, this allows for very precise measurements of flow rates in the order of $\sim 0.01\,\mathrm{nl/s}$. Prior to an experiment, the low pressure side is manually filled with liquid, so that the flowing liquid immediately reaches the capacitor. Here, great care has to be taken to avoid entrapped air bubbles. However, by applying a moderate pressure $P \approx 15\,\mathrm{bar}$ over several days, the system can be flushed in preparation of an experiment, gradually removing the air pockets.

It should be noted that there are a few limitations with this experimental setup: Due to the limited mechanical stability of Vycor glass discussed in Sec. 2.1.3, the samples are prone to cracking. As a consequence of this critical failure, only a limited range of pressure gradients is accessible using this experimental technique. Furthermore, due to the vent on the low pressure side, liquid can slowly evaporate from the capacitor for volatile substances. In the experiments in this work though, only 1-butanol exhibited a significant rate of evaporation in the order of $\approx 10\,\%$ of the lowest measured flow rate. However, it needs to be quantified for accurate flow rate calculations.

8.2.2. Calibration measurements

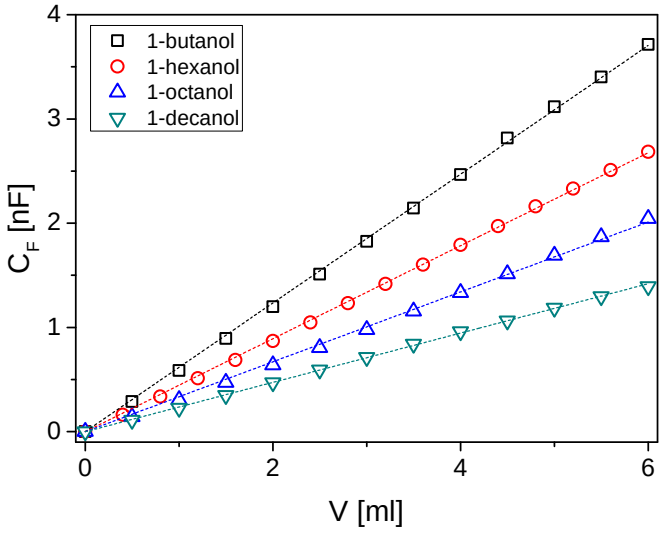

Figure 8.3.: Calibration of flow rate capacitance in forced throughput apparatus. A linear relation between the filling and the capacitance is found for a volume range of $\approx 6\,\mathrm{ml}$. The dashed lines correspond to the respective fits.

The conversion between change in capacitance and flow rate requires a calibration of the cylinder capacitor in relation to the amount of liquid inserted. This was achieved by step-wise manual filling with defined portions of liquid and evaluation of the resulting capacitance. A linear increase is measured for all liquids within a volume range of $\approx 6\,\mathrm{ml}$, as depicted in Fig.

8.3. Note that the capacitance at the beginning of the linear range (= empty capacitor + liquid in the stray field) has been offset to $C_F(V = 0) = 0$ for better comparison of the calibration curves.

From the inverse slopes of the linear fits in Fig. 8.3, a calibration coefficient $k_C = \Delta V/\Delta C_F$ can be extracted that relates the absolute volume of liquid and the resulting capacitance,

$$V = k_C C_F. \tag{8.1}$$

The results for k_C obtained from the calibration measurements are listed in Tab. 8.1.

Table 8.1.: Flow rate calibration coefficients in forced throughput experiments.

liquid	**flow rate coefficient** k_C [ml/nF]	**uncertainty** δk_C [ml/nF]
1-butanol	1.592	± 0.005
1-hexanol	2.21	± 0.005
1-octanol	2.878	± 0.015
1-decanol	4.184	± 0.005

8.2.3. Experimental Procedure

In a typical stationary flow experiment, the flow rates were measured as a function of pressure for pressures from $P = 10\,\mathrm{bar}$ to $100\,\mathrm{bar}$ or to the point of sample breakage. In the process, a fixed pressure was applied over a certain amount of time, resulting in a continuous increase of the capacitance C_F.

Exemplary results are depicted for 1-octanol in Fig. 8.4. When changing the applied pressure, a minute, quasi-instantaneous step in capacitance on the low-pressure side is observed which is interpreted as a physical deformation of the membrane, see the very beginning and end of Fig. 8.4(b). Besides these discontinuities, a linear increase in capacitance was observed over time. In comparison to results from Gruener [48] who exhibited frequent passage of dissolved gas bubbles and resulting artifacts in the flow rate signal, this is a significant improvement of experimental conditions.

In order to gain flow rates from the capacitance data, a linear fit is applied to the respective segments of $C_F(t)$ for a constant pressure, and the average pressure P in this time range is calculated. Both results are depicted as a red and purple line in Fig. 8.4(b), respectively. Using the calibration coefficients k_C from Sec. 8.2.2, the slopes $\Delta C_F(t)/\Delta t$ can then be evaluated

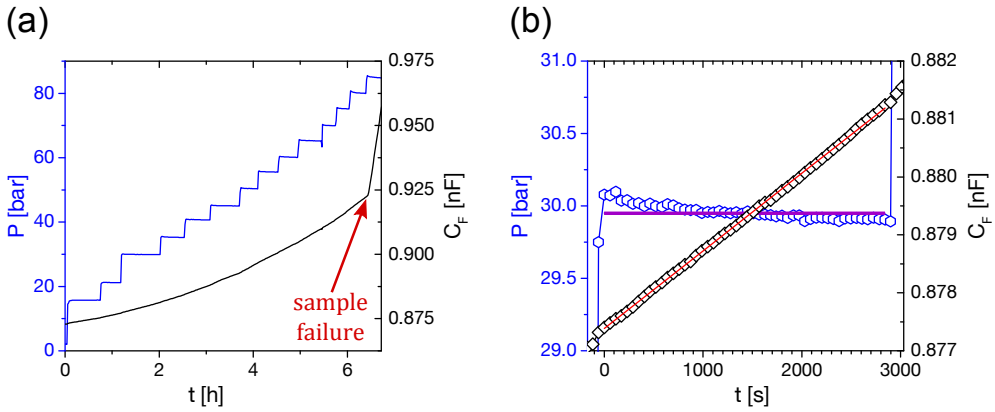

Figure 8.4.: Pressure and flow capacitance during a stationary flow experiment: (a) overview of all pressure steps and corresponding increase in C_F with critical failure at the last pressure step, (b) details for a single step with included mean pressure (purple line) and linear fit to flow (red line). The small steps in C_F when increasing the pressure are interpreted as differences in mechanical strain with increased loading.

to an average volume flow rate

$$Q = \frac{\Delta V}{\Delta t} = \frac{k_C \Delta C_F}{\Delta t}. \tag{8.2}$$

A corresponding mean velocity in the pore space, $\bar{v}$ then results from the network flow model in Eq. (7.11):

$$\begin{aligned} Q &= \frac{N}{\tau} \pi r_0^2 \bar{v} \\ \Leftrightarrow \bar{v} &= \frac{\tau}{\phi A} Q. \end{aligned} \tag{8.3}$$

For 1-butanol, the measured flow rate Q has to be corrected for the evaporation of liquid from the low-pressure side of the setup. Hence, a control measurement with no pressure difference has been conducted over three days. A nearly linear decrease in capacitance was observed, as depicted in Fig. 8.5. Analogous to Eq. (8.2), the slope can be interpreted as a flow of $\delta Q_{\text{evap,C4}} = -0.84\,\text{nl/s}$, which corrects the total flow rate,

$$Q' = Q + \delta Q_{\text{evap}}. \tag{8.4}$$

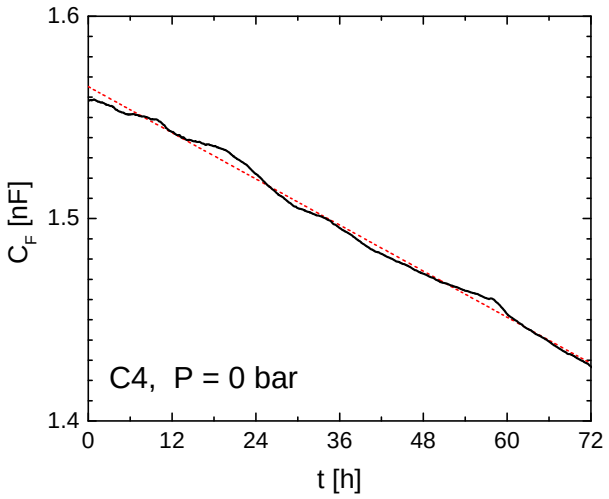

Figure 8.5.: Evaporation of 1-butanol in forced throughput apparatus. When no pressure difference is applied to the liquid, the capacitance gradually drops due to evaporation of liquid. A linear drop over time is found, the slope of which can be multiplied with k_C to gain a flow rate correction $\delta Q_{\text{evap,C4}}$.

8.3. Results and Discussion

8.3.1. Comparison for n-alcohols

The experimental flow rates for different alcohols are shown as a function of pressure in Fig. 8.6. For all liquids, the qualitative results confirm the premise of Darcy's law, i.e. a linear increase of volume flow with the applied pressure. This answers one of the questions in this experimental part: In the pressure range of the experiments, there are no detectable, systematic changes in the flow boundary condition causing a modified transport rate. This indicates that the boundary layer at the solid-liquid interface is in a stable configuration in the presence of a stationary flow for the present flow rates.

Based on Eq. (7.14), a linear fit of the experimental data can be used to quantify the hydraulic permeability for all alcohols, see solid lines in Fig. 8.6. According to the sample dimensions (see Fig. 8.2), the length L of the flow geometry is identified as the sample thickness d, the cross-sectional area is equal to a circular area $A = \pi R^2$ with the sample radius $R = 7\,\mathrm{mm}$. Then, a mean value for κ can be calculated in all experiments from the slope k_F of the linear fits in Fig. 8.6,

$$\kappa = \frac{d\,\eta}{\pi R^2} \underbrace{\frac{\Delta Q}{\Delta P}}_{k_F}. \tag{8.5}$$

Numerical values of κ for the individual n-alcohols are listed in Tab. 8.2.

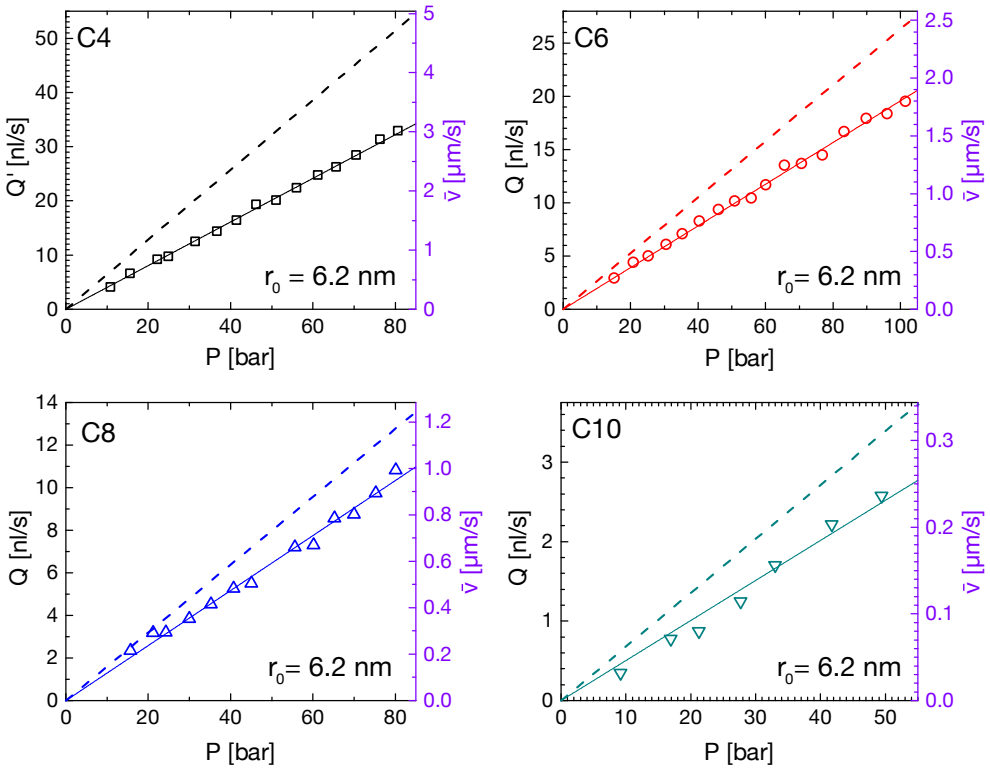

Figure 8.6.: Stationary flow rates (and equal mean pore velocities, see Eq. (8.3)) for different pressures and liquids. Uncertainties are in the order of symbol sizes. In all graphs, the experimental data confirms a linear relation between flow rate and pressure, thus a linear fit corresponding to Darcy's law has been applied (solid lines). When comparing to theoretical flow rates with no-slip boundary condition (Eq. (8.6), dashed lines), the measured flow rates are considerably lower, indicating an interfacial effect due to strong molecular interactions.

In comparison to the experiment, a theoretical relation for a no-slip boundary condition ($r_h = r_0$) is calculated using Eqs. (7.14) and (7.15). In the above situation, the theoretical no-slip flow rate in the nanoporous solid corresponds to

$$Q_{\text{no-slip}} = \underbrace{\frac{\Phi r_0^2}{8\tau}}_{\kappa_{\text{no-slip}}} \frac{\pi R^2}{\eta} \frac{P}{d}. \tag{8.6}$$

Obviously, $\kappa_{\text{no-slip}}$ is a constant that only depends on the matrix parameters (pore size, tortuosity, porosity). For the Vycor samples used for these experiments ($r_0 = 6.2\,\text{nm}$, $\tau = 3.6$, $\Phi = 0.255$), $\kappa_{\text{no-slip}} = 0.3404\,\text{nm}^2$ could be calculated. A plot of Eq. (8.6) is also included as a dashed line for each liquid in Fig. 8.6. As expected for a sticking boundary layer, the

Table 8.2.: Mean hydraulic permeabilities and slip lengths of forced throughput experiments.

liquid	**hydraulic permeability** κ $[\mathrm{nm}^2]$	**slip length** b $[\mathrm{nm}]$
1-butanol	0.213 ± 0.005	-0.68 ± 0.03
1-hexanol	0.253 ± 0.005	-0.44 ± 0.04
1-octanol	0.275 ± 0.007	-0.32 ± 0.07
1-decanol	0.253 ± 0.010	-0.44 ± 0.18

experimental hydraulic permeabilities and flow rates exhibit considerably lower values for all applied pressures. Hence, Darcy's law with slip-boundary condition as described in Eqs. (7.14) and (7.15) can be used to determine the (negative) slip length b,

$$Q = \frac{\pi R^2 \Phi}{8\eta\tau} \frac{(r_0 + b)^4}{r_0^2} \frac{P}{d} \tag{8.7}$$

$$\Leftrightarrow b = r_0 \left(\sqrt[4]{\frac{8\eta\tau d}{\pi R^2 r_0^2 \Phi} \frac{Q}{P}} - 1 \right) \tag{8.8}$$

The results for the individual data points are shown in Fig. 8.7 and compared to the molecular dimensions of the respective alcohol (shaded areas), see App. B.

For all alcohols, the experimental slip lengths are negative and in the order of magnitude of typical molecular geometries, confirming the hypothesis of a sticking molecular layer. In line with the corresponding flow rates, no systematic variation of slip length with the applied pressure is found. Hence, in the following, only the average slip lengths for the alcohols will be compared, as listed in Tab. 8.2. In compliance with the analysis of Gruener [48], these have been calculated from the slope $\Delta Q/\Delta P$ of linear fits in Fig. 8.6 using Eq. (8.8).

Before further discussing these results, it should be noted that with this experimental technique, only an effective slip length in spatial averaging is accessible on the macroscopic scale. This does not allow the determination of exact microscopic structures or local variations thereof. Still, the absolute value for b can be compared to the molecule geometry of the involved compounds, which provides a good reference for the average make-up of the surface layer. Differences between individual liquids can be interpreted accordingly.

With this in mind, the results for hexanol, octanol and decanol exhibit a very similar slip length. The numerical values are in reasonably good agreement to a flat molecular layer of alcohols on the surface $b_{\mathrm{C,flat}} \approx -0.4\,\mathrm{nm}$, assuming homogeneous coverage. However, due to the large uncertainty in the matrix parameters (pore size, tortuosity), the uncertainty in slip

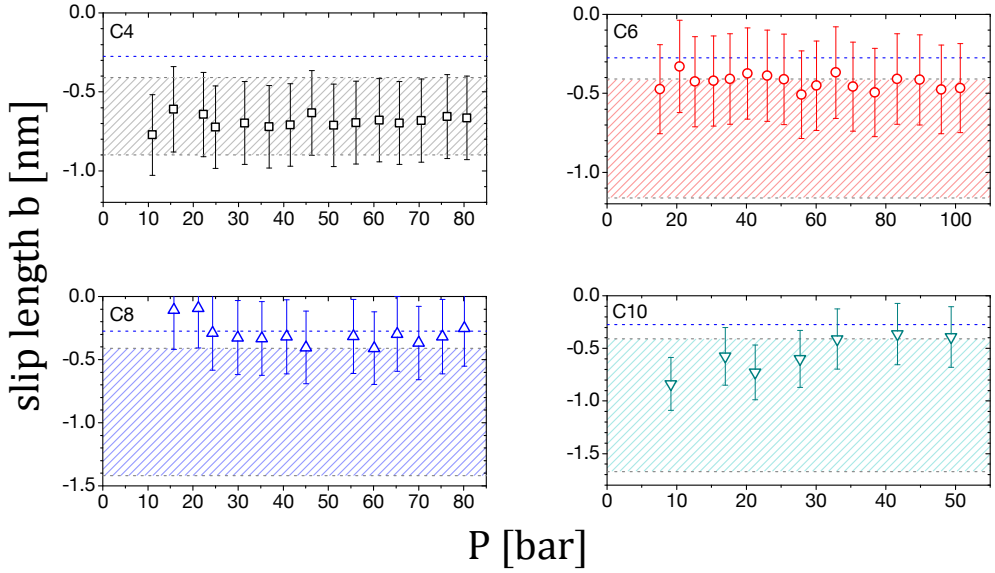

Figure 8.7.: Slip length of stationary flows for different n-alcohols and pressures in Vycor pores of radius $r_0 = 6.2\,\mathrm{nm}$. The results show a good match to the range of molecular dimensions (molecule width w to length l, see App. B), which are shown as shaded areas in the respective graph. Moreover, a typical thickness of a water monolayer (which is expected as the main contaminant) is shown in comparison as a blue dashed line.

lengths is quite large. Thus, a monomolecular layer of water ($b_{H_2O} \approx -0.275\,\mathrm{nm}$) could also explain these findings within the error margin, see the blue dashed lines in Fig. 8.7. Since the samples in these experiments were not treated at temperatures $T > 190\,^\circ\mathrm{C}$ [23], a water monolayer is an expected contaminant for all alcohols on the solid interface. Assuming that both the alcohol and water molecules are competing for the adsorption spots on the surface, the interfacial layer then consists of a combination of both molecular species, resulting in a local variation of the layer thickness. Thus, effective values $b_{H_2O} < b < b_{C,flat}$ are also very plausible and consistent with expectations.

Interestingly, the smallest molecules (1-butanol) exhibit the lowest slip lengths of all alcohols. While still comparable to molecular dimensions of 1-butanol, this could also hint to a multilayer sticking, contrary to other alcohols. Two possible configurations shall be mentioned: a stacked layer of water and butanol (as is plausible for a residual water monolayer from sample preparation) and the local formation of butanol multilayer clusters, see Fig. 8.8.

In experiments on planar silica, it has been observed experimentally that short-chain alcohols like ethanol form H-bonded macroclusters to hydroxylated silica in a static situation [100]. A similar arrangement is conceivable for stationary flow in nanopores if molecular interactions are sufficiently strong compared to shear stress. Indeed, a short-range order on the

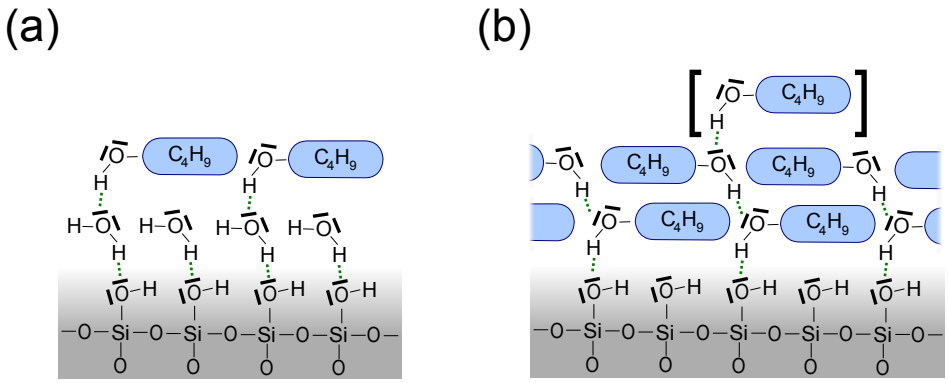

Figure 8.8.: Possible structures of butanol interface layer. (a) Stacked layer of H-bonded water and butanol (b) butanol multilayer clusters, H-bonded in alternating directions, as proposed by Mizukami et al. for ethanol on planar surfaces [100].

surface and multilayer sticking of strongly interacting molecules was also confirmed in MD simulations for cylindrical pores [101].

At first, this seems to contradict the hypothesis of autophobicity of the monolayer from equilibrium gas sorption experiments (see Sec. 4.3.6). There, the directional H-bond of the interfacial layer resulted in a partial repulsion of the second molecular layer upon dynamic capillary condensation. However, for stationary liquid flow, the entire pore is already populated with butanol molecules which is accompanied by a shift in the interaction potential landscape. As a result, a multilayer cluster could present a second stable configuration of the boundary layer.

A comparison of all proposed boundary layer configurations for 1-butanol is depicted in Fig. 8.9. A best match to the experimental data is observed for a stacked layer of water and butanol ($b_{\mathrm{C4+H_2O}} = 0.685\,\mathrm{nm}$). Notably, this is consistent with the monolayer thickness observed for equilibrium adsorption ($t_{\mathrm{ML+H_2O}} = 0.75 \pm 0.10\,\mathrm{nm}$), see Sec. 4.3.5.

The difference in boundary conditions for the different alcohol chain lengths could indicate a dynamic desorption and elution of the residual water monolayer with the continuous flow of alcohol through the pores. Analogous to gas phase sorption, an equilibrium concentration in liquid solutions is reached by dynamic ad- and desorption on the pore wall. For long-chain alcohols, which exhibit a low concentration of water as a contaminant due to low solubility [102], a partial desorption of the residual water monolayer from sample preparation and co-adsorption of n-alcohols would explain the intermediate slip lengths. In contrast to this, 1-butanol has a high solubility for water and is hygroscopic [102], so that the intrinsic water concentration is potentially high enough to maintain a full water monolayer. In analogy to

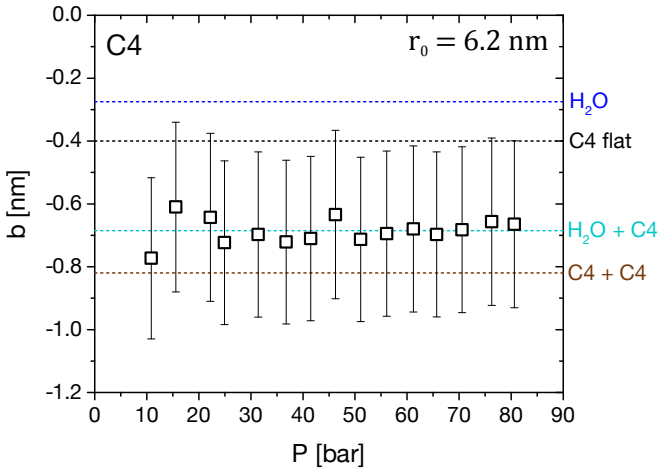

Figure 8.9.: Comparison of 1-butanol slip lengths to different surface layers (dashed lines). From top to bottom: water monolayer (H_2O), flat butanol monolayer (C4 flat), stacked water and butanol as depicted in Fig. 8.8(a) (H_2O+C4) and butanol double layer (C4+C4) as depicted in Fig. 8.8(b).

equilibrium adsorption, an alcohol monolayer can then only adsorb on top of this strongly bound water layer.

8.3.2. Dependence on pore size

For 1-butanol, stationary flow was also probed for a smaller pore size $r_0 = 3.1\,\mathrm{nm}$. With regards to the discussion in the previous section, this experiment can determine whether the structure of the butanol interfacial layer depends on the geometric confinement.

Measured flow rates are depicted in Fig. 8.10(a) and compared to the no-slip prediction (dashed line). Qualitatively, the behaviour is analogous to large pores: A linear relation between pressure and flow rate at a lower slope than the no-slip prediction. Using Eq. (8.8), slip lengths have been calculated, see Fig. 8.10(b). An average value $b(r_0 = 3.1\,\mathrm{nm}) = -0.24 \pm 0.06\,\mathrm{nm}$ has been calculated from the slope of the linear fit in Fig. 8.10(a). This value is in good agreement to a water monolayer, as depicted by the blue dashed line.

In comparison to the value for larger pores, see the red dashed line in Fig. 8.10(b), the measured slip length in smaller pores indicates a smaller extent of the sticking layer. This result is contradictory to findings by Gruener [48], who reported smaller slip lengths for smaller pores for the flow of water and n-hexane, although admittedly, experimental complications due to segregation of dissolved gas could not be ruled out as a factor influencing these results. As this problem does not occur in the present experimental setup, it is advisable that the stationary flow experiments with non-polar alkanes should be revisited.

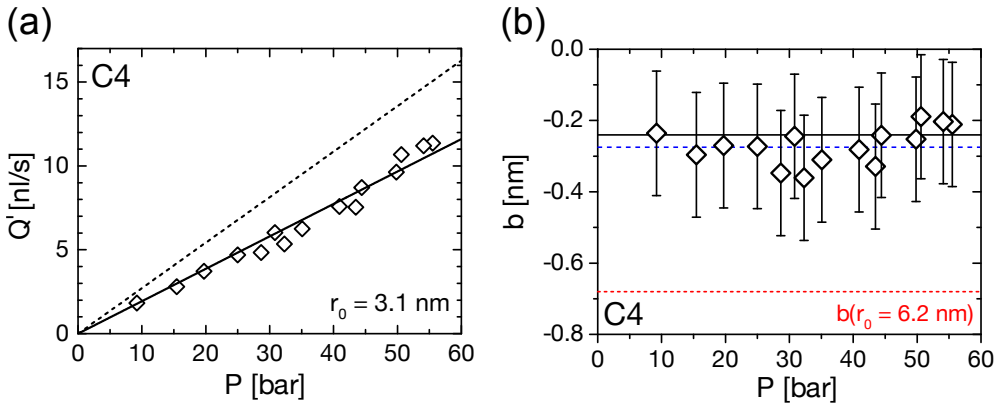

Figure 8.10.: Flow rates and slip lengths of stationary flows for butanol in small pores. (a) Experimental flow rates (◇) with linear fit and theoretical no-slip prediction (dashed line). (b) Slip lengths and average value (black line) in comparison to a water monolayer (blue dashed line) and the average value from larger pores (red dashed line).

The difference in effective slip length between both pore sizes amounts to $\Delta b = 0.45\,\mathrm{nm}$, which is in good agreement to a flat layer of butanol molecules. This supports the hypothesis of a transition from a boundary condition with multilayer sticking in large pores to monolayer sticking in small pores. In this interpretation, the detachment of the butanol layer from the water monolayer for smaller pores can be interpreted as a result of a modified rheology. As fewer molecular layers contribute to flow, the local shear stress could exceed the attractive forces on the interface which allows a collective flow of this layer. Here, a more in-depth investigation of the effect of pore size on the stationary boundary condition is needed.

8.3.3. Dielectric results

During the stationary flow experiments, dielectric spectra were continuously recorded as real and imaginary parts of the sample impedance $Z^*(\nu) = Z'(\nu) + iZ''(\nu)$. As shown in Sec. 4.1.2, these can be converted to a real and imaginary part of the permittivity $\varepsilon^*(\nu) = \varepsilon'(\nu) - i\varepsilon''(\nu)$ using the geometric capacitance $C_0 = \varepsilon_0 A_{\mathrm{el}}/d$. Here, as the electrodes area A_{el} is smaller than the sample faces (to avoid short-circuiting with the copper sample fixture), a small contribution of the stray field remains in the measured spectra despite a calibration procedure for the sample fixture, see App. C. This however does mainly impact the absolute values of the spectra, which are disregarded in this section. Any relative changes in the complex permittivity of the liquid inside the pores, e.g. sufficiently strong correlations between dipolar mobility and the flow velocity, should result in an equal effect in the stray field and thus in a proportional change in the spectra.

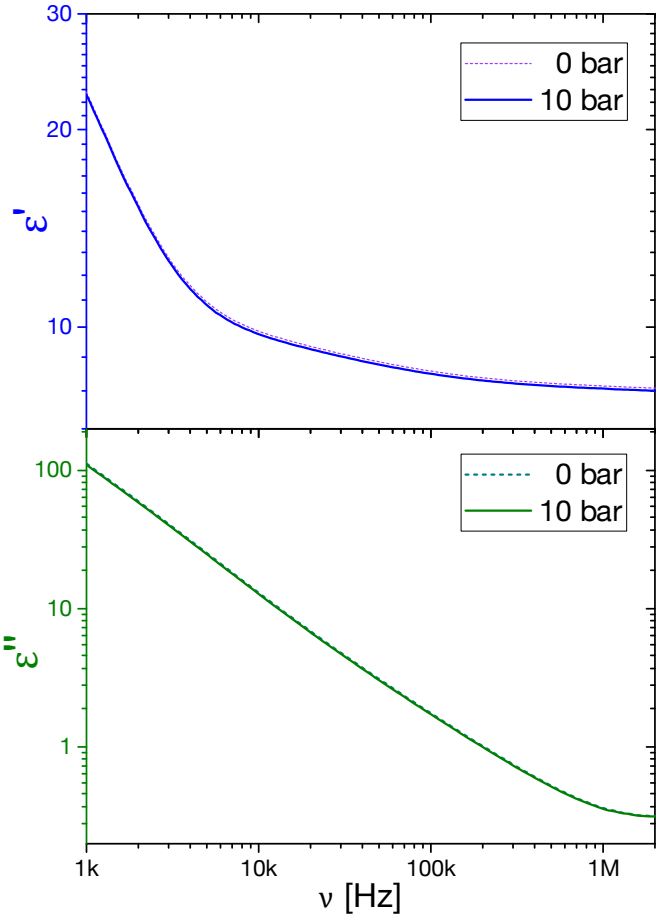

Figure 8.11.: Spectra of 1-octanol in Vycor with and without applied pressure at room temperature $T = 294\,\mathrm{K}$. Only a small change in the real permittivity could be detected that results from the mechanical deformation of the membrane.

A typical spectrum of 1-octanol in Vycor is depicted in Fig. 8.11, for zero velocity and shortly after enabling a pressure of $P = 10\,\mathrm{bar}$. Both spectra exhibit the characteristics discussed in Sec. 2.3.2: High conductivity induces high values of ε' and ε'' towards lower frequencies and for high frequencies, the real part approaches a plateau value. When comparing the situations with and without applied pressure, only a very small difference between the real parts is noticeable. In the experiment, it occurs instantaneously when switching on the pressure. As the compressibility of the liquid is only minute, this effect is attributed to a mechanical deformation of the membrane.

Over the course of several days in the experiment, a gradual, asymptotic shift in both the real and imaginary parts could be measured, which shows no correlation to the applied pres-

sure but rather a time dependence. For different liquids, both increasing and decreasing permittivities could be detected. This is shown for a fixed frequency of $\nu = 1\,\mathrm{MHz}$ in Fig. 8.12

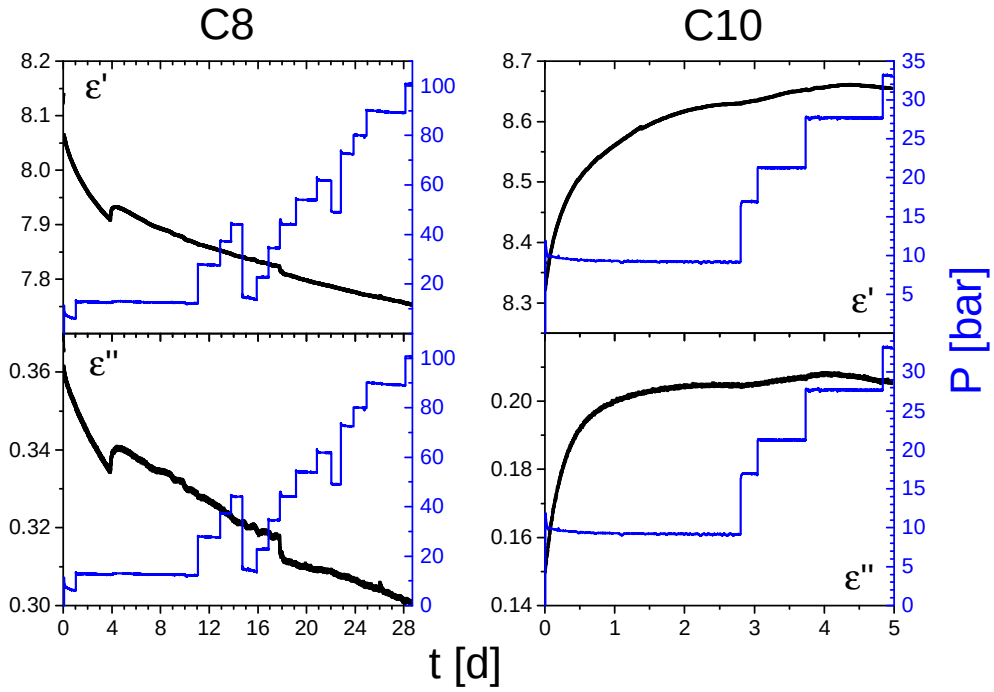

Figure 8.12.: Complex permittivity over time during stationary flow of octanol and decanol, for a fixed frequency $\nu = 1\,\mathrm{MHz}$.

Regarding the slow time scales and the independence of pressure, it is most likely that the observed shifts are due to a parasitic contribution rather than a flow-induced effect on dipolar mobility. Here, the spectra in Fig. 8.11 give a clue to a possible reason: The conductivity in these experiments is so large that the high-frequency plateau in ε' is not completely reached at $\nu = 1\,\mathrm{MHz}$. Any change in conductivity then results in the same qualitative changes in the real and imaginary parts, as observed experimentally.

As introduced in Sec. 2.3.2, the conductivity of alcohols directly relates to the concentration of ions in the liquid. Due to the continuous flushing of the membrane, it is expected that ions are either accumulated or removed inside the pores (by ad-/desorption on the pore walls) until an equilibrium ion concentration in the liquid is reached. Depending on the initial conditions in the liquid and matrix, either an increase or decrease in conductivity ensues. This is consistent with the different graphs depicted in Fig. 8.12.

Since the parasitic effect of conductivity dominates the entire spectra for the frequency range in the experiments, any simultaneously occurring effects need to be of comparable

order of magnitude to be detectable in an experiment. As this is not the case, this gives a first indication that the suspected flow-induced change in static permittivity is very small. Then, one can only resolve the relative changes if low frequency effects can be excluded.

In future setups, this could be achieved by either raising the frequency range or by cooling which causes a shift of dielectric spectra towards lower frequencies. As a side effect, if the frequency shift is large enough, this additionally allows studying of the dipolar relaxation of the liquids. However, both of these modifications entail technical difficulties: On one hand, cooling massively reduces the flow rate due to the temperature dependent viscosities, so that the resolution of the flow measurement needs to be sufficiently high. On the other hand, dielectric spectroscopy in the high MHz and GHz-range requires a redesign of the experimental setup for high-frequency compliance.

8.4. Summary

In conclusion, the results of stationary flow experiments confirm the validity of Darcy's law with a sticking wall layer boundary condition for all alcohols. The effective slip length in flow experiments is comparable to typical molecular dimensions for all liquids.

For chain lengths $n \geq 6$, a slip length $b_{\mathrm{H_2O}} < b < b_{\mathrm{C,flat}}$ indicates co-adsorption of water and alcohol molecules in a monolayer due to partial elution. Contrary to this behaviour, the smallest molecules probed (1-butanol) exhibited the largest extent of the sticking layer in large pores ($r_0 = 6.2\,\mathrm{nm}$). Here, multilayer sticking for a stacked layer of water and alcohol molecules results in a very good agreement to experimental flow rates. When conducting the same experiment in smaller pores ($r_0 = 3.1\,\mathrm{nm}$), a smaller interface layer in the order of a water monolayer was detected. This can be interpreted as a dynamic transition from multi- to monolayer sticking depending on the pore rheology.

In all the above experiments, the results do rely on effective quantities in spatial averaging. In order to safely confirm or exclude certain configurations, further microscopic investigation of the interfacial layer in nanopores is needed.

Regarding the dielectric results, no correlation between flow rate and permittivity could be proven with the experimental data. In the frequency range of the experiments, a variable ionic conductivity due to a change in concentration of contaminants presents a dominant effect that appears to be significantly stronger than any flow-dependent change in the complex permittivity. In order to avoid these parasitic contributions, either lower temperatures or a higher frequency range are required.

9 Theory of Spontaneous Liquid Uptake in Porous Media

9.1. Capillary Rise in Cylindrical Tubes

9.1.1. Introduction to Capillary Rise

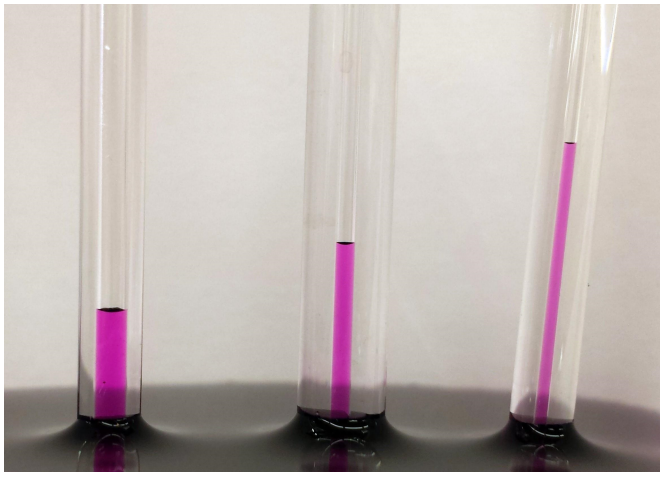

Figure 9.1.: Equilibrium capillary rise in macro-capillaries. Here, glass capillaries of different diameters $d = 1.2\,\mathrm{mm}$, $0.8\,\mathrm{mm}$ and $0.4\,\mathrm{mm}$ (left to right) have been inserted into an aqueous solution of $KMnO_4$. A spontaneous uptake of liquid results in an equilibrium situation as depicted in the photograph. Note the increasing rise height for smaller diameters of the glass tube.

The spontaneous uptake of liquid by capillary flows is a commonplace phenomenon in our day-to-day lives: In natural occurrences such as rain water draining into porous rocks and granular soils, but also in many widespread technical applications, e.g. sponges or tissues for soaking up spilled liquids. Even this very document (given that you are reading a physical copy) is produced by spontaneous uptake of ink in porous paper in the printing process.

The phenomenology of capillary rise can be demonstrated with a simple experiment: When dipping a small glass tube into a wetting liquid, a liquid column rises on the inside, against the force of gravity, until an equilibrium state is reached[1]. The equilibrium rise height of liquid

[1] Using a non-wetting liquid results in capillary depression, i.e. air displacing liquid in immersed capillaries.

in the capillaries depends on the radius of the tube, as depicted in Fig. 9.1.

From a physical standpoint, an energy difference is needed for the ascension of liquid above its reservoir. As no external forces are applied besides gravity, this energy needs to be supplied from an internal source inside the capillary. Here, it is the solid interface that undergoes a critical transition between the unwetted and wetted state, which causes a change in specific surface energy due to intermolecular interactions between particles in the solid and the liquid. As spontaneous wetting is observed, the specific surface energy between the solid and the gas needs to be larger than between the solid and the liquid $\gamma_{\text{s-g}} > \gamma_{\text{s-l}}$. This difference in specific energy is in turn transferred to the potential energy of the liquid column. Based on this simple consideration, a first qualitative reason for the observed r-dependence can be given: The difference in surface energy depends on the surface area of the capillary tube, whereas the increase in potential energy depends on the volume of liquid. Hence the surface-to-volume ratio determines the maximum rise height, which increases towards smaller tube diameters.

9.1.2. The Young-Laplace Equation

A quantitative description of the capillary forces is given by the formulation of Young and Laplace [89]. Let us assume that a liquid interface is characterized by an interfacial tension γ, which manifests as equal forces acting in all four tangential directions for a finite surface element $\mathrm{d}A = \mathrm{d}x\,\mathrm{d}y$. For any mean, non-zero surface curvature r_c of macroscopic interfaces, the superposition of these tangential forces results in a force vector perpendicular to the surface element (see Fig. 9.2) and thus an integral pressure difference of ΔP_L on both sides of the integral macroscopic interface,

$$\Delta P_L = \frac{2\gamma}{r_c}. \tag{9.1}$$

Eq. (9.1) constitutes the Young-Laplace equation. The pressure difference ΔP_L is also known as the Laplace pressure, it is positive if the curvature is convex, i.e. a stabilizing pressure for liquid drops, and negative for concave surfaces.

The latter case corresponds to the situation of spontaneous capillary rise in a cylindrical capillary of radius r_0: The interface between the liquid and air is characterized by the constant surface tension $\gamma_{\text{l-g}} = \sigma$. When a solid capillary is put in contact with the interface, a concave interface is induced by the cohesion between the liquid molecules covering the pore walls and nearby particles in the liquid. The local radius of curvature depends on the relative importance of adhesive and cohesive forces in the liquid. A contact angle θ of the liquid and the solid capillary can be introduced. For full wetting ($\theta = 0$), the liquid interface is hemispherical and $r_c = r_0$, in line with the definition of curvature from Sec. 3.4.2. Then, Eq. (9.1) can be

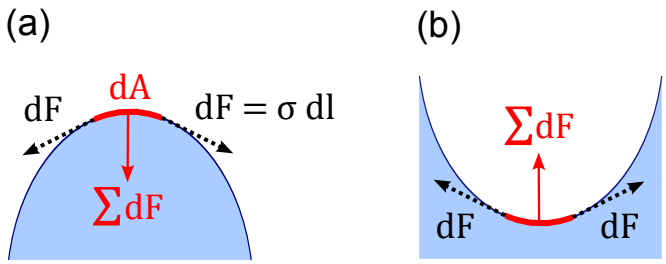

Figure 9.2.: Illustration of forces on curved liquid surfaces. For a finite surface element $\mathrm{d}A$, the forces from neighbouring surface elements amount to $\mathrm{d}F = \sigma\,\mathrm{d}l$, where $\mathrm{d}l$ is the length of the border line between both elements. For curved surfaces, the superposition of multiple contributions $\mathrm{d}F$ results in a normal force that points into the liquid volume for convex interfaces (a) and outwards for concave surfaces (b). When integrated over the entire surface A, this can be equally described as a pressure difference ΔP_L between both phases.

rewritten to

$$\Delta P_L = \frac{2\sigma}{r_0}. \tag{9.2}$$

Similarly, a finite contact angle θ results in a larger curvature $r_c = r_0/\cos\theta$ and thus a reduced Laplace pressure (also see Fig. 4.13),

$$\Delta P_L = \frac{2\sigma\cos\theta}{r_0}. \tag{9.3}$$

In an equilibrium situation of capillary rise, the Laplace pressure counteracts the hydrostatic pressure of the liquid column at an equilibrium height h_{eq},

$$\begin{aligned} P_H &= \Delta P_L \\ \Leftrightarrow \rho g h_{\mathrm{eq}} &= \frac{2\sigma\cos\theta}{r_0} \\ \Leftrightarrow h_{\mathrm{eq}} &= \frac{2\sigma\cos\theta}{\rho g}\frac{1}{r_0} \end{aligned} \tag{9.4}$$

Here, ρ denotes the liquid density and g the local gravitational acceleration.

Due to the proportionality to the inverse radius in Eqs. (9.3) and (9.4), both the Laplace pressure and the maximum rise height scale by orders of magnitude in nanopores. A numerical comparison of macroscopic and nanoscopic pores is shown for water in Tab. 9.1, revealing the enormous dimensions of capillary pressures and equilibrium rise heights on the length scale of Vycor nanopores.

Table 9.1.: Laplace pressure and equilibrium rise height for water in silica pores of different pore sizes at room temperature ($T = 298\,\mathrm{K}$, $\sigma = 0.072\,\frac{\mathrm{N}}{\mathrm{m}}$, $\theta = 0°$).

pore radius r_0	**Laplace pressure** P_L	**equilibrium rise height** h_{eq}
$1\,\mathrm{mm}$	$1.45\,\mathrm{mbar}$	$14.8\,\mathrm{mm}$
$1\,\mu\mathrm{m}$	$1.45\,\mathrm{bar}$	$14.8\,\mathrm{m}$
$10\,\mathrm{nm}$	$145\,\mathrm{bar}$	$1.48\,\mathrm{km}$

9.1.3. The Lucas-Washburn Equation

The dynamics of spontaneous capillary rise in cylindrical tubes results from the same principles as the stationary flow discussed in Sec. 7. Note that technically, the combined flow of the imbibing liquid and the displaced medium in the capillary have to be considered. The total uptake rate thus results from the hydraulic resistance for both phases. However, if the pores initially contain a gas, the displacement flow is typically neglected [103]. This is particularly reasonable in the Knudsen regime for gas flow (see Sec. 5.2.3) when interactions between gas particles are insignificant, but also applies to the hydrodynamic gas flow regime (see Sec. 5.2.2) due to the small viscosity in comparison to a liquid. As this is the case in the experiments, only the liquid flow will be considered in the following description of uptake dynamics.

If laminar flow is assumed, which is typically the case for small capillaries and flow velocities, the volumetric flow rate can then be modelled using the Hagen-Poiseuille law with a dynamic channel length corresponding to the rise height $h(t)$, since the liquid column moves through the capillary as a whole.

The driving pressure generally results from the superposition of hydrostatic and Laplace pressure. Though, for nanoscale capillaries, on the length scales for capillary experiments in this work, the hydrostatic pressure is negligible in comparison to the Laplace pressure $|\Delta P_L| \gg |P_H|$ and the pressure difference simplifies accordingly to $\Delta P = \Delta P_L$. Using Eqs. (7.8) and (9.3), the flow rate equation yields

$$Q = \frac{\pi\sigma\cos\theta r_0^3}{4\eta}\frac{1}{h(t)}. \tag{9.5}$$

This volume flow in turn advances the liquid column with a velocity

$$\dot{h}(t) = \frac{Q}{\pi r_0^2}. \tag{9.6}$$

Eqs. (9.5) and (9.6) can be combined to a differential equation

$$\dot{h}(t)h(t) = \frac{\sigma \cos\theta r_0}{4\eta}. \tag{9.7}$$

The solution for $h(t)$ in Eq. (9.7) is given by a $\sqrt{t}$ law,

$$h(t) = \sqrt{\frac{\sigma \cos\theta r_0}{2\eta}}\sqrt{t}, \tag{9.8}$$

which is known as the Lucas-Washburn law honouring the independent discovery of this equation by both researchers [104, 105]. At the time, the experimental observation of a $\sqrt{t}$ law has already been made by Bell and Cameron [106], so that Eq. (9.8) is also sometimes referred to as the BCLW law.

The Lucas-Washburn law is valid for experimental situations in which gravity, evaporation, and adsorption of liquid can be neglected in good approximation. The combined case of spontaneous capillary flow with a significant additional adsorption from the vapour phase will be discussed in Sec. 11.

Due to the scaling to the square root of the capillary radius, the dynamics in small pores is slowed down significantly, which allows the experimental study of imbibition using dielectric spectroscopy with a good resolution in time. In conjunction with the scaled equilibrium rise heights h_{eq}, the time to reach the maximum height is inversely proportional to the third power of the radius. For nanoscale capillaries, this is already in the order of $\sim 1 \cdot 10^8$ years, without considering the slowdown resulting from the hydrostatic pressure! Thus, in the experiments in this work, the sample height has been limited to practical sizes $h_0 \approx 10\,\mathrm{mm} \ll h_{\mathrm{eq}}$, which also restricts the stage of dynamics studied to a limited time span at the beginning of the filling process. Still, for some liquids, filling times in the order of days were observed.

9.2. Imbibition Kinetics in Porous Media

9.2.1. Capillary Rise in Pore Networks

Analogous to stationary flows [98], the pore network model from Sec. 7.2.1 can also be adapted for the description of capillary flows in porous solids on the time scales of the experiment. If the cross-sectional area of the sample is constant along the rise height, the flow rate equation in Eq. (7.13) can be used as a quantitative model. By replacing the flow channel length with the variable rise height $h(t)$ and the pressure difference with the Laplace pressure as given by

Eq. (9.3), an average flow rate is given by

$$\bar{Q} = \frac{\Phi A \sigma \cos\theta}{4\eta\tau} \frac{\bar{r}_h^4}{r_0^3} \frac{1}{h(t)}, \tag{9.9}$$

where $\bar{r}_h$ is the average hydraulic radius of the pore network. Note that the rise height $h(t)$ also becomes a spatial average of the pore network for a distribution of pore radii of the porous matrix. Then, instead of a homogeneous rise of liquid, a variable height of filling $h(x, y, t)$ emerges throughout the sample. This fringed border between filled and unfilled pore space will from now on be referred to as the 'imbibition front'. As a consequence of pore interconnectivity, the local dynamics of individual menisci results from variation of pore radii in the complex network, which will be addressed in Sec. 9.2.2. However, an average velocity of the advancing imbibition front can be calculated from the volume flow in Eq. (9.9),

$$\dot{h}(t) = \frac{\bar{Q}}{\Phi A}. \tag{9.10}$$

By combining Eqs. (9.9) and (9.10), a modified differential equation $\dot{h}h = \text{const}$ for porous matrices can be formulated. A solution is found analogous to the Lucas-Washburn law in Eq. (9.8),

$$h(t) = \underbrace{\sqrt{\frac{\sigma}{2\eta}}}_{c_{\text{liq}}} \underbrace{\sqrt{\frac{\bar{r}_h^4 \cos\theta}{\tau r_0^3}}}_{c_{\text{mat}}} \sqrt{t} \tag{9.11}$$

$$= c_h \sqrt{t}. \tag{9.12}$$

Notably, Eq. (9.11) does not contain a cross-sectional area or porosity of the sample, yet relies on both being constant along the direction of capillary rise. As shown in Eq. (9.11), the coefficient c_h can be separated into two partial contributions of the liquid, c_{liq}, and the matrix c_{mat}. The interactions between liquid and matrix are incorporated by using a general boundary condition containing a hydraulic radius $\bar{r}_h = r_0 + b$ as well as a contact angle θ, as depicted in Fig. 9.3. This will be discussed in more detail in Sec. 9.2.3.

The robustness of the Lucas-Washburn law for mesoporous solids has been established experimentally and by means of simulation [5, 95, 107]. In simulations for the flow of liquid Xe, a good match to a $\sqrt{t}$ law is observed down to pore sizes $r_0 \approx 1\,\text{nm}$ in the microporous regime.

It should however be noted that for very short times at the beginning of the filling process,

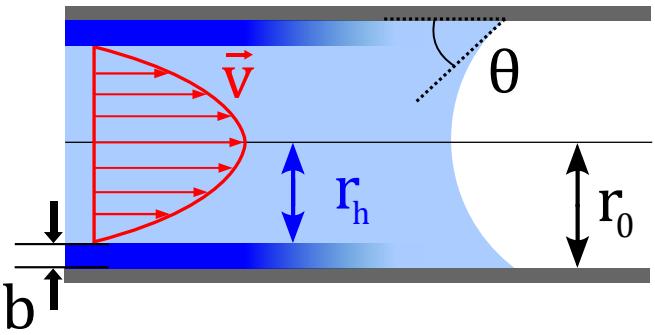

Figure 9.3.: Boundary condition for the Lucas-Washburn law in porous media. For the average flow in the porous solid, a reduced hydraulic radius $r_h = r_0 + b$ with slip lengths $b < 0$ and a contact angle θ of the liquid meniscus is assumed.

the front velocity diverges, $\dot{h} \to \infty$, which is due to systematic model errors based on the simplifications made in the solution of the Navier-Stokes equation, e.g. no effects of inertia and an established, laminar velocity profile, see Secs. 7.1.1 and 7.1.2. It can be shown that this critical phase is limited to very small times $t \approx 10\,\mathrm{ps}$, as Reynolds numbers rapidly reach values in the laminar regime. After that, a $\sqrt{t}$-law persists even for small time scales [108, 109]. In conclusion, for the experimental work, the assumptions are satisfied at all times and spontaneous capillary flows should obey Eq. (9.11).

9.2.2. Imbibition Front Broadening

As mentioned in the previous section, the local dynamics of capillary rise in a pore network are determined by the distribution of pore radii and the topology of the pore network. While a description of the spatial average allows the derivation of an equivalent form of the Lucas-Washburn equation, the local dynamics result from a more complex situation depending on the interplay of different local pressures. Here, the most important factors are the distribution and connectivity of filled and unfilled pores in the matrix, causing a variation of Laplace pressures.

This can be demonstrated for a simple mechanism of a Y-shaped pore intersection as depicted in Fig. 9.4. If a filled pore splits into two empty pores of different diameters d_1 and d_2, the smaller pore exerts a stronger pressure on the connection and fills up first. A temporary impediment of flow into the larger pore is observed until the pressure drop ΔP along the small pore is large enough to allow a simultaneous flow into both pores [110, 111].

In a complex pore network, many of these or similar intersections are connected as nodes in a network with flow channels of different lengths. Then, the pressure drop alongside the

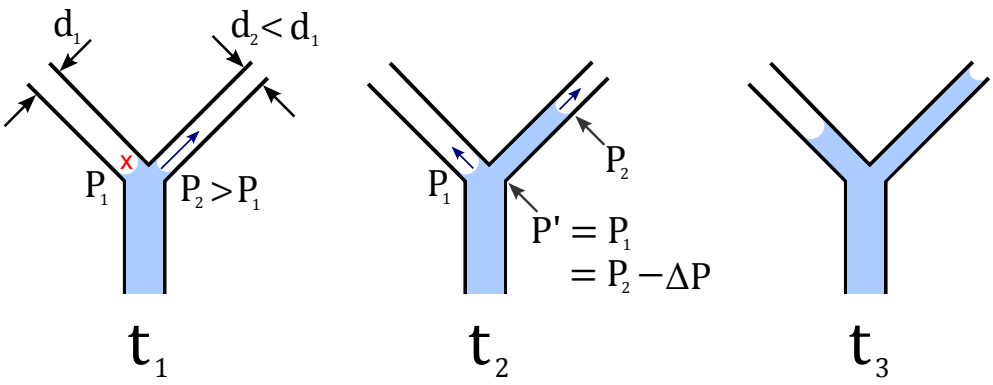

Figure 9.4.: Meniscus halting in pore connections. Due to the different Laplace pressures $P_{1,2}$ in pores of different diameters $d_{1,2}$, the flow in a Y-shaped connection is dominated by the stronger pressures of smaller pores at first. Only when the pressure drop along the small pore reaches a critical value $\Delta P = P_2 - P_1$, a flow into the larger pore is allowed.

connecting pores between two nodes may not suffice to overcome the pressure difference that causes meniscus halting. As a consequence, the capillary flow continues in other accessible pores until a certain state of filling is achieved in the overall network and a cascading pressure drop allows liquid to enter these voids. In this situation, the imbibition front as the border between filled and unfilled pore space is clearly not a simple plane but exhibits a much more complex shape. However, a macroscopic description of the imbibition front is still possible using the height of the partially filled region Δh. Over time, Δh increases systematically as a function of $\sqrt{t}$ to macroscopically large sizes, which has been shown both in experiments and simulations [48, 112].

9.2.3. Dynamic Effects in the Boundary Layer

In the derivation of the Lucas-Washburn equation for porous solids (see Eq. (9.11)), a general boundary condition at the pore walls has been chosen, exhibiting a finite slip length $b = \bar{r}_h - r_0$ as well as a contact angle θ of the liquid meniscus, see Fig. 9.3. In a dynamic situation of spontaneous imbibition, these parameters do not necessarily correspond to values derived for stationary or static equilibrium situations, see Secs. 8.3 and 4.3.6.

As for the slip boundary condition, the strong interaction between the interfacial liquid layer and the solid wall within a molecular range is always expected in the liquid-filled pores. The results from Sec. 8 suggest that b exhibits no variation for the probed flow velocities. Thus, if rise velocities $\dot{h}(t)$ are of comparable order of magnitude, a slip length in the order of one molecular layer $b \approx 0.5\,\mathrm{nm}$ should apply.

In case of the contact angle, the characteristics during capillary rise are different from an

equilibrium situation. Two aspects should be discussed that could potentially result in a modified contact angle: Dynamic contact angles and precursor wetting.

A dynamic contact angle of the liquid results from contact line movement on the solid interface, see Fig. 9.5(a). As the wetted area of a solid interface changes, whether it is increasing or decreasing, different situational contact angles are observed which are both different from the equilibrium angle [113]. For macroscopic droplets, the advancing angle (θ_A) is generally larger and the receding angle (θ_R) is smaller than the equilibrium contact angle ($\theta_R < \theta < \theta_A$). This is also referred to as 'contact angle hysteresis'.

The dependencies of the dynamic contact angle can be bundled into a capillary number $\mathrm{Ca} = \eta v/\sigma$, with the velocity v of the interface [114]. An empirical relation between θ_A and Ca can then be determined for specific systems. However, as already discussed in Sec. 9.2.1, the velocity $v \propto \dot{h}(t)$ drops off by orders of magnitude in the initial phase and, due to the proportionality $\propto 1/\sqrt{t}$, results only in small changes of the capillary number afterwards. Accordingly, Martic et al. found in simulations that an initially increased advancing contact angle rapidly approaches a nearly constant value close to the static equilibrium angle [115]. In line with the other initial effects of capillary rise, a rapid decay on a time scale of $\sim 10\,\mathrm{ps}$ was observed, so that this effect can be neglected on the experimental time scales.

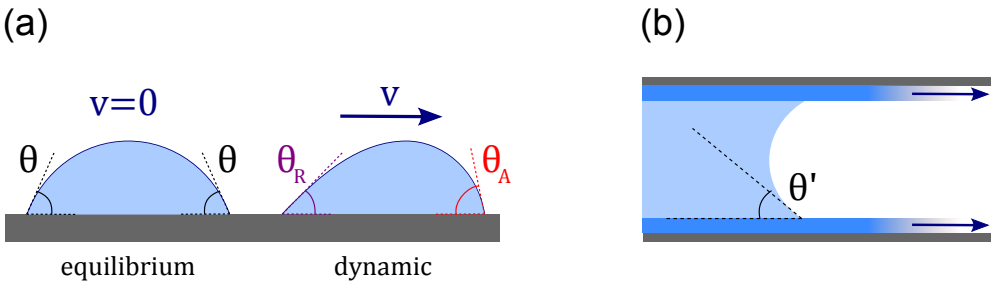

Figure 9.5.: Dynamic wetting phenomena in nanopores. (a) Dynamic contact angle for moving interfaces, i.e. contact angle hysteresis, results in a different contact angle for advancing or receding menisci that are both different from the equilibrium value $\theta_R < \theta < \theta_A$. (b) Dynamic precursor wetting for strongly interacting liquids also results in a modified contact angle.

On the other hand, in strongly interacting liquids, another difference in contact angle arises due to the formation and propagation of a precursor layer on the walls, as observed in MD and hydrokinetic simulations for spontaneous imbibition by Chibbaro et al. [116], see Fig. 9.5(b). Here, a thin adsorbate layer preceding the liquid meniscus is formed by both the advancement of a layer on the walls (surface diffusion) and dynamic recondensation of evaporated particles from the meniscus. In comparison to the static layer adsorbate in isotherms, the liquid precursor is not in a state of equilibrium and thus most likely exhibits a different structure. Due

to this local variation of interactions of the liquid molecules at different positions in the liquid interface, the meniscus curvature also varies locally in the presence of a precursor layer. This results in a change in local driving force, which can be accounted for by a modified contact angle for the driving Laplace pressure.

In conclusion, a complex interplay of dynamic wetting, precursor layer formation and the Laplace pressure is expected during spontaneous imbibition of strongly interacting liquids. On the experimental time scales though, short-time effects due to high flow velocities have subsided and a steady state for the meniscus shape is reached. However, the values for θ and b for this non-equilibrium process cannot be quantified *a priori*. Thus, the experimental results will be compared to different assumed boundary conditions using both as tunable free parameters in the system.

10 Spontaneous Imbibition Experiments with n-Alcohols

10.1. Experimental Methods

10.1.1. Experimental Imbibition Setup

The experiments on spontaneous imbibition are carried out in a custom setup described in more detail in [22], which uses dielectric spectroscopy as a means to detect the amount of liquid imbibed by the sample, as depicted in Fig. 10.1. The basic required components, a porous sample and a container for the liquid are placed inside a sealed vacuum chamber with a controllable atmosphere (He + alcohol vapour). This prevents water and other contaminants from the outside and ensures a defined atmosphere inside, which is a significant improvement to previous experiments [48, 117].

The working liquid is stored in a sealed container on the outside and can be inserted on demand and in a controlled manner by pressurizing the tank with He gas. This allows two different experimental modes: Spontaneous imbibition (inserted liquid in contact with the sample) and spontaneous vapour filling (no contact between liquid and sample).

The sample consists of a cuboid piece of porous Vycor glass (length $l\times$ height $h_0\times$ depth d, typically $10 \times 10 \times 2\,\mathrm{mm}$). Depending on the experiment, either solid copper plates or sputter coated gold electrodes were attached to the sample surface, see Fig. 10.2. One of the advantages of dielectric spectroscopy in comparison to other measuring methods, e.g. gravimetric measurement [95], is spatial selectivity for the detection, depending on the electrode placement. This has been exploited in the study of the concurrent vapour adsorption during liquid imbibition, see Sec. 11. In addition, the sample surface can be sealed which completely prevents the uptake of external vapour. For this purpose, the Vycor blocks are first encased in epoxy resin *UHU plus sofortfest* and subsequently reopened by mechanical abrasion on the facet that is in contact with the liquid[1]. The different sample configurations are illustrated in Fig. 10.2.

In preparation of an experiment, each sample is subjected to the cleaning procedure from Sec. 2.1.4. After that, samples are mounted into the imbibition setup in which a strong vacuum

[1]The entrapped He gas can easily dissolve in the imbibing liquid during the uptake process.

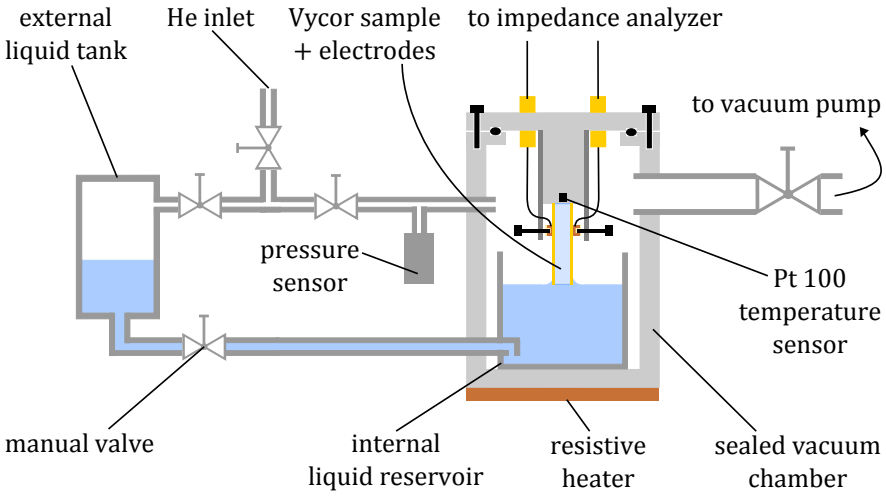

Figure 10.1.: Experimental setup for spontaneous imbibition and vapour filling experiments, see text for description. Depending on the amount of liquid inserted, either spontaneous imbibition or uptake through the vapour phase can be studied.

($\approx 10^{-6}$mbar) with additional heating ($T \approx 350\,\mathrm{K}$) is applied for at least 12 hours. This removes most volatile contaminants from the matrix, although the temperature is insufficient to remove the strongly bound water monolayer [23].

When starting a new imbibition experiment, the sample is first cooled to ambient temperature $T = 294\,\mathrm{K}$ and a protective atmosphere of He gas is inserted at a pressure $P_{\mathrm{He}} \approx 800\,\mathrm{mbar}$. As discussed in more detail in Sec. 6.2.2, the goal of this additional gas filling during imbibition is to systematically reproduce laboratory pressure conditions while avoiding accompanying problems (contaminants, varying conditions, continuous evaporation). As helium gas does not adsorb on Vycor for typical experimental conditions, it only acts as a small diffusion barrier due to intermolecular diffusion. Though, this change in total diffusivity is only in the order of $< 10\,\%$.

10.1.2. Dielectric Measurement of Spontaneous Imbibition

The dielectric measuring setup is identical to the one used in stationary flow experiments, see Sec. 8.2.1: An impedance analyser *Agilent 4294* periodically probes a frequency range $\nu = 1\,\mathrm{kHz}$ to $2\,\mathrm{MHz}$ and records the real and imaginary parts of the connected impedance for each frequency. By performing an initial fixture compensation (see App. C), the signal is free from line impedances. The measured impedance then results from the parallel circuit of the complex sample capacitance C_S^* and a parasitic capacitance of the sample fixture. If the electrodes are equal in size to the sample facet, the latter can be identified as the real stray

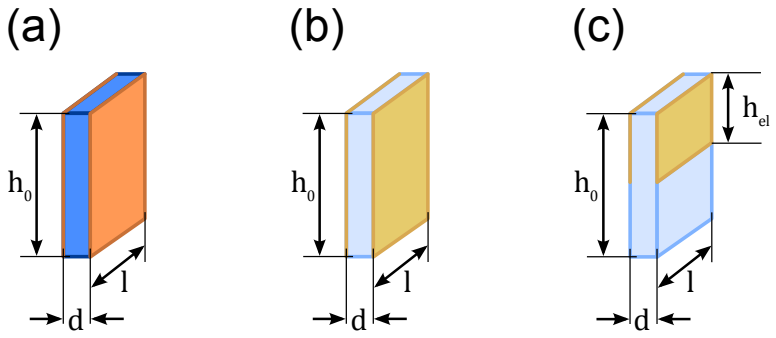

Figure 10.2.: Overview of sample and electrode configurations for imbibition experiments: (a) Vycor sample sealed with epoxy resin (except bottom facet) and glued on copper plate electrodes; (b) untreated Vycor with sputter coated gold electrodes (full coverage); (c) untreated Vycor samples with selectively applied electrodes (partial coverage). The samples in (b) and (c) allow the study of vapour uptake (see Sec. 6.2) and the combined uptake of vapour and liquid (see Sec. 11). Typical dimensions are $h_0 \approx l \approx 10\,\mathrm{mm}$, $d \approx 2\,\mathrm{mm}$, $h_{\mathrm{el}} \approx 5\,\mathrm{mm}$

capacitance C_{str} of the inhomogeneous field, which yields

$$Z^*(t) = \frac{1}{i2\pi\nu\left(C_S^*(t) + C_{\mathrm{str}}(t)\right)}. \tag{10.1}$$

For any given situation of capillary rise in the porous sample, C_S^* can be modelled as a parallel circuit of complex capacitances $\mathrm{d}C^*(h)$ for infinitesimal height elements $\mathrm{d}h$. Each $\mathrm{d}C^*(h)$ is characterized by a variable complex permittivity $\varepsilon^*(f(h))$ which in turn depends on the relative local volume fraction of filled pore space, $f(h) \in [0,1]$. The total sample capacitance is then given by

$$C_S^* = \varepsilon_0 \frac{l}{d} \int_{h=0}^{h_0} \varepsilon^*(f(h))\,\mathrm{d}h, \tag{10.2}$$

which is also represented by a complex sample permittivity

$$\begin{aligned} \varepsilon_S^* &= \frac{d}{\varepsilon_0 l h_0} C_S^* \\ &= \frac{1}{h_0} \int_{h=0}^{h_0} \varepsilon^*(f(h))\,\mathrm{d}h. \end{aligned} \tag{10.3}$$

In analogy to the considerations from Secs. 2.3.2 and 4.3.3, the local permittivity $\varepsilon'(h)$ for the high frequency plateau ($\nu = 1\,\mathrm{MHz}$) is assumed as a linear function of relative filling f,

$$\varepsilon'_S(h) = \varepsilon'(f=0) + f(h)\left(\varepsilon'(f=1) - \varepsilon'(f=0)\right). \tag{10.4}$$

By definition, this is accurate for the completely filled and empty parts of the sample, while in the partially filled section of the imbibition front, it is still expected to hold in good approximation if the distribution of liquid filled pores is reasonably homogeneous. Inserting Eq. (10.4) into Eq. (10.3) as the real part yields a simple relation

$$\varepsilon'_S = \varepsilon'(f=0) + \frac{1}{h_0}\int_0^{h_0} f(h)\,\mathrm{d}h\,\left(\varepsilon'(f=1) - \varepsilon'(f=0)\right). \tag{10.5}$$

Here, the integral can be identified as the definition of the mean rise height $h(t)$, as introduced in Sec. 9.2.1. Thus, Eq. (10.5) can be rearranged to

$$\frac{h(t)}{h_0} = \frac{\overbrace{\varepsilon'_S(t) - \varepsilon'(f=0)}^{\Delta\varepsilon'(t)}}{\underbrace{\varepsilon'(f=1) - \varepsilon'(f=0)}_{\Delta\varepsilon'_{\mathrm{max}}}}. \tag{10.6}$$

Hence, the normalized increase of the sample permittivity is equal to the normalized rise height. It will be demonstrated below that these differences can be easily gained from the total impedance signal without corrections.

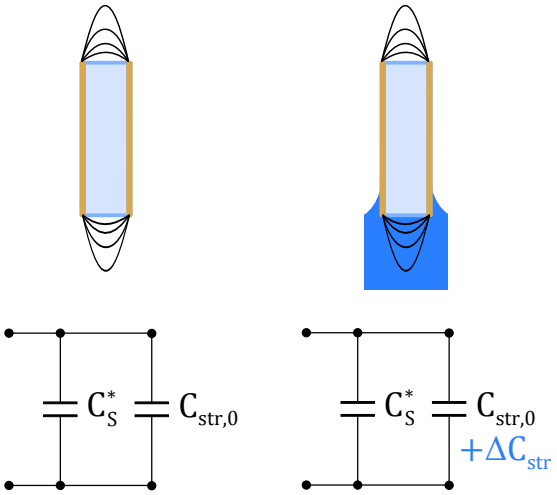

Figure 10.3.: Stray capacitance during imbibition experiments, without inserted liquid (left) and with inserted liquid (right) with the corresponding equivalent circuit.

As mentioned above, the total measured capacitance always contains the additional stray capacitance, see Fig. 10.3. When the measurements are started, the sample is empty and no liquid is inside the internal reservoir. The stray capacitance is then given by a constant $C_{\mathrm{str},0}$.

At the point when liquid is inserted and reaches the sample, the stray capacitance is suddenly increased by ΔC_{str} due to the high relative permittivity of the liquid dielectric entering the stray field. However, besides this initial snap-in of the liquid menisci on the macroscopic sample surface, the stray capacitance remains constant over time for the remaining experiment, which has been probed with non-porous glass samples.

As the measured permittivity $\varepsilon'(t)$ is calculated from the total real capacitance, it will therefore contain an erroneous contribution from the stray capacitance,

$$\varepsilon'(t) = \frac{d}{\varepsilon_0 l h_0}\left(C'_S(t) + C_{\text{str}}(t)\right) \tag{10.7}$$

$$= \varepsilon'_S(t) + \underbrace{\frac{d}{\varepsilon_0 l h_0} C_{\text{str}}(t)}_{\Delta\varepsilon'(t)} \tag{10.8}$$

However, in a constant situation after liquid insertion, this results in a constant offset $\Delta\varepsilon'_{\text{str}}$. Then, every difference $\Delta\varepsilon'(t) = \varepsilon'(t_1) - \varepsilon'(t_2)$ is automatically corrected for stray field effects. This allows to use $\varepsilon'(t)$ instead of $\varepsilon'_S(t)$ in Eq. (10.6), if the constants $\varepsilon'(f = 0)$ and $\varepsilon'(f = 1)$ are determined from the total capacitance signal with inserted liquid. However, no absolute values of ε'_S can be measured using this method.

It should be noted that an uncertainty for the normalization factor $\Delta\varepsilon'_{\text{max}}$ in Eq. (10.6) remains at the start of the imbibition experiment: Between liquid insertion and the first impedance measurement, a certain time span δt passes during which spontaneous liquid uptake in the porous matrix is expected. The effect on the measured $\varepsilon'(f = 0)$ can be estimated by extrapolating the initial uptake rate from the first recorded data points. This is included as an uncertainty in all error calculations in Sec. 10.2.2.

10.2. Results and Discussion

10.2.1. Corrupted Permittivity Signals and Correction

The spontaneous imbibition of n-alcohols of chain lengths $n = 4$ to 10 has been studied experimentally for sealed Vycor samples (see Fig. 10.2(a)). Following the considerations of the previous section, the measured real part of the permittivity at $\nu = 1\,\text{MHz}$ is used to analyse the filling of the sample. The permittivity values $\varepsilon'(t)$ are calculated with the known sample geometry using Eqs. (10.1) and (10.7) to

$$\varepsilon'(t) = \frac{d}{\varepsilon_0 l h_0}\frac{1}{2\pi\nu}\frac{-Z''(t)}{Z'(t)^2 + Z''(t)^2}. \tag{10.9}$$

Experimental data for $\varepsilon'(t)$ is shown exemplarily for 1-heptanol in Fig. 10.4(a). The sudden jump of the signal at $t \approx 0$ corresponds to the point of liquid insertion, in agreement with the abrupt increase of stray capacitance. After that, a gradual increase in ε' is observed until a maximum plateau value is reached. Note that the permittivity data exhibits small, systematic errors, see the magnified inset of Fig. 10.4(a). Over the course of an experiment, multiple random and instantaneous steps of increase in ε' were measured for all liquids. As we shall see in Sec. 11, this effect is limited to the samples sealed with epoxy resin, indicating an undesired liquid uptake in this additional layer. Here, as alcohols weaken the adhesive at the epoxy-electrode interface, entrapped air bubbles could suddenly become accessible for liquid imbibition, which entails dynamics orders of magnitude faster than in the nanopores, leading to a step-wise uptake.

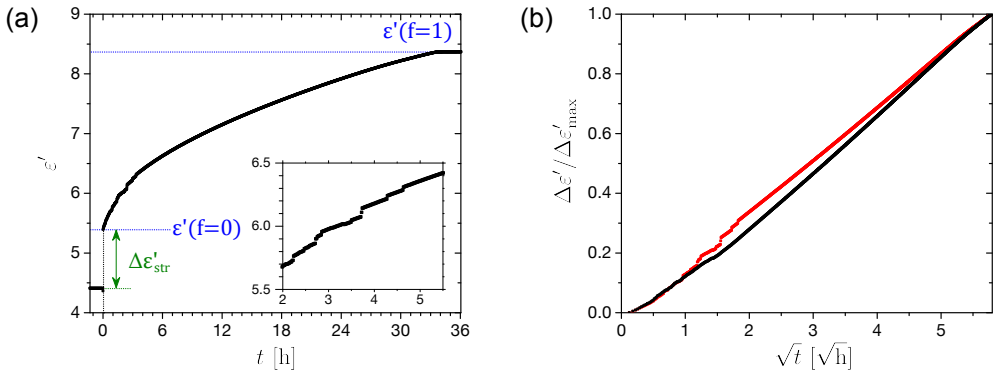

Figure 10.4.: Measured real permittivity during imbibition of 1-heptanol at $\nu = 1\,\mathrm{MHz}$. (a) raw data as a function of linear time: The time of liquid insertion is set to $t = 0$. From the start value $\varepsilon'(f = 0)$, the permittivity rises with liquid uptake in the sample until a plateau of complete filling $\varepsilon'(f = 1)$ is reached. Inset: For sealed samples with plate electrodes, unpredictable, parasitic jumps are observed in addition. (b) The normalized permittivity plotted over $\sqrt{t}$ allows to compare dynamics of the mean rise height to the predicted Lucas-Washburn equation (see Sec. 10.2.2). Here, systematic errors in the local slope resulting from the parasitic uptake are very noticeable (see steps for red symbols). A step correction algorithm can remove these artifacts (black symbols, see below).

According to the normalization procedure from Sec. 10.1.2, the permittivity after liquid insertion corresponds to $\varepsilon'(f = 0)$ and the first measured value on the saturation plateau to $\varepsilon'(f = 1)$, see Fig. 10.4(a). Using Eq. (10.6), this allows to calculate the normalized mean rise height $h(t)/h_0$ of the imbibition front from a normalized permittivity $\Delta\varepsilon'/\Delta\varepsilon'_{\mathrm{max}}$, which is shown graphically in Fig. 10.4(b). It will be shown in Sec. 10.2.2 that this is a function of $\sqrt{t}$ for the majority of the experiment as predicted by Lucas-Washburn dynamics according to Eq. (9.11), thus the scaling of the x axis. In this representation, the parasitic, step-wise liquid uptake is particularly problematic: As the permittivity for the full sample $\varepsilon'(f = 1)$ is

artificially increased, a false normalization factor $\Delta\varepsilon'_{\mathrm{max}}$ is assumed.

This problem can be overcome using computational data processing. In a plot of the numerical derivative of the data in Fig. 10.4(b), the occurrences of the parasitic flow (steps) are clearly discernible as outliers, as opposed to the underlying behaviour of the regular imbibition in the nanoporous matrix causing a nearly constant value with respect to experimental noise, see Fig. 10.5.

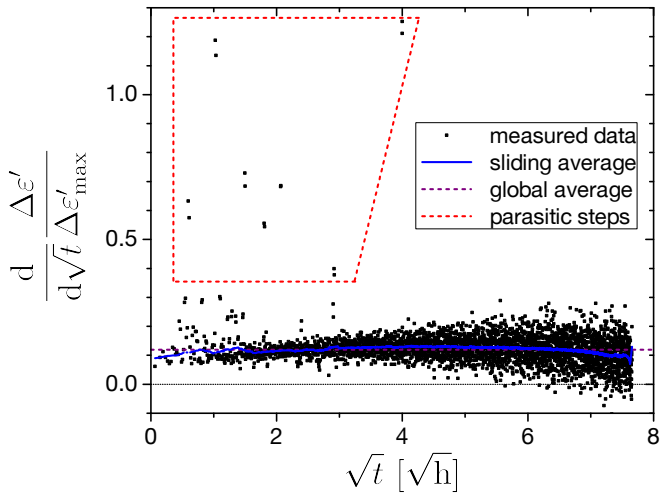

Figure 10.5.: Step detection for an imbibition experiment with 1-nonanol. When applying a numerical differentiation on the normalized permittivity over $\sqrt{t}$, the parasitic steps are easily recognizable by their large deviation from a sliding average value (sample size for averaging $N = 50$).

The detection and removal of steps can be automated as shown in Fig. 10.6: Starting at $t = 0$, discontinuities are detected by their deviation from a sliding average in a numerical differentiation of the normalized permittivity over the square root of time. Usually, all values within three standard deviations of the local average slope are interpreted as valid results; if this detection threshold is exceeded, a step is detected. In this case, the step height is quantified as the difference between the measured value and an extrapolation resulting from the local slope. Finally, the cumulated height for all previously detected steps (purple curve) is subtracted from the raw data for all data points.

The result of these data operations is a smooth curve for as shown in 10.6. Since the maximum change in permittivity has been reduced by the total step height $\Delta\varepsilon'_{\mathrm{step}}$, the old normalization does not apply to the corrected data. Instead, the maximum difference in permittivity in Eq. (10.6) has to be replaced with

$$\Delta\varepsilon'_{\mathrm{max,corr}} = \Delta\varepsilon'_{\mathrm{max}} - \Delta\varepsilon'_{\mathrm{step}}. \tag{10.10}$$

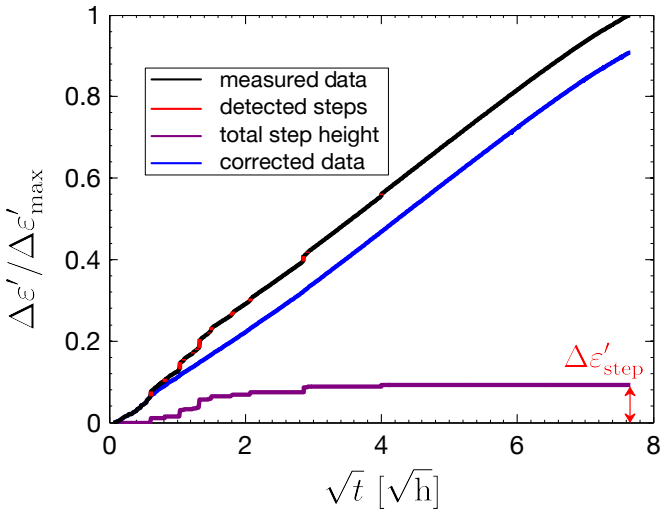

Figure 10.6.: Step correction algorithm and results for 1-nonanol. An algorithm scans the measured data (black line) and detects deviations in the local slope (indicated by red markings). At these points, the step height is evaluated and added to the total step height (purple line). In order to produce a corrected signal (blue line), the cumulated step height is subtracted from the raw data at each point. The sensitivity of the algorithm depends on the chosen detection threshold.

The difference between the raw and the corrected, renormalized data is depicted for 1-heptanol in Fig. 10.4(b). The uncertainty introduced by the correction algorithm can be quantified through the variation of $\Delta\varepsilon'_{\text{step}}$ for different step detection thresholds and is subsequently included in error calculations.

10.2.2. Imbibition Dynamics for n-Alcohols

The uptake curves for different alcohols have been processed and renormalized with the algorithm introduced in the previous section. After that procedure is applied, the rise height $h(t)$ can be calculated using Eqs. (10.6) and (10.10) to

$$h(t) = h_0 \frac{\Delta\varepsilon'_{\text{corr}}(t)}{\Delta\varepsilon'_{\text{max,corr}}} \tag{10.11}$$

Exemplary results for 1-butanol are depicted in a double logarithmic plot of $h(t)$ over t, see 10.7. Three stages of dynamics can be distinguished: In the initial stage (I), the rise dynamics are gradually changing and only slowly approach a linear section, i.e. power law. This is attributed to the collective variations of the initial experimental conditions, e.g. the temperature differences of the liquid inserted from the outside being reduced over time as well as imperfections of the sample surface inducing a preexisting imbibition front curvature that will flatten

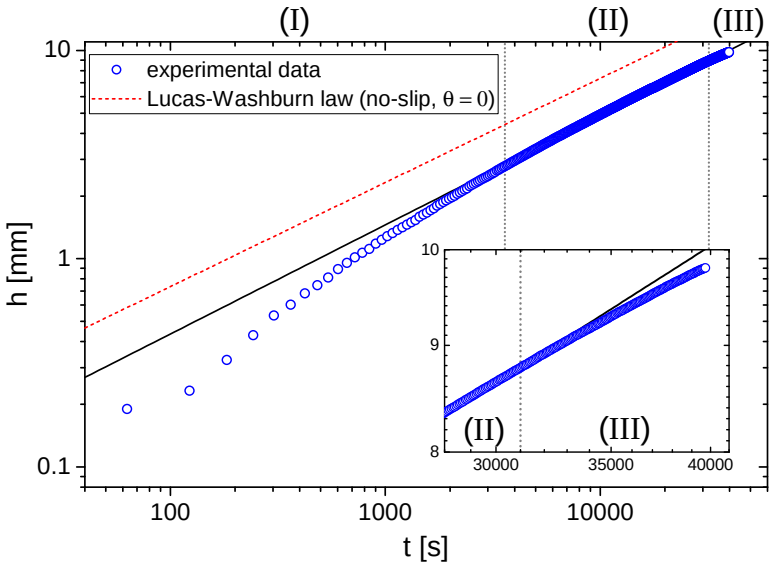

Figure 10.7.: Dynamics of 1-butanol imbibition in double logarithmic scaling. Three stages with distinct dynamics are observed: (I) initial stage, gradually changing dynamics approaching a linear function over time. (II) linear stage, constant slope ≈ 0.5 indicates Lucas-Washburn dynamics. (III) dynamics gradually slow down as broadened imbibition front reaches upper bound of the sample.

out eventually, see App. D. Due to these numerous uncertainties in the flow process, the first stage is disregarded for the analysis of dynamics.

After the initial phase has passed, a stage with a constant slope in the log-log plot is observed for the majority of the experiment (II). Accordingly, the exponent of the corresponding power law $h = \alpha \cdot t^{\beta}$ has been evaluated to $\beta = 0.524 \pm 0.001$. This is in very good agreement to the expected value $\beta = 0.5$ from Lucas-Washburn dynamics, see Eq. (9.11). Hence, the dynamics of this phase can also be studied in a plot versus $\sqrt{t}$, see Fig. 10.8, which has already been exploited for step correction.

In the final stage (III), dynamics slow down again, see the inset of Fig. 10.7. This is a result of the imbibition front broadening discussed in Sec. 9.2.2. Depending on the local state of filling, the upper boundary of the sample is reached at different times and the overall flow rate is reduced gradually. As the effects of front broadening are not of primary interest in this work, the analysis of dynamics will be limited to times before the first onset of stage (III).

The same qualitative dynamics were systematically observed for all other alcohols, with stage (II) exponents in the range $0.52 \leq \beta \leq 0.63$. For these values, a plot of $h(t)$ over $\sqrt{t}$ exhibits a distinct quasi-linear stage, as depicted for $n = 5$ to 10 in Fig. 10.9. A linear fit to stages (II) in this representation then directly yields the respective Lucas-Washburn coefficient

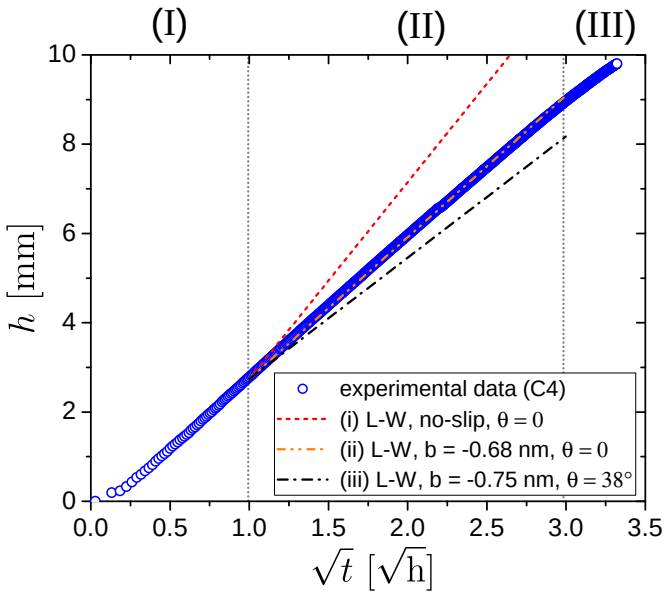

Figure 10.8.: Lucas-Washburn dynamics during 1-butanol imbibition. In a plot of h over $\sqrt{t}$, stage (II) of the dynamics constitutes a linear section, confirming the validity of the Lucas-Washburn law for n-alcohols in Vycor. Theory curves of the Lucas-Washburn law with different boundary conditions are shown in comparison.

c_h. Note that the initial effects of stage (I) cause a small shift of the graph so that the y-intersect $\neq 0$, which has to be included in the fit.

When comparing the experimental Lucas-Washburn stages (II) to quantitative predictions of Eq. (9.11), the choice of boundary condition is of utmost importance, as discussed in Sec. 9.2.3. In contrast to stationary flow dynamics, there are now two variables, the slip length b and the contact angle θ. Figs. 10.8 and 10.9 include a comparison to the following cases:

(i) [$b = 0$, $\theta = 0$]: A no-slip boundary condition with zero contact angle. This can be considered an upper bound for the maximum possible uptake for defined macroscopic liquid material constants and matrix parameters. [shown for all alcohols]

(ii) [$b = b_{st}$, $\theta = 0$]: A slip boundary condition, using the stationary slip lengths from Sec. 8.3.1. As for the contact angle, it is assumed that precursor wetting leads to very small contact angles, so that $\cos\theta \approx 1$. [shown for $n \in \{4, 6, 8, 10\}$].

(iii) [$b = t_{ML+H_2O}$, $\theta = \theta_{eq}$]: A special boundary condition assuming the stacked water and alcohol monolayer thickness and the autophobicity contact angle from the static adsorption for 1-butanol, see Sec. 4.3. It is suspected that these properties do not persist in a dynamic situation. [shown for $n = 4$]

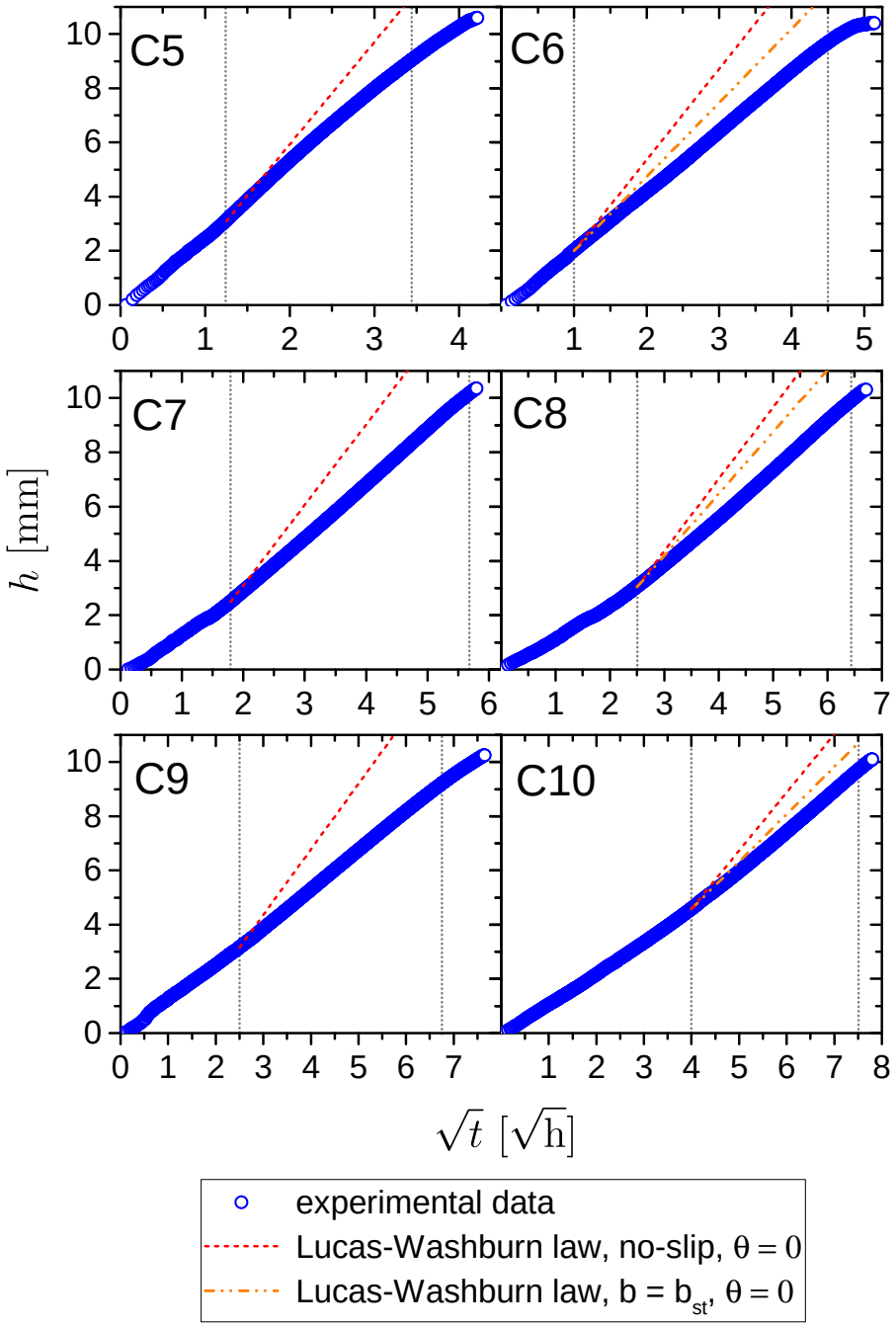

Figure 10.9.: Comparison of Lucas-Washburn imbibition dynamics for n-alcohols. All liquids used in the experiments exhibit a quasi-linear stage in a plot versus $\sqrt{t}$. The slope in this region corresponds to the respective coefficient c_h. In comparison to the Lucas-Washburn laws with no-slip boundary condition and with a slip length from stationary flow experiments ($\theta = 0$ in both cases), the experimental slope is lower for all alcohols.

For all graphs, the no-slip boundary condition is clearly not suited to reproduce the experimental slope for imbibition, which indicates that a finite sticking layer and possibly an additional contact angle is required.

In case of butanol in Fig. 10.8, the other two boundary conditions show much better agreement to the experimental data, with a best match of the slope for the stationary boundary condition with zero contact angle (ii). This apparent match is consistent with both the stationary boundary condition as well as the expected dynamic reduction in θ discussed in Sec. 9.2.3.

As for the other liquids covered in stationary flow experiments (hexanol, octanol, decanol), the stationary slip lengths from Sec. 8.3.1 are still insufficient to reach the slope of the imbibition experiments in Fig. 10.9 for contact angles $\theta = 0$. A different boundary condition is required.

In order to further study the experimental boundary conditions, the experimental Lucas-Washburn coefficient c_h can be analysed (slope in (II) for Figs. 10.8 and 10.9). Numerical values for c_h of the different n-alcohols and the respective uncertainties are listed in Tab. 10.1 for future reference.

Table 10.1.: Experimental Lucas-Washburn coefficients for n-alcohols.

n	**LW-coefficient** c_h $[\mu m/\sqrt{s}]$	**uncertainty** $\pm\delta c_h$ $[\mu m/\sqrt{s}]$
4	52.2	5.7
5	45.5	4.7
6	37.0	3.9
7	33.3	3.7
8	29.7	3.2
9	26.0	2.8
10	25.0	2.7

Eq. (9.11) relates c_h to both microscopic variables, the contact angle θ and the slip length b. As no other relations for these quantities in a dynamic situation can be found, an assumption needs to be made either for b or θ in order to determine the other. In case of the slip length b, we can rearrange Eq. (9.11) to

$$b = \left(c_h^2 \frac{2\eta\tau}{\sigma \cos\theta} r_0^3 \right)^{1/4} - r_0. \tag{10.12}$$

For now, let us choose $\cos\theta = 1$ in accordance to dominant precursor wetting causing a small

contact angle $\theta \approx 0$. When applied to c_h for each alcohol, this yields a slip length b_{exp}. The uncertainty in b_{exp} can be estimated from the errors in the matrix parameters and the error δc_h in the Lucas-Washburn coefficient. The latter is given by the combination of fit errors as well as the uncertainties from the step correction algorithm and the normalization procedure. Fig. 10.10 shows the results and error bars for all alcohols.

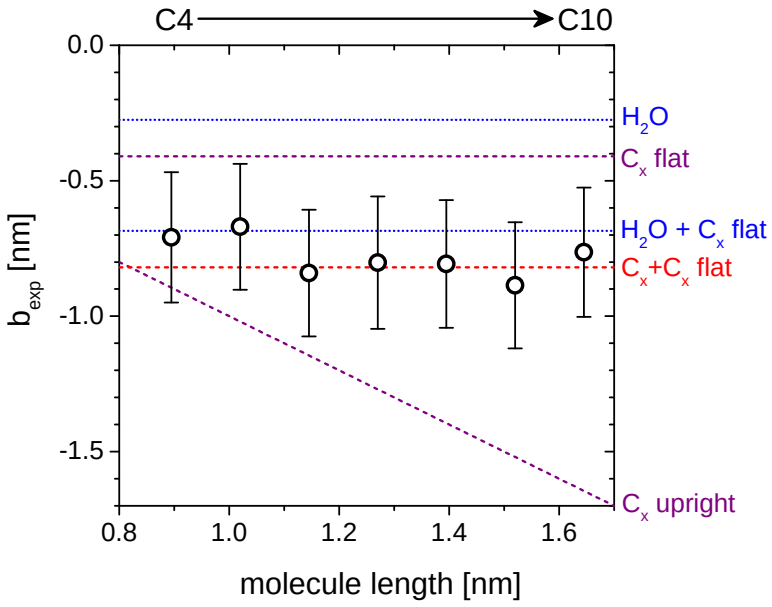

Figure 10.10.: Comparison of slip lengths for the imbibition of n-alcohols for zero contact angle. The experimental data exhibits a nearly constant slip length in the range of typical molecular dimensions, suggesting a similar boundary layer thickness for all alcohols. The lines indicate the molecular geometry for some wall layer structures, see text.

Analogous to the considerations from Sec. 8.3.1, the slip lengths constitute a macroscopic average of the local slip length which can exhibit considerable variations. Still, the qualitative and quantitative distribution of these values provides an insight into the average make-up of the surface layer.

For all liquids, b_{exp} is comparable to molecular dimensions. Fig. 10.10 depicts the comparison to five different configurations: A residual water monolayer ('H_2O'), a monolayer of alcohol molecules, either parallel ('C_x flat') or perpendicular ('C_x upright') to the pore walls as well as a stacked layer. As introduced in 8.3.1, a combined layer of water and flat alcohol molecules ('H_2O + C_x flat') and a multilayer of parallel, flat alcohol molecules ('C_x + C_x flat') are two likely configurations.

Most notably, the calculated slip lengths b_{exp} exhibit a nearly constant value for all liquids. This implies that the upright alcohol layer can be ruled out as the slip length should sys-

tematically decrease towards longer chain lengths in this case. Likewise, a water monolayer and a flat monolayer of alcohol molecules are also outside the range of the error bars if the assumption $\theta \approx 0$ holds. The experimental data shows a great match to both stacked layer configurations within the error margin.

Judging from previous results and considerations, a combined layer of water and alcohol is a very probable configuration: Not only do we expect a residual water layer from sample preparation, this is also consistent with the results for 1-butanol from equilibrium adsorption (see Sec. 4.3.5) and stationary flow experiments (see Sec. 8.3.1). Regarding the assumption made for θ when determining b_{exp}, this could indicate that the choice of zero contact angle and the hypothesis of dominant precursor wetting by surface flow and recondensation (see Sec. 9.2.3) are appropriate.

However, for chain lengths $n \geq 6$, the imbibition slip length b_{exp} is larger than the respective parameter from stationary flow (compare Figs. 8.7 and 10.10). This disparity can be equally explained by two effects. On one hand, an altered boundary condition for spontaneous capillary rise could arise as no significant desorption of the water monolayer occurs in the limited liquid volume imbibed, in contrast to the continuous elution for liquid throughput. The adsorption of n-alcohols is then limited to an additional layer, as opposed to the co-adsorption within a monolayer suspected in Sec. 8.3.1. On the other hand, if the boundary condition from stationary flow still applies to imbibition, a larger dynamic contact angle $\theta > 0$ for longer chain lengths could also explain these findings.

So far, it has been assumed that dynamic precursor wetting causes a small contact angle that justifies the approximation $\cos\theta \approx 1$. As the magnitude of this effect results from the attraction to the surface in conjunction with the molecular mobility [116], there is likely some degree of variation of the dynamic θ for the series of n-alcohols. In analogy to a slip length in Eq. (10.12), a contact angle could be equally calculated from c_h if an assumption is made for b. However, since very little is known on the dynamic contact angles in the nanoporous matrix, there is no comparison to be made with the resulting values.

As an alternative, one can make use of the error margins $c_h \pm \delta c_h$. For both values, contact angles θ_- to θ_+ can be calculated by rearranging Eq. (10.12) to

$$\theta_{\mp} = \arccos\left[\left(c_h \pm \delta c_h\right)^2 \frac{2\eta\tau}{\sigma} \frac{r_0^3}{\left(r_0 + b\right)^4}\right]. \tag{10.13}$$

The resulting range $[\theta_-, \theta_+]$ then defines an experimental confidence interval of contact angles for a given slip length b. Here, Eq. (10.13) is applied for three cases: A residual water monolayer ($b = 0.275\,\text{nm}$), a flat alcohol monolayer ($b = 0.41\,\text{nm}$) and a stacked water and alcohol

layer ($b = 0.685\,\mathrm{nm}$), as listed in Tab. 10.2. For all alcohols and slip lengths, the confidence intervals cover a broad range of contact angles up to an intermediate wetting regime. These results are quantitatively plausible considering the autophobicity of n-alcohols. Though the data is limited, equilibrium contact angles as high as $42°$ for 1-octanol on planar silica and $59°$ for 1-butanol in Vycor ($r_0 = 3\,\mathrm{nm}$) have been reported in literature [68, 66].

Table 10.2.: Confidence range of contact angles for defined imbibition boundary conditions.

n	**H_2O**		**C_x flat**		**H_2O + C_x flat**	
	θ_- [°]	θ_+ [°]	θ_- [°]	θ_+ [°]	θ_- [°]	θ_+ [°]
4	37.3	59.0	25.1	54.1	0	39.2
5	34.8	57.0	20.8	51.7	0	35.0
6	46.5	63.3	38.3	59.2	0	47.5
7	43.4	62.5	34.2	58.2	0	45.9
8	44.4	62.2	35.5	58.0	0	45.5
9	49.0	64.7	41.7	60.9	9.6	50.0
10	41.3	60.9	31.2	56.4	0	43.0

A notable result from this estimation is that the most likely configuration for zero contact angle, a stacked layer of water and alcohol molecules, remains valid even when the approximation $\cos\theta \approx 1$ fails. In addition, a monolayer boundary condition, which was previously excluded for this assumption, now becomes a possible option for either water or flat alcohol molecules and large enough contact angles.

At this point, even if a dynamic contact angle θ could be estimated, one cannot safely distinguish between these boundary conditions for θ within the large overlap of confidence ranges. This is a consequence of the limited experimental precision, mainly due to the uncertainty in the permittivity normalization discussed in Sec. 10.2.1.

10.3. Summary

In summary, the spontaneous imbibition of n-alcohols in Vycor exhibits three stages of different dynamics. While stages (I) and (III) show the influence of parasitic effects, e.g. initial conditions and front broadening, stage (II) is in very good agreement to the expected Lucas-Washburn dynamics. A plot of measured $h(t)$ over $\sqrt{t}$ produces linear segments whose slopes are equal to the different coefficients c_h in Eq. (9.11). The same dynamics were observed in imbibition experiments using different detection techniques of pore filling [118, 48], which confirms that the dielectric measurement is a valid option.

The underlying flow boundary condition cannot be determined definitely using this experimental technique. For the most part, this results from the single parameter c_h gained in the experiment, which in turn depends on both the slip length b and the dynamic contact angle θ of the liquid. Moreover, the Lucas-Washburn coefficient is a macroscopically averaged quantity that neglects local variations as well as the pore size distribution.

Still, c_h can be interpreted in terms of an average boundary layer, which reveals a striking consistency: Assuming a reduced dynamic contact angle $\theta \approx 0$ due to precursor wetting, all calculated slip lengths are comparable to a stacked layer of flat alcohol molecules on top of water, the latter is expected as a contaminant from sample preparation. For 1-butanol, this perfectly matches the results from stationary flow in Sec. 8.3.1. However, the other alcohols used in stationary flow experiments exhibit lower slip lengths for imbibition. This could either indicate a difference between boundary conditions in both cases as a result of elution of the water layer during stationary flow experiments or a larger contact angle for longer alcohol molecules.

Finally, when assuming the slip lengths to wall layer configurations encountered in stationary flow experiments (flat water or alcohol layer, stacked water and alcohol layer), a confidence range of contact angles can be derived from the experimental error margins for c_h. All three boundary conditions yield ranges compatible with an intermediate wetting regime. Notably, the upper confidence bound for the stacked layer is far from the range of validity for $\cos\theta \approx 1$. Though, a large overlap of all ranges is noted due to the experimental errors and none of the conditions could be excluded based on this estimation.

11 Combined Vapour and Liquid Uptake

11.1. Outline

So far, both the spontaneous filling by vapour adsorption (Sec. 6.2) and the liquid imbibition (Sec. 10) have been studied individually. While the liquid and vapour phase uptake can be separated in a controlled laboratory setup, this is generally not the case in day-to-day applications for porous media. For a finite vapour pressure, liquid molecules continuously evaporate on an interface and populate the vapour phase. If an unsealed porous adsorbent is in contact with the liquid, an additional diffusion flux of these particles enhances the total flow into the pore space. The goal of this chapter is to shed light on the dynamics of this combination of transport mechanisms.

On their own, the spontaneous vapour filling dynamics critically depends on the microscopic properties of the matrix and the current spatial distribution of adsorbate in the pores. The presence of an imbibition front with pre-existing concave liquid-gas interfaces provides additional adsorption spots due to the reduced vapour pressure. This could cause significant changes in transport through the gaseous phase. Similarly, pre-adsorbed wall layers induced by an external vapour phase could result in a different boundary condition for capillary flows. Thus, it is crucial to understand the interdependence of both transport processes in order to gain information on total dynamics.

This chapter will focus on answering these two central questions: Is there a notable difference in the respective dynamics for adsorption or imbibition resulting from the interplay of both mechanisms? And what are the qualitative and quantitative dynamics of the combined process?

11.2. Experimental Study of Combined Uptake

The experiments in this chapter were carried out in the imbibition setup described in Sec. 10.1.1. In order to allow uptake from both a liquid reservoir and the vapour phase, sputter coated gold electrodes were deposited on untreated Vycor samples. In contrast to the epoxy

sealing, these do not obstruct the gas transport into the pore space. Two different electrode configurations were used, see Fig. 10.2: A full coverage of the two largest faces (b) and a partial coverage of the upper parts on the same sides (c).

For the electrodes with partial coverage, two types of experiments were conducted, as illustrated in Fig. 11.1. The first series covered the spontaneous vapour uptake kinetics without contact to the liquid (a) which has already been presented in Sec. 6.2. The kinetics of the resulting vapour filling represents the intrinsic process without interference by additional liquid menisci.

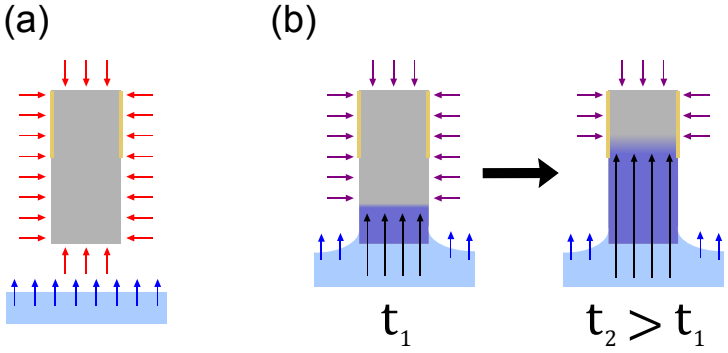

Figure 11.1.: Illustration of experiments using spatially selective electrodes: (a) vapour uptake only, without contact to the liquid, see Sec. 6.2, (b) combined imbibition and vapour uptake which allows to study the potentially modified vapour uptake dynamics until the imbibition front reaches the electrodes.

For the second series of experiments (b), these samples are put in contact with a liquid. This causes a spontaneous liquid uptake with an additional concurrent vapour adsorption. Here, the reason for this specific electrode placement on the upper part of the sample becomes obvious: At first, the advancing imbibition front is well outside the electrode area. The detected increase in permittivity in this initial stage thus originates from other transport mechanisms, e.g. the adsorbed vapour. Only after a certain time, the imbibition front advances to the sensitive area and a change in dynamics reflecting the combined uptake is expected. By comparing the initial stages for both experiments (a) and (b), it is possible to assess any qualitative and quantitative differences that may arise, which will be shown in Sec. 11.3.1.

For the study of the combined uptake process, the electrodes with sputter coated electrodes of full surface coverage are used to repeat the imbibition experiments from Sec. 10. The resulting signal then shows the total uptake of liquid and vapour for all times. It is expected that these results show clearly enhanced dynamics in comparison to both individual mechanisms, which will be tested in Sec. 11.3.2.

11.3. Results and Discussion

11.3.1. Interplay of Vapour and Liquid Uptake

Comparative adsorption and imbibition experiments on samples with partial electrodes were conducted for the series of n-alcohols from $n = 4$ to 10. As discussed for the vapour uptake experiments in Sec. 6.2, the sample geometry has a great impact on adsorption kinetics, which also became apparent in preliminary works [119]. In order to ensure comparable results, the same sample (*vyc_im_1*, see App. A) was used in all experiments. In between measurements, the Vycor piece was thoroughly cleaned using the procedure described in Sec. 2.1.4.

The uptake is detected by means of dielectric spectroscopy. In line with previous results for adsorption experiments, it is expected that the increase of the real permittivity $\Delta\varepsilon'$ at $\nu = 1\,\mathrm{MHz}$, normalized to its maximum value $\Delta\varepsilon'_{\mathrm{max}}$ for complete filling, is a good indicator for the relative filling fraction $f = N/N_0$. This again includes the assumption that the distribution of adsorbate is reasonably homogeneous over the sample cross-section for infinitesimal heights $\mathrm{d}h$, so that the linear approximation $\varepsilon' \propto f$ prevails.

As already mentioned in Sec. 6.2, the samples with partial electrodes exhibit a parasitic stray capacitance for the lower part of the sample not covered with electrodes. In addition to the constant part $C'_{\mathrm{str,gas}}$ through the gas phase, this results in a variable part $C'_{\mathrm{str,Vyc}}(t)$ of the stray capacitance for gradual uptake of vapour. However, it is assumed that uptake dynamics and thus the permittivity are the same in the homogeneous field between the plates as well as in the sample volume in the stray field. Accordingly, a constant scaling factor K_{str} and a constant offset $\delta\varepsilon'$ alter the measured permittivity signal $\varepsilon'_{\mathrm{meas}}(t)$,

$$\begin{aligned} C'(t) &= C'_S + C'_{\mathrm{str,Vyc}} + C'_{\mathrm{str,gas}} \\ \Leftrightarrow \frac{h_{\mathrm{el}} l}{d}\varepsilon_0\varepsilon'_{\mathrm{meas}}(t) &= \frac{h_{\mathrm{el}} l}{d}\varepsilon_0\varepsilon'(t) + C_{0,\mathrm{str}}\varepsilon'(t) + C'_{\mathrm{str,gas}} \\ \Leftrightarrow \varepsilon'_{\mathrm{meas}}(t) &= \varepsilon'(t)\underbrace{\left(1 + \frac{d}{h_{\mathrm{el}} l \varepsilon_0} C_{0,\mathrm{str}}\right)}_{K_{\mathrm{str}}} + \underbrace{\frac{d}{h_{\mathrm{el}} l \varepsilon_0} C'_{\mathrm{str,gas}}}_{\delta\varepsilon'} . \end{aligned} \tag{11.1}$$

Here, $C_{0,\mathrm{str}}$ denotes the constant, unknown geometric capacitance of the stray field in the Vycor volume. Still, when calculating a normalized difference $\Delta\varepsilon'_{\mathrm{meas}}/\Delta\varepsilon'_{\mathrm{meas,max}}$, the stray field contribution cancels out automatically, which yields a relative filling f. Though, in case of varying dynamics in the sample volume, e.g. due to a broadened imbibition front reaching the stray field, a gradually changing error is expected. The quantitative analysis of the imbibition experiments with partial electrodes is thus limited to the stage of initial adsorption.

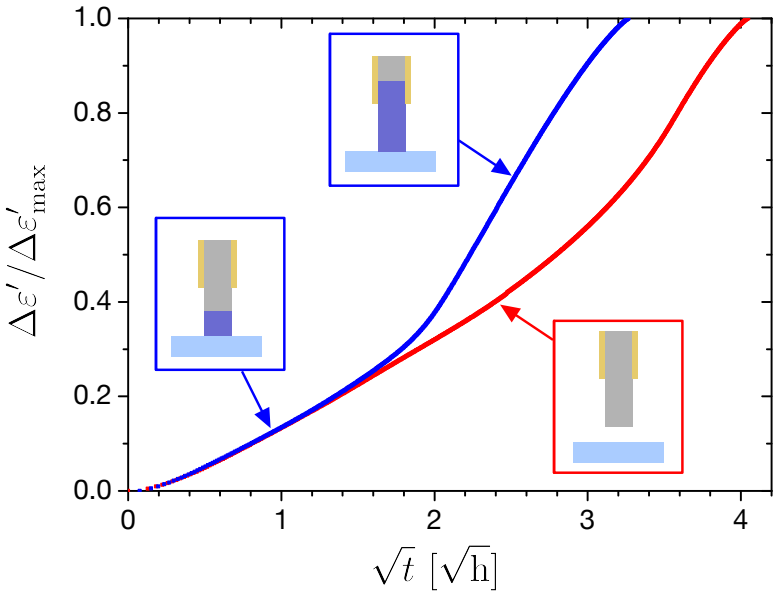

Figure 11.2.: Comparison of uptake experiments with partial electrodes for 1-hexanol. Two different uptake experiments were conducted: One suspended in the vapour phase (red curve, also see Sec. 6.2) and one in contact with the liquid. The latter results in two different stages of dynamics: At first, only vapour adsorption is resolved, which shows a great match to the red curve. After the imbibition front reaches the sensitive electrode area, the combined vapour and liquid uptake is measured.

Exemplary results of the normalized increase in permittivity for the imbibition experiment with 1-hexanol are depicted in Fig. 11.2 and for the rest of the liquids in Fig. 11.3. In all diagrams, the vapour filling curves from Sec. 6.2 are shown in comparison. It should be noted that for the most volatile alcohols, both uptake processes exhibit comparable times of complete filling, which once again underlines the importance of spontaneous vapour adsorption as a transport mechanism for liquids with high vapour pressures.

All measured imbibition curves (blue symbols in Figs. 11.2 and 11.3) exhibit two stages of dynamics. This is consistent with the expectations: At first, only vapour adsorption is permitted as an uptake mechanism in the monitored part of the sample, until the imbibition front reaches the electrode area and a combined uptake ensues. Note that the x axis has been scaled to $\sqrt{t}$ which clearly shows a good match to Lucas-Washburn dynamics for a majority of the second stage of the experiments. In agreement with the results from Sec. 10.2.2, there is a slowdown of the uptake rate when approaching full filling that is again attributed to the imbibition front broadening. On a similar note, the transition between both stages is also not a discrete point but rather a gradual shift, which is a consequence of both front broadening and the error due to the variable stray capacitance discussed above.

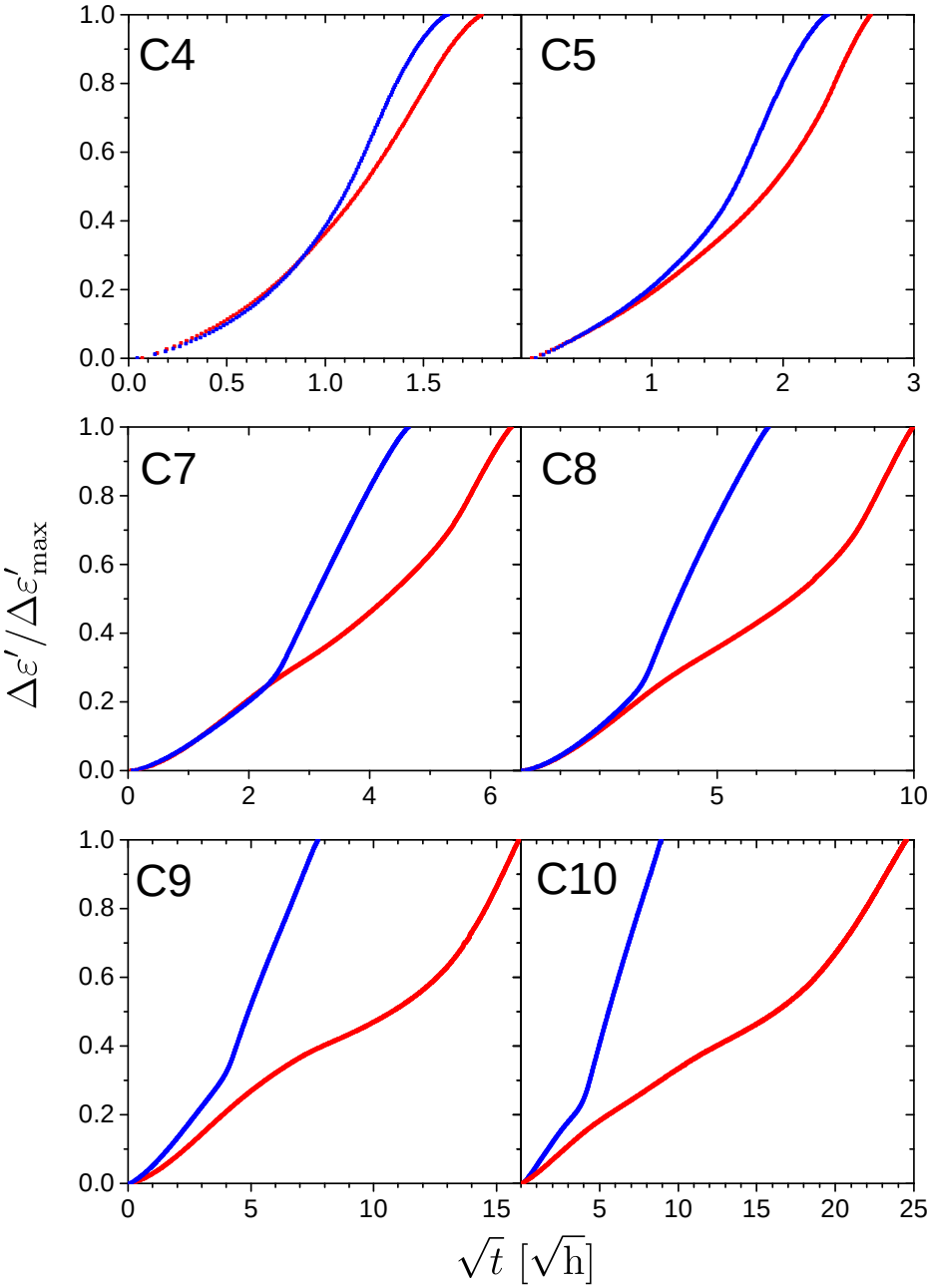

Figure 11.3.: Comparison of uptake experiments with partial electrodes for various n-alcohols. In each graph, the blue and red curves depict the experiments in contact to a liquid and suspended in the vapour phase, respectively, as sketched in Fig. 11.2. See text for a detailed discussion and interpretation.

A comparison of dynamics for both experiments for the respective alcohols reveals some interesting effects:

Most notably, the vapour uptake stages during imbibition show a great match to the adsorption experiments for chain lengths $n = 4$ to 8. This indicates that the transport mechanism of vapour diffusion and adsorption remains unchanged in the presence of the additional adsorption spots at the advancing menisci of the imbibition front. Because of this result, the vapour uptake $f_{\text{ads}}(t)$ in a combined process can be evaluated from a fit to the dynamics of pure gas adsorption (red curves in Figs. 11.2 and 11.3). Sec. 11.3.2 will make use of these empirical f_{ads} in order to derive a combined uptake model.

A peculiar difference between vapour adsorption dynamics could be resolved for the longest chain lengths $n = 9$ and 10, see Fig. 11.3. Both experiments show a higher uptake rate during spontaneous imbibition. This hints to a different mechanism needed in the presence of liquid in the pores.

So far, the combined uptake process has been interpreted as a dynamic capillary rise and an additional diffusion flux from the outside. This, however is only part of the total picture: The liquid menisci of the imbibition front also act as sources for molecular diffusion, in particular on the pore interfaces as a surface diffusion flux. As shown in Sec. 6.1, this is a considerable transport mechanism for 1-butanol in Vycor. As the surface diffusivity is primarily determined by the constant properties of the matrix and the interactions of the adsorbate with the matrix and within itself, a similar order of magnitude is plausible for the other alcohols, which in turn results in a constant contribution by this surface diffusion flux. In contrast to this, the gas phase diffusion flux scales with the vapour pressure and the analogous reduction of the pressure gradient according to Fick's first law (Eq. (5.6)). Due to this dependence, the transport on the surface becomes more and more important for total diffusion for less volatile liquids, as illustrated in Fig. 11.4. Qualitatively, this is consistent with the experimental observations. Quantitatively, an order of magnitude estimation can be made using the diffusivities calculated in Sec. 6.1: For 1-butanol, a ratio of diffusivities $D_{\text{Kn}}/D_S \sim 500$ was measured. In conjunction with the drop in vapour pressure by approximately three orders of magnitude from 1-butanol to 1-decanol (see App. B), a dominant surface diffusion flux for long chain lengths is expected.

Also note that the surface transport mechanism is equally expected for imbibition in sealed samples according to Sec. 10, which might slightly increase the measured Lucas-Washburn coefficients.

In addition, Figs. 11.2 and 11.3 also show a good match of the later stage of adsorption experiments to the second stage of the imbibition experiments for $n \leq 8$. The accelerated vapour uptake in this stage (III) of adsorption has been attributed to an additional mechanism

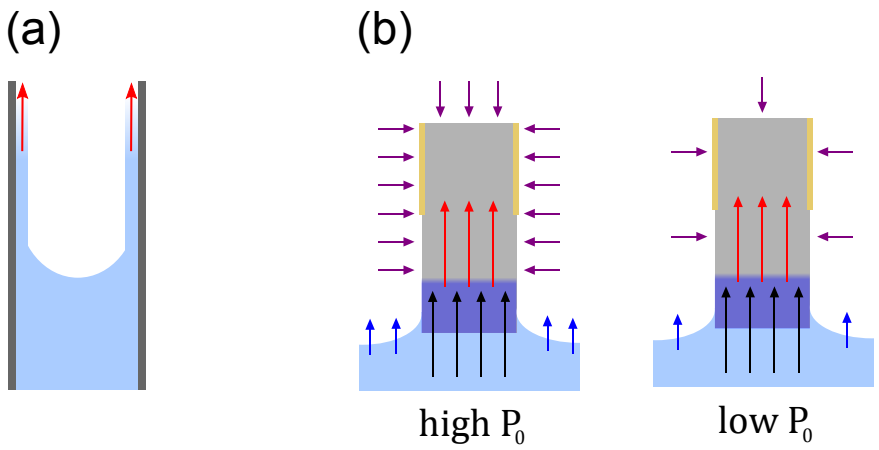

Figure 11.4.: Additional surface diffusion mechanism from liquid menisci. (a) For strongly interacting molecules, a surface diffusion flow contributes to the total transport. The liquid imbibition front acts as a diffusion source. This mechanism does not rely on evaporation and gas phase diffusivity, so that it is largely independent of the vapour pressure. (b) For high vapour pressures, if a gas phase diffusion flux is much higher than surface diffusion, adsorption from the gas phase is preferred and the additional mechanism is negligible. In contrast to this, for very low vapour pressures, adsorption from the gas phase is much lower and surface diffusion can become the dominant mechanism.

of spontaneous flow of the capillary condensate for high relative pore loadings, as discussed in Sec. 6.2.3. This hypothesis is confirmed at least qualitatively for all alcohols since a proportionality $f \propto \sqrt{t}$ is measured over a significant time span, starting at a consistent filling fraction $f \approx 0.6$. It is likely that this transition point is related to the network properties of the Vycor matrix. In the later stages, both depicted curves exhibit matching slopes for $n \leq 8$, while longer chain-lengths deviate from one another. This indicates a geometric similarity for the liquid flow mechanisms in both experiments. In case of the additional capillary flow during vapour adsorption, this in turn hints at a preferred condensation at the sample facet closest to the liquid reservoir instead of an isotropic liquid uptake. Further investigation of this final stage in terms of geometry dependence is needed in order to fully understand the dynamics. For now, the late stage of adsorption dynamics will not be considered for quantitative analysis.

In summary, the concurrent vapour uptake dynamics during imbibition of n-alcohols remains largely unchanged. For small chain lengths, there is no measurable difference to the vapour filling experiments from Sec. 6.2, while for long chain lengths, the uptake dynamics are slightly enhanced. This is attributed to an additional surface diffusion from the liquid menisci that is negligible when the gas phase diffusion flux is orders of magnitude larger, but significant otherwise. However, this effect is equally expected for imbibition in sealed

samples. Therefore, the experimental vapour adsorption curve that do not contain this third mechanism (red curves in Figs. 11.2 and 11.3) will be used later on in order to quantify the uptake rate of the additional adsorption.

11.3.2. Combined Uptake Dynamics

A series of imbibition experiments with n-alcohols ($n = 4$ to 10) has been conducted with sputter coated gold electrodes with full coverage of the sample sides (see Fig. 10.2(b)). For this configuration, a superposition of filling mechanisms is expected: spontaneous imbibition from the liquid reservoir and additional vapour uptake in the parts of the sample that are not yet reached by the liquid imbibition front.

Concerning the dielectric measurement, the same consideration from previous Secs. 4.1.2 and 10.1.2 apply to the combined uptake: First, it is assumed that a linear relation prevails between the local relative filling fraction $f(h)$ and the plateau value $\varepsilon'(\nu = 1\,\mathrm{MHz})$ in the real permittivity. Based on the results from the individual experiments, this has proven to be a good description in both the liquid-filled parts and the parts subjected to vapour adsorption. The total filling fraction $f(t)$ resulting from a superposition of both mechanisms can then be calculated from the normalized measured permittivity ε' of the entire sample,

$$\begin{aligned} f(t) &= \frac{\varepsilon'(t) - \varepsilon'(f=0)}{\varepsilon'(f=1) - \varepsilon'(f=0)} \\ &= \frac{\Delta\varepsilon'(t)}{\Delta\varepsilon'_{\mathrm{max}}}. \end{aligned} \tag{11.2}$$

In analogy to imbibition experiments, $\varepsilon'(f = 0)$ and $\varepsilon'(f = 1)$ denote the minimum and maximum permittivity measured after liquid insertion and sample immersion, which ensures an equal contribution from the stray capacitance that is removed in a difference $\Delta\varepsilon'$ (see Sec. 10.1.2). The individual permittivities are evaluated from the measured impedance spectra at $\nu = 1\,\mathrm{MHz}$ using the known sample geometry (l, d, h_0) using Eq. (10.9)

Experimental results of the normalized permittivity $\Delta\varepsilon'(t)/\Delta\varepsilon'_{\mathrm{max}}$ are shown in Fig. 11.5(a) and (b). Both graphs depict the data as a function of $\sqrt{t}$ in order to compare to Lucas-Washburn dynamics. The measured permittivity signals for the combined uptake process qualitatively feature the same three stages introduced for pure imbibition: An initial phase with rapid changes and an approach to stationary dynamics (I), a linear stage (II) in $\sqrt{t}$-scaling consistent with the Lucas-Washburn model, and a final stage (III) that exhibits a gradual slowdown of dynamics, which is attributed to the imbibition front broadening.

On closer inspection, it is evident that the effects in the initial stage (I) are even more pro-

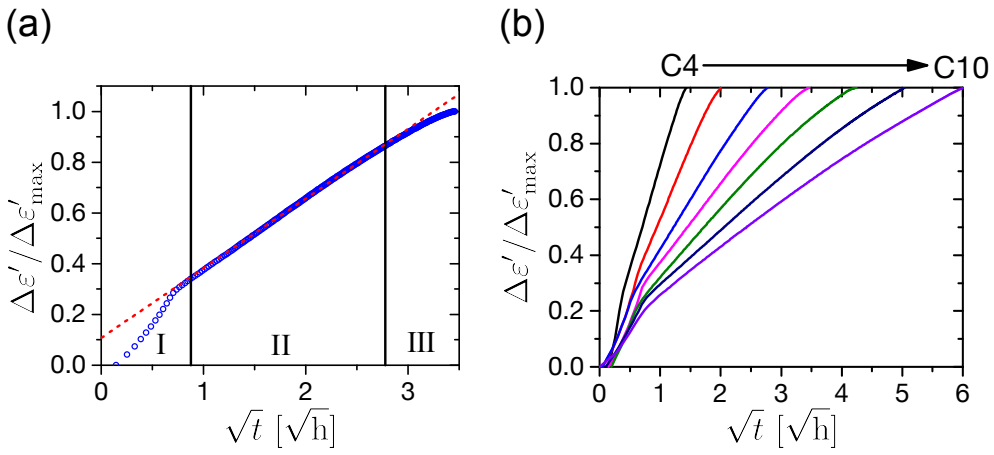

Figure 11.5.: Dynamics of combined liquid and vapour uptake for n-alcohols. (a) The combined uptake experiments share many characteristics with pure imbibition dynamics: Three different stages are observed (I) initial effects dominate, (II) linear stage over $\sqrt{t}$ indicates Lucas-Washburn dynamics, (III) broadened imbibition front gradually reaches upper bound of the sample. (b) The same qualitative observations are made for all alcohols. In accordance to the fitting of pure imbibition curves, apparent Lucas-Washburn coefficients can be extracted from stages (II), see text.

nounced than for imbibition dynamics in sealed samples. Two reasons can be given for this behaviour: First, the additional vapour uptake is particularly strong in the beginning. This results from the intrinsic dynamics measured in Sec. 6.2.3 and the high ratio of accessible sample volume for vapour adsorption in relation to the liquid-filled part of the sample. Second, an additional flow contribution is given by parasitic imbibition from the adhering liquid menisci on the sample sides, which is depicted in Fig. 11.6. Since the sample surface is not sealed, liquid enters the pore space from all adjacent sources, including the curved macroscopic menisci. At first, this leads to an inherent curvature of the imbibition front. However, numerical simulations show that this curvature flattens the farther the liquid-filled regions proceed in the sample volume, see App. D. After that, liquid uptake is qualitatively and quantitatively consistent with Lucas-Washburn theory, so that stage (II) is not concerned by this effect.

Accordingly, as depicted in Fig. 11.5(b), linear stages (II) for all alcohols constitute the majority of the duration of the experiments. Due to this apparent match to the imbibition dynamics, a modified Lucas-Washburn coefficient $\tilde{c}_h$ can be extracted from the slopes $\Delta f/\Delta\sqrt{t}$ of a linear fit according to

$$\tilde{c}_h = h_0 \frac{\Delta f}{\Delta\sqrt{t}} = h_0 \frac{\Delta\left[\frac{\Delta\varepsilon'(t)}{\Delta\varepsilon'_{\max}}\right]}{\Delta\sqrt{t}}. \tag{11.3}$$

A comparison between these apparent coefficients $\tilde{c}_h$ and the results from imbibition ex-

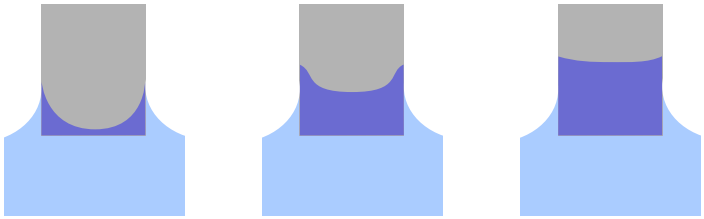

Figure 11.6.: Illustration of parasitic imbibition from adhering liquid. For unsealed samples, the liquid menisci on the macroscopic sample surface are additional sources for liquid entering the pore space. In the initial phase (I), this produces an artificially enhanced uptake rate as well as a curved imbibition front. Over the course of the experiment, as resolved by numerical simulation (see App. D), the front curvature flattens continuously, so that stage (II) dynamics are not affected.

periments with sealed samples is shown in Fig. 11.7. In comparison to the experiments with sealed samples, the coefficients for combined uptake are systematically higher, consistent with an additional uptake mechanism. The deviation from the results of Sec. 10.2 is particularly strong for short alcohol chain lengths and gradually approaches these values for long chain lengths which is expected from the scaling of the diffusion flux with the vapour pressure. Only 1-decanol ($P_0 \approx 1\,\mathrm{Pa}$) exhibits comparable Lucas-Washburn coefficients for both experiments

In an experimental context, this shows that in an environment containing an additional vapour phase, the measured Lucas-Washburn coefficients tend to higher values than for the sole imbibition process. The more volatile a liquid, the larger the impact on apparent dynamics. For moderate vapour pressures, the additional vapour uptake could easily be mistaken as a different flow boundary condition in a Lucas-Washburn law, as different theoretical c_h fit the resulting data in Fig. 11.7 for heptanol to decanol.

It should be noted that the studied case of a saturated atmosphere constitutes an upper bound for the expected deviation. For experiments in a reduced vapour atmosphere, e.g. in an open laboratory setup, the contribution from vapour uptake is expected to be lower, since the uptake rate directly relies on the pressure gradient. Still, if not explicitly considered in total dynamics, the derived boundary conditions are erroneous for partial pressures $\gtrsim 1\,\mathrm{Pa}$.

11.3.3. Empirical Modelling of Combined Uptake

In [119], a first approach to empirical modelling of the combined uptake has been proposed: By quantifying the concurrent adsorption dynamics during imbibition with a fit function $f_{\mathrm{ads}} = c_a/h_0\sqrt{t}$, a coefficient c_a for the adsorption dynamics as a Lucas-Washburn equivalent has been evaluated. Assuming a constant contribution, independent of the rise height of liquid, a corrected imbibition coefficient $c_{\mathrm{h,corr}} = c_h - c_a$ could be calculated. For 1-butanol,

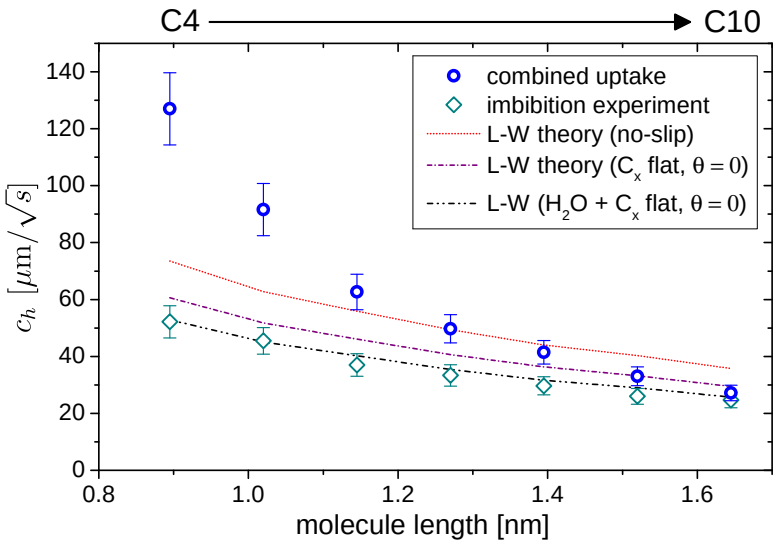

Figure 11.7.: Comparison of Lucas-Washburn coefficients for pure imbibition and combined liquid and vapour uptake. The apparent $\tilde{c}_h$ for combined uptake are systematically larger than the values obtained for sealed samples, with a critical deviation for the most volatile alcohols. This is consistent with the different time scales of vapour uptake dynamics, see Sec. 6.2. Solely for 1-decanol, the results show an approximate match between both experiments. For liquids in the intermediate range, if misinterpreted as an imbibition process, the combined dynamics will result in different Lucas-Washburn boundary conditions fitting the experimental data, as shown in comparison by the different lines.

this resulted in an approach to the theoretical prediction but still, the resulting $c_{\mathrm{h,corr}}$ did not accurately match the experimental observations.

A better empirical model for a combined liquid and gas uptake has been derived as part of this work, which has been published in [120]. First, let us assume that both partial processes occur in a non-interacting superposition. Based on the unchanged adsorption dynamics in the presence of an imbibition front, this approximation can be justified for the experimental time frame of Sec. 11.3.2. In terms of the liquid uptake, this implies that Lucas-Washburn dynamics also remain unchanged, i.e. the preadsorbed layers result in the same boundary condition as for intrinsic imbibition process.

The momentary filling $f(t)$ at any point of combined uptake can be expressed by the sum of Lucas-Washburn imbibition $f_{\mathrm{LW}}(t) = h(t)/h_0$ and a contribution for vapour adsorption, $f_{\mathrm{ads}}(t)$,

$$f(t) = f_{\mathrm{LW}}(t) + f_{\mathrm{ads}}(t). \tag{11.4}$$

Here, the partial filling $f_{\mathrm{ads}}(t)$ results from the successive uptake of vapour with a variable rate $r_{\mathrm{ads}}(t)$ in the continuously shrinking part of the sample volume without liquid filling. At

a specific time t, it can be evaluated by the integration

$$\begin{aligned} f_{\text{ads}}(t) &= \int_{\tilde{t}=0}^{t} \frac{h_0 - h(\tilde{t})}{h_0} r_{\text{ads}}(\tilde{t})\, \mathrm{d}\tilde{t} \\ &= \int_{\tilde{t}=0}^{t} \left(1 - f_{\text{LW}}(\tilde{t})\right) r_{\text{ads}}(\tilde{t})\, \mathrm{d}\tilde{t}. \end{aligned} \tag{11.5}$$

As discussed in Sec. 11.3.1, it is possible to make an empirical prediction of $r_{\text{ads}}(t)$ by quantifying the adsorption dynamics with partial electrodes using an appropriate fit. In these experiments, the entire sample volume is accessible for adsorption at all times and Eq. (11.5) simplifies to

$$\begin{aligned} \tilde{f}_{\text{ads}}(t) &= \int_{\tilde{t}=0}^{t} r_{\text{ads}}(\tilde{t})\, \mathrm{d}\tilde{t} \\ \Leftrightarrow r_{\text{ads}}(\tilde{t}) &= \frac{\partial}{\partial \tilde{t}} \tilde{f}_{\text{ads}}(\tilde{t}). \end{aligned} \tag{11.6}$$

A third order polynomial fit in $\sqrt{t}$ has been applied to the experimental data,

$$\tilde{f}_{\text{ads}}(t) = \sum_{i=1}^{3} a_i \sqrt{t^i}, \tag{11.7}$$

which is a good empirical model for the experimental data (red curves in Figs. 11.2 and 11.3) within the time frame $t \in [0, t_{\text{max}}]$, where t_{max} is the respective time to reach complete filling in the combined adsorption and imbibition experiment. Tab. 11.1 lists the respective set of coefficients a_i derived for the different alcohols.

Table 11.1.: Third order polynomial fit parameters for adsorption dynamics of n-alcohols in the sample *vyc_im_1*, see App. A. The non-linear fit function $f = \sum_{i=1}^{3} a_i \sqrt{t^i}$ was applied to each experimental vapour uptake curves for partial electrodes (red symbols in Figs. 11.2 and 11.3).

n	a_1 $[1/\sqrt{\text{h}}]$	a_2 $[1/\text{h}]$	a_3 $[1/\sqrt{\text{h}^3}]$
4	0.096	0.232	0.0333
5	0.115	0.0722	0.00218
6	0.097	0.039	-0.00382
7	0.0741	0.0148	-0.00109
8	0.0374	0.0137	-0.00135
9	0.0138	0.0161	-0.0016
10	0.0256	0.0052	-0.0006

According to Eq. (11.6), the differentiation of Eq. (11.7) yields an empirical expression for $r_{\text{ads}}(t)$ for the specific liquid and sample geometry. In turn, this can be used in the integration of vapour uptake in Eq. (11.5),

$$f_{\text{ads}}(t) = \int_{\tilde{t}=0}^{t} \left(1 - f_{\text{LW}}(\tilde{t})\right) \frac{\partial}{\partial \tilde{t}} \sum_{i=1}^{3} a_i \sqrt{\tilde{t}^i}\, \mathrm{d}\tilde{t}. \tag{11.8}$$

By omitting stages (I) and (III) of the imbibition dynamics, Lucas Washburn dynamics can be assumed ($f_{\text{LW}}(\tilde{t}) = c_h \tilde{t}^{1/2}/h_0$), where c_h can be chosen to a specific boundary condition. The integral can then be calculated easily and $f_{\text{ads}}(t)$ takes the simple form

$$f_{\text{ads}}(t) = \tilde{f}_{\text{ads}}(t) - f_{\text{LW}}(t) \sum_{i=1}^{3} \frac{i}{i+1} a_i \sqrt{t^i}. \tag{11.9}$$

Finally, inserting Eq. (11.9) into Eq. (11.4) yields the total empirical uptake model,

$$f(t) = \tilde{f}_{\text{ads}}(t) + f_{\text{LW}}(t) \left[1 - \sum_{i=1}^{3} \frac{i}{i+1} a_i \sqrt{t^i}\right]. \tag{11.10}$$

Fig. 11.8 depicts a model comparison for 1-pentanol to the experimental results from Sec. 11.3.2. In the calculation of Eq. (11.10), the Lucas-Washburn coefficient has been chosen to the experimental value for sealed samples, $c_h = 45.5\,\mu\text{m}/\sqrt{\text{s}}$, see Tab. 10.1.

Although $f(t)$ is obviously not proportional to $\sqrt{t}$ according to Eq. (11.10), the sum of Lucas-Washburn dynamics and the first order of adsorption dominate total dynamics when higher order coefficients a_i for the empirical adsorption are sufficiently small. For the experimental values, this results in a quasi-linear graph for $\sqrt{t} \geq 0.5\sqrt{\text{h}}$, which is in good agreement with stage (II) of the combined uptake dynamics. The model only exhibits a constant difference from the experimental values due to the parasitic initial effects, e.g. additional imbibition from menisci. For further quantitative comparison, the averaged slopes of the empirical curves were extracted for the time interval of experimental stages (II), which yields an equivalent $c_h' = h_0 \Delta f / \Delta\sqrt{t}$. This procedure has been applied to all alcohols and results are compared as a red dashed line to experimental values in Fig. 11.9.

For all liquids, the empirical c_h' are in good agreement with the apparent Lucas-Washburn coefficients of the combined experiments. It can be concluded that the assumption of a simple superposition of vapour uptake and capillary flow provides a good description of the total dynamics within the experimental stage (II).

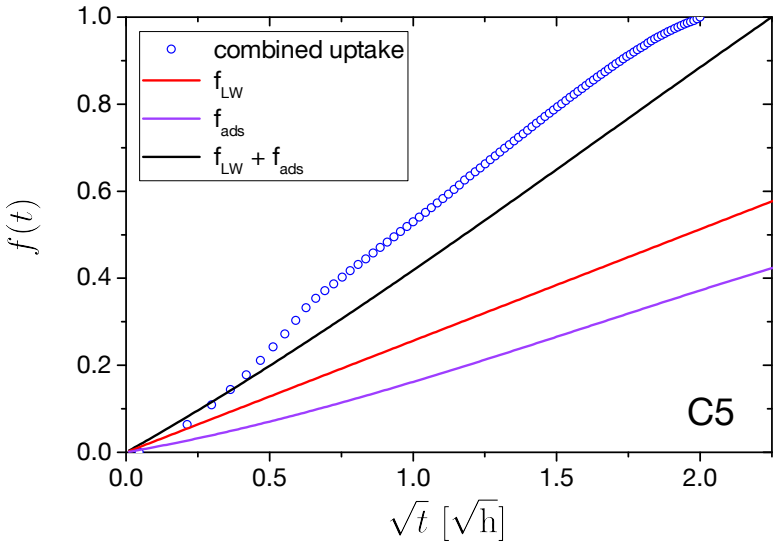

Figure 11.8.: Empirical combined uptake model for 1-pentanol in comparison to experimental data. Here, Lucas Washburn dynamics f_{LW} with the experimental coefficient c_h for a sealed sample have been assumed. With the empirical adsorption parameters from Tab. 11.1, Eq. (11.9) can be used to calculate the relative uptake via the vapour phase, f_{ads}. The sum of both partial mechanisms produces a quasi-linear curve that is in good agreement with the slope of stage (II) in the combined uptake experiment. The mean slope of the empirical curve in this region (black line) has been evaluated to an equivalent c_h' (red dashed line in Fig. 11.9.

11.4. Summary

When gas and liquid uptake in a nanoporous matrix occur in parallel, the dynamics of the individual mechanisms add up to total transport. By studying the concurrent vapour adsorption dynamics far from the imbibition front, it could be shown that for short-chain alcohols, no alteration of uptake rates results from the additional liquid filling. In contrast to this, long-chain alcohols show an increased uptake rate, which is interpreted as an additional mechanism of surface diffusion flow that originates from the liquid menisci.

The combined uptake has been studied experimentally for samples with permeable surfaces in a saturated vapour phase, which revealed an apparent qualitative match to imbibition dynamics for sealed samples. However, a systematic quantitative discrepancy could be noted that increased dramatically towards more volatile liquids. While the apparent Lucas-Washburn coefficients for short-chain alcohols are far above the maximum theoretical flow rate for volatile liquids, only slightly increased c_h were measured for moderate vapour pressures. From an experimental point of view, this entails that measured Lucas-Washburn coefficients without sufficient environmental control or sealing of the samples can be mistaken for

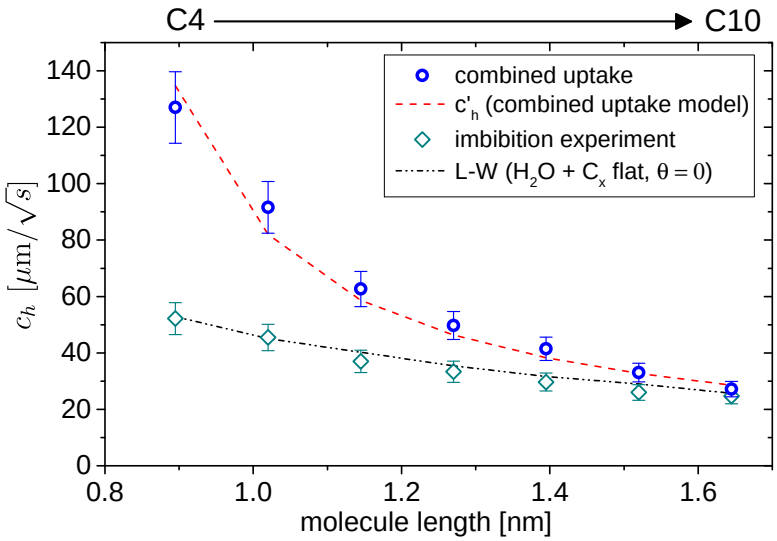

Figure 11.9.: Comparison of apparent Lucas-Washburn coefficients to empirical modelling. The coefficients c_h' derived from the combined imbibition and adsorption model show a good match to experimental data for all alcohols. For the calculation of $f(t)$ in Eq. (11.10), c_h has been assumed to the experimental values for sealed samples.

erroneous boundary conditions of capillary flow, e.g. smaller extent of the sticking wall layer than expected.

For all alcohols, the dynamics of the combined uptake process has been compared to an empirical model using a non-interacting superposition of Lucas-Washburn capillary dynamics as measured in Sec. 10.2.2 and a simple representation of vapour uptake dynamics obtained by a third order polynomial fit to adsorption data. The resulting superposition of both partial contributions results in a nearly linear function over $\sqrt{t}$. This indicates that Lucas-Washburn dynamics are robust for this additional mechanism, which is consistent with qualitative observations made for permeable samples. In a quantitative comparison to the combined uptake experiments, the empirical model provides a good match to the apparent Lucas-Washburn coefficients within the experimental error margin.

IV

Concluding Remarks

12 Conclusion

In this work, the equilibrium and dynamic uptake of n-alcohols in mesoporous Vycor glass was studied extensively. The experimental part includes a sorption isotherm and step-wise adsorption kinetics, stationary liquid flow experiments as well as dynamic filling by vapour adsorption, liquid capillary flow and a combination of both mechanisms.

The main experimental method used is dielectric spectroscopy in a frequency window from $\nu = 1\,\mathrm{kHz}$ to $2\,\mathrm{MHz}$. Although the spectra for Vycor with additional n-alcohol filling exhibit large effects of ionic conductivity and interfacial polarization due to intrinsic matrix contaminations, the real permittivity for higher frequencies $\nu \approx 1\,\mathrm{MHz}$ exhibits a section of only weak frequency dependence. In good approximation, a linear relation between this effective permittivity and the product of the static liquid permittivity and the relative filling fraction N/N_0 is found. This allows the detection of pore filling in the effective sample permittivity, with consistent and reproducible results. Moreover a spatial selectivity for an uptake measurement could be achieved by limiting the electrode area on the sample, which is a key advantage to gravimetric experiments.

Using the dielectric setup, the isothermal equilibrium adsorption of 1-butanol has been studied at room temperature, reproducing a gravimetric sorption isotherm recorded by Jones and Wade [66]. The butanol layer adsorption is limited to a monolayer on top of a residual water layer, indicating strong but short-ranged interactions resulting from H-bonds with the pore walls. The determined layer thickness including water, $t_{\mathrm{ML+H_2O}} = 0.75 \pm 0.10\,\mathrm{nm}$, is in good agreement to a stacked layer of water and butanol and other results below. When applying the Kelvin equation to the stage of capillary condensation, a finite contact angle $\theta = 38^\circ$ is needed. This autophobicity of the continuum-like alcohol capillary bridge to the strongly adsorbed wall layer can be explained by modified intermolecular interactions due to the directional H-bonds and is known to occur in this system [66].

The same experiment also yields gas uptake kinetics for incremental pressure steps. The asymptotic uptake curves were analysed for layer adsorption and desorption with an analytical model [86]. A variation of the diffusivity with pore filling could be deduced for different filling states, in good agreement to experimental results for NMR measurements [88]. The total pore diffusivity systematically exceeds the estimate for Knudsen diffusion in the gas phase, which is interpreted as a significant additional hopping mechanism in the partially occupied adsorbate layer. The corresponding surface diffusivity shows an equal qualitative dependence

on relative pore filling for adsorption and desorption, with a defined maximum for a nearly complete monolayer, indicating repulsive forces between the adsorbate molecules.

In addition, the continuous vapour uptake $N/N_0 = 0 \rightarrow 1$ has been probed for all alcohols. All kinetics exhibited three characteristic stages: (I) fast initial changes, indicating variable surface diffusion and onset of capillary condensation, (II) stationary uptake $\propto t$, interpreted as a constant diffusion flux to capillary bridges with homogeneous distribution in the matrix, (III) increased uptake rates for high pore loadings $N/N_0 > 0.6$ due to an additional mechanism of liquid capillary flow $\propto \sqrt{t}$. The relative importance of stages varies critically with the vapour pressure in accordance to the scaling of vapour pressure, so does the required time for total filling. For volatile alcohols, filling times are comparable to liquid uptake.

Stationary, pressure-driven flow rates for liquid n-alcohols in Vycor systematically indicate a sticking wall layer independent of the applied pressure. For all liquids, the needed slip lengths b for pore radii $r_0 = 6.2\,\mathrm{nm}$ are comparable to typical molecular dimensions. In detail, for $n \geq 6$, the findings indicate a co-adsorption of a flat alcohol and water monolayer, the latter of which is expected from sample preparation, whereas for 1-butanol, a better match is found for a stacked multilayer of water and flat alcohol molecules. For smaller pore radii $r_0 = 3.1\,\mathrm{nm}$, a reduction in slip length for 1-butanol to the range of a water monolayer was measured, indicating a transition from multi- to monolayer sticking.

The dynamics of spontaneous capillary rise for n-alcohols in Vycor are in very good agreement to classical Lucas-Washburn theory $h(t) = c_h\sqrt{t}$ for the majority of the experiment. The determined coefficients c_h require a sticking wall layer for all liquids. As two parameters (slip length b, contact angle θ) are unknown for the dynamic situation, no definite boundary condition can be derived. However, assuming a very small contact angle $\cos\theta \approx 1$ due to precursor wetting, a remarkably constant slip length is calculated for all alcohols that is also in good agreement to the stacked water and alcohol layer. If the assumption for θ is indeed correct, a disagreement between boundary conditions for stationary and capillary flow of long-chain alcohols is found. This could result from a partial elution of the water monolayer for stationary flow experiments which can be excluded for imbibition. Otherwise, a finite contact angle is needed: For this case, a confidence range of θ was calculated from the experimental error margins. Due to the limited precision of the experimental technique, multiple boundary layer structures (water or flat alcohol, stacked water + alcohol) are then plausible if autophobicity persists in a dynamic situation.

In addition to the individual mechanisms, the combined spontaneous liquid and vapour uptake dynamics were studied. Results show a remarkable qualitative similarity to the spontaneous imbibition dynamics, albeit with larger parasitic effects in the initial stage. Though, when

trying to evaluate an apparent Lucas-Washburn coefficient c_h, a quantitative deviation from the values for imbibition is noted for all liquids. In particular, volatile alcohols exhibit coefficients exceeding the maximum theoretical uptake for no-slip flow, whereas the coefficients for longer chain lengths could be mistakenly interpreted as different flow boundary conditions. This is an important consideration when interpreting Lucas-Washburn coefficients obtained without environmental control or sample sealing.

For the concurrent vapour adsorption during spontaneous imbibition, it has been suspected that the presence of liquid menisci results in a difference of adsorption kinetics compared to pure vapour uptake. By a selective placement of electrodes on the upper part of the sample, this could be largely excluded as long as the liquid-filled regions are well outside the electrode range. A perfect match of concurrent and pure vapour uptake dynamics was observed for short-chain alcohols ($n < 8$). In case of 1-nonanol and 1-decanol, an increased uptake rate during imbibition hints to a third transport mechanism by surface diffusion from the liquid menisci that is consistent with the suspected precursor wetting.

Finally, an empirical combined uptake model has been derived using a non-interacting superposition of Lucas-Washburn capillary flow and vapour adsorption limited to the pores containing no liquid. The adsorption dynamics can be quantified using a third order polynomial fit, the liquid flow is modelled using the experimental Lucas-Washburn coefficients c_h from imbibition experiments. Then, a total empirical uptake curve nearly proportional to $\sqrt{t}$ is found, in accordance to the observed dynamics of combined uptake experiments. A quantitative comparison of the average slopes also shows a very good match to the measured apparent c_h of combined flows.

In summary, when comparing the results for all individual experiments, it is clear that the alcohol boundary layer on the pore walls has outstanding physical characteristics in comparison to the rest of the pore volume. During dynamic adsorption, a partially occupied wall layer shows a remarkable contribution to molecular diffusion by a relatively strong additional surface hopping mechanism, enhancing the total transport significantly. For complete occupation though, a significant immobilization and modified intermolecular interactions to the remaining pore filling become apparent as a finite contact angle to capillary condensate. For liquid flow, the boundary layer manifests as a universal negative slip length comparable to typical molecular dimensions. Most notably, a great consistency for 1-butanol could be observed for equilibrium adsorption, stationary, and spontaneous flow. The extent of the boundary layer indicates a stacked layer structure of water with a flat alcohol monolayer $b \approx 0.685\,\mathrm{nm}$ in all experiments, which demonstrates the impressive capability of the macroscopic techniques to resolve effects on a sub-nanometre scale.

13 Outlook

In the present work, the experimental technique of dielectric spectroscopy has not been used to its full extent. In the low-frequency domain, effects of high conductivity have dominated the spectra and dipolar relaxations could not be resolved for any liquid. By either extending the measuring range to higher frequencies or cooling, one can access this additional information. In turn, the relaxation behaviour can possibly help in the interpretation of confinement induced effects on molecular mobility.

For equilibrium adsorption, a combined measurement of a volumetric and dielectric isotherm has already been planned for this work but ultimately failed due to experimental problems discussed in Sec. 4.3.2. Instead of the assumed linearity $\varepsilon' \propto f$, a comparison of both isotherms yields a precise calibration function $\varepsilon'(f)$, which can be individually determined for adsorption and desorption.

The transient and equilibrium adsorption study can also be extended for more alcohols ($n \in 1, 2, 3, 5, 6, ...$) in order to compare kinetics and sorption isotherms. Concerning the kinetics, this could be used to determine the variation of surface diffusivity as a function of the molecular properties. As for the sorption isotherms, it is interesting to check for variations of the adsorbate layer thickness, Frenkel-Halsey-Hill interaction exponent and a potential autophobicity contact angle.

For dynamic vapour uptake experiments, a lack of theoretical modelling did not allow for an in-depth quantitative comparison. As analytical models depend on specific knowledge of the pore network geometry, a better alternative is to compare the measured kinetics to MD computer simulations in a pore network. In particular, the three individual stages each pose questions: Is stage I correlated with a surface diffusivity? What is the reason for the constant uptake rate in stage II? And finally, what is the nature of the capillary flow mechanism and its defined onset at $N/N_0 \approx 0.6$ in stage III?

As a continuation of the stationary flow experiments, the pore size dependent change in slip length for 1-butanol could be investigated for more liquids and matrices. This should allow a more in-depth analysis on the transition between mono- and multilayer sticking. The above considerations for dielectric spectroscopy also apply to this experiment: If a dipole relaxation can be resolved, the experimental study of velocity dependent effects in the spectra should be revisited.

With the equilibrium adsorption, stationary flow and spontaneous imbibition experiments in this work, a consistent study on the macroscopically averaged aspects of the n-alcohol boundary layer and possible microscopic interpretations have been presented. It would be of great interest to use appropriate structure resolving methods in a dynamic environment, e.g. for flows on planar substrates, in order to check the hypothesis of a stacked layer formation. Here, specific knowledge on the dynamic boundary condition allows a better comparison of the experimental data.

Last but not least, the empirical combined uptake model has shown promising results when a specific sample geometry is used. It would be beneficial to systematically study the geometry dependence of vapour filling dynamics in order to improve the predictive capabilities. Ideally, a generalized model incorporating a relation to vapour and liquid material constants and matrix parameters can be derived.

V

Appendix

A Sample Reference

A.1. Supplier Information for Vycor

Since Corning Inc. discontinued the production of porous Vycor glasses, the raw material for the samples in this work was purchased from a secondary supplier: 'Advanced Glass & Ceramics', St. James, NC, USA. The Vycor samples were produced according to the same specifications [4] albeit with a variation in pore diameters and porosities, likely due to variability of the production process. Thus, a characterization isotherm according to Sec. 4.2 was performed for every Vycor batch.

A.2. Reference Data

In the following, the samples used in this work are listed with their respective macroscopic geometries and microscopic parameters. The lists are split for the different sample geometries depending on the experimental application. Analogous to the isotherm shown in Sec. 4.2, the samples have been subjected to high temperatures $T > 200\,^{\circ}\mathrm{C}$ so that no residual water is present upon characterization, resulting in $\bar{r}_0$ and Φ without preadsorbed layers.

A.2.1. Thin, Irregularly Shaped Samples

For the equilibrium and transient adsorption experiments in Secs. 4.3 and 6.1 as well as the dielectric reference spectra in Sec. 2.3, thin, polished samples were used. In the process of polishing, the sample edges are slightly damaged, causing an irregular shape. This however has no significant impact on the experiments, since no stray field effects remain in the measuring signal, see Sec. 4.1.2 and App. C. Table A.1 lists these samples. The sample area has been evaluated by image analysis.

Table A.1.: Sample reference for thin, irregularly shaped samples.

sample ID	**thickness** d [µm]	**area** A [mm^2]	**porosity** Φ	**mean pore radius** $\bar{r}_0$ [nm]
vyc_iso_1	651	81.4	$27.5 \pm 0.5\,\%$	4.5 ± 0.2
vyc_iso_2	658	43.2	$27.5 \pm 0.5\,\%$	4.5 ± 0.2

A.2.2. Cylindrical samples

In forced throughput experiments, cylindrical Vycor samples were used, see Sec. 8. These all exhibit the same radius $R = 7\,\mathrm{mm}$. The electrodes on these samples cover a concentric circular part of both parallel sides with radius $r_{\mathrm{el}} = 5\,\mathrm{mm}$. Table A.2 lists these samples along with the respective liquid used.

Table A.2.: Sample reference for cylindrical samples used in forced throughput experiments.

sample ID	**liquid used**	**thickness** d [mm]	**porosity** Φ	**mean pore radius** $\bar{r}_0$ [nm]
vyc_tp_1	1-decanol	5.52	$25.5 \pm 0.5\,\%$	6.2 ± 0.2
vyc_tp_2	1-octanol	5.32	$25.5 \pm 0.5\,\%$	6.2 ± 0.2
vyc_tp_3	1-hexanol	3.82	$25.5 \pm 0.5\,\%$	6.2 ± 0.2
vyc_tp_5	1-butanol	2.90	$25.5 \pm 0.5\,\%$	6.2 ± 0.2
vyc_tp_7	1-octanol	3.74	$25.5 \pm 0.5\,\%$	6.2 ± 0.2
vyc_tp_8	1-butanol	1.96	$29.1 \pm 0.5\,\%$	3.1 ± 0.2

A.2.3. Cuboid samples

For spontaneous uptake experiments in Secs. 6.2, 10 and 11, a cuboid sample geometry has been used. Details for the samples are listed in Tab. A.3.

Depending on the experiment, the electrodes either covered the entirety of the two largest faces ('full electrodes') or a limited rectangular part from the top of the sample ('partial electrodes'). In experiments with sealed samples, the empty Vycor matrices were coated with epoxy resin *UHU plus sofortfest* on all sides[1], copper plates were applied as electrodes ('solid electrodes'). Subsequently, one side was reopened for liquid uptake by mechanical grinding.

All cuboid samples were prepared from the same Vycor batch, resulting in an identical porosity $\Phi = 32.3 \pm 0.5\,\%$ and mean pore radius $\bar{r}_0 = 4.5 \pm 0.2\,\mathrm{nm}$.

[1] Due to the extremely high viscosities and entangled structure of epoxy molecules, the uptake into the pores and the resulting reduction in pore volume is negligible.

Table A.3.: Sample reference for cuboid samples used in imbibition and vapour filling experiments.

sample ID	**electrode**	**depth** d [mm]	**length** l [mm]	**height** h_0 [mm]	**remarks**
samples for (concurrent) vapour uptake					
vyc_im_1	partial	1.77	13.4	13.35	$h_{\mathrm{el}} = 6.7\,\mathrm{mm}$, all liquids
sealed samples for imbibition experiments					
vyc_im_2	solid	1.95	9.8	9.6	butanol
vyc_im_3	solid	1.9	10.6	13.8	pentanol
vyc_im_4	solid	1.55	10.4	12.2	hexanol
vyc_im_5	solid	1.75	10.35	13.5	heptanol
vyc_im_6	solid	1.55	10.3	12.2	octanol
vyc_im_7	solid	1.7	10.3	13.5	nonanol
vyc_im_8	solid	1.55	10.1	13.5	decanol
samples for combined uptake experiments					
vyc_im_9	full	2.2	10.45	13.3	but-/oct-/nonanol
vyc_im_10	full	2.2	10.65	13.55	pent-/hex-/hept-/decanol

B Properties of the Liquids

B.1. General Properties of n-Alcohols

The n-alcohols are a class of organic, aliphatic molecules containing a functional OH-group. The molecular formula for this regular series can be represented in the form $C_nH_{2n+2}O$. At room temperature ($T = 298\,\mathrm{K}$), they are colourless liquids for $n = 1$ to 11.

Structurally, n-alcohols consist of an alkyl chain with a terminating, functional OH-group, see Fig. B.1. Due to a difference in electronegativity between oxygen and hydrogen, the O−H-bond is permanently polarized, resulting in a constant dipole moment for the molecules and therefore a high static permittivity, see Tab. B.2. This makes n-alcohols a suitable choice for dielectric spectroscopy experiments, as a high resolution to molecular concentrations can be achieved.

For this work, the chain lengths $n = 4$ to 10 have been used, as listed in Tab. B.1.

Table B.1.: Reference of alcohols used.

n	name	manufacturer	purity	remarks
4	1-butanol	Grüssing GmbH	$\geq 99\,\%$	for imbibition
4	1-butanol	Sigma-Aldrich	$\geq 99.8\,\%$	for equilibrium adsorption
5	1-pentanol	Sigma-Aldrich	$\geq 99\,\%$	$< 0.1\,\%$ H_2O
6	1-hexanol	Alfa Aesar	$\geq 99\,\%$	–
7	1-heptanol	Alfa Aesar	$\geq 99\,\%$	–
8	1-octanol	Merck	$\geq 99\,\%$	–
9	1-nonanol	Merck	$> 98\,\%$	–
10	1-decanol	Alfa Aesar	$> 98\,\%$	–

B.2. Material Constants

For the experiments, all material constants of the alcohols have been extracted from the Landolt-Börnstein compendium for the appropriate temperatures. As a reference of material constants, Tab. B.2 lists these parameters for a fixed temperature $T = 298\,\mathrm{K}$.

Table B.2.: Material constants for n-alcohols. The temperature for all material constants is $T = 298\,\mathrm{K}$.

n	**viscosity** η [mPa s] [121]	**surface tension** σ [$\frac{\mathrm{mN}}{\mathrm{m}}$] [122]	**density** ρ [$\mathrm{kg/m^3}$] [123]	**vapour pressure** P_0 [Pa] [124]	**permittivity** $\varepsilon(\nu = 0\,\mathrm{Hz})$ [36]
4	2.81	23.89	807	850	17.5
5	3.50	25.15	811	255	15.1
6	4.45	25.31	815	58.0	13.2
7	5.85	26.02	819	32.4	11.3
8	7.41	26.65	822	11.1	10.1
9	9.35	26.97	824	3.76	8.54
10	11.4	27.74	827	1.17	7.76

B.3. Molecule Geometry

A visual representation of the three-dimensional molecular structure can be found in Fig. B.1. In the present structure, n-alcohols are rod-like molecules that exhibit a nearly constant height and width over the length of the carbon chain, see Fig. B.2, with a variable chain length depending on the number of carbon atoms.

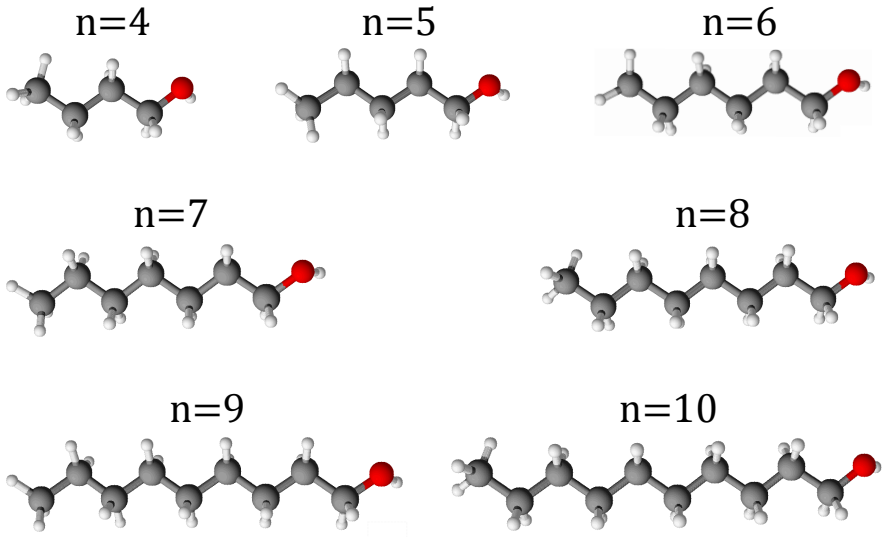

Figure B.1.: Molecular structure of n-alcohols. Different atoms are colour-coded: black: C, red: O, white: H. Bond lengths and angles persist for different chain lengths, see text.

Numerical values for molecular dimensions can be approximated from bond lengths, bond angles and the van-der-Waals radii of the outermost atoms (hydrogen). Bond lengths and van-

der-Waals radii are known from crystallographic data obtained by x-ray or neutron diffraction [125, 126], bond angles are largely determined by the hybridization state of the molecules: all carbon atoms and oxygen atoms in n-alcohols are sp^3-hybridized, resulting in bond angles close to the tetrahedral angle $\alpha \approx 109.5°$ [127].

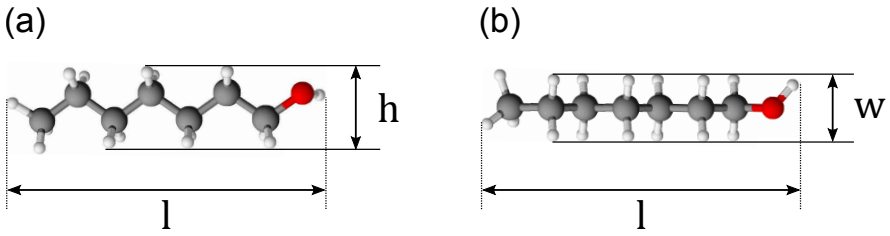

Figure B.2.: Molecular dimensions of n-alcohols, here 1-heptanol. (a) front view, (b) top view. The height h, width w and length l of the molecules can be calculated using structural data.

For all alcohols, the molecular width w and height h as indicated in Fig. B.2 is equal in size as it does not depend on the number of carbon atoms but only the spatial arrangement of the opposing CH_2-groups in the alkyl chain. Both parameters can be evaluated to $w = 418\,\mathrm{pm}$ and $h = 420\,\mathrm{pm}$. Regarding the molecular length l, a constant contribution for all alcohols results from the terminating CH_3 and OH-groups, which sums up to $l_1 = 520\,\mathrm{pm}$. Besides this first carbon atom, each added CH_2-group results in an additional length $l_2 = 128\,\mathrm{pm}$. Thus, a general formula for the length of n-alcohols is given by

$$l(n) = 520\,\mathrm{pm} + (n-1)128\,\mathrm{pm}. \tag{B.1}$$

The geometric values are tabulated for all used alcohols in Tab. B.3.

Table B.3.: Molecular geometry of n-alcohols.

n	**width** w [pm]	**height** h [pm]	**length** l [nm]
4	418	420	0.904
5	418	420	1.032
6	418	420	1.160
7	418	420	1.288
8	418	420	1.416
9	418	420	1.544
10	418	420	1.672

C Dielectric Calibration

C.1. Equivalent circuit of the Spectroscopy Setup

In dielectric spectroscopy experiments, the real and imaginary parts of the total connected impedance are measured for the different frequencies, $\tilde{Z}^*(\nu) = \tilde{Z}'(\nu) + i\tilde{Z}''(\nu)$. These signals, besides the desired information on the sample impedance, also contain parasitic contributions from the line impedance and the impedance caused by an additional capacitance of the stray field around the sample.

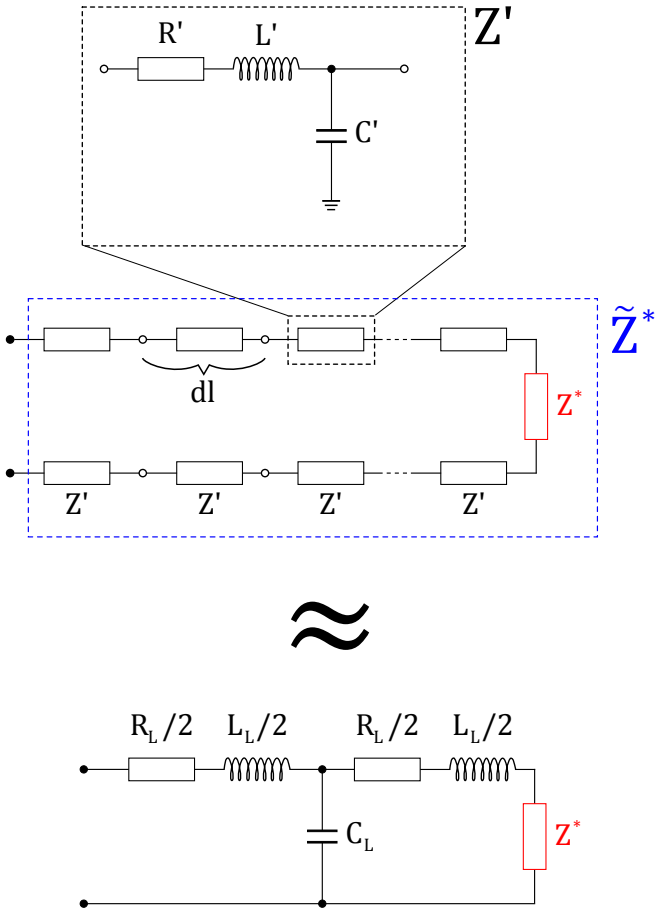

Figure C.1.: Equivalent circuit of line impedance and connected sample fixture impedance Z^*.

The line impedance is theoretically described by resistance, inductance and capacitance loads R', L', C' per unit length $\mathrm{d}l$ of cable, see Fig. C.1. For the experimental frequency range and length of connections, this can be approximated by concentrated R_L, L_L and C_L for the entirety of both connecting lines. In each line to and from the sample, the capacitance is assumed in the middle, bisecting the concentrated resistances and capacitances. The resulting equivalent circuit for both connections is depicted in Fig. C.1.

The total connected impedance Z^* contains the complex impedance of the sample itself Z_S^* and a parallel, parasitic impedance Z_P^* resulting from the complex capacitance of the sample fixture and the additional stray field in the vicinity. In case of a surrounding medium with small dielectric losses and low conductivity, which is given for gaseous media and pure liquid alcohols in the experimental frequency range, Z_P^* can be replaced with a real capacitance C_P in the equivalent circuit. The resulting total equivalent circuit is shown in Fig. C.2.

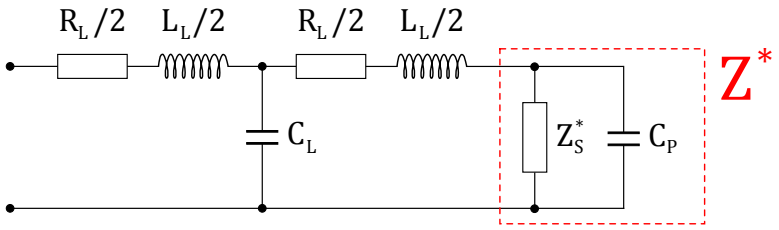

Figure C.2.: Total equivalent circuit for dielectric spectroscopy experiments.

Depending on the experiment, C_P may change over time, e.g. when the medium in the stray field changes gradually or abruptly. Then, it is inevitable that a variable stray capacitance remains in the measured data. Still, an automated fixture compensation can be performed in order to remove most effects of line impedance from the signal. In the process, the connected sample cell is replaced with a set of calibration pieces: A short circuit $R \approx 0\,\Omega$, a defined capacitance $C = 1\,\mathrm{pF}$ and resistor $R = 50\,\Omega$, respectively. By pre-recording a calibration spectrum for each, the impedance analyzer *Agilent 4294* can automatically eliminate the line resistance, inductance and capacitance. The corrected spectrum then reflects the total connected impedance $Z^*(\nu)$ as depicted in Fig. C.2, with a small remaining uncertainty due to the different fixtures of samples and calibration pieces. This method is used for all experiments in the imbibition setup, see Sec. 10.1.1 and the forced throughput apparatus, see Sec. 8.2.1.

For equilibrium and transient gas adsorption (see Sec. 4.1.2), the gaseous medium exhibits a relative permittivity $\varepsilon_R \approx 1$ for all partial pressures, resulting in a constant C_P at all times. A manual *in situ* calibration procedure then allows to calculate Z_S^* directly, see App. C.2, which is a preferable method.

C.2. Manual Calibration

The following two-step calibration procedure for the experimental setup described in Sec. 4.1.2 has been adopted from the work of Desclaux [63]. The main advantage of this calibration technique is a precise measurement of absolute permittivity values due to the complete elimination of parasitic impedances.

The first calibration measurement replaces the sample with a metal ring that acts as a short circuit. Then, both fixture capacitor plates are on the same potential and no parasitic capacitance C_P can occur, see Fig. C.3.

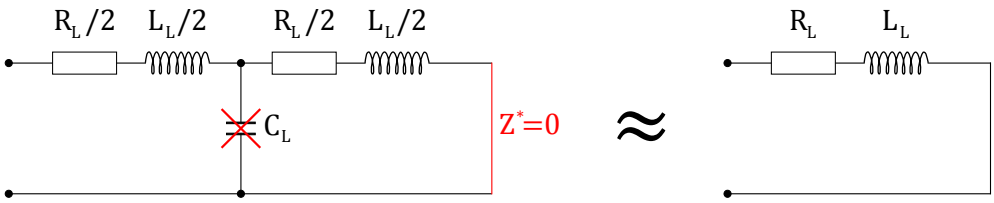

Figure C.3.: Equivalent circuit of short-circuit calibration.

For the experimental frequencies $\nu = 1\,\mathrm{kHz}$ to $2\,\mathrm{MHz}$, the impedance caused by the line capacitance C_L is very large in comparison to the other contributions, [63]. The equivalent circuit for the short-circuit calibration can then be simplified to a serial connection of R_L and L_L, see Fig. C.3. Both quantities are then calculated individually from the measured complex impedance spectrum for the metal ring, $Z^*_M(\nu)$,

$$R_L(\nu) = Z'_M(\nu) \tag{C.1}$$

and

$$L_L(\nu) = \frac{Z''_M(\nu)}{2\pi\nu}. \tag{C.2}$$

In the second calibration step, a PTFE ring (inner and outer radius r_i, r_o; thickness t) is used in lieu of a sample. In accordance with sample dimensions, this ring is smaller than the circular fixture capacitor electrodes (radius r_{el}). In the frequency range $1\,\mathrm{kHz}$ to $2\,\mathrm{MHz}$, the polymer material exhibits neither dipole relaxation nor conductivity effects, so that the relative permittivity is real and constant, $\varepsilon_{\mathrm{PTFE}} = 2.05$. Thus, the complex sample impedance is replaced with a constant, real capacitance C_S that can be calculated for the specified geometry of the calibration piece,

$$C_S = \varepsilon_0 \varepsilon_{\mathrm{PTFE}} \underbrace{\pi \left(r_o^2 - r_i^2\right)}_{A_{\mathrm{PTFE}}} \frac{1}{t}. \tag{C.3}$$

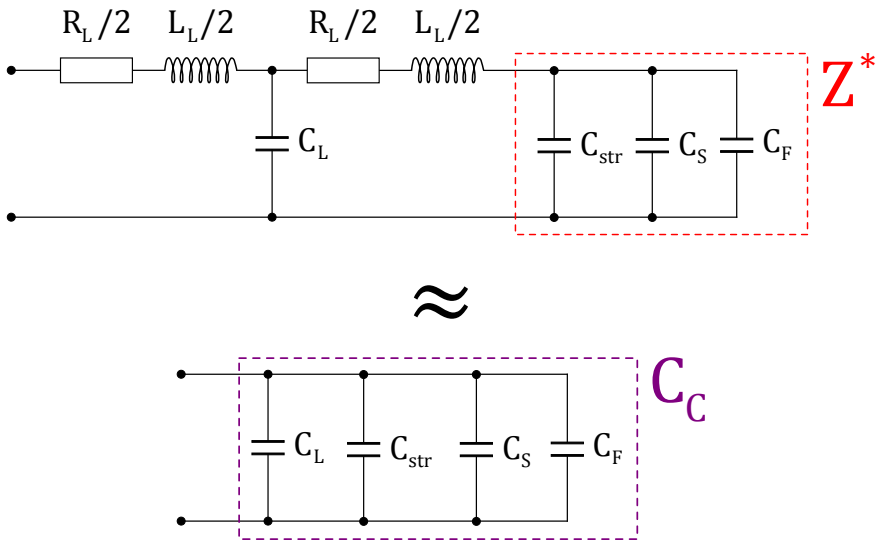

Figure C.4.: Equivalent circuit of PTFE calibration for $\frac{1}{2\pi\nu C_C} \gg R_L, 2\pi\nu L_L$.

The additional parasitic capacitance C_P is made up of a parallel circuit of the capacitance for the empty part of the fixture capacitor, C_F and the capacitance of the inhomogeneous stray field on the outside of the fixture, C_{str}. In theory, both values can be calculated for the known geometry of the fixture capacitor. However, any simple formula of the stray field capacitance critically relies on an idealized geometry, which would introduce an error when applied to estimate C_{str}. Thus, only C_F can be calculated using the known dimensions of the fixture and the calibration piece (with $\varepsilon_R \approx 1$),

$$C_F = \varepsilon_0 \frac{\pi r_{\text{el}}^2 - A_{\text{PTFE}}}{t}. \tag{C.4}$$

The equivalent circuit, as depicted in Fig. C.4, then contains two unknown capacitances C_{str} and C_L. Analogous to the short-circuit calibration, the impedance evoked by these capacitances is larger than the contributions from line resistance R_L and inductance L_L, so that a parallel circuit of all capacitances is an adequate approximation. Hence, from the measured calibration spectrum $Z_C^*(\nu)$, a complex capacitance can be calculated as

$$C_C^* = \frac{1}{2\pi\nu Z_C^*(\nu)}. \tag{C.5}$$

The imaginary part of this complex capacitance corresponds to an imaginary line capacitance that is negligible for the experimental frequency range $C_C'' = C_L'' \approx 0$. The real part C_C' on the other hand is equal to the parallel circuit of capacitances depicted in Fig. C.4. From this

total capacitance, C_L and C_{str} cannot be quantified separately, only their sum is known as

$$\begin{aligned} C_L + C_{\text{str}} &= C'_C - C_S - C_F \\ &= \frac{1}{2\pi\nu} \frac{-Z''_C(\nu)}{Z'_C(\nu)^2 + Z''_C(\nu)^2} - C_S - C_F. \end{aligned} \tag{C.6}$$

However, by choosing the thickness t of the PTFE calibration piece equal to the sample thickness, the stray capacitance C_{str} is equal for the calibration and the experiment. Moreover, when conducting a measurement on an unknown sample impedance, the same parallel circuit can be assumed for C_L and C_{str}, see Fig. C.5. This is a good approximation if the combined impedance $Z^*_{\text{S+F}}$ of the sample and fixture is much larger than the line impedance, as is the case in the frequency range of the experiments.

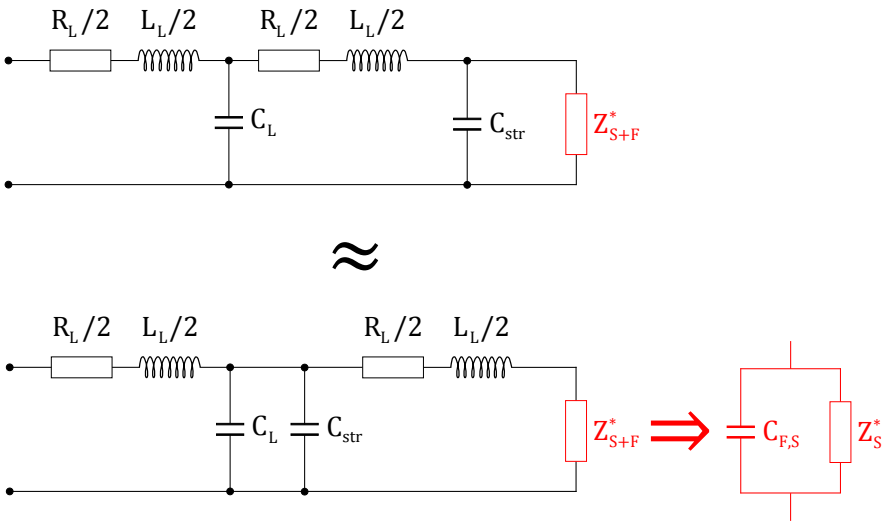

Figure C.5.: Modified equivalent circuit of sample measurement.

At this point, all elements of this equivalent circuit are known except $Z^*_{\text{S+F}}$, which in turn can be calculated from the complex measured spectrum of the entire circuit, $\tilde{Z}^*$,

$$Z^*_{\text{S+F}} = \left[\left(\tilde{Z}^* - \frac{R_L}{2} - i\omega \frac{L_L}{2} \right)^{-1} - i\omega \left(C^*_L + C_{\text{str}} \right) \right]^{-1} - \frac{R_L}{2} - i\omega \frac{L_L}{2}. \tag{C.7}$$

Finally, the fixture capacitance $C_{\text{F,S}}$ needs to be removed from the signal. In analogy to Eq.

(C.4), this constant value can be calculated from the known area of the sample,

$$C_{\mathrm{F,S}} = \varepsilon_0 \frac{\left(\pi r_{\mathrm{el}}^2 - A_{\mathrm{sample}}\right)}{t}. \tag{C.8}$$

$Z^*_{\mathrm{S+F}}$ is made up of a parallel circuit of the sample, Z^*_S, and the fixture capacitance $C_{\mathrm{F,S}}$,

$$\frac{1}{Z^*_{\mathrm{S+F}}} = \frac{1}{Z^*_S} + i\omega C_{\mathrm{F,S}}\ , \tag{C.9}$$

so that Z^*_S can be calculated accordingly using Eqs. (C.7), (C.8) and (C.9).

This calculation has been implemented as a MATLAB program. The calibration and experimental spectra are provided as input files (for equal frequency values) and the sample and PTFE geometry parameters as constants. The output is a series of corrected spectra for the real and imaginary parts of Z^*_S.

D Numerical Simulation of Multi-Sided Imbibition

D.1. Simulation Algorithm

A simple numerical flow simulation has been conducted in order to estimate the impact of additional parasitic imbibition from liquid menisci adhering to the macroscopic sample surface. The following procedure has been implemented in a custom MATLAB program for variable liquid parameters and sample sizes, which allowed a comparison to the experiments in Sec. 11.3.2.

The porous sample is modelled as a three-dimensional array of discrete finite volume elements. The individual cells with indices (i, j, k) are connected along the principal axes x, y, z. The volume cells are assumed as localized points on a cubic lattice with an inter-point connection length $\Delta x = \Delta y = \Delta z = l_C$[1] that doubles as the assumed volume of the cells $V_C = l_C^3$. The spatial resolution for simulation has been chosen so that l_C is in a range $\sim 10\,\mu\mathrm{m}$, which allows the application of macroscopic concepts for an average flow in the pore network instead of an individual pore modelling. An illustration of a typical situation of filling is depicted for a 2D cross-section through the sample geometry in Fig. D.1.

Due to the symmetry of the problem, only a quarter of the sample needs to be simulated. Infinite sources for liquid flow are placed on the bottom and on each of the sides where a meniscus is expected, up to a tunable height h_{men}. The remaining sample boundary is modelled as an infinite sink for liquid. From the sources, liquid can enter the pore space, which is quantified using Hagen-Poiseuille flow through the pore ensemble (of constant radius r_0), driven by a constant Laplace pressure. The flow boundary condition is chosen as no-slip ($b = 0$) and zero contact angle ($\theta = 0$). As a computational simplification, the flow from each source is limited to a specific direction (x, y or z) with no change allowed along the flow path. In accordance to Eq. (9.9), the volumetric flow rate for an exemplary x-distance $\Delta x = l_C \Delta i$

[1] Alternatively, a cuboid lattice with discretisations l_x, l_y, l_z has been used as well, which produced the same qualitative results

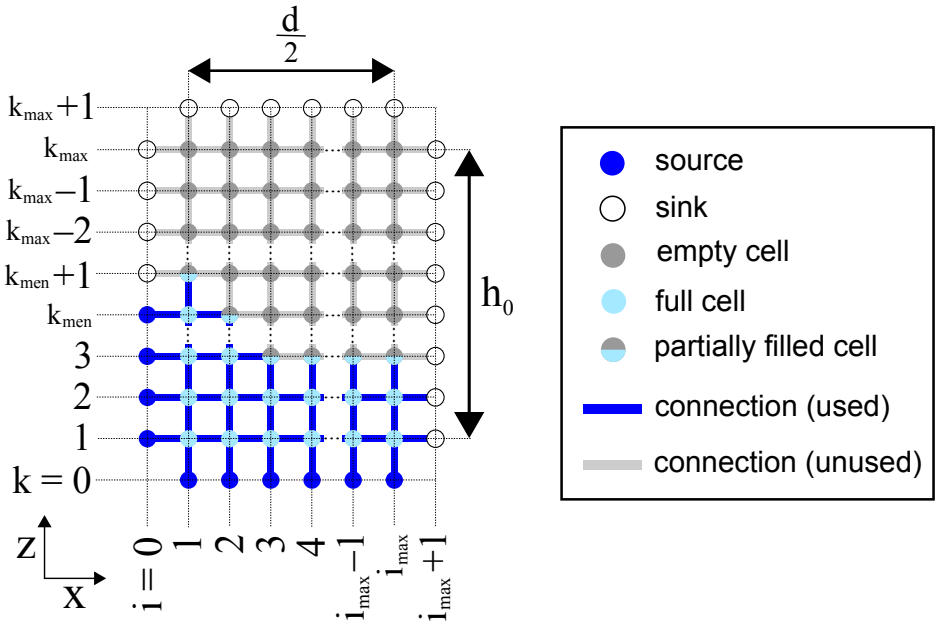

Figure D.1.: Illustration of the simulation geometry for the study of parasitic imbibition.

between a source and a target cell is then given by

$$Q_x = \frac{\Phi l_C \sigma r_0}{4\eta\tau} \frac{1}{\Delta i}. \tag{D.1}$$

Equivalent forms apply to the y and z directions. For a discrete simulation time step Δt, a flow rate Q increases the relative filling in the target cell by

$$\Delta f = Q / l_C^3 \Delta t. \tag{D.2}$$

By design of the simulation procedure, cells are required to fill up completely before liquid can advance to neighbouring cells, hence the flow from each source only reaches one destination at a time (or an infinite sink at the sample boundary). The first step of the simulation algorithm is to find these pairs of sources and target cells and to quantify the respective flows.

When all sources have been checked for their flow contributions, the respective Δf is added to the individual cell fillings. If a cell surpasses full filling ($f = 1$) during a simulation step, the remaining filling is redirected to an adjacent empty cell in the same direction of the flow. After this cell update has completed, the new total filling state $f(t)$ of the sample and additional simulation parameters are calculated, e.g. the coordinates of partially filled cells as an imbibition front profile. Finally, the simulation time is incremented to $t' = t + \Delta t$ with

a variable time step Δt for equidistant points on a $\sqrt{t}$ scale and the next simulation step is initiated if the sample is not completely filled.

In total, the simulation algorithm can be summarized by the following rules:

1. Find target for each liquid source and calculate Δf for a discrete time step.
2. Refresh the filling state of all target cells. In case of overfilling ($f > 1$), distribute the additional liquid to neighbouring cells.
3. Evaluate global filling and other simulation parameters.
4. Advance time and repeat until full.

Due to the simplifications of this modelling approach, there are some inherent weaknesses that should be mentioned: First, flow dynamics are modelled as averaged macroscopic flows. By definition, the pore size distribution and the resulting local flow rate differences are thus neglected in simulation. Second, the limitation of liquid flows to straight paths in parallel to the axes x, y and z, which simplifies the computation, is an arbitrary choice. In general, liquid is expected to spread isotropically in the matrix volume. This induced anisotropy is expected to result in a more angled shape of the simulated imbibition front. As a consequence, the shape of the profile should only be interpreted qualitatively, i.e. flat front or varying heights.

In conclusion, although the simple simulation algorithm does not allow to predict accurate distribution of liquid, it should still clearly indicate whether or not the initial liquid uptake from the sides causes a significant effect in total uptake dynamics. The qualitative results can then be compared with experimental observations for the first phase of imbibition experiments in Sec. 11.3.2.

D.2. Simulation Results

A simulated imbibition front profile for 1-decanol is shown in Fig. D.2. The resulting profile exhibits a rectangular trench in the centre of the sample for the first phase of imbibition, which is a consequence of the limitation to flows in x, y and z directions in the simulation algorithm. Over time, the empty central zone shrinks in all three dimensions until completely filled either by flows from the sides or from the bottom face. Depending on the geometry, this transition can be abrupt, which also reflects as discontinuities in the dynamics of total filling over time $f(t)$, as shown in Fig. D.3.

For all times, the liquid in the cells closest to the sample surface is always further ascended than in the core of the sample, resulting in an overall curvature of the imbibition front.

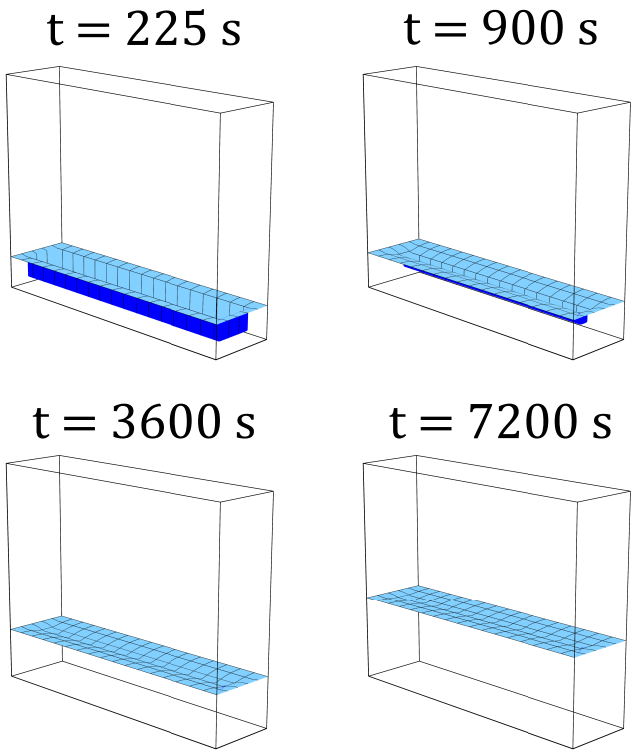

Figure D.2.: Simulated imbibition front profile for 1-decanol, simulated for a relative external meniscus height $h_{\mathrm{men}}/h_0 = 0.14$.

However, as the simulation progresses, the height difference is gradually reduced until the imbibition front is quasi-flat. From this point, it is expected that Lucas-Washburn dynamics prevail, see Sec. 9.2.

The simulated relative filling $f(t)$ for 1-decanol is depicted as a function of $\sqrt{t}$ in Fig. D.3. Here, as it is not known *a priori*, the height of external menisci has been varied. Notably, the simulation for all meniscus heights shows a limited time frame of the initial effects and a subsequent linear segment indicating Lucas-Washburn dynamics. An increase of h_{men} leads to both a larger extent as well as a longer time span for the initial effects, though no significant alteration of the second stage dynamics remains in the long-time limit.

From experimental observations, a meniscus height in the range $1\,\mathrm{mm}$ to $2\,\mathrm{mm}$ is expected. Accordingly, a comparison of the experimental uptake curve to the simulation for $h_{\mathrm{men}} = 1.5\,\mathrm{mm}$ is depicted in Fig. D.4. Both curves exhibit similar characteristics of the initial effects. In particular, the duration of the approach to linear dynamics are identical. Note that the flow calculation in this simulation has been scaled in order to match the Lucas-Washburn coefficient of the experiment.

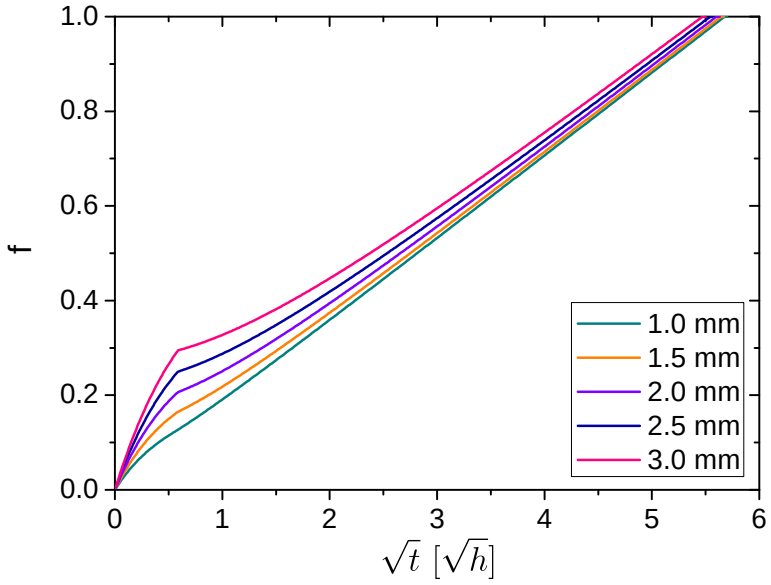

Figure D.3.: Simulated liquid uptake for 1-decanol for variable external meniscus height h_{men}. Two different stages of uptake are resolved, exhibiting a major stage of Lucas-Washburn dynamics for large times.

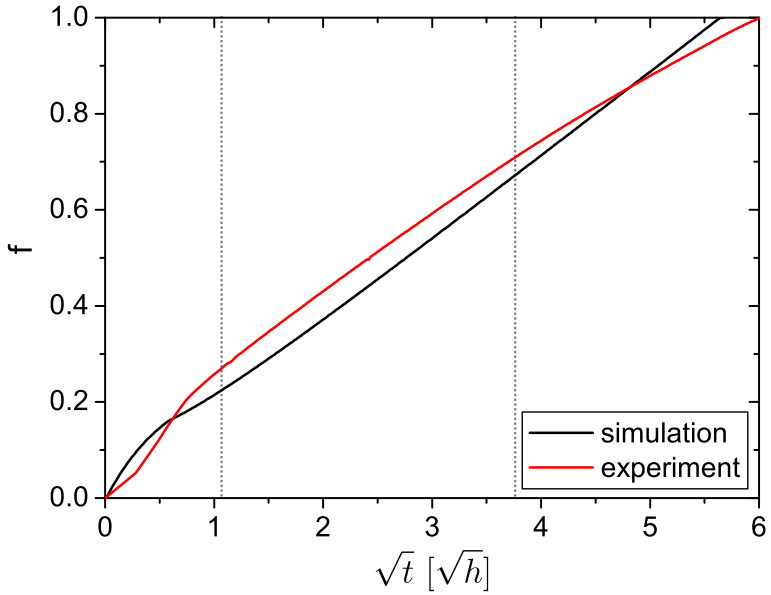

Figure D.4.: Comparison of simulated and experimental uptake for 1-decanol. The flow rate calculation in simulation has been scaled to match the experimental Lucas-Washburn coefficient.

Bibliography

[1] Yiu H.H.P., Botting C.H., Botting N.P., und Wright P.A. Size Selective Protein Adsorption on Thiol-functionalised SBA-15 Mesoporous Molecular Sieve. *Physical Chemistry Chemical Physics*, **3**:2983–2985 (2001).

[2] Mao Z. und Sinnott S.B. Separation of Organic Molecular Mixtures in Carbon Nanotubes and Bundles: Molecular Dynamics Simulations. *The Journal of Physical Chemistry B*, **105**(29):6916–6924 (2001).

[3] Huber P. Soft Matter in Hard Confinement: Phase Transition Thermodynamics, Structure, Texture, Diffusion and Flow in Nanoporous Media. *Journal of Physics: Condensed Matter*, **27**(10):103102 (2015).

[4] Elmer T. *Engineered Materials Handbook, Volume 4: Ceramics and Glasses*, Kap. Porous and Reconstructed Glasses, (S. 427–432). ASM International (1991).

[5] Gruener S. und Huber P. Spontaneous Imbibition Dynamics of an n-Alkane in Nanopores: Evidence of Meniscus Freezing and Monolayer Sticking. *Physical Review Letters*, **103**:174501 (2009).

[6] Taguchi A. und Schüth F. Ordered Mesoporous Materials in Catalysis. *Microporous and Mesoporous Materials*, **77**(1):1–45 (2005).

[7] Takahashi T., Yanagimoto Y., Matsuoka T., und Kai T. Hydrogenation Activity of Benzenes on Nickel Catalysts Supported on Porous Glass Prepared from Borosilicate Glass with Small Amounts of Metal Oxides. *Microporous Materials*, **6**(4):189–194 (1996).

[8] Janowski F., Fischer G., Urbaniak W., Foltynowicz Z., und Marciniec B. Aminopropylsilane Treatment for the Surface of Porous Glasses Suitable for Enzyme Immobilisation. *Journal of Chemical Technology and Biotechnology*, **51**(2):263–272 (1991).

[9] Anglin E.J., Cheng L., Freeman W.R., und Sailor M.J. Porous Silicon in Drug Delivery Devices and Materials. *Advanced Drug Delivery Reviews*, **60**(11):1266–1277 (2008).

[10] Schoch R.B., Han J., und Renaud P. Transport Phenomena in Nanofluidics. *Review of Modern Physics*, **80**:839–883 (2008).

[11] Gad-El-Hak M. Gas and Liquid Transport at the Microscale. *Heat Transfer Engineering*, **27**(4):13–29 (2006).

[12] Sparreboom W., van den Berg A., und Eijkel J.C.T. Transport in nanofluidic systems: a review of theory and applications. *New Journal of Physics*, **12**(1):015004 (2010).

[13] McNaught A. und Wilkinson A. *Compendium of Chemical Terminology: IUPAC Recommendations (Gold Book).* IUPAC International Union of Pure and Applied Chemistry (1997).

[14] Ciesla U. und Schüth F. Ordered Mesoporous Materials. *Microporous and Mesoporous Materials*, **27**(2-3):131–149 (1999).

[15] Zhao D., Feng J., Huo Q., Melosh N., Fredrickson G.H., Chmelka B.F., und Stucky G.D. Triblock Copolymer Syntheses of Mesoporous Silica with Periodic 50 to 300 Angstrom Pores. *Science*, **279**(5350):548–552 (1998).

[16] Masuda H., Hasegwa F., und Ono S. Self-Ordering of Cell Arrangement of Anodic Porous Alumina Formed in Sulfuric Acid Solution. *Journal of The Electrochemical Society*, **144**(5):L127–L130 (1997).

[17] Dorcheh A.S. und Abbasi M. Silica Aerogel; Synthesis, Properties and Characterization. *Journal of Materials Processing Technology*, **199**(1-3):10 – 26 (2008).

[18] Porter H. und Emery N. Treated Borosilicate Glass, US Patent 2106744A (1934).

[19] Enke D., Janowski F., und Schwieger W. Porous Glasses in the 21st Century - a Short Review. *Microporous and Mesoporous Materials*, **60**(1-3):19–30 (2003).

[20] Cahn J.W. und Hilliard J.E. Free Energy of a Nonuniform System. I. Interfacial Free Energy. *The Journal of Chemical Physics*, **28**(2):258–267 (1958).

[21] Eyre D.J. Unconditionally Gradient Stable Time Marching the Cahn-Hilliard Equation. In *MRS Proceedings*, vol. 529, (S. 39). Cambridge Univ Press (1998).

[22] Bohr N. *Dielektrische Untersuchung zur Dynamik des Kapillarsteigens und der Gasadsorption in Nanoporen, Staatsexamensarbeit.* Saarland University (2013).

[23] Zhuravlev L. The Surface Chemistry of Amorphous Silica. Zhuravlev Model. *Colloids and Surfaces A: Physicochemical and Engineering Aspects*, **173**(1-3):1–38 (2000).

[24] Parida S.K., Dash S., Patel S., und Mishra B. Adsorption of Organic Molecules on Silica Surface. *Advances in Colloid and Interface Science*, **121**(1-3):77–110 (2006).

[25] Gallo P., Ricci M.A., und Rovere M. Layer Analysis of the Structure of Water Confined in Vycor Glass. *The Journal of Chemical Physics*, **116**(1):342–346 (2002).

[26] Kremer F. und Schönhals A., Herausgeber. *Broadband Dielectric Spectroscopy*. Springer-Verlag (2003).

[27] Daniel V.V. *Dielectric Relaxation*. Academic Press (1967).

[28] Havriliak S. und Negami S. A Complex Plane Representation of Dielectric and Mechanical Relaxation Processes in Some Polymers. *Polymer*, **8**:161–210 (1967).

[29] Pissis P., Laudat J., Daoukaki D., und Kyritsis A. Dynamic Properties of Water in Porous Vycor Glass Studied by Dielectric Techniques. *Journal of Non-Crystalline Solids*, **171**(2):201–207 (1994).

[30] Sinha G.P. und Aliev F.M. Dielectric Spectroscopy of Liquid Crystals in Smectic, Nematic, and Isotropic Phases Confined in Random Porous Media. *Physical Review E*, **58**:2001–2010 (1998).

[31] Sihvola A.H. *Electromagnetic Mixing Formulas and Applications*. 47. The Institution of Engineering and Technology (1999).

[32] Bergman D.J. Rigorous Bounds for the Complex Dielectric Constant of a Two-Component Composite. *Annals of Physics*, **138**(1):78–114 (1982).

[33] Bergman D.J. Exactly Solvable Microscopic Geometries and Rigorous Bounds for the Complex Dielectric Constant of a Two-Component Composite Material. *Physical Review Letters*, **44**:1285–1287 (1980).

[34] Hallouet B. *Mikrostruktur und effektive Eigenschaften von dielektrischen Kompositen: das inverse Problem, Dissertation*. Saarland University (2014).

[35] Kaatze U., Behrends R., und Pottel R. Hydrogen Network Fluctuations and Dielectric Spectrometry of Liquids. *Journal of Non-Crystalline Solids*, **305**(1-3):19–28 (2002).

[36] Wohlfarth C. und Madelung O. *Landolt-Börnstein - Group IV Physical Chemistry: Static Dielectric Constants of Pure Liquids and Binary Liquid Mixtures*, vol. IV/6 of *Landolt-Börnstein - Group IV Physical Chemistry*. Springer-Verlag (1991).

[37] Pelster R. Dielectric Spectroscopy of Confinement Effects in Polar Materials. *Physical Review B*, **59**:9214–9228 (1999).

[38] Butt H.J., Graf K., und Kappl M. *Physics and Chemistry of Interfaces*. John Wiley & Sons (2006).

[39] Rouquerol J., Rouquerol F., Llewellyn P., Maurin G., und Sing K.S. *Adsorption by Powders and Porous Solids: Principles, Methodology and Applications*. Academic press (2013).

[40] Baumert J., Asmussen B., Gutt C., und Kahn R. Pore-Size Dependence of the Self-Diffusion of Hexane in Silica Gels. *The Journal of Chemical Physics*, **116**(24):10869–10876 (2002).

[41] Schappert K. und Pelster R. Unexpected Sorption-Induced Deformation of Nanoporous Glass: Evidence for Spatial Rearrangement of Adsorbed Argon. *Langmuir*, **30**(46):14004–14013 (2014).

[42] Dunne J.A., Mariwala R., Rao M., Sircar S., Gorte R.J., und Myers A.L. Calorimetric Heats of Adsorption and Adsorption Isotherms. 1. O2, N2, Ar, CO2, CH4, C2H6, and SF6 on Silicalite. *Langmuir*, **12**(24):5888–5895 (1996).

[43] Brunauer S., Emmett P.H., und Teller E. Adsorption of Gases in Multimolecular Layers. *Journal of the American Chemical Society*, **60**(2):309–319 (1938).

[44] Thommes M.and Kaneko K., Neimark A.V., Olivier J.P., Rodriguez-Reinoso F., Rouquerol J., und Sing K.S.W. Physisorption of Gases, with Special Reference to the Evaluation of Surface Area and Pore Size Distribution (IUPAC Technical Report). *Pure and Applied Chemistry*, **87**(9-10):1051–1069 (2015).

[45] Gregg S. und Sing K. *Adsorption, Surface Area, and Porosity*. Academic Press (1982).

[46] Sing K., Everett D., Haul R., Moscou L., Pierotti R., Rouquerol J., und Siemieniewska T. Reporting Physisorption Data for 1, 0x10-3 1, 2x10-3 1, 4x10-3 1, 6x10-3 1, 8x10-3 2, 0x10-3-8-6-4-2 0 2 4-1 K) I II III Gas/Solid Systems with Special Reference to the Determination of Surface Area and Porosity. *Pure and Applied Chemistry*, **57**:603–619 (1985).

[47] Wallacher D. und Knorr K. Melting and freezing of Ar in nanopores. *Physical Review B*, **63**:104202 (2001).

[48] Gruener S. *Rheology and Dynamics of Simple and Complex Liquids in Mesoporous Matrices, Dissertation.* Saarland University, Saarbrücken, Germany (2010).

[49] Bommer S. *Gas- und Proteinpermeabilitätsmessungen an biomimetischen Festkörpermembranen, Diplomarbeit.* Saarland University, Saarbrücken, Germany (2008).

[50] Seaton N. Determination of the Connectivity of Porous Solids from Nitrogen Sorption Measurements. *Chemical Engineering Science*, **46**(8):1895–1909 (1991).

[51] de Boer J., Lippens B., Linsen B., Broekhoff J., van den Heuvel A., und Osinga T.J. The t-Curve of Multimolecular N_2-Adsorption. *Journal of Colloid and Interface Science*, **21**(4):405–414 (1966).

[52] Harkins W.D. und Jura G. Surfaces of Solids. XIII. A Vapor Adsorption Method for the Determination of the Area of a Solid Without the Assumption of a Molecular Area, and the Areas Occupied by Nitrogen and Other Molecules on the Surface of a Solid. *Journal of the American Chemical Society*, **66**(8):1366–1373 (1944).

[53] Halsey G. Physical Adsorption on Non-Uniform Surfaces. *The Journal of Chemical Physics*, **16**(10):931–937 (1948).

[54] Lowell S., Shields J.E., Thomas M.A., und Thommes M. *Characterization of Porous Solids and Powders: Surface Area, Pore Size and Density*, vol. 16. Springer Science & Business Media (2012).

[55] Pierce C. The Frenkel-Halsey-Hill Adsorption Isotherm and Capillary Condensation. *The Journal of Physical Chemistry*, **64**(9):1184–1187 (1960).

[56] Barrett E.P., Joyner L.G., und Halenda P.P. The Determination of Pore Volume and Area Distributions in Porous Substances. I. Computations from Nitrogen Isotherms. *Journal of the American Chemical Society*, **73**(1):373–380 (1951).

[57] Sing K. The Use of Nitrogen Adsorption for the Characterisation of Porous Materials. *Colloids and Surfaces A: Physicochemical and Engineering Aspects*, **187-188**:3–9 (2001).

[58] Fisher L.R. und Israelachvili J.N. Experimental Studies on the Applicability of the Kelvin Equation to Highly Curved Concave Menisci. *Journal of Colloid and Interface Science*, **80**(2):528–541 (1981).

[59] Saam W.F. und Cole M.W. Excitations and Thermodynamics for Liquid-Helium Films. *Physical Review B*, **11**:1086–1105 (1975).

[60] Gelb L.D., Gubbins K.E., Radhakrishnan R., und Sliwinska-Bartkowiak M. Phase Separation in Confined Systems. *Reports on Progress in Physics*, **62**(12):1573 (1999).

[61] Ravikovitch P.I. und Neimark A.V. Characterization of Nanoporous Materials from Adsorption and Desorption Isotherms. *Colloids and Surfaces A: Physicochemical and Engineering Aspects*, **187-188**:11–21 (2001).

[62] Schappert K. und Gor G. Comparison of Kelvin and NLDFT Pore Size Distributions for Vycor. Private communication.

[63] Desclaux P. *Dielektrische Analyse von Interphasen in Polymer-Kompositen, Diplomarbeit.* Saarland University (2008).

[64] Vogelgesang J. *Gasadsorption von Alkohol in mesoporösem Vycor, Staatsexamensarbeit.* Saarland University (2016).

[65] Argyris D., Tummala N.R., Striolo A., und Cole D.R. Molecular Structure and Dynamics in Thin Water Films at the Silica and Graphite Surfaces. *Journal of Physical Chemistry C*, **112**(35):13587–13599 (2008).

[66] Jones B. und Wade W. Adsorption Hysteresis for Alcohols in Porous Vycor. *Journal of Colloid and Interface Science*, **28**(3):415–420 (1968).

[67] Milischuk A.A. und Ladanyi B.M. Structure and Dynamics of Water Confined in Silica Nanopores. *The Journal of Chemical Physics*, **135**(17):174709 (2011).

[68] Hare E. und Zisman W. Autophobic Liquids and the Properties of Their Adsorbed Films. *The Journal of Physical Chemistry*, **59**(4):335–340 (1955).

[69] Mitropoulos A. Small-Angle X-ray Scattering Studies of Adsorption in Vycor Glass. *Journal of Colloid and Interface Science*, **336**(2):679–690 (2009).

[70] Novotny V. und Marmur A. Wetting Autophobicity. *Journal of Colloid and Interface Science*, **145**(2):355–361 (1991).

[71] Barto J., Durham J., Baston V., und Wade W. The Gas Phase Autophobicity of Alcohols Adsorbed on Alumina. *Journal of Colloid and Interface Science*, **22**(5):491–501 (1966).

[72] Einstein A. Über die von der molekularkinetischen Theorie der Wärme geforderte Bewegung von in ruhenden Flüssigkeiten suspendierten Teilchen. *Annalen der Physik*, **322**(8):549–560 (1905).

[73] Kärger J., Ruthven D.M., und Theodorou D.N. *Diffusion in Nanoporous Materials.* John Wiley & Sons (2012).

[74] Crank J. *The Mathematics of Diffusion.* Oxford University Press (1979).

[75] Beskok A. und Karniadakis G.E. Report: A Model For Flows in Channels, Pipes, and Ducts at Micro and Nano Scales. *Microscale Thermophysical Engineering*, **3**(1):43–77 (1999).

[76] Cao B.Y., Chen M., und Guo Z.Y. Temperature Dependence of the Tangential Momentum Accommodation Coefficient for Gases. *Applied Physics Letters*, **86**(9):091905 (2005).

[77] Beskok A. und Karniadakis G. *Micro Flows - Fundamentals and Simulation.* Springer-Verlag (2002).

[78] Malek K. und Coppens M.O. Effects of Surface Roughness on Self- and Transport Diffusion in Porous Media in the Knudsen Regime. *Physical Review Letters*, **87**:125505 (2001).

[79] Chapman S. und Cowling T.G. *The mathematical theory of non-uniform gases: an account of the kinetic theory of viscosity, thermal conduction and diffusion in gases.* Cambridge university press (1970).

[80] Marrero T.R. und Mason E.A. Gaseous Diffusion Coefficients. *Journal of Physical and Chemical Reference Data*, **1**(1):3–118 (1972).

[81] Scott D.S. und Dullien F.A.L. Diffusion of Ideal Gases in Capillaries and Porous Solids. *AIChE Journal*, **8**(1):113–117 (1962).

[82] Reed D.A. und Ehrlich G. Surface Diffusion, Atomic Jump Rates and Thermodynamics. *Surface Science*, **102**(2):588–609 (1981).

[83] Kiepsch S. *Einfluss von Wandrauhigkeiten auf den Gasfluss in mesoporösen Festkörpermembranen, Diplomarbeit.* Saarland University (2011).

[84] Ruthven D.M., DeSisto W., und Higgins S. Diffusion in a Mesoporous Silica Membrane: Validity of the Knudsen Diffusion Model. *Chemical Engineering Science*, **64**(13):3201–3203 (2009).

[85] Lin M.Y., Abeles B., Huang J.S., Stasiewski H.E., und Zhang Q. Viscous Flow and Diffusion of Liquids in Microporous Glasses. *Physical Review B*, **46**:10701–10705 (1992).

[86] Costa E., Calleja G., und Domingo F. Adsorption of Gaseous Hydrocarbons on Activated Carbon: Characteristic Kinetic Curve. *AIChE Journal*, **31**(6):982–991 (1985).

[87] Valiullin R., Kortunov P., Kärger J., und Timoshenko V. Concentration-Dependent Self-Diffusion of Liquids in Nanopores: A Nuclear Magnetic Resonance Study. *The Journal of Chemical Physics*, **120**(24):11804–11814 (2004).

[88] Valiullin R., Naumov S., Galvosas P., Kärger J., Woo H., Porcheron F., und Monson P.A. Exploration of Molecular Dynamics During Transient Sorption of Fluids in Mesoporous Materials. *Nature*, **443**(7114):965–968 (2006).

[89] Vogel H. *Gerthsen Physik, 18. Auflage*. Springer-Verlag (1995).

[90] Wade W. Spontaneous Imbibition of Fluids in Porous Vycor. *Society of Petroleum Engineers Journal*, **14**(02):139–144 (1974).

[91] Raviv U., Laurat P., und Klein J. Fluidity of Water Confined to Subnanometre Films. *Nature*, **413**(6851):51–54 (2001).

[92] Israelachvili J.N. Measurement of the Viscosity of Liquids in Very Thin Films. *Journal of Colloid and Interface Science*, **110**(1):263–271 (1986).

[93] Voronov R.S., Papavassiliou D.V., und Lee L.L. Boundary Slip and Wetting Properties of Interfaces: Correlation of the Contact Angle with the Slip Length. *The Journal of Chemical Physics*, **124**(20):204701 (2006).

[94] Barrat J.L. und Bocquet L. Large Slip Effect at a Nonwetting Fluid-Solid Interface. *Physical Review Letters*, **82**:4671–4674 (1999).

[95] Gruener S., Hofmann T., Wallacher D., Kityk A.V., und Huber P. Capillary Rise of Water in Hydrophilic Nanopores. *Physical Review E*, **79**:067301 (2009).

[96] Cheikh C. und Koper G. Stick-Slip Transition at the Nanometer Scale. *Physical Review Letters*, **91**:156102 (2003).

[97] Gruener S., Wallacher D., Greulich S., Busch M., und Huber P. Hydraulic Transport Across Hydrophilic and Hydrophobic Nanopores: Flow Experiments with Water and n-hexane. *Physical Review E*, **93**:013102 (2016).

[98] Debye P. und Cleland R.L. Flow of Liquid Hydrocarbons in Porous Vycor. *Journal of Applied Physics*, **30**(6):843–849 (1959).

[99] Lamberti C. *Dielektrische Spektroskopie an strömenden Flüssigkeiten in mesoporösen Materialien, Staatsexamensarbeit.* Saarland University (2014).

[100] Mizukami M., Moteki M., und Kurihara K. Hydrogen-Bonded Macrocluster Formation of Ethanol on Silica Surfaces in Cyclohexane. *Journal of the American Chemical Society*, **124**(43):12889–12897 (2002).

[101] Heinbuch U. und Fischer J. Liquid Flow in Pores: Slip, No-Slip, or Multilayer Sticking. *Physical Review A*, **40**:1144–1146 (1989).

[102] Stephenson R. und Stuart J. Mutual Binary Solubilities: Water-Alcohols and Water-Esters. *Journal of Chemical & Engineering Data*, **31**(1):56–70 (1986).

[103] Alava M., Dubé M., und Rost M. Imbibition in Disordered Media. *Advances in Physics*, **53**(2):83–175 (2004).

[104] Lucas R. Über das Zeitgesetz des kapillaren Aufstiegs von Flüssigkeiten. *Kolloid Zeitschrift*, **23**(1):15–22 (1918).

[105] Washburn E.W. The Dynamics of Capillary Flow. *Physical Review*, **17**:273–283 (1921).

[106] Bell J.M. und Cameron F.K. The Flow of Liquids through Capillary Spaces. *The Journal of Physical Chemistry*, **10**(8):658–674 (1905).

[107] Dimitrov D.I., Milchev A., und Binder K. Capillary Rise in Nanopores: Molecular Dynamics Evidence for the Lucas-Washburn Equation. *Physical Review Letters*, **99**:054501 (2007).

[108] Gelb L.D. und Hopkins A.C. Dynamics of the Capillary Rise in Nanocylinders. *Nano Letters*, **2**(11):1281–1285 (2002).

[109] Yamashita K. und Daiguji H. Molecular Dynamics Simulations of Water Uptake into a Silica Nanopore. *The Journal of Physical Chemistry C*, **119**(6):3012–3023 (2015).

[110] Rieger H., Thome C., und Sadjadi Z. Meniscus Arrest Dominated Imbibition Front Roughening in Porous Media with Elongated Pores. *Journal of Physics: Conference Series*, **638**(1):012007 (2015).

[111] Sadjadi Z. und Rieger H. Scaling Theory for Spontaneous Imbibition in Random Networks of Elongated Pores. *Physical Review Letters*, **110**:144502 (2013).

[112] Gruener S., Sadjadi Z., Hermes H.E., Kityk A.V., Knorr K., Egelhaaf S.U., Rieger H., und Huber P. Anomalous front broadening during spontaneous imbibition in a matrix with elongated pores. *Proceedings of the National Academy of Sciences of the United States of America*, **109**(26):10245–10250 (2012).

[113] Siebold A., Nardin M., Schultz J., Walliser A., und Oppliger M. Effect of Dynamic Contact Angle on Capillary Rise Phenomena. *Colloids and Surfaces A: Physicochemical and Engineering Aspects*, **161**(1):81–87 (2000).

[114] Joos P., Remoortere P.V., und Bracke M. The Kinetics of Wetting in a Capillary. *Journal of Colloid and Interface Science*, **136**(1):189–197 (1990).

[115] Martic G., Gentner F., Seveno D., Coulon D., De Coninck J., und Blake T.D. A Molecular Dynamics Simulation of Capillary Imbibition. *Langmuir*, **18**(21):7971–7976 (2002).

[116] Chibbaro S., Biferale L., Diotallevi F., Succi S., Binder K., Dimitrov D., Milchev A., Girardo S., und Pisignano D. Evidence of thin-film precursors formation in hydrokinetic and atomistic simulations of nano-channel capillary filling. *Europhysics Letters*, **84**(4):44003 (2008).

[117] Robert E. *Dielectric Capillary Rise in Nanoporous Vycor-Glass, Bachelor thesis*. Saarland University (2011).

[118] Huber P., Grüner S., Schäfer C., Knorr K., und Kityk A.V. Rheology of Liquids in Nanopores: A Study on the Capillary Rise of Water, n-Hexadecane and n-Tetracosane in Mesoporous Silica. *The European Physical Journal Special Topics*, **141**(1):101–105 (2007).

[119] Jacob J. *Einfluss der Gasadsorption auf das Kapillarsteigen in Nanoporen, Staatsexamensarbeit*. Saarland University (2015).

[120] Kiepsch S. und Pelster R. Interplay of Vapor Adsorption and Liquid Imbibition in Nanoporous Vycor Glass. *Physical Review E*, **93**:043128 (2016).

[121] Wohlfarth C. und Wohlfarth B. *Landolt-Börnstein - Group IV Physical Chemistry: Viscosity of Pure Organic Liquids and Binary Liquid Mixtures*, vol. IV/18B. Springer-Verlag (2002).

[122] Wohlfarth C. und Wohlfarth B. *Landolt-Börnstein - Group IV Physical Chemistry: Surface Tension of Pure Liquids and Binary Liquid Mixtures*, vol. IV/16. Springer-Verlag (1997).

[123] Frenkel M., Hong X., Wilhoit R., und Hall K. *Landolt-Börnstein - Group IV Physical Chemistry: Thermodynamic Properties of Organic Compounds and their Mixtures*, vol. IV/8G. Springer-Verlag (1998).

[124] Dykyj J., Svoboda J., Wilhoit R., Frenkel M., und Hall K. *Landolt-Börnstein - Group IV Physical Chemistry: Vapor Pressure of Chemicals - Vapor Pressure and Antoine Constants for Oxygen Containing Organic Compounds*, vol. IV/20B. Springer-Verlag (2000).

[125] Allen F.H., Kennard O., Watson D.G., Brammer L., Orpen A.G., und Taylor R. Tables of Bond Lengths Determined by X-ray and Neutron Diffraction. Part 1. Bond Lengths in Organic Compounds. *Journal of the Chemical Society, Perkin Transactions 2*, (S. S1–S19) (1987).

[126] Bondi A. van der Waals Volumes and Radii. *The Journal of Physical Chemistry*, **68**(3):441–451 (1964).

[127] Chen B., Potoff J.J., und Siepmann J.I. Monte Carlo Calculations for Alcohols and Their Mixtures with Alkanes. Transferable Potentials for Phase Equilibria. 5. United-Atom Description of Primary, Secondary, and Tertiary Alcohols. *The Journal of Physical Chemistry B*, **105**(15):3093–3104 (2001).

List of Tables

List of Figures

Danksagung

Mein besonderer Dank gilt Herrn Prof. Dr. Rolf Pelster für die Möglichkeit, diese Arbeit unter seiner Betreuung anzufertigen. Sein stets offenes Ohr bei theoretischen und praktischen Fragen, die wertvollen Anregungen und die Diskussion der physikalischen Interpretationen meiner Ergebnisse waren entscheidend für das Gelingen dieser Arbeit.

Weiterhin danke ich allen heutigen oder ehemaligen Mitgliedern der Arbeitsgruppe von Prof. Dr. Pelster, die mir stets hilfsbereit zur Seite standen und ein wunderbares Arbeitsumfeld in freundlicher Gemeinschaft boten. Hervorgehoben seien vor allem Christina Werle, Dr. Béatrice Hallouet, Dr. Daniel Rau, Dr. Klaus Schappert und Tobias Weber.

Ein großer Dank gebührt auch Nico Bohr, Christian Lamberti, Johannes Jacob und Jeannette Vogelgesang, die unter meiner Betreuung im Rahmen ihrer durchgeführten Abschlussarbeiten einen sehr wertvollen Beitrag zu dieser Arbeit geleistet haben.

Für die Umsetzung und Instandhaltung der experimentellen Aufbauten möchte ich mich bei der feinmechanischen Werkstatt unter Leitung von Michael Schmidt und der Elektronikwerkstatt von Stefan Loew bedanken. Mit viel Erfahrung, Rat und Tat setzten sie meine Ideen vom Papier in die Praxis um und haben oft auch in kurzer Zeit eine Lösung für technische Probleme finden können.

Darüber hinaus danke ich allen weiteren Personen, die meine Zeit an der Universität des Saarlandes angenehm, interessant und kurzweilig gestaltet haben.

Zu guter Letzt danke ich meiner Familie und Freunden und für ihre vielfältige Unterstützung in allen Belangen innerhalb der letzten Jahre. Insbesondere meinen Eltern Mathilde und Andreas Kiepsch gilt mein herzlichster Dank für ihre Hilfe und Ermutigung. Ihre Förderung meiner Interessen für Naturwissenschaften und Technik hat mich überhaupt erst auf diesen Pfad gebracht.